

# **Single and multiphase flow properties of fault rocks: implications for petroleum production**

**JAVED HANEEF**

Submitted in accordance with requirement for the degree of

**Doctor of Philosophy**



**The University of Leeds**

**School of Earth and Environment**

**May 2016**

## **Declaration of Authorship**

The candidate confirms that the work submitted is his own, except where work which has formed part of jointly-authored publications has been included. The contribution of the candidate and the other authors to this work has been explicitly indicated below.

The candidate confirms that appropriate credit has been given within the thesis where reference has been made to the work of others.

This copy has been supplied on the understanding that it is copyright material and that no quotation from the thesis may be published without proper acknowledgement.

© 2016 The University of Leeds and Javed Haneef

*To..*

*My Mother, my wife, daughters and all of my family ...*

# ACKNOWLEDGMENT

First of all, thanks to almighty Allah for giving me the strength and guidance all the way to accomplish this goal.

I would like to express my heartiest gratitude to my supervisors Professor Quentin Fisher and Dr. Carlos Grattoni for their continuous help, guidance and encouragement throughout my studies. The completion of this thesis would not have been possible without their help, guidance and support. They have given me knowledge, training and problem solving skills which will be the great asset for my future life. I can say that it is a privilege to be a student of my supervisors and learned from them. I cannot express my thanks in words for their kindness in completion of my thesis.

I would also like to thanks to Phil Guise and John Martin for their technical help in lab work and their kind encouragement during my studies. Special thanks to Dr. Pirooska for her moral support and giving me the opportunity for demonstrations in her courses which refreshes my reservoir engineering. I would also thanks to my all colleagues who always with me to support me, specially Sam, Tom Lynch, Ida, Fridon, Dewan, Ieva, Yameen, Afridi and all others who I have not mentioned individually for their help. I would like to thank to NED University for supporting me to study at University of Leeds. It was an honour for me to study at University of Leeds.

Last, but never least, great and very sincere thanks to my mother, my wife Uroos and my daughters Maham, Aena, and Rida who missed me a lot, for their patience, sacrifice, emotional support and encouragement. Similarly loads of thanks to my sisters, brothers and all other family members for their best wishes and encouragement to accomplish this task.

## **Abstract**

Geological faults are known to have a major impact on fluid flow in the subsurface and may developed isolated compartments for hydrocarbon reservoirs. The knowledge of their properties is important for petroleum industries within interests that include oil and gas production, CO<sub>2</sub> storage and radioactive waste disposal. Large data sets have been collected on the single-phase permeability of fault rocks but these have been collected under inappropriate laboratory conditions such as low confining pressures and using distilled water as the permeant. Some data have been published on the gas relative permeability of fault rocks but no data is available on oil-water relative permeabilities or from fault rocks that are not strongly water-wet. The current thesis aims to produce high quality experimental data to partly fill these knowledge gaps by collecting gas and brine absolute permeability data from fault rocks at reservoir stress conditions using a formation compatible brine as well as oil-water relative permeabilities from fault rocks that are water-wet and after wettability alteration so that they become less water wet.

The key findings of this thesis show that the absolute permeability of fault rocks is very stress sensitive due to the presence of microfractures created during coring or core-retrieval. The stress sensitivity of permeability increases with decreasing permeability. On average, fault rocks have a permeability at in situ stress which is ~ 20% that measured at ambient conditions. Permeability is also found to be less sensitive to brine composition, with permeabilities to distilled water being around 20% those when measured with brine. So the effects of two poor laboratory practises cancel each other out meaning that much published data remain usable.

The obtained results from oil water relative permeability measurements of water-wet cataclastic faults are consistent with what is known about grain-sorting controlling relative permeability. The changes in wettability resulting from aging the samples in crude oil are also consistent with what would be expected when the wettability of samples is altered to being neutral to oil-wet. These results raise the possibility that fault rocks in some reservoirs may not be strongly water-wet and will therefore not act as capillary barriers.

A new clay-mixing model is also presented, which explains the scatter on permeability vs clay content that is used as input for calculating fault transmissibility multipliers in production simulation models. The obtained results can be used as the analogues for similar fault rock types and implemented in the reservoir simulation models for the future forecast of hydrocarbon production.

# **Table of Contents**

<b>Chapter 1: Introduction .....</b>	<b>17</b>
1.1 Thesis outline .....	22
<b>Chapter 2: Fault rock types and properties: A review .....</b>	<b>24</b>
2.1 Introduction .....	24
2.2 Fault rocks developed within siliciclastic petroleum reservoirs.....	25
2.3 Fluid flow properties of fault rocks .....	30
2.4 Evaluation of fault sealing capacity .....	37
2.5 Fault seal analysis work flow .....	45
2.5.1 Structure of the fault.....	46
2.5.2 Incorporation of Multiphase flow properties .....	51
2.5.3 Criticality of evaluation of the fault sealing data .....	51
2.6 Knowledge gaps in fault rock properties.....	52
<b>Chapter 3: Background geology of samples and microstructure analysis .....</b>	<b>56</b>
3.1 Introduction .....	56
3.2 Company A samples.....	56
3.2.1 General Location.....	56
3.2.2 Stratigraphy of field A .....	57
3.2.3 Pressure regimes and hydrocarbon-water contacts in Field A.....	60
3.3 Outcrop samples:.....	62
3.3.1 Orange, France .....	62
3.3.2 Outcrop samples: Hopeman Sandstone, Scotland.....	65
3.3.3 Outcrop samples: Miri, Airport Road, Malaysia.....	67
3.4 Samples analysis.....	68
3.4.1 Samples nomenclature .....	70

3.5	Methodology .....	71
3.5.1	Sample preparation.....	72
3.5.2	Mercury injection porosimetry.....	74
3.5.3	Porosity .....	75
3.5.4	Scanning Electron Microscopy (SEM) .....	79
3.5.5	Image analysis of SEM images .....	80
3.5.6	Quantitative X-Ray Diffraction (XRD) .....	81
3.6	Microstructure, mineralogy, porosity and Hg-injection curves of samples	83
3.6.1	Microstructure and mineralogy of cataclastic samples .....	83
3.6.2	Microstructure and mineralogy of (PFFR) and their associated host sandstones.	88
3.6.3	Microstructure and mineralogy of Orange fault samples.....	89
3.6.4	Microstructure and mineralogy of Hopeman sandstone samples .....	91
3.6.5	Microstructure of the Miri fault and associated sandstone .....	91
3.6.6	Porosity of fault and host samples .....	92
3.6.7	Mercury injection results of cataclastic and PFFR samples.....	95
3.7	Discussion: .....	98
3.8	Conclusions: .....	101
<b>Chapter 4: The stress dependence of the gas permeability of fault rocks .....</b>		<b>102</b>
4.1	Introduction .....	102
4.2	Single phase permeability .....	104
4.3	Permeability models .....	104
4.3.1	Darcy law .....	105
4.3.2	Capillary Tube Model .....	106
4.3.3	Kozeny permeability model .....	108
4.4	Controls on permeability .....	109



4.4.1	Pore volume and size .....	109
4.4.2	Fluid flow velocity .....	111
4.4.3	Overburden or confining pressure.....	112
4.4.4	Heterogeneity and anisotropy .....	115
4.4.5	Limitations of Darcy Law .....	117
4.5	Methods for measuring gas permeability .....	121
4.5.1	Steady-state gas permeability.....	122
4.5.2	Unsteady-state or pulsed-decay permeability measurement .....	126
4.5.3	De-convolved Permeability.....	129
4.5.4	Stress-free samples preparation: .....	130
4.6	Results .....	132
4.7	Discussion: .....	141
4.7.1	Influence of clay contents on fault rock gas permeability .....	141
4.7.2	Causes of the stress dependence of gas permeability.....	150
4.7.3	Fracture permeability modelling .....	154
4.7.4	Overall permeability decay .....	157
4.7.5	Conceptualization model for permeability reduction.....	165
4.7.6	Mathematical modelling of permeability decay.....	168
4.7.7	Results for permeability decay.....	171
4.8	Conclusion:.....	175
<b>Chapter 5: Stress dependent brine permeability .....</b>		<b>177</b>
5.1	Introduction: .....	177
5.2	Liquid permeability .....	178
5.3	Methods .....	180
5.3.1	Unsteady-state liquid permeability measurements.....	180

5.3.2	Steady-state liquid permeability measurements.....	183
5.4	Results .....	185
5.5	Discussion .....	194
5.5.1	Gas vs brine permeability.....	194
5.5.2	Stress dependence of brine permeability.....	195
5.5.3	Impact of brine salinity on liquid permeability.....	198
5.5.4	Sample heterogeneity .....	201
5.5.5	Brine permeability decaying modeling .....	203
5.6	Conclusions .....	207
<b>Chapter 6: Evaluation of wettability and relative permeability of fault rock.. 209</b>		
6.1	Introduction .....	209
6.2	Wettability .....	210
6.2.1	Wettability states .....	211
6.2.2	Wettability alteration.....	214
6.2.3	Evaluation of wettability .....	214
6.3	Relative permeability .....	219
6.3.1	Factors affecting relative permeability.....	220
6.3.2	Relative permeability measurement techniques.....	224
6.4	Experiments and methodologies .....	226
6.4.1	Contact angle measurement .....	227
6.4.2	Relative permeability measurement.....	227
6.4.3	Wettability alteration.....	229
6.4.4	Wettability assessment .....	230
6.5	Results .....	232
6.5.1	Measurements made on samples before aging.....	232

6.5.2	Measurements made on aged samples .....	234
6.6	Discussion .....	235
6.7	Conclusion.....	238
<b>Chapter 7: Conclusions and recommendations for future work:.....</b>		<b>239</b>
7.1	Introduction .....	239
7.2	Absolute permeability of fault rocks .....	240
7.2.1	Stress sensitivity of permeability .....	240
7.2.2	Impact of fluid composition on fault permeability .....	241
7.3	Oil water relative permeability measurements .....	242
7.4	Clay permeability relationships.....	243
7.5	Recommendation for the future work.....	244
<b>References .....</b>		<b>246</b>
<b>Appendix A – 1 .....</b>		<b>272</b>
A1.1	Exponential decay modelling.....	272
A1.2	Power law modelling: .....	274
<b>Appendix A – 2 .....</b>		<b>278</b>

## Table of Figures

Figure 1-1: Juxtaposition of reservoir sand to the a sealing fault results in compartmentalization. The second well is totally missed the reservoir and results in dry well. ....	17
Figure 1-2: Rotliegend gas reservoir in southern North Sea show two completely isolated compartment with high pressure differential. Initially GIIP (gas initially in place) shows high values, while at later stage the dynamic GIIP shows very low reserves as the production was only from compartment. ....	18
Figure 2-1: A: Hand specimen containing isolated fault developed in Brent North Sea sandstone. B and C: Backscattered-electron images showing microstructure of (B) disaggregation zone and (C) cataclasite along with their associated undeformed sandstones (from Fisher et al. 2003). ....	25
Figure 2-2: Illustration of the processes controlling fault zone properties. The grain of rock are crushed during faulting process and compacted at high burial depth (from Sperrvik et al., 2002). ....	27
Figure 2-3: Plot of porosity (dashed line) and $p/p^*$ (continuous line) vs. burial depth for medium-grained sandstone ( $r = 150 \mu\text{m}$ ) with initial porosity of 30% buried at rate of 0.05 km/m.y. under geothermal gradient of 30 °C/km. Predicted modes of deformation, base based on porosity and $p/p^*$ , and their consequences for fault permeability are shown. After Fisher et al. (2003). ....	29
Figure 2-4: Summary of the fault rock permeability data from the North Sea and Norwegian Continental Shelf. Permeability is plotted against clay content for the various fault rock types. Also shown on the diagram is two of the main c controls on the permeability of the faults in clean sandstones and impure sandstones (i.e. burial depth at the time of faulting and maximum post-deformation burial depth respectively). After Fisher and Knipe (2001). ....	32
Figure 2-5: 3D plot showing the relationship between measured clay content, permeability, and maximum burial depth for host rocks. The plane represents the exponential least squares regression. After Sperrvik et al. (2002). ....	33
Figure 2-6: Structural map of the Don Field, which is showing the fault sealing trap for hydrocarbon. After Harman and Booth (1991). ....	35
Figure 2-7: Fault sealing evaluation. Rd and Ru are different lithologies. After Skerlec, (1999).	38
Figure 2-8: Fault leaking evaluation. Rd and Ru are different lithologies. After Skerlec, (1999).	39
Figure 2-9: Plot of capillary threshold pressure vs. permeability for fault samples (solid symbols) and un-faulted rock samples (crosses and open symbols) from a variety of lithologies (from Manzocchi et al., 2002). The boxes (Fisher & Knipe 1998) are summaries of data from (i) faults in clean sandstone, (ii) dirty sandstone and (iii) shale-rich fault gouge. The two lines are published model relationships (thinner line from Ringrose et al. (1993) and Fisher &	

Knipe (1998), thicker line from Harper & Lundin (1997)). Capillary threshold pressures have been normalized for a water-wet system with a hydrocarbon–water interfacial tension of 40 dynes  $\text{cm}^{-1}$ , and a contact angle of  $30^\circ$ . Legend: filled triangles and crosses, Sperrevik et al. (2002); filled squares, Harper & Lundin (1997); empty squares, Schowalter (1979); filled circles, Gibson (1998); filled diamonds, Fulljames et al. (1997); Ibrahim et al. (1970); empty circles, Schlomer & Krooss (1997). ..... 41

Figure 2-10: Conceptual model, based on Fisher et al. (2001) for multi-phase flow across a fault in a petroleum reservoir. (a) The fluid saturations within the reservoir and fault, red for hydrocarbon, blue for water. (b) The capillary pressure. (c) The  $i$ -directional water-wet relative permeability curves for the fault rock. After Busafi et al. (2004). ..... 42

Figure 2-11: Schematic illustration of capillary pressure and relative permeability relationships in traditional and low-permeability reservoir rocks. Critical water saturation ( $S_{wc}$ ), critical gas saturation ( $S_{gc}$ ), and irreducible water saturation ( $S_{wirr}$ ) are shown. After Shanley et al. (2004). ..... 44

Figure 2-12: Top reservoir depth map of a Brent field in which faults identified from the seismic survey (red lines) are shown with those incorporated into the production simulation model (black lines). Blue lines are the well trajectories. (a) Model-1: note significant inconsistencies between the faults mapped from seismic and those incorporated into the static and simulation models (white circles). Some faults have been joined within the simulation model, which appear not to be linked within the seismic survey and vice versa. (b) Model-2: the geometrical integrity of the fault pattern is preserved between seismic interpretation, static and simulation models. The effect of preserving the fault juxtaposition geometries, is shown by comparing the simulation results from both models (adapted from Jolley et al., 2007). ..... 47

Figure 2-13: Representation of a fault between grid-blocks  $i$  and  $j$ . (a) The transmissibility multiplier ( $T$ ) acts on the transmissibility ( $Trans_{ij}$ ) between two grid-block centres.  $Trans_{ij}$  is a function of grid-block permeabilities and lengths. (b) To calculate the value of the multiplier, the thickness of low permeability fault-rock is considered explicitly. (c) A transmissibility multiplier assigned between blocks  $i$  and  $j$  modifies only  $Trans_{ij}$ . (d) A permeability multiplier applied to block  $j$  modified both  $Trans_{ij}$  and  $Trans_{jk}$ . ..... 49

Figure 2-14: Diagram illustrating the meaning of algorithms commonly used to estimate the continuity of clay smears or the clay content of fault zones: (a) clay smear potential (CSP); (b) shale smear factor (SSF) (Lindsay et al. 1993); (c) shale gouge ratio (SGR). Based on Yielding et al. (1997). ..... 50

Figure 2-15: Stress dependence of the absolute gas permeability of tight gas sands. Note that the low permeability samples can have up to two orders of magnitude lower permeability when measured at reservoir stress conditions compared to 100 psi (After Byrnes et al., 2009). .... 54

Figure 2-16: Water-sensitivity of the Spiney sandstone, Moray Firth Basin. Note the large decrease in permeability when the brine is changed to 1% NaCl (from Lever and Dawe, 1987). .....	54
Figure 3-1: Generalized pre-Cretaceous stratigraphy of the Field A. ....	58
Figure 3-2: Conceptual model for pod-interpod accumulation and preservation in areas of early pod grounding such as the UK Western Platform. Initial mini-basin formation during deposition of the Smith Bank Formation (A) evacuated the underlying halite, resulting in pod grounding on the Rotliegend Group (B). Subsequent progradation of Bunter Formation and lower Judy Sandstone Member terminal splay complexes occurred across the region, with localised thickening in interpod areas where salt continued to be evacuated and/or dissolved (B). This process continued through the Middle and Late Triassic as the region was blanketed by sediment as the basin continued to subside (C), but subsequent erosion during Middle Jurassic thermal doming (D) eroded much of the Triassic stratigraphy, leaving erosional remnants of Skagerrak Formation terminal splays in interpod troughs. The geometries of the troughs do not reflect the depositional geomorphology and aresites of preferential preservation of formerly unconfined distal sheets (From McKie, 2005). ....	59
Figure 3-3: Cross-section through the field A, illustrating the major Triassic pods, the inter-pod areas and gas-water contacts in the pods.....	60
Figure 3-4: Variation in fluid gradient and formation pressure in the Field A. Figure is showing separate aquifers pressure in different pods. ....	62
Figure 3-5: Summary structural map of the Southeast Basin, Provence, southeastern France, showing the distribution of Cretaceous strata and the location of the site of sampling. North-south cross section (modified from Champion). From Sallet and Wibberley, (2010). ....	63
Figure 3-6: Actual location of the Southeast Basin, Provence, south-eastern France, from where the samples were taken. ....	64
Figure 3-7: Photograph showing a typical example of the samples taken from the Orange quarry. Note the high density of faults present within the samples. ....	65
Figure 3-8: Location and geology of the Hopeman sandstone (Modified from Edwards et al., 1993). ....	66
Figure 3-9: Photograph and structural section of the quarry at Clashach Cove East; note the main fault plane is surrounded by a damage zone containing a high density of deformation bands. ....	67
Figure 3-10: A) Actual location, Airport road near Miri, Malaysia from where the samples have taken. B) Cross sectional view of the Miri outcrop (from Van der Zee and Urai, 2005). ....	68
Figure 3-11: Summary of workflow for sample preparation.....	71
Figure 3-12: Sample 5A- CT scan image of actual sample and core plugs taken form main sample. ....	72

Figure 3-13: Soxhlet distillation extractor. Solvent in the distillation flask (left) is gently heated until it vaporizes. The solvent vapours rise from the flask and cool when they reach the condenser. The cooled liquid solvent drips onto the core to permeate the sample. The solvent condensate carries away the hydrocarbons and brine from the sample. When distilled solvent in the extractor reaches its spill point, the used solvent siphons back into the flask to be redistilled (right). This process is repeated continuously and can be sustained as long as needed. The hydrocarbons from the core are retained and concentrated in the distillation, or boiling, flask. Some Soxhlet devices can accommodate multiple core plugs (Andersen et al., 2013). .....	73
Figure 3-14: Samples prepared for mercury injection. (a) Sample 7A (b) Sample 7F and (c) Sample 10/3B.....	74
Figure 3-15: Double-Cell Boyle’s Law Porosimeter (from Recommended Practices for Core Analysis; RP40). .....	79
Figure 3-16: Samples prepared for SEM analysis.....	80
Figure 3-17: Bruker D8 Advance XRD setup. ....	81
Figure 3-18: BSEM micrograph of cataclastic host sample 3A. ....	86
Figure 3-19: BSEM micrograph of cataclastic fault sample 3A. ....	86
Figure 3-20: Porosity of cataclastic fault sample 3A by image analysis.....	87
Figure 3-21: BSEM micrograph of phyllosilicate host sample 7D. ....	88
Figure 3-22: BSEM micrograph of phyllosilicate fault sample 7D.....	89
Figure 3-23: BSEM micrograph of outcrop Orange fault sample ORG-1. ....	90
Figure 3-24: BSEM micrograph of outcrop fault sample oRG-3.....	90
Figure 3-25: BSEM images of Hopeman fault and host samples. ....	91
Figure 3-26: BSEM images of Miri fault and host samples.....	92
Figure 3-27: Hg injection data for the phyllosilicate fault rock and associated host sandstone (sample 7D).....	96
Figure 3-28: Hg injection for the phyllosilicate fault rock and associated host sandstone (sample 5A). ....	96
Figure 3-29: Hg injection for the cataclastic fault and its associated host sandstone (sample 7B). ....	97
Figure 4-1: Permeability measurement for a core plug.....	105
Figure 4-2: Capillary tube model (Bear, 1972). ....	107
Figure 4-3: Porosity and permeability correlation (after Tiab 2004). ....	110
Figure 4-4: Porosity permeability correlation for the different grains sizes (Tiab and Donaldson, 1996). ....	111
Figure 4-5: Change in permeability with overburden pressure (after Fatt 1952). ....	113

Figure 4-6: Stress dependency of tight gas samples also showing the hysteresis during loading and unloading cycles of confining pressure where red is loading and blue is unloading. (from Al-Hinai, 2007). .....	115
Figure 4-7: Linear flow through parallel beds.....	116
Figure 4-8: Linear flow through series of beds. ....	116
Figure 4-9: Relationship between Fanning’s friction factor and Reynolds number for flow through granular porous media (Rose, 1945). ....	119
Figure 4-10: Darcy and non-Darcy flow classification in a porous media (Bear, 1972).....	120
Figure 4-11: Setup for steady-state permeability measurement (API RP40, 1998). ....	122
Figure 4-12: Graph for Klinkenberg permeability measurement. ....	124
Figure 4-13: Darcy and non-Darcy flow behaviour for Sample ORG – A1. ....	126
Figure 4-14: Unsteady-state permeability measurement by pulse decay technique (Jones, 1988). .....	127
Figure 4-15: Pulse decay setup from CoreLab located at Wolfson laboratory, University of Leeds. .....	128
Figure 4-16: Samples in resin for measurement of permeability at low confining pressure and their CT images. ....	131
Figure 4-17: Normalized stress dependent gas permeability of cataclastic samples from North Sea reservoir. ....	137
Figure 4-18: Stress dependent gas permeability of Orange fault samples. ....	137
Figure 4-19: Ternary diagram for the mineralogy of samples analysed. ....	141
Figure 4-20: Plot showing fault rock permeability against fault rock clay content measured on faults in cores. The data are grouped according to maximum burial depth. Exponential least-squares regression lines are shown for each group of data, showing a systematic decrease in permeability both with fault rock clay content and with depth (from Sperrevik et al., 2002). .....	143
Figure 4-21: Relationship between porosity, grain-size and grain-sorting of a sand pack (after Beard and Weyl, 1973). ....	145
Figure 4-22: Results from numerical modelling showing the impact of (left) grain-size and (right) grain-sorting on porosity and permeability (from Cade et al., 1994). ....	146
Figure 4-23: Plot of permeability of a sand-clay mixture as a function of clay content where the initial sands have different grain-sizes and grain-sorting, hence porosity and permeability. .....	146
Figure 4-24: The relation between fault rock and clay contents; permeabilities were measured at 5000 psi. ....	148



Figure 4-25: The same data as Figure 4.25 but also included is the results from the model of Sperrevik et al. (2002).....	149
Figure 4-26: Plot of the gas permeability of fault rocks vs clay content against various sand-clay mixing models of Revil and Cathles (1999).....	149
Figure 4-27: BSEM of fault rock samples are showing micro-cracks. The cracks are also visible with the grain boundaries. ....	152
Figure 4-28: BSEM shows small scale (0.1 to 3 $\mu\text{m}$ ) wide fractures at grain boundaries .....	152
Figure 4-29: BSEM image of fault sample, showing fracture. Magnified portion is used to measure the fracture width by ImageJ software as well its porosity. ....	155
Figure 4-30: Experimental gas permeability data and the fracture modelled data for three fractures. ....	156
Figure 4-31: Plot of gas permeability of fault (core) samples. Fault permeability measured at 1000 psi net stress vs the permeability measured as 5000 psi. Regression line is plotted. ....	157
Figure 4-32: Plot of gas permeability of fault permeability measured at 5000 psi net confining pressure vs the permeability extrapolated to 70 psi by power law fit. ....	159
Figure 4-33: Gas permeability data of fault rock samples compared with tight gas sandstone samples, tight gas data is taken from University of Leeds for the confining pressure of 500 and 5000 psi. ....	160
Figure 4-34: Plot of gas permeability extrapolated and experimental data. ....	163
Figure 4-35: Conceptualisation models for the change in grain compaction due to increase in confining pressure. ....	166
Figure 4-36: Step wise change in permeability in percentage by increasing confining pressure. ....	167
Figure 4-37: Comparison of experimental permeability with extrapolated permeabilities by power and exponential correlations (Sample 3AF2). ....	174
Figure 4-38: Comparison of experimental permeability with extrapolated permeabilities by power and exponential correlations (Sample 10/3AF1). ....	175
Figure 5-1: Pulse decay brine permeability measurement setup at Wolfson laboratories, University of Leeds. ....	182
Figure 5-2: A) Hassler core holder with both end plugs, left one is threaded. B) End plug having circular and radial grooves for evenly flow at the face of sample. ....	182
Figure 5-3: Pressure decay curve for estimation of permeability in the pulse decay technique. ....	183
Figure 5-4: Schematic of the liquid steady-state permeability measurement setup. ....	184
Figure 5-5: Plot between $q/A$ and $\Delta P/L$ , the slope is equal to $k/\mu$ , used to calculate the permeability. ....	185
Figure 5-6: Plot of brine permeabilities (mD) of cataclastic fault plugs vs confining pressure (psi) on semi-log scale. ....	190

Figure 5-7: Plot of brine permeabilities (mD) of phyllosilicate framework fault (PFFR) plugs vs confining pressure (psi) on semi-log scale.....	190
Figure 5-8: Plot of brine permeability vs confining pressure for the outcrop samples. ....	191
Figure 5-9: Plot of brine permeability vs gas permeability for the fault rock “cubes”. ....	193
Figure 5-10: Plot of brine permeability vs distilled water permeability of the fault rock “cubes”. The red line is a 1:1 correlation.....	193
Figure 5-11: Brine (30%) permeability vs gas permeability for cataclastic and PFFR samples .	194
Figure 5-12: Brine (30%) permeability vs gas permeability for outcrop samples .....	195
Figure 5-13: Plot of gas and brine permeability shows less stress dependency on confining pressure with brine permeability. ....	197
Figure 5-14: Plot between permeabilities of fault rocks measure at 500 psi and 5000 psi. The data plotted is for cataclastic, PFFR and outcrop samples.....	198
Figure 5-15: Cube samples Brine (30%) permeability correlation with reservoir samples at 5000 psi on log-log scale. ....	201
Figure 5-16: Brine permeability decay rate (Exponential) for samples 3AF1 and 3AF2.....	202
Figure 5-17: Brine permeability decay rate (Power) for samples 3AF1 and 3AF2.....	203
Figure 5-18: Comparison of permeabilities experimental, exponential and power law model. ..	204
Figure 5-19: Extrapolated brine permeability of sample 3AF1 by exponential and power model. .....	204
Figure 6-1: Contact angle in oil-water system for a water wet rock. ....	211
Figure 6-2: Different scenarios for rock wettability on the basis of contact angle (from Anderson, 1986a) .....	212
Figure 6-3: Wettability measurements by USBM method: Curve-I is showing primary drainage, curve-II is showing forced imbibition and curve-III is showing secondary drainage. (a) Untreated water wet core; (b) Treated core with 10% DRI-FILM 99, (showing oil wet behaviour) (c) aged core sample for 14 days at 60°C; the concentration of the brine is 1000 ppm of sodium tripolyphosphate.....	218
Figure 6-4: Relative permeability curve for wetting and non-wetting cases (from Naar et al., 1962). .....	220
Figure 6-5: The distribution of oil and water in (a) water wet rock and (b) oil wet rock (from Raza et al., 1968). ....	223
Figure 6-6: Typical relative permeability curves for (a) water wet rock and (b) oil wet rock (from Craig, 1970) .....	224
Figure 6-7: Relative permeability curves for strongly water to strongly oil wet cores (from Donaldson and Thomas, 1971). ....	225

Figure 6-8: Workflow diagram for oil-water relative permeability experiments Orange fault rock samples.....	227
Figure 6-9: Basic pump setup for unsteady state relative permeability experiments. ....	228
Figure 6-10: Contact angle measurement for fault rock sample with brine droplet, showing that the Orange fault sample is water wet. ....	232
Figure 6-11: Relative permeability curves of ORG-1 and ORG-2 showing high cross over saturations. ....	233
Figure 6-12: Relative permeability curves for Orange sample, before aging.....	233
Figure 6-13: Relative permeability curves of Orange samples after aging. ....	235

# Nomenclature

$\Delta P$	Pressure differential
$A$	Cross sectional area
$BSEM$	Back-scattered scanning electron microscopy
$CSP$	Clay smear potential
$D$	Depth
$d$	Fault displacement
$dP/dL$	Pressure differential per unit length
$F$	Fanning friction factor
$f_w$	Fracture width
$FWL$	Free water level
$GIIP$	Gas initially in place
$h$	Height of hydrocarbon column
$k$	Permeability
$k_f$	Fault permeability
$k_i$ & $k_j$	Permeability in $i$ th and $j$ th grid block
$k_m$	Permeability at specific depth
$k_{nw}$	Relative permeability of non-wetting phase
$k_{rw}$	Relative permeability of wetting phase
$L$	Length
$L_i$ & $L_j$	Length of $i$ th and $j$ th grid block
$MICP$	Mercury injection capillary pressure
$ORG$	Orange fault rock samples
$P$	Pressure

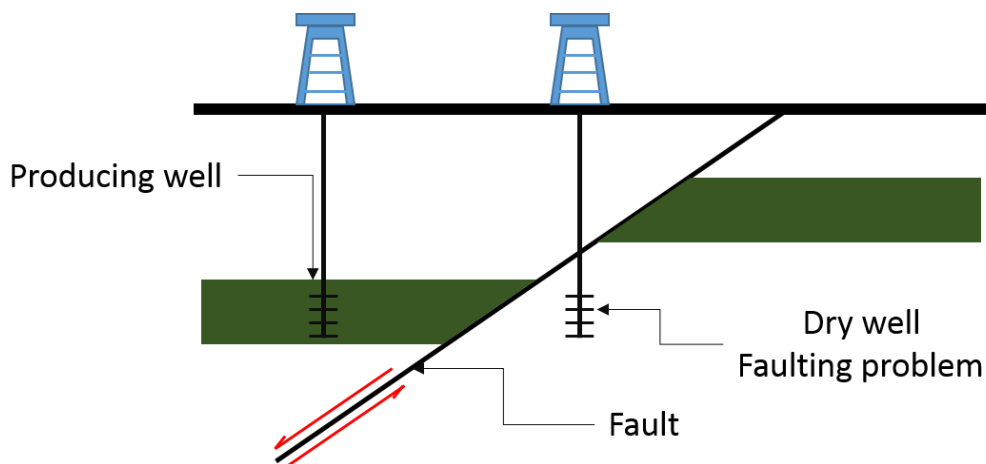
$P^*$	Critical effective pressure
$P_b$	Buoyancy pressure
$P_c$	Capillary pressure
$PFFR$	Phyllosilicate frame-work fault rock
$PV$	Pore volume
$q$	Volumetric flow rate
$q_{nw}$	Flow rate of non-wetting phase
$q_w$	Flow rate of wetting phase
$QXRD$	Quantitative X-Rsy diffraction
$r_c$	Capillary / pore throat radius
$Re$	Reynold's number
$S_e$	Effective saturation
$SEM$	Scanning electron microscopy
$S_{gc}$	Critical gas saturation
$SGR$	Shale gouge ratio
$S_{or}$	Residual oil saturation
$SSF$	Shale smear factor
$S_{wc}$	Critical water saturation
$S_{wirr}$	Irreducible water saturation
$T$	Fault throw
$t_f$	Thickness of fault
$TM$	Transmissibility multipliers
$TransF_{ij}$	Fault transmissibility multipliers in ith and jth cells
$Trans_{ij}$	Transmissibility multipliers in ith and jth cells
$V_{cl}$	Clay or shale fraction

$V_{clay}$	Clay content (percentage)
$Z_m$	Burial depth
$Z_{max}$	Maximum burial depth
$\alpha, \alpha_n$	Roots of transcendental equation
$\beta$	Fluid compressibility
$\beta_s$	Porous media compressibility
$\gamma$	Interfacial tension
$\phi$	Porosity
$\mu$	Viscosity
$\mu_{nw}$	Viscosity of non-wetting phase
$\mu_w$	Viscosity of wetting phase
$\rho_{hc}$	Density of hydrocarbon
$\rho_w$	Density of water

# Chapter 1: Introduction

The geological fault is a discontinuity or fracture in rock layers, which is developed due to the tectonic movements. The shearing of rocks layer may developed a boundary between the layers, which may have different structural as well as flow properties. The fault rock may have high capillary entry pressure, which may seal the rock and now allowing the fluid flow across it. The fluid can flow when the entry pressure is higher than the capillary pressure. Different seal mechanisms are documented (Watts, 1992; Knipe, 1992), which are:

- i) Juxtaposition: low permeability rock (e.g. shale) juxtaposed to the reservoir sand and developed a separate compartment (**Figure 1-1**).
- ii) Clay smear: during faulting, clay smeared into the fault and developed a low permeability fault itself with high capillary pressure.

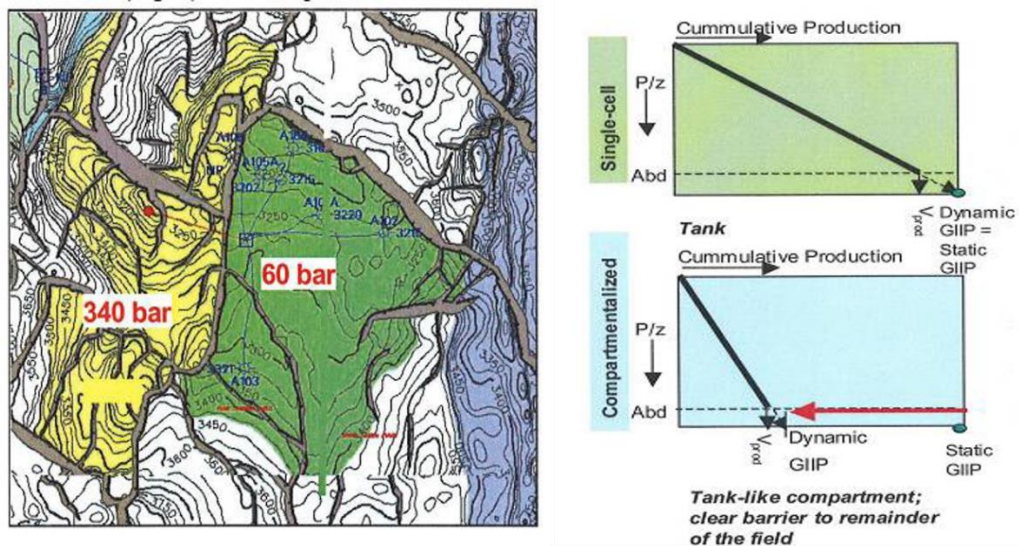


**Figure 1-1: Juxtaposition of resevoir sand to the a selaing fault results in compartmentalization. The second well totally missed the resevoir and results in dry well.**

- iii) Cataclasis: the grains of the rock crushed due to shearing and developed a fault gouge, which is made up of very fine grains and has a high entry capillary pressure.

- iv) Diagenesis: the diagenetic process in grains cementation reduces the porosity remarkably resulting in hydraulic seal.

Geological faults can act as barriers or conduits for fluid in the subsurface in general as well as specifically in petroleum reservoirs. For example, faults can provide traps for oil but they can also compartmentalize the reservoirs, reducing the ultimate recovery or increasing the number of wells needed to reach production targets. Molen et al. (2003) presented the case study of Rotliegend gas fields in southern North Sea, where the initial pressure of the reservoir was found to be 340 bars and high initial gas reserves were estimated (**Figure 1-2**).



**Figure 1-2: Rotliegend gas reservoir in southern North Sea show two completely isolated compartment with high pressure differential. Initially GIIP (gas initially in place) shows high values, while at later stage the dynamic GIIP shows very low reserves as the production was only from compartment.**

In early stages of production, the reservoir pressure dropped by 280 bars and reached to 60 bars only and the dynamic gas reserves showed less than 50% of reserves what estimated in early stage. A detailed analysis has shown that the reservoir was divided into two compartments due to the sealing fault, which did not allow the compartments to communicate with each other. This example shows that the fault detection and its properties evaluation is crucial for production estimations.



According to Corrigan (1993), the Brent province oil fields are a good example of where fault compartmentalization has resulted in lower than expected oil production rates. In other fields, such as the Clair Field, faults can behave as conduits resulting in higher than expected production rates and ultimate petroleum recovery (Coney et al., 1993). The presence of fault-related conduits is not always advantageous as they may lead to mud losses and early water breakthrough (Rawnsley and Wei, 2001).

Quantitative data on fault properties, such as permeability and capillary pressure, are important for the petroleum industry as they can be used to assess the impact of faults on the movement and distribution of hydrocarbon in the subsurface. In particular, knowledge of fault properties can improve production forecasts and reserve estimates (Fisher and Jolly, 2007).

Over the last 20 years, a large amount of research has been undertaken to both measure fault properties and to improve methods to integrate these properties into production simulation models. For example, Fisher and Knipe (1998, 2001) published a large amount of absolute permeability data after conducted experiments on fault rocks. Manzocchi et al. (1999) incorporated fault rock permeability data and developed a method in which transmissibility multipliers have calculated by the experimental permeability values and applied to the faces of grid blocks on either side of faults. Calculation of transmissibility multipliers requires information on fault thickness and permeability. Fault thickness can be estimated based on the throw of the fault (Hull, 1988).

Several studies have suggested that the type and petrophysical properties of fault rocks are partly controlled by their clay content and maximum burial depth (Fisher and Knipe, 1998, 2001). Manzocchi et al. (1999) developed a workflow to

calculate transmissibility multipliers which first estimated the clay content of the fault and then used empirical correlations to estimate fault permeability from their clay content. In particular, Manzocchi (1999) provided the relationship:-

$$\log(k_f) = 0.4 - 4 \times (SGR) - 0.25 \log(D) \times (1 - SGR)^5 \quad \text{Eq. (1-1)}$$

where  $k_f$  is fault permeability (md),  $D$  is the maximum burial depth (m), and  $SGR$  is the shale gouge ratio calculated using the methodology of Yielding et al. (1997). According to Jolley et al. (2007) it is better to measure the permeability of fault rocks found within cores from the field of interest rather than using global databases.

Several studies that have applied this methodology have found that it improves the history match of dynamic simulation models (e.g. Knai & Knipe, 1998; Jolley et al. 2007). However, other studies have shown that the methodology often overestimates the transmissibility of faults in petroleum reservoirs (e.g. Fisher, 2005). A potential reason why this methodology overestimates fault transmissibility is that it does not take into account the multiphase flow behavior of fault rocks (e.g. Fisher and Knipe, 2001, Manzocchi et al. 2002; Al-Busafi et al., 2005; Al-Hinai et al., 2008). Indeed, Zijlstra et al. (2007) showed that history matches of production simulation models from several Rotliegend reservoirs of the southern North Sea were improved by calculating transmissibility multipliers using both absolute and relative permeabilities.

Another potential reason for the mismatch between the results of fault seal analysis studies and production data is that such studies often calculate fault transmissibility multipliers based on laboratory measurements of fault permeability conducted under inappropriate laboratory conditions. For example, most fault

permeability data that have been published and are contained within databases collected by industry was measured at ambient stress using distilled water as the permeant measurements (e.g. Fisher and Knipe, 1998, 2001; Tueckmantel et al., 2011, 2012; Gibson et al., 1998; Sperrevik et al., 2002; Ellevset et al., 1998; Knai and Knipe, 1998). This is clearly problematic considering that it is well known that the permeability of low permeability rocks is very sensitive to the applied stress (e.g. Byrnes and Castle, 2000; Morrow and Brower, 1986) and the fluid composition (Lever and Dawe, 1987).

To improve understanding of causes for discrepancies between production data and results of fault seal studies more data on fault rock properties are required. In particular, very little data exist on the permeability of fault rocks at reservoir stress conditions using a formation compatible brine. Also only gas relative permeability measurements from strongly water-wet cataclastic faults have been published; no data are available from more clay-rich fault rocks or those that are oil wet or have mixed wettability. Also, no data are available on oil-water relative permeabilities of fault rock.

However, it is well documented that the permeability of tight rocks was found to be very stress sensitive during measurements taken in laboratory. For example, routine core analysis permeability measurements made on tight gas sandstones may be several orders of magnitude higher than measurements made at in situ stress conditions (e.g. Byrnes et al., 2010). If this is the case for fault rocks, the most commonly used workflow (e.g. Fisher and Knipe, 2001) to calculate fault transmissibility multipliers to incorporate fault rock properties into simulations models could be based on measurements that underestimate fault permeability.

The current thesis aims to partially fill these knowledge gaps by presenting high measurements of the single and multiphase flow properties of fault rocks conducted at reservoir conditions. Measurements have been conducted on reservoir core samples of North Sea fields and outcrops samples taken from Orange France, Miri, Malaysia and Hopeman, Scotland. The thesis presents the first ever data on the oil-water relative permeability of strongly water wet fault rocks as well as fault rocks whose wettability has been altered to a more oil-wet state using a crude oil.

## 1.1 Thesis outline

The remainder of the thesis is divided into the following six chapters:-

**Chapter 2** is provides a review of the type and properties of fault rocks found in petroleum reservoirs. This review also includes a description of deformation mechanisms and fault seal processes, an overview of fault seal analysis workflows used by industry and the importance of fault seal analysis in industry.

**Chapter 3** presents the background geology of the samples used in this study. The general properties and locations of the fault samples is presented for reservoir and outcrops. The main methodologies used for sample preparation and core analysis are described, including CT scanning, MICP, SEM image analysis, QXRD etc.

**Chapter 4** presents data on the gas permeability of fault rocks. It begins by outlining gas flow mechanisms before going on to describe the analytical methodologies using in this research. Results are presented and discussed on the stress dependence of the gas permeability of fault rocks as well as relationships between gas permeability and clay content.

**Chapter 5** investigates the impact of brine composition on permeability measurements and compared these results with the gas permeability results.

**Chapter 6** presents new data oil-water relative permeability of strongly water-wet fault and compares the results to measurements made on samples that have had their wettability altered by aging in crude oil.

**Chapter 7** discusses the results from the thesis, provides conclusions as well as recommendations for further work.

# Chapter 2: Fault rock types and properties: A review

## 2.1 Introduction

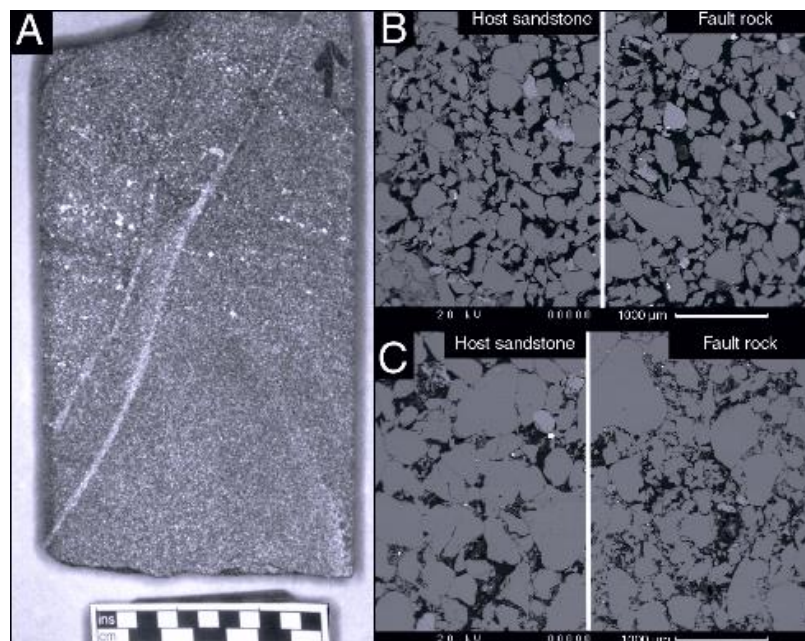
Geological faults are shear localizations developed when tectonic forces or changes in pore pressure are sufficiently large that the effective stresses acting on the rock overcome its shear strength. Faults can form in all types of rocks and at a variety of burial depths (i.e. at different stresses and temperatures) so they are highly variable in terms of the processes that have accommodated shear strain (deformation mechanisms); their structure on both a macroscopic and microscopic scale; their mineralogy; and petrophysical properties (porosity, permeability, capillary pressure and relative permeability). It is therefore not surprising that the extent to which faults may impact subsurface fluid flow is highly variable (Fisher et al., 2003; Knipe, 1993; Jolly et al., 2007; Fisher and Knipe, 1998; Mandl et al., 1976; Evans and Fredrich, 1990; Yielding et al., 1997). Indeed, the influence of faults on fluid flow is not just controlled by the properties of the fault itself but also the properties of the surrounding rock mass. For example, a fault with a permeability of 0.5 mD may act as a barrier to fluid flow if present in a rock of 1D permeability, but as a conduit if present in a rock with 1nD permeability (Fisher and Knipe, 2001).

This chapter aims to present a review of the type and petrophysical properties of fault rocks found within petroleum reservoirs as well as their impact on fluid flow. Key knowledge gaps are then discussed with particular emphasis being placed on the topics that the current thesis aims to address. The review is mainly targeted at fault rocks found within siliciclastic reservoirs; fault rocks in carbonates warrant a completely separate study.

## 2.2 Fault rocks developed within siliciclastic petroleum reservoirs

Faults often have a very complex geometry comprising fault planes that contain the products of deformation usually referred to as fault rock or gouge separated by lenses, horses and duplexes of undeformed material (Gabrielsen and Clausen, 2001; Childs et al., 1997). On a microstructural-scale, fault rocks can be divided into several distinct types depending upon their composition and the deformation processes that accommodated strain during faulting (Fisher and Knipe, 1998; Sibson, 1990).

The initial rock that forms the fault as well as any material that subsequently becomes entrained within the fault plane is deformed by a range of processes. These processes may alter the grain-size and grain sorting of the faulted material, which leads to a change in petrophysical properties such as porosity and permeability.

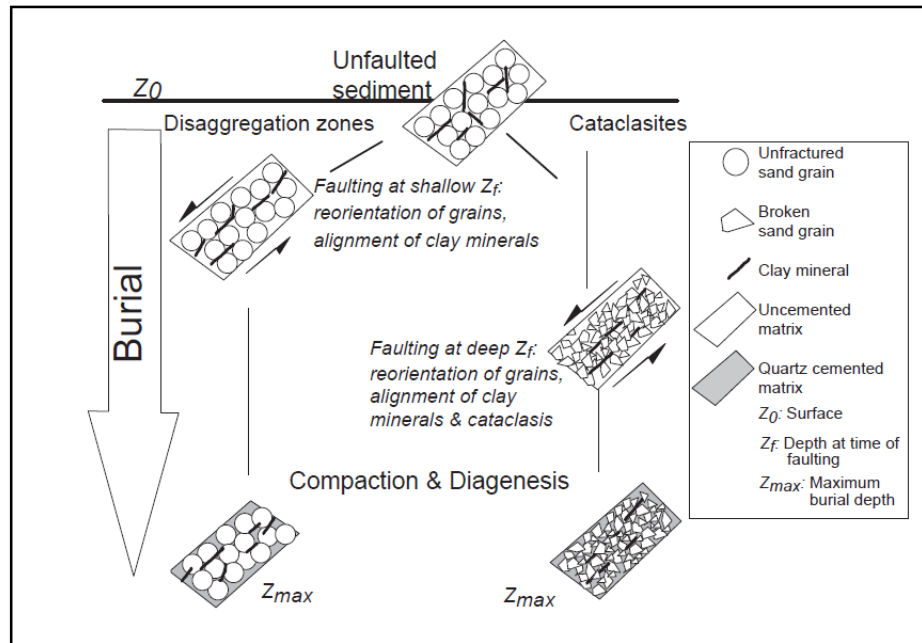


**Figure 2-1: A: Hand specimen containing isolated fault developed in Brent North Sea sandstone. B and C: Backscattered-electron images showing microstructure of (B) disaggregation zone and (C) cataclasite along with their associated undeformed sandstones (from Fisher et al. 2003).**

Key controls on fault rocks microstructure and petrophysical properties in siliciclastic sediments are stress and temperature conditions prior to, during and following faulting as well as the composition of the protolith (Dunn et al., 1973; Engelder, 1974; Mandl et al., 1977; Fisher and Knipe, 1998; Sperrevik et al., 2002).

In the shallow subsurface, where the effective stress is low, or at deeper depths if fluid pressures are high, sediments deform by a process known as independent particulate flow (Borradaile, 1981; Fisher and Knipe, 1998). This process involves the relative movement of grains by rotation and grain-sliding but does not result in significant grain fracturing. Particulate flow, involving pore collapse and grain crushing, occurs if faulting occurs under higher effective stress conditions; this process is often referred to as cataclasis (Mandl et al., 1977). The effective stress above which cataclasis starts to become important is not well constrained. Fisher and Knipe (1998) speculated that the transition from independent particulate flow to cataclasis may occur at around 5 MPa effective stresses, which is around 500 m burial depth in a normally pressured sedimentary basin. However, the transition from independent particulate flow to cataclasis is likely to vary depending upon the grain-size, composition and diagenetic history of the rock prior to faulting (Fisher et al., 2003, 2007). It should be noted that the petrophysical properties of a fault rock may continue to evolve following faulting as a result of the same diagenetic processes, such as grain contact dissolution and mineral precipitation, that affect undeformed sedimentary rocks (Fisher and Knipe, 1998, 2008); these processes are summarized in **Figure 2-2**.





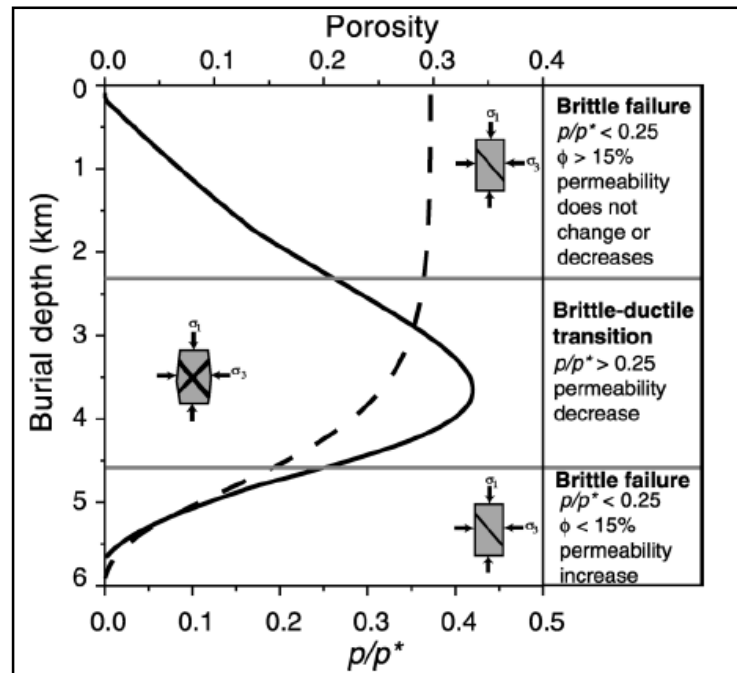
**Figure 2-2: Illustration of the processes controlling fault zone properties. The grain of rock are crushed during faulting process and compacted at high burial depth (from Sperrvik et al., 2002).**

Independent particulate flow does not radically alter the microstructure of clean sands (Fisher and Knipe, 1998); such fault rocks are often referred to as disaggregation zones. Deformation of impure sands (15 to 40% clay) and clay-rich rocks (>40 clay) by independent particulate flow may create low permeability faults. The redistribution of clay minerals by faulting of impure sandstones tends to result in a loss of macro-porosity and also renders the fault rock susceptible to grain-contact quartz dissolution once buried beyond 90°C, which is the temperature where quartz cementation becomes rapid (Fisher and Knipe, 1998). The fault rocks generated by the deformation of poorly lithified impure siliciclastic sediments have been referred to as phyllosilicate-framework fault rocks (Fisher and Knipe, 1998). Poorly lithified clay-rich rocks (>40% clay) may deform in a ductile manner and become smeared or injected along faults; these are often referred to as clay smears (Weber et al, 1978; Lehner and Pilaar, 1997).

Cataclastic deformation reduces grain-size and increases reactive surface area making the fault rocks more susceptible to quartz cementation if the rock is exposed to temperatures greater than 90°C following faulting. Fault rocks formed by the cataclastic deformation of clean sands are often referred to as cataclasites (Fisher and Knipe, 1998). Cataclastic deformation can also in principle occur in more clay-rich rocks so in principle these could also be classed as cataclastic faults. So Fisher and Knipe (1998) suggested the term quartz-rich cataclastic fault if developed from clean sandstone. The terms cataclastic phyllosilicate framework fault rock or cataclastic clay smear could then be used to describe fault rocks developed by the cataclastic deformation of impure and clay-rich sediments respectively. This classification does, however, seem overly cumbersome and it would appear far more straightforward to replace the terms phyllosilicate-framework fault rock with impure-disaggregation zone, cataclastic fault and impure cataclastic fault depending on the deformation mechanism. There have been no reported cases of cataclastic deformation within clay smears so there is no need to qualify the term with either disaggregation zone or cataclastic fault.

Processes such as cataclasis, mixing and smearing of clays, as well as enhanced diagenesis often give fault rocks reduced porosity and permeability than the adjacent undeformed material (Fisher and Knipe, 1998; 2001). However, this is not always the case. Compaction and diagenesis gradually reduce the porosity and increase the strength of sediments. Faulting of low porosity rocks may result in dilation, creating a fault which has a higher permeability than the undeformed material. Fisher et al. (2003) combined results from sandstone deformation experiments with a simple model for quartz cementation to explain key controls on fault permeability. This model predicts that faults in sandstone can act as conduit to fluid flow, if the burial depth is

below the ductile to brittle transition. This model is used to predict the burial depth of the ductile to brittle transition as a function of grain-size, geothermal gradient and burial rate (**Figure 2-3**). No such model currently exists for impure and clay-rich rocks although a similar behaviour is likely. The remainder of this thesis will concentrate on the lower permeability fault rocks formed above the ductile-to-brittle transition.



**Figure 2-3: Plot of porosity (dashed line) and  $p/p^*$  (continuous line) vs. burial depth for medium-grained sandstone ( $r = 150 \mu\text{m}$ ) with initial porosity of 30% buried at rate of 0.05 km/m.y. under geothermal gradient of 30 °C/km. Predicted modes of deformation, base based on porosity and  $p/p^*$ , and their consequences for fault permeability are shown. After Fisher et al. (2003).**

## 2.3 Fluid flow properties of fault rocks

In this section, the fluid flow properties of the fault rock and their controls are discussed. The petroleum industry is interested in how faults impact fluid flow on both a production time-scale (i.e. decades) and geological time-scale (i.e. millions of years). In this regard, fluid flow simulation modelling for the reservoir is found to be the best tool. Fluid flow simulation models are also helpful to mimic the fluid behaviour in the reservoir (Dake, 2001). Fluid flow in petroleum reservoirs is generally modelled by using Darcy's law (Darcy, 1856), the following equation shows the special case for horizontal fluid flow:

$$\frac{q}{A} = \frac{k \Delta P}{\mu L} \quad \text{Eq. (2-1)}$$

Where  $q$  is the flow rate in cubic centimetre per second ( $\text{cm}^3/\text{s}$ ),  $k$  is the permeability of porous media in Darcy (D),  $A$  is the cross sectional area of the porous media in square centimetre ( $\text{cm}^2$ ),  $\Delta P$  is the differential pressure in atmosphere (atm) across the length  $L$  in centimetre (cm) and  $\mu$  is the viscosity of the fluid passing through the porous media in centipoises (cp). The use of Darcy's law for fluid flow simulation modelling in petroleum reservoirs has resulted in many studies measuring the permeability of fault rocks.

Manzocchi et al. (1999) has modified the Eq. (2-1) as:

$$\frac{q}{A} = \frac{k_f \Delta P}{\mu t_f} \quad \text{Eq. (2-2)}$$

to predict the rate of fluid flow across faults. This is the same as Darcys law except  $k$  is replaced by  $k_f$  and  $L$  is replaced by  $t_f$ , where  $k_f$  is the permeability of fault and  $t_f$  is the thickness of fault. According to this modification, the flow rate across the

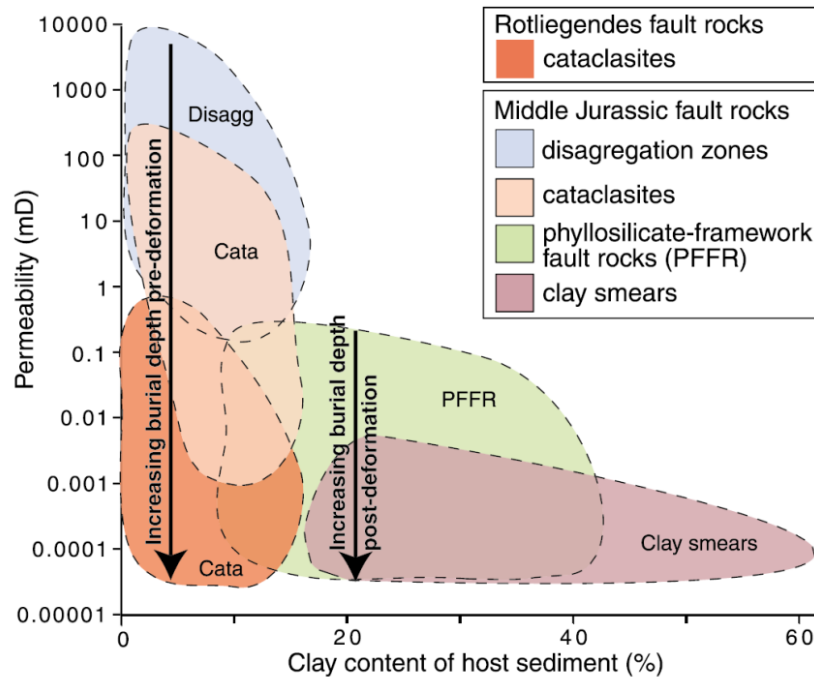
fault is highly influenced by its thickness and permeability as well as the viscosity of fluid.

Fault thickness has been measured by several authors (Evans, 1990; Childs et al., 1997) on the basis of different assumptions. Sperrevik et al. (2002) have taken a zone, which is highly altered due to deformation process, as the thickness  $t_f$ , of the fault. However, Caine et al. (1996) argue that fault thickness is the region where most of the displacement has been accommodated. Thickness of the fault zone,  $t_f$ , has been correlated with the fault throw ( $T$ ) at the surface of the fault and there is general assumption is that  $t_f$  and  $T$  has a linear relationship with each other (Walsh et al. 1998; Evans, 1990; Hull, 1988; Knott et al. 1996).

Sperrevik et al. (2002) stated that there is a large amount of scatter on plots of  $t_f$  vs.  $T$ , which may be due to: problems with dimensional estimation of fault zone, dissimilarity in fault system (based on fault system i.e. normal fault, strike-slip fault and thrust fault), dissimilar lithologies, complex structure of faults, large variation in overburden pressure when deformed. Therefore, a reasonable measurement of the fault thickness is mandatory to use in reservoir simulation models if robust results are to be obtained.

A fault may affect fluid flow in the reservoirs by a variety of processes including: (i) juxtaposition of different lithologies; (ii) creation of a low permeability fault rock, or (iii) creation of a high permeability pathway that acts as a conduit for fault-parallel fluid flow (Manzocchi et al., 2010; Fisher et al., 2001; Aydin, 2000; Knipe, 1993). In all cases it is necessary to understand and model the fluid flow in the reservoir for the enhanced hydrocarbon recovery. This may help in making decisions of appropriate position to drill production wells.

Fisher and Knipe (1998) have published the first systematic study regarding the evaluation of fluid flow properties of the fault rocks within the petroleum reservoirs. The study showed that fault permeability was broadly related to its clay content (**Figure 2-4**) but was also controlled by factors such as overburden pressure (stress) when faulting occurred and the maximum depth of burial of fault.

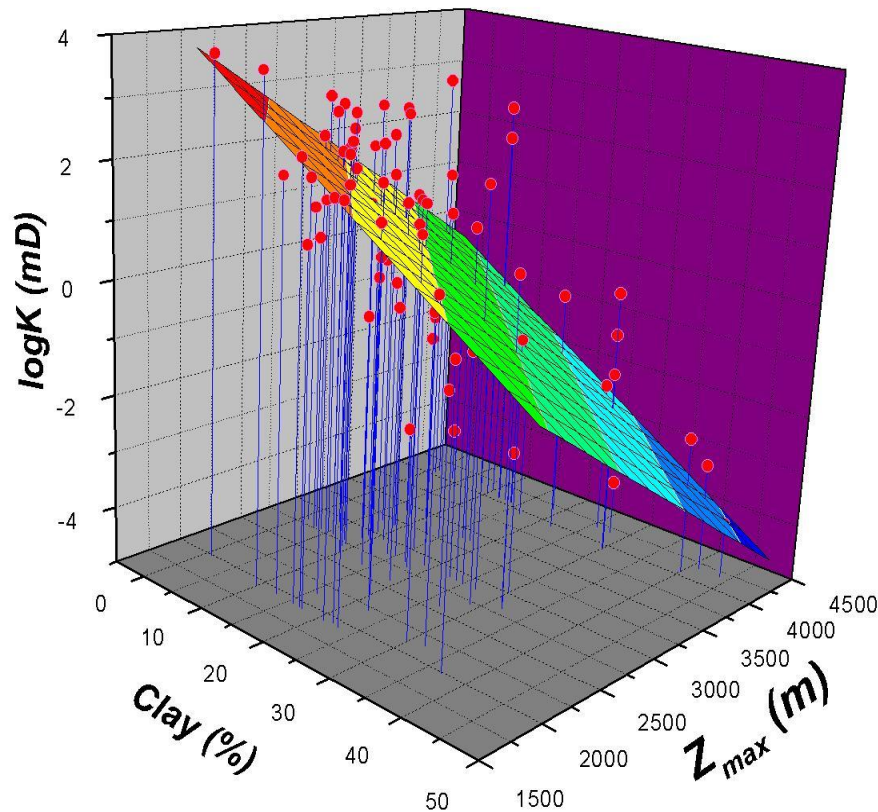


**Figure 2-4: Summary of the fault rock permeability data from the North Sea and Norwegian Continental Shelf. Permeability is plotted against clay content for the various fault rock types. Also shown on the diagram is two of the main c controls on the permeability of the faults in clean sandstones and impure sandstones (i.e. burial depth at the time of faulting and maximum post-deformation burial depth respectively). After Fisher and Knipe (2001).**

Similarly Sperrevik et al. (2002) produced a correlation between the permeability of fault rocks, their clay content and the maximum depth of burial experienced (**Figure 2-5**). This 3-D plot is expressing the negative exponential correlation between the two above mentioned parameters, which are the content of clay  $V_{Clay}$  and the rock permeability  $k_m$  at specific burial depth. Similarly, the permeability  $k_m$  is found to have the same relationship with maximum burial depth,  $Z_m$

at some specific clay content,  $V_{clay}$ . The regression equation for this correlation is given as:

$$k_m = 1.39 \times 10^7 \times e^{-(0.194V_{clay}-0.0043Z_{max})} \quad \text{Eq. (2-3)}$$



**Figure 2-5: 3D plot showing the relationship between measured clay content, permeability, and maximum burial depth for host rocks. The plane represents the exponential least squares regression. After Sperrevik et al. (2002).**

It is also very worthwhile for petroleum industry to be able to predict the possibility that fault rocks can trap petroleum over geological time. In this case, trapping is envisaged to occur by capillary processes being higher than buoyancy forces. Buoyancy force causes oil and gas to move in an upwards direction. The buoyancy driven migration of petroleum through the pores of the porous media is restricted by forces, which mainly depend on the size of pore throats of porous media,

the interfacial tension between hydrocarbon and water (brine), and the contact angle between the petroleum, brine and rock i.e. wettability. The combination of all three factors is generally called “capillary pressure” (Schowalter, 1979). Leverett (1941) defined the capillary pressure as the pressure difference between the wetting phase and the non-wetting phase. The knowledge of capillary pressure is important as it explains the trapping mechanism of hydrocarbon in subsurface (Berg, 1975). In particular, the non-wetting phase (oil or gas in a water wet rock system) in a two phase system cannot enter a pore until its phase pressure is higher than that of the wetting phase (brine in a water wet rock system) by an amount which is capillary entry pressure of pore-throat. The capillary entry pressure,  $P_c$ , can be calculated from the **Eq. (2-4)** which is developed by Washburn’s (1921) on the basis of steady state flow assumption and later modified by Rideal (1922) and Sezekely et al. (1971) for inertial “vena contracta” effects respectively. This equation has used the pore throat size of the porous media and the interfacial tension of the brine-petroleum system to calculate the capillary pressure.

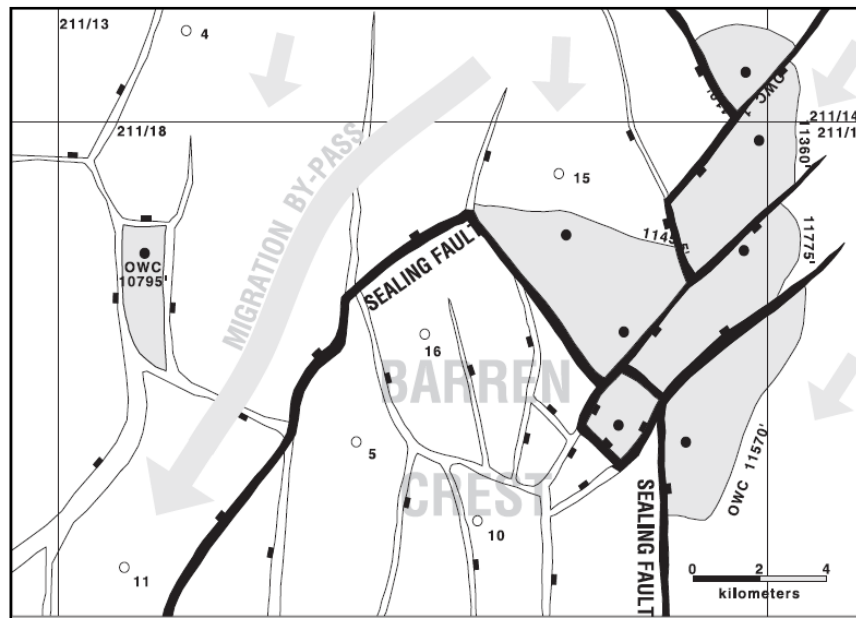
$$P_c = \frac{2\gamma \cos \theta}{r_c} \quad \text{Eq. (2-4)}$$

Where  $P_c$  is capillary pressure and measured in Pascal ( $P_a$ ),  $\gamma$  is the interfacial tension between hydrocarbon and water and measured in Newton/metre (N/m);  $\theta$  is the contact angle between the fluid and porous media (rock) surface measured in degrees, and  $r_c$  is the radius of pore throat measured in metre (m). A fault rock usually consists of a range of pore throat sizes and the minimum pressure that is necessary for a non-wetting fluid to completely pass through its pore system is controlled by the pore throats which have the minimum radii. These minimum pore throats are connected with largest pore throats to make a complete flowing path and the pressure



required for fluid to pass through them is called threshold pressure (Katz and Thompson, 1986). For a non-wetting phase to flow through a porous medium it must have a pressure higher than the wetting phase by the threshold pressure.

It is argued that fault rocks have the potential to act as barriers to the flow of oil and gas over geological time because they often have small pore sizes and therefore high capillary entry pressures. In this regard, Hardman and Booth (1991) has given an example of the Don Field, North Sea where fault sealing behaviour has prevented petroleum migration into the faulted compartment located at the crest of the field (**Figure 2-6**). Alternatively, trapping of hydrocarbon may have occurred at the flank of the geological structure alongside the fault that has sealed due to the juxtaposition of different lithologies. This compartmentalization was result in three dry wells, which were drilled at the crest of the reservoir, namely 211/18-5, 10 and 16 (**Figure 2-6**).



**Figure 2-6: Structural map of the Don Field, which is showing the fault sealing trap for hydrocarbon. After Harman and Booth (1991).**

Schowalter (1979) mentioned in his paper that buoyancy force is the main reason for secondary migration in hydrostatic conditions. The buoyancy force is developed between wetting and non-wetting phases due to the density difference; this buoyancy force is often referred as the buoyancy pressure. The relationship between the densities of two fluids and the buoyancy pressure can be expressed as (Fisher et al., 2001a):

$$P_b = (\rho_w - \rho_{hc})gh \quad \text{Eq. (2-5)}$$

similar equation in field units is

$$P_b = 0.433h(\rho_w - \rho_{hc}) \quad \text{Eq. (2-6)}$$

where  $P_b$  is buoyancy pressure measured in pound per square inch (psi),  $\rho_w$  is the density of water in gram per cubic centimetre ( $\text{g/cm}^3$ ),  $\rho_{hc}$  is the density of the hydrocarbon in gram per cubic centimetre ( $\text{g/cm}^3$ ), and  $h$  is the height of the hydrocarbon column in feet (ft) (Fisher et al., 2001a; Skerlec, 1999; Watts, 1987). To flow through a porous medium, the buoyancy pressure in petroleum column must exceed the threshold pressure. The height of hydrocarbon column trapped by a fault rock can be calculated by using the criteria that buoyancy pressure must be equal to the capillary pressure (Schowalter, 1979; Fisher et al., 2001a; Skerlec, 1999; Watts 1987). The fault or seal starts leaking if the buoyancy pressure exceeds the capillary pressure. In case of maximum hydrocarbon column exist when:

$$P_b = P_c$$

$$0.433h(\rho_w - \rho_{hc}) = \frac{2\gamma \cos \theta}{r_c} \quad \text{Eq. (2-7)}$$

$$h = \frac{\frac{2\gamma \cos \theta}{r_c}}{0.433(\rho_w - \rho_{hc})} \quad \text{Eq. (2-8)}$$

$$h = \frac{P_c}{0.433(\rho_w - \rho_{hc})} \quad \text{Eq. (2-9)}$$

According to Leverett, (1941):

$$P_c = P_{wetting} - P_{non-wetting} \quad \text{Eq. (2-10)}$$

Eq. (2-9) becomes:

$$h = \frac{P_{wetting} - P_{non-wetting}}{0.433(\rho_w - \rho_{hc})} \quad \text{Eq. (2-11)}$$

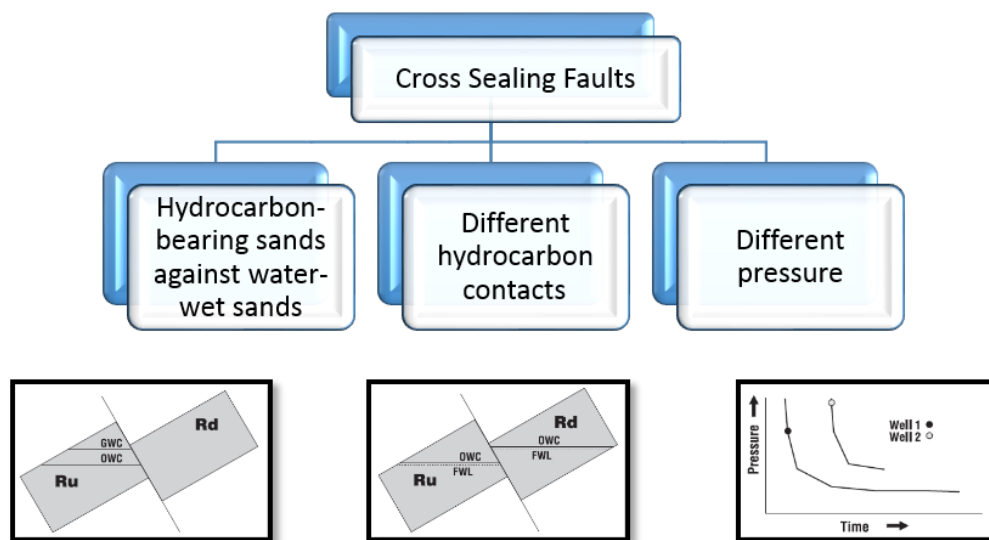
The height of the hydrocarbon column has been used to assess the fault sealing capacity (Fisher et al., 2000; Skerlec, 1999; Watts, 1987).

## 2.4 Evaluation of fault sealing capacity

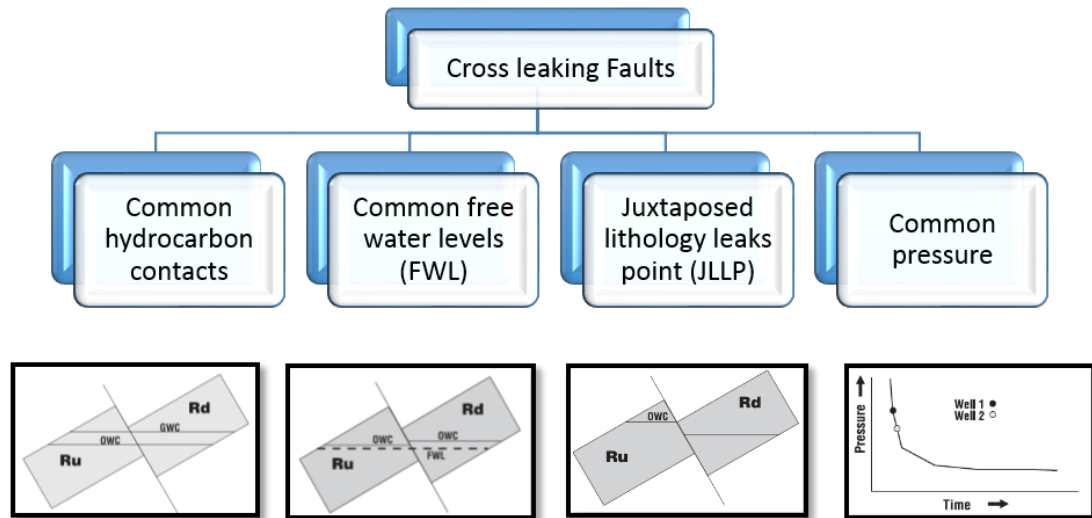
Fault sealing behaviour assessment is a prerequisite for an oil reservoir field development and production forecasting. Fault sealing is usually risked in a qualitative way even though scientists have understanding about the variables which control sealing capacity (Downey, 1984). The success ratio for fault analysis can be increases by using available quantitative techniques but they are few in number. The estimated fault sealing/leaking properties then can be incorporated in to reservoir simulation models to have a robust model and reduces expensive inaccuracies in field development (Skerlec, 1999).

Fault sealing leaking behaviour can be defined by two basic ways which are:

- i) **Cross sealing and leaking:** describing the lateral connection or communication of the fault developed by the juxtaposition of different sand materials.
- ii) **Dip sealing and leaking:** describing the vertical connection or communication of the fault across the stacked lithologies of sands, alongside the fault (Skerlec, 1999). The criteria of cross and dip sealing/leaking is presented in **Figure 2-7** and **Figure 2-8** respectively.



**Figure 2-7: Fault sealing evaluation. Rd and Ru are different lithologies. After Skerlec, (1999).**



**Figure 2-8: Fault leaking evaluation. Rd and Ru are different lithologies. After Skerlec, (1999).**

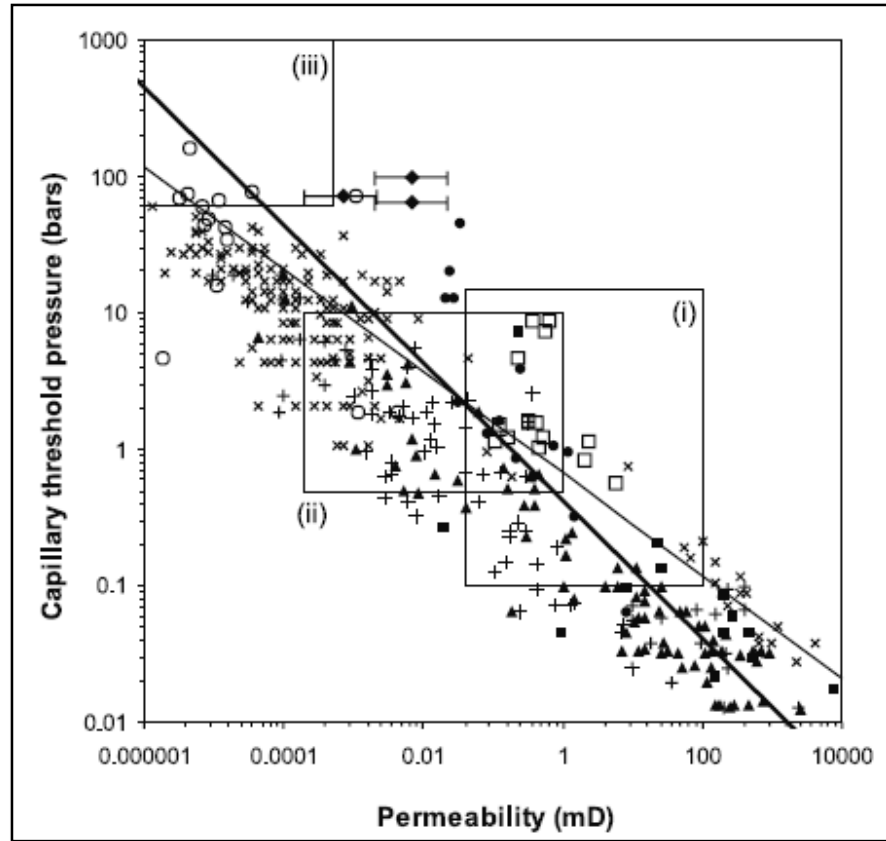
Fisher et al. (2000) has used the theoretical aspect for the fault seal analysis given by Watts (1987) and explained some implications for fault seal analysis. Firstly, the same pressure of fluid across faults does not guarantee that the fault will not act as a barrier during production. It is observed that the production rate in Brent Fields was far lower than initially expected probably because due to fault-related compartmentalization (Corrigan, 1993). Secondly, the difference in column heights of hydrocarbon may be due the insufficient charging of hydrocarbon to equilibrate the columns heights and pressure or the fault showing leaking behaviour, the faults have sealing capacity. Thirdly, the fault itself has a very complex structure and assumption of similar sealing capacity alongside the fault may lead to unfavourable results. Overall, Fisher et al. (2001) suggest that differential pressure between pore water and the hydrocarbon should be taken to evaluate the sealing capacity of the fault.

Broad correlations exist between threshold pressure and absolute permeability, which allow potential petroleum column heights that a fault can seal to be calculated if no detailed capillary pressure data are available. Manzocchi et al. (2002) has

presented sets of data for the fault rock permeability and capillary threshold pressure (**Figure 2-9**). It was concluded that the threshold pressure of the higher permeability fault rock is the same as that of the unfaulted rock while at same permeability the clay-rich rock showed higher values. Manzocchi, et al. (2002) has described the correlation defined by Ringrose et al. (1993) for calculating the capillary pressure of fault rock:

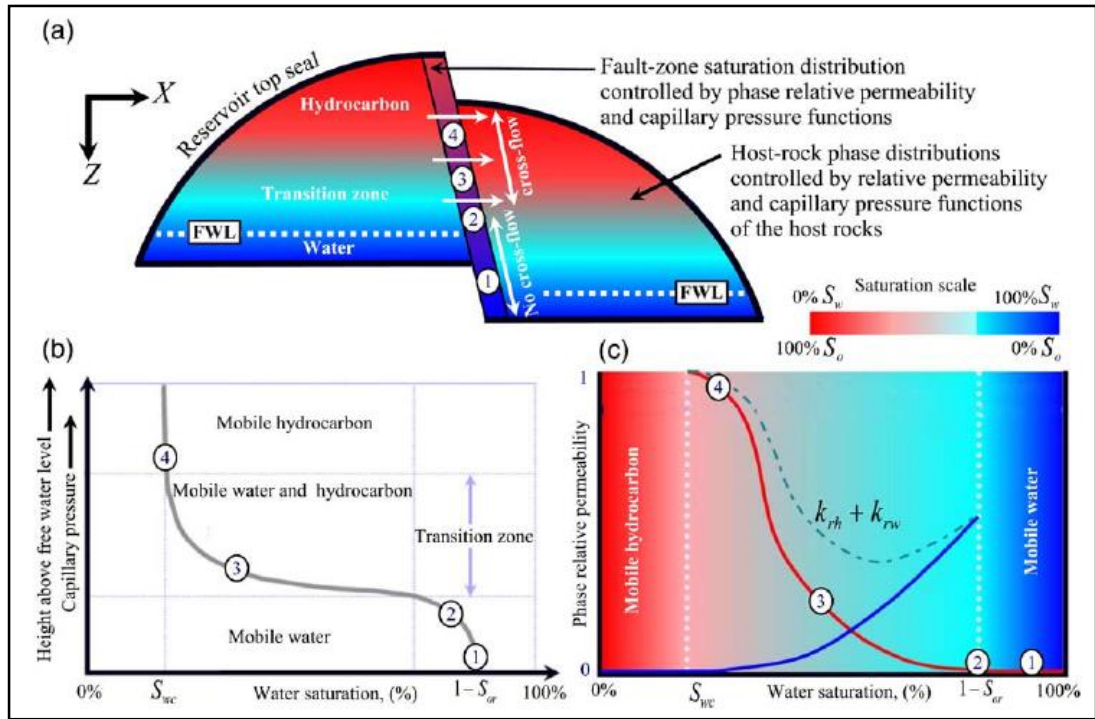
$$P_c = C' S_e^{-2/3} \left( \frac{\phi}{k} \right)^{0.5} \quad \text{Eq. (2-12)}$$

Where  $P_c$  is capillary pressure, value of  $C'$  is taken as 3,  $\phi$  is the porosity,  $S_e$  is the effective saturation of the wetting phase,  $k$  is the single phase permeability measured in milli Darcy (mD).



**Figure 2-9: Plot of capillary threshold pressure vs. permeability for fault samples (solid symbols) and un-faulted rock samples (crosses and open symbols) from a variety of lithologies (from Manzocchi et al., 2002). The boxes (Fisher & Knipe 1998) are summaries of data from (i) faults in clean sandstone, (ii) dirty sandstone and (iii) shale-rich fault gouge. The two lines are published model relationships (thinner line from Ringrose et al. (1993) and Fisher & Knipe (1998), thicker line from Harper & Lundin (1997)). Capillary threshold pressures have been normalized for a water-wet system with a hydrocarbon–water interfacial tension of 40 dynes  $\text{cm}^{-1}$ , and a contact angle of 30°. Legend: filled triangles and crosses, Sperrevik et al. (2002); filled squares, Harper & Lundin (1997); empty squares, Schowalter (1979); filled circles, Gibson (1998); filled diamonds, Fulljames et al. (1997); Ibrahim et al. (1970); empty circles, Schlomer & Krooss (1997).**

For many years, the paradox existed whereby those dealing with the impact of faults on petroleum production concentrated on the absolute permeability, which is a single-phase, whereas those working on petroleum exploration concentrated on the capillary entry pressure, which is a two-phase property. Fisher et al. (2001) addressed this paradox when they published a conceptual model for multi-phase flow across a fault in a petroleum reservoir (**Figure 2-10**).



**Figure 2-10: Conceptual model, based on Fisher et al. (2001) for multi-phase flow across a fault in a petroleum reservoir. (a) The fluid saturations within the reservoir and fault, red for hydrocarbon, blue for water. (b) The capillary pressure. (c) The i- directional water-wet relative permeability curves for the fault rock. After Busafi et al. (2004).**

This model explains the multiphase flow phenomenon in the subsurface. Sealing faults usually have very small pore throats, which results in a very high capillary entry pressure in comparison to the host rock of the reservoir. Around the free water level (FWL) which is described by points 1 and 2 in **Figure 2-10**, the buoyancy pressure of hydrocarbon column is insufficient to surmount the fault's capillary entry pressure and there is no possibility that petroleum with flow across the fault in this region. As the hydrocarbon column height increases, the buoyancy pressure eventually exceeds the threshold pressure of the fault (point 2 **Figure 2-10**), allowing petroleum to flow across the fault. Here the rate of fluid is controlled by the absolute and relative permeability of the fault and can be measured by the adaptation of Darcy's Law:



$$q_w = \frac{kk_{rw}A}{\mu_w} \frac{dP}{dL} \quad \text{Eq. (2-13)}$$

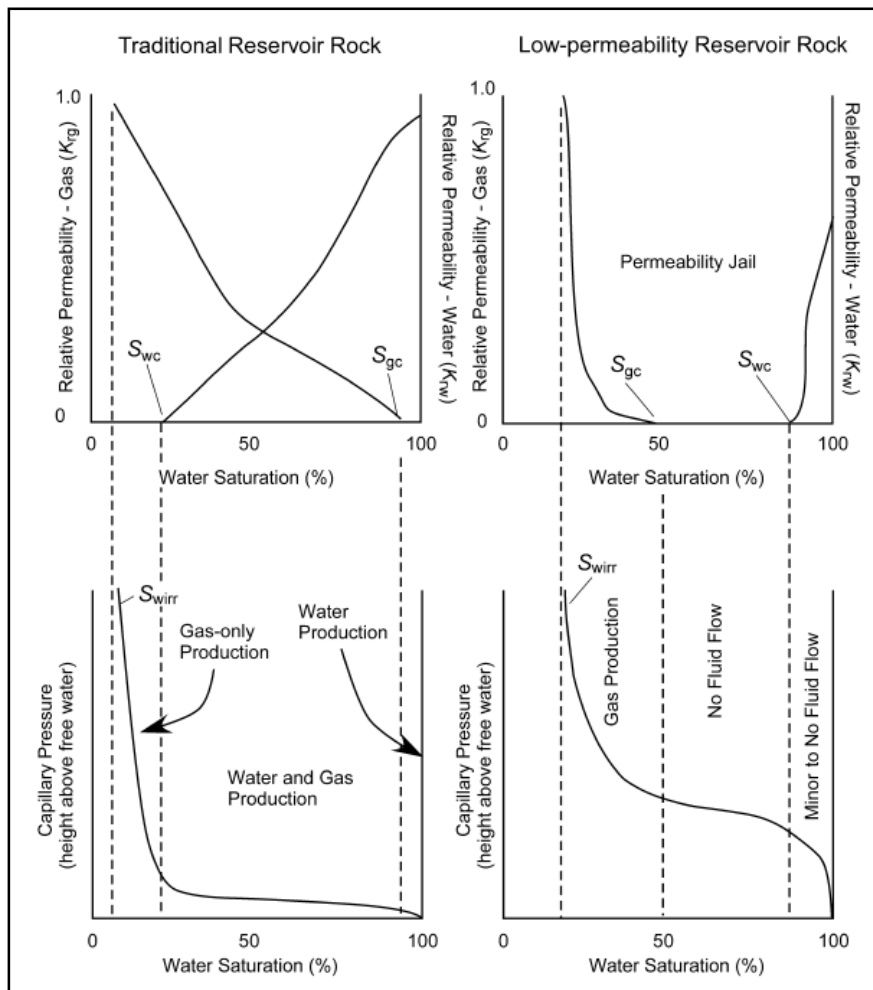
$$q_{nw} = \frac{kk_{rnw}A}{\mu_{nw}} \frac{dP}{dL} \quad \text{Eq. (2-14)}$$

where  $q_w$  and  $q_{nw}$  are the flow rates for the wetting (w) and non-wetting (nw) phases respectively and in units  $\text{cm}^3/\text{s}$ ,  $k_{rw}$  and  $k_{rnw}$  are the relative permeability (effective permeability divided by absolute permeability) of the wetting phase and non-wetting phase respectively and these are dimensionless,  $A$  is the cross sectional area of the rock facing the fluid flow and its unit is square centimetre ( $\text{cm}^2$ ),  $\mu_w$  and  $\mu_{nw}$  are the viscosities of the wetting and non-wetting fluids and the unit is centipoise (cp), and  $dP/dL$  is the pressure drop across the length of the fault and its unit is atmosphere (atm).

The relative permeability is a function of the saturation of the wetting and non-wetting fluids. In water wet rock system, the wetting phase minimum saturation is called ‘irreducible water saturation’, ( $S_{wirr}$ ), which can be obtained by displacing the wetting phase (water) by non-wetting phase (e.g. oil). In contrast, the non-wetting phase saturation is the highest at this point. At ‘residual oil saturation’, ( $S_{or}$ ), or ‘critical gas saturation’, ( $S_{gc}$ ), the non-wetting phase is immobile and wetting phase saturation is highest.

Shanley et al. (2004) has explained how saturation affects the relative permeability of both of wetting and non-wetting fluids (**Figure 2-11**). They have compared the relative permeability results of high and low permeability rocks. In low permeability rocks the irreducible (connate) water saturation ( $S_{wirr}$ ) and critical water saturation ( $S_{wc}$ ) can be considerably different; however, in traditional reservoirs rock they are similar. Shanley et al. (2004) presented a case in which traditional reservoir is showing an

extensive range of water saturation in which gas and water can flow simultaneously. In contrast, in low permeability rock's reservoir, they have shown that there is large range of saturations of water in which none of the wetting and non-wetting phase can flow (Figure 2-11). It is also found that in some extremely low permeability reservoirs, even at very high water saturations, there is no mobility of water reported.



**Figure 2-11: Schematic illustration of capillary pressure and relative permeability relationships in traditional and low-permeability reservoir rocks. Critical water saturation ( $S_{wc}$ ), critical gas saturation ( $S_{gc}$ ), and irreducible water saturation ( $S_{wirr}$ ) are shown. After Shanley et al. (2004).**

Relative permeability is usually measured as the function of saturation of the wetting phase. Such experiments are generally difficult to conduct and interpret even in high permeability rocks. Measurements in low permeability rocks are far more

difficult and only a few laboratories have attempted such measurements. In this thesis, oil-brine permeability experiments have been performed and the methodology and results will be discussed in next chapters. The use of relative permeability data in reservoir simulation modelling has been proved to give a better understanding. Manzocchi et al. (2002) have published a methodology to use the fault's multiphase flow properties. They developed simulation models for production by adding in the transmissibility multipliers. No data was available on the relative permeability of fault rocks until Al-Hinai et al. (2008) published results from gas relative permeability measurements conducted on the cataclastic fault rock the Hopeman Quarry in Scotland. Recently, Tückmantel et al. (2011) has published relative permeability data for the cataclastic fault rock.

## **2.5 Fault seal analysis work flow**

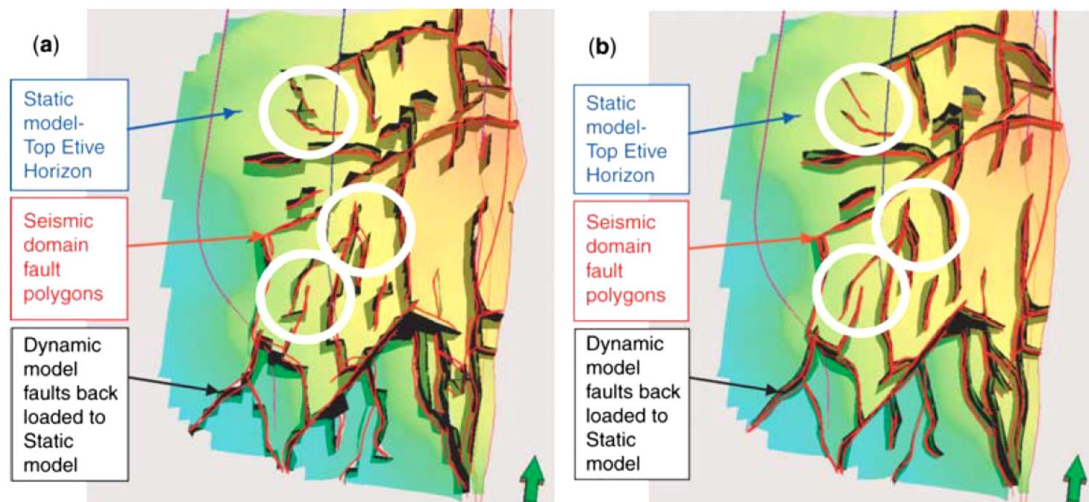
It is found that the faults can be the reason of the reduction in cross-fault flow and non-incorporation of this effect may lead to the erroneous simulation results (Fisher and Jolley, 2007). The faults impacts for compartmentalization and reduction in hydrocarbon recovery is also well documented (Corrigan, 1993; Childs et al., 2002). The fault sealing capacity is depend on the magnitude of pressure it can withstand, which is exerted by the hydrocarbon columns across the fault (Fisher et al., 2001). During production the pressure gradients are continuously changing and depending on the rate of production. In this regard, fault seal analysis is playing a very vital role to understand the fault seal behaviour and define the oil, gas and water flow rate across the fault when production is going on (Fisher and Jolley, 2007). The 'dynamic model' which are incorporated in 'prediction mode' are used for the flow simulation and future decision can be made for production and well planning in very feasible way (Dake, 2001). The very early attempt for the incorporation of faults in reservoir

simulation was made by Bentley and Barry (1991). They used clay smearing and sand-shale juxtaposition as the fault sealing criteria which is main reason for the restriction of flow. The production history matching is used to calibrate the transmissibility values which were applied to the corresponding grid block of the reservoir simulation model. In past decade, some data were made available for fault structure (Harris et al., 2003a) and single phase permeability for cataclastic and phyllosilicate fault rocks (Fisher and Knipe, 1998, 2001). The availability of the data for the fault thickness and absolute permeability made easy to calculate the faults transmissibility multipliers which then used in reservoir simulation models to predict the fluid flow across the faults (Jolley et al., 2007; Manzoochi et al., 1999; Kani and Knipe, 1998). The further development has suggested that the incorporation of the capillary pressure and relative permeability made simulation models more accurate and robust (Ziljstra et al., 2007; Al-Hinai et al., 2006; Al-Busafi et al., 2005; Manzoochi et al., 2002; Fisher and Knipe, 2001). In this section, the workflow for fault seal analysis is discussed to identify the importance of availability of data for developing the realistic revoir model e.g. fault structure data flow properties of fault.

### **2.5.1 Structure of the fault**

The correct identification of the structure of the fault as cross-fault, sand-sand or sand-shale juxtaposition should be required to made realistic model. The seismic data are used to identify the faults and developing the geological model of the reservoir which will used for production simulation model (Fisher and Jolley, 2007). Jolley et al. (2007) pointed out the discrepancy of the geological models developed for the Brent Province of the North Sea by scaling up the factor of 4 from original fine-scale model (**Figure 2-12**). After running 270 simulations, the Model-1 was not able to match the production history which is mainly due to the inappropriate juxtaposition

arrangements of faults. Then is Model-2 the juxtaposition is finely tuned and by running only 70 simulations the model is mostly matching the production history. The correct interpretation of the seismic model to develop geological model with fault is the base of realistic production simulation model.



**Figure 2-12:** Top reservoir depth map of a Brent field in which faults identified from the seismic survey (red lines) are shown with those incorporated into the production simulation model (black lines). Blue lines are the well trajectories. (a) Model-1: note significant inconsistencies between the faults mapped from seismic and those incorporated into the static and simulation models (white circles). Some faults have been joined within the simulation model, which appear not to be linked within the seismic survey and vice versa. (b) Model-2: the geometrical integrity of the fault pattern is preserved between seismic interpretation, static and simulation models. The effect of preserving the fault juxtaposition geometries, is shown by comparing the simulation results from both models (adapted from Jolley et al., 2007).

### 2.5.1.1 Rock flow properties

The development of the realistic geological model is the first step and after this step the fluid flow properties of the fault rock are required. Manzoochi et al. (1999) presented the equation for transmissibility multipliers which are incorporated into the simulation models to get the realistic results. The transmissibility,  $Trans_{ij}$ , of two grid blocks namely  $i$  and  $j$  having fault of constant thickness between them (**Figure 2-13**), can be calculated by following equation:

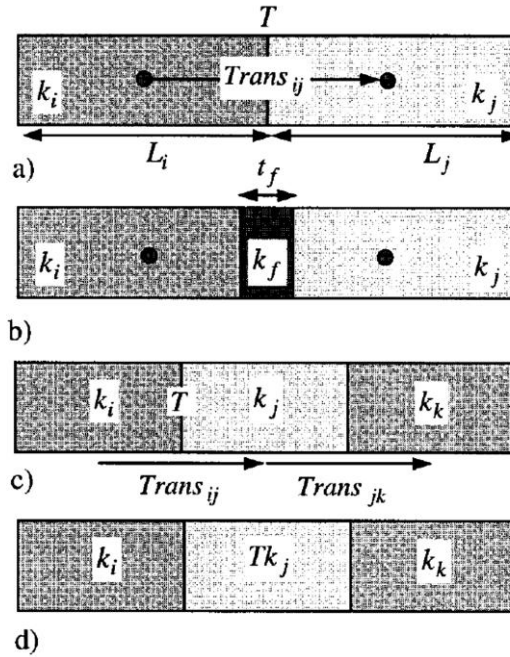
$$Trans_{ij} = \left( \frac{2}{\left(\frac{L_i}{k_i}\right) + \left(\frac{L_j}{k_j}\right)} \right) \quad \text{Eq. (2-15)}$$

where  $L_i$  and  $L_j$  are the lengths of the  $i$ th and  $j$ th grid blocks,  $k_i$  and  $k_j$  are the permeabilities of the undeformed blocks. Similarly the transmissibility of fault ( $TransF_{ij}$ ) having constant thickness lying between two grid blocks  $i$  and  $j$  can be calculated by using following equation:

$$TransF_{ij} = \left( \frac{2}{\frac{(L_i - t_f)}{k_i} + \frac{2t_f}{k_f} + \frac{(L_j - t_f)}{k_j}} \right) \quad \text{Eq. (2-16)}$$

where  $t_f$  representing the thickness of fault and  $k_f$  is its permeability. In production simulation models the impact of fault is incorporated by applying the transmissibility multipliers to the having these transmissibility, the transmissibility multipliers then can be calculated by following equation:

$$TM = \frac{TransF_{ij}}{Trans_{ij}} \quad \text{Eq. (2-17)}$$



**Figure 2-13: Representation of a fault between grid-blocks  $i$  and  $j$ .** (a) The transmissibility multiplier ( $T$ ) acts on the transmissibility ( $Trans_{ij}$ ) between two grid-block centres.  $Trans_{ij}$  is a function of grid-block permeabilities and lengths. (b) To calculate the value of the multiplier, the thickness of low permeability fault-rock is considered explicitly. (c) A transmissibility multiplier assigned between blocks  $i$  and  $j$  modifies only  $Trans_{ij}$ . (d) A permeability multiplier applied to block  $j$  modified both  $Trans_{ij}$  and  $Trans_{jk}$ .

The fault thickness of fault and its permeability are required to calculate the transmissibility multipliers as shown in **Eq. (2-16)**. Empirical correlation are used to calculate the thickness of fault, for example Manzoochi et al. (1999) have used the following equation

$$t_f = \frac{d}{170} \quad \text{Eq. (2-18)}$$

where  $d$  is the fault displacement. It is assumed that thickness obtained by **Eq. (2-18)** is the effective thickness of fault by which the fluid is flowing across the fault. Harris et al. (2005, 2007) found that this effective thickness of fault is only supported for single phase fluid flow properties. In practice it is very difficult to calculate multiphase fluid flow properties for fault rock. The fault permeability can be calculated from the correlation presented by Manzoochi et al. (1999) as given in Eq.

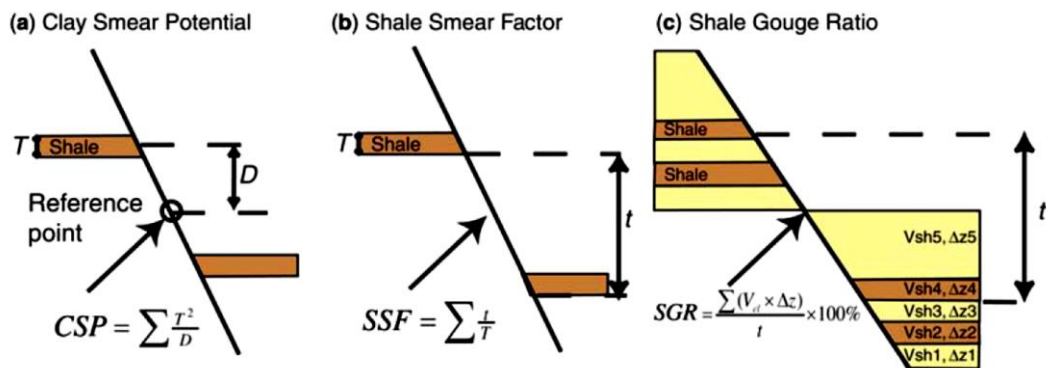
(1-1). Shale gouge ratio is defined by Fristad et al. (1997) and Yielding et al. (1997) as:

$$SGR = \frac{\sum(V_{cl} \times \Delta z)}{t} \times 100\% \quad \text{Eq. (2-19)}$$

where  $V_{cl}$  is the clay or shale fraction in each layer of thickness  $\Delta z$  and  $t$  is the fault throw (**Figure 2-14-c**). Other important algorithms are also widely used for the relationship between clay content and the fault thickness. The first proposed was Clay Smear Potential (CSP) defined by Bouvier et al. (1989) as:

$$CSP = \sum \frac{T^2}{D} \quad \text{Eq. (2-20)}$$

where  $T$  is the thickness of a shale bed and  $D$  is the distance along the fault from the source bed (**Figure 2-14-a**)



**Figure 2-14: Diagram illustrating the meaning of algorithms commonly used to estimate the continuity of clay smears or the clay content of fault zones: (a) clay smear potential (CSP); (b) shale smear factor (SSF) (Lindsay et al. 1993); (c) shale gouge ratio (SGR). Based on Yielding et al. (1997).**

The clay smear potential is found to be valid for the ductile clay smear present in the fault. The shale Smear Factor (SSF) as presented by Lindsay et al. (1993) shows the relationship between fault throw and thickness of shale bed.

$$SSF = \sum \frac{t}{T}$$



where  $T$  is the thickness of the shale bed,  $t$  is the fault throw (**Figure 2-14-b**). SSF was used to predict the continuity of abrasion-type clay smears in lithified siliciclastic rocks.

### **2.5.2 Incorporation of Multiphase flow properties**

More realistic results have been found for production simulations after incorporating the multi-phase properties of faults in production models (Al Hinai et al., 2006; Al Busafi et al., 2005; Rivenæs and Dart, 2002; Fisher and Knipe, 2001; Manzocchi et al., 1998, 2002; Manzocchi, 1999). High water saturation is expected around the free water level (FWL) if water wet fault rock has small pore throats. In this region the relative permeability of hydrocarbon ( $k_{rh}$ ) will be very low but water can flow. It is also possible for the undeformed regions where the water saturation is low and water relative permeability of water ( $k_{rw}$ ) can be low. At some certain distance from free water level the buoyancy forces may reach to the threshold pressure value and fault can have finite value of relative permeability (Fisher et al., 2001; Al Busafi et al., 2005; Zijlstra et al., 2007). It is stated by Al Hinai (2006) that the use of only single phase permeability in production simulation model can cause the estimation of production by over two orders of magnitude higher than if transmissibility multipliers are used for multiphase properties. So it is very useful to incorporate the multiphase properties of the fault rock in simulation model for realistic modelling.

### **2.5.3 Criticality of evaluation of the fault sealing data**

The data related with the prediction of subsurface fluid flow properties have wide range of uncertainties:

- The seismic data acquired which later used for structural mapping and fault modelling, has different issues that may affect the modelling: azimuth used for data gathering; methodology used for seismic data interpretation; depth conversion methodology used; seismic data interpretation skills, etc (Suter and Berryhill, 1985; Ottesen et al., 2005)
- Uncertainties in estimation of  $V_{\text{shale}}$  and  $V_{\text{clay}}$  by using well logs as no standard method is used so uncertainties may found in defining discrete sand-shale layering and model property ( i.e clay, porosity-permeability) grids (Fisher and Jolley, 2007)
- Uncertainties in estimation of SGR, CSP and SSF as different algorithms gives different estimates (Foxford et al., 1998)
- Uncertainty for the permeability of fault rock measurement, which is found to be excessive by order of magnitude (Fisher and Knipe 2001) and similarly for the thickness of fault rock (Manzocchi et al. 1999).

It is required to standardise the fault seal analysis methodologies by evaluating that they are reliable with the subsurface data.

## 2.6 Knowledge gaps in fault rock properties

A large amount of data on the single phase permeability fault rocks has been published. This has been incorporated into reservoir simulations to understand the impact of faults on fluid flow. But doubt has been identified for their correctness as what conditions has been applied while measurements (Byrnes, 1997; Castle and Byrnes, 1998; Cluff et al., 2010; Fisher et al., 2003). Indeed, close inspection of the laboratory methods used to measure fault rock properties as well as the values

themselves give reasons to suspect that the published values could be in error. In particular,

- Most measurements of fault rock permeability (e.g. Fisher and Knipe, 1998, 2001) were made at ambient stress (~70 psi). However, recent measurements have shown that the permeability of fault rocks and tight gas sandstones (**Figure 2-15**) are highly stress dependent. Jones and Owens (1980) has explained the complex structure of low permeability rocks due to which these rock are very sensitive to stress. Brynes et al. (2003) has presented the comparative data (**Figure 2-15**) which is showing that the low permeability rocks have 10 to 100 times lower permeability if the confining stress is increased from 100 psi to 4000 psi. In this thesis, different stresses have been used to evaluate the stress dependency of the cataclastic fault rocks and compared with the published data in forthcoming chapters.
- Most measurements of fault rock permeability were conducted using de-ionised water despite the fact that the rocks usually contain clay which makes their permeability very sensitive to brine composition (Baptist and Sweeney, 1955; Hewitt, 1963; Land and Baptist, 1965). For example, sandstones that have interstitial smectite lose their permeability completely when flooded with deionised water (**Figure 2-16**) due to the swelling of clay (Lever and Dawe, 1987). In this thesis different composition of the brine has been used to evaluate the behaviour of fault rock samples.

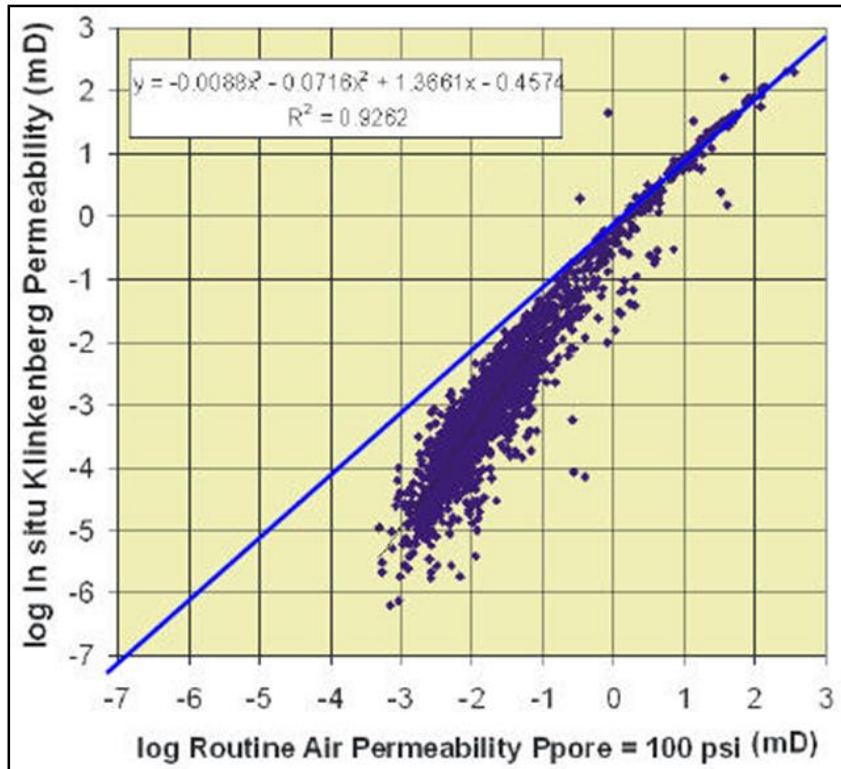


Figure 2-15: Stress dependence of the absolute gas permeability of tight gas sands. Note that the low permeability samples can have up to two orders of magnitude lower permeability when measured at reservoir stress conditions compared to 100 psi (After Byrnes et al., 2009).

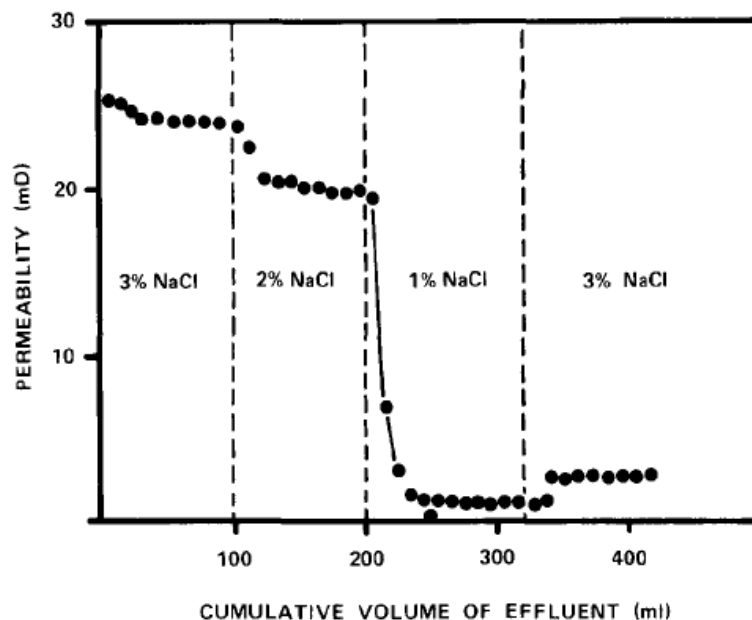


Figure 2-16: Water-sensitivity of the Spiney sandstone, Moray Firth Basin. Note the large decrease in permeability when the brine is changed to 1% NaCl (from Lever and Dawe, 1987).

In addition to uncertainties regarding the single-phase permeability it should be noted that there is very little data related with fault rock are available. Indeed, very few papers have been published on the topic of relative permeability of siliciclastic fault rocks. So currently there are no data available for:

- Brine relative permeabilities of fault rocks in the gas-water system
- Oil water relative permeabilities of fault rocks
- Relative permeability data from more clay-rich fault rocks
- Relative permeability from fault rocks that are not strongly water-wet.

# Chapter 3: Background geology of samples and microstructure analysis

## 3.1 Introduction

Core samples for this study from a North Sea oil reservoir were provided by an operator; the name of the company and exact locations remain confidential. Outcrop samples from (i) Orange, France, (ii) and Hopeman, Scotland and (iii) Miri, Malaysia have also been analysed. The following chapter provides background information on the samples such as their location, depositional environment, structural setting etc. as well as details on the microstructural characteristics of the samples. The chapter is divided into the following eight subsections:

- The background to the core and outcrop samples are described in **Section 3.2** and **Section 3.3** respectively.
- The sample analysis and nomenclature described in **Section 3.4**.
- Experimental methodologies are described in **Section 3.5**.
- Microstructural analysis results are provided in **Section 3.6**.
- Results are discussed in **Section 3.7**.
- Discussion and conclusions are presented in **Section 3.8** and **Section 3.9** respectively.

## 3.2 Company A samples

### 3.2.1 General Location

Fault rock samples from four wells in a Triassic HP-HT (high pressure – high temperature) gas condensate reservoir a reservoir in the North Sea have been provided

by Company A for this study. The field is situated in the Central Graben around 200 km to the south east of Aberdeen. The samples provided were half cuts of 5 inch core.

### **3.2.2 Stratigraphy of field A**

The generalized stratigraphy of field A is shown in **Figure 3-1**, due to confidentiality of the data, the formation names are hidden. The horst of field A is thought to contain Devonian basement on the basis of the seismic interpretation and comparison with similar formations. The main reservoir within field A, from which samples were taken, was deposited in an arid fluvially-dominated environment. Vertical communication in the reservoir is limited by the presence of mudstones deposited in a playa lake. Parts of the field also contain Upper Jurassic sandstones deposited in a shallow marine environment that also contain producible condensate. Kellar et al. (2005) has identified a large variation in movement of Zechstein salt during the time of early Triassic to pre-Triassic on the basis of the seismic data gathered in this area. Zenella and Coward (2003) has related the central North Sea structure with Late Jurassic to early Cretaceous rifting events.

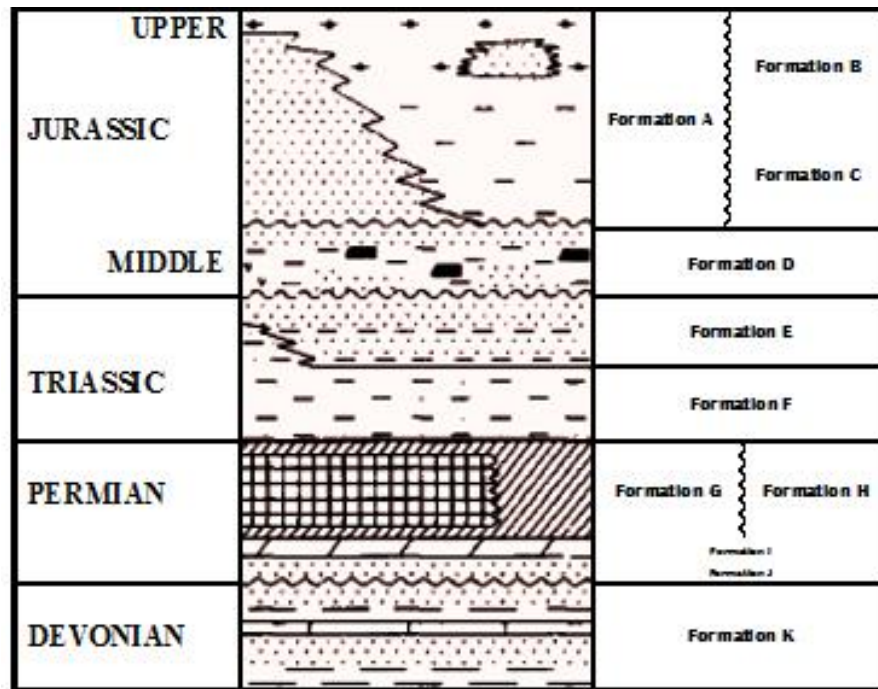


Figure 3-1: Generalized pre-Cretaceous stratigraphy of the Field A.

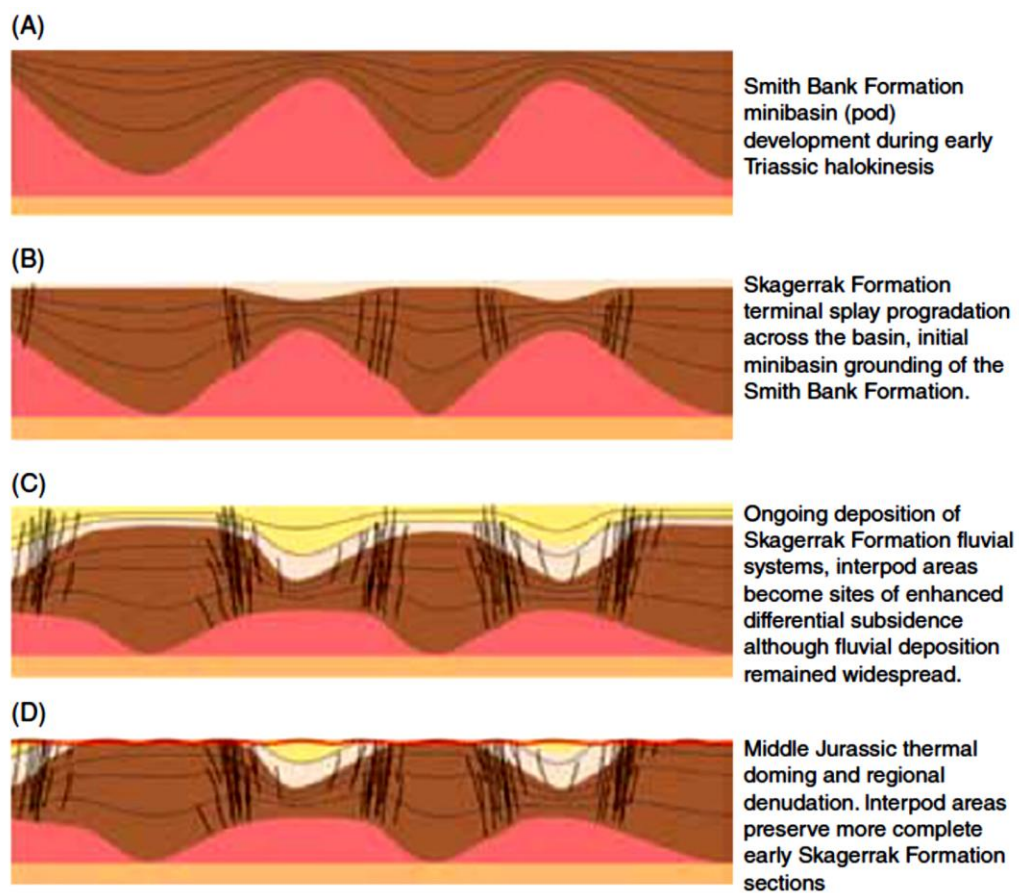
### 3.2.2.1 Structural evolution

The structural evaluation of the field A has been interpreted using a pod-inter-pod model, which was described by Hodgson et al. (1992) and Smith et al. (1993) as the most archetypal structure of central North Sea salt tectonics. The movement of salt, often referred to as halokinesis, is a very important control on sedimentation of the Smith Bank and Skagerrak formations in the central North Sea. Here the movement of salt and salt bodies in the subsurface was affected by both tectonic and gravitational forces (Goldsmith et al., 1995). Salt withdrawal results in a network of synclines (pods) and areas of salt preservation (interpods), the former provide accumulation space for sediment deposition. McKie (2005) explained the conceptual model for pod-inter-pod architecture (**Figure 3-2**). The salt movement occurred throughout the Triassic period but its impact on depositional architecture decreased during with time. Smith et al. (1993)



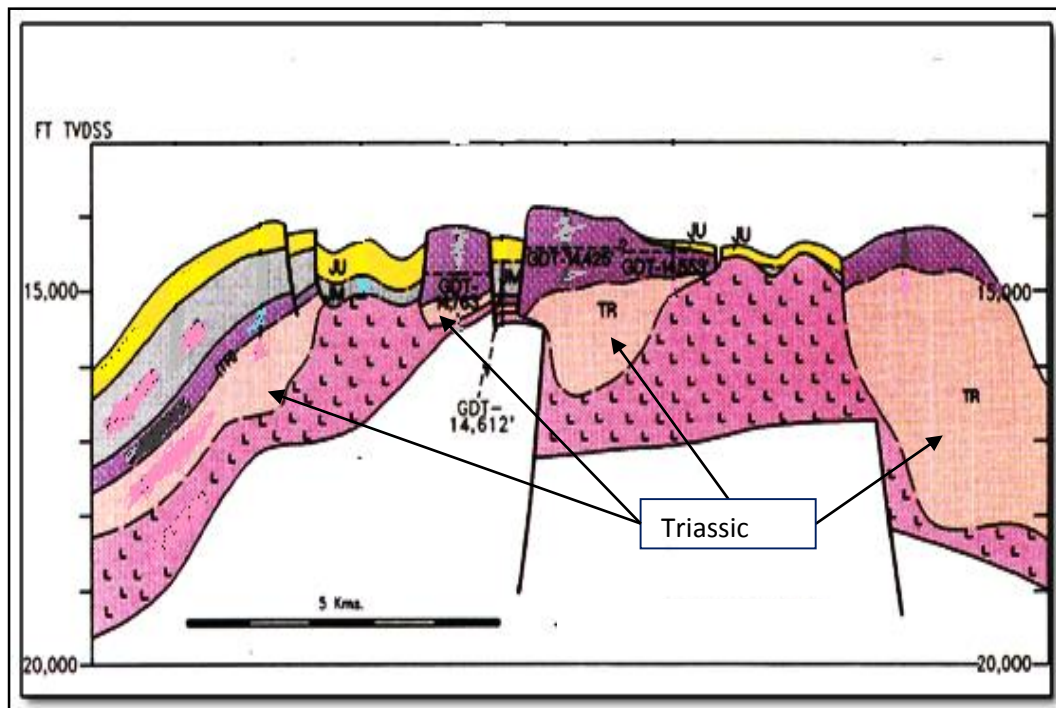
described these pods as alternated grounded pods of Triassic age where the Zechstein salt has been entirely evacuated.

The petroleum discoveries in this area comprises of diverse formations such as, the Triassic Skagerrak formation, the Upper Jurassic Fulmar Formation, the Upper Cretaceous chalk and Paleocene sandstone. Compartmentalization of reservoirs is significant, which is demonstrated by differences in pressure between different parts of these fields (Archer et al., 2010).



**Figure 3-2: Conceptual model for pod-interpod accumulation and preservation in areas of early pod grounding such as the UK Western Platform. Initial mini-basin formation during deposition of the Smith Bank Formation (A) evacuated the underlying halite, resulting in pod grounding on the Rotliegend Group (B). Subsequent progradation of Bunter Formation and lower Judy Sandstone Member terminal splay complexes occurred across the region, with localised thickening in interpod areas where salt continued to be evacuated and/or dissolved (B). This process continued through the Middle and Late Triassic as the region was blanketed by sediment as the basin continued to subside (C), but subsequent erosion during Middle Jurassic thermal doming (D) eroded much of the Triassic stratigraphy, leaving erosional remnants of Skagerrak Formation terminal splays in interpod troughs. The geometries of the troughs do not reflect the depositional geomorphology and are sites of preferential preservation of formerly unconfined distal sheets (From McKie, 2005).**

This model provides an explanation for the rapid variations of thickness of different formations; mainly in Triassic and Jurassic (**Figure 3-3**). The analytical value of the pod-inter-pod model has been established by the data gathered while drilling. Four major pods can be identified where wells (1 – 4) have been drilled in Triassic strata (**Figure 3-3**). The sediments contained within these pods show significant variation in thickness and sedimentology. It is also evident from the samples obtained from these wells that they are different in structure as well their flow properties (discussed in next chapter).



**Figure 3-3: Cross-section through the field A, illustrating the major Triassic pods, the inter-pod areas and gas-water contacts in the pods.**

### **3.2.3 Pressure regimes and hydrocarbon-water contacts in Field A**

Repeat Formation Tester (RFT) data are used to analyse the hydrocarbon and water pressure gradients in field A. It is found that the hydrocarbon gradient ranges

between 0.19 psi/ft to 0.22 psi/ft and the water gradient is 0.54 psi/ft (Figure 3-4). Different hydrocarbon-water contacts have been identified while analysing wire-line log and RFT data, which may be an indication of the presence of sealing faults as described earlier in Section 2.3 (fault seal analysis). Further evidence for the presence of sealing faults is the presence of different pressure compartments (**Figure 3-4**). It is reported that the aquifers in the pods lie on different pressure gradients. For example, in well C-2 and A-4 there is pressure differential of 400 psi, suggesting perhaps that these wells are separated by a sealing fault. It should, however, be emphasised that other mechanisms could be responsible for the lack of pressure communication between these wells such as sedimentary heterogeneity or the presence of salt walls/welds.

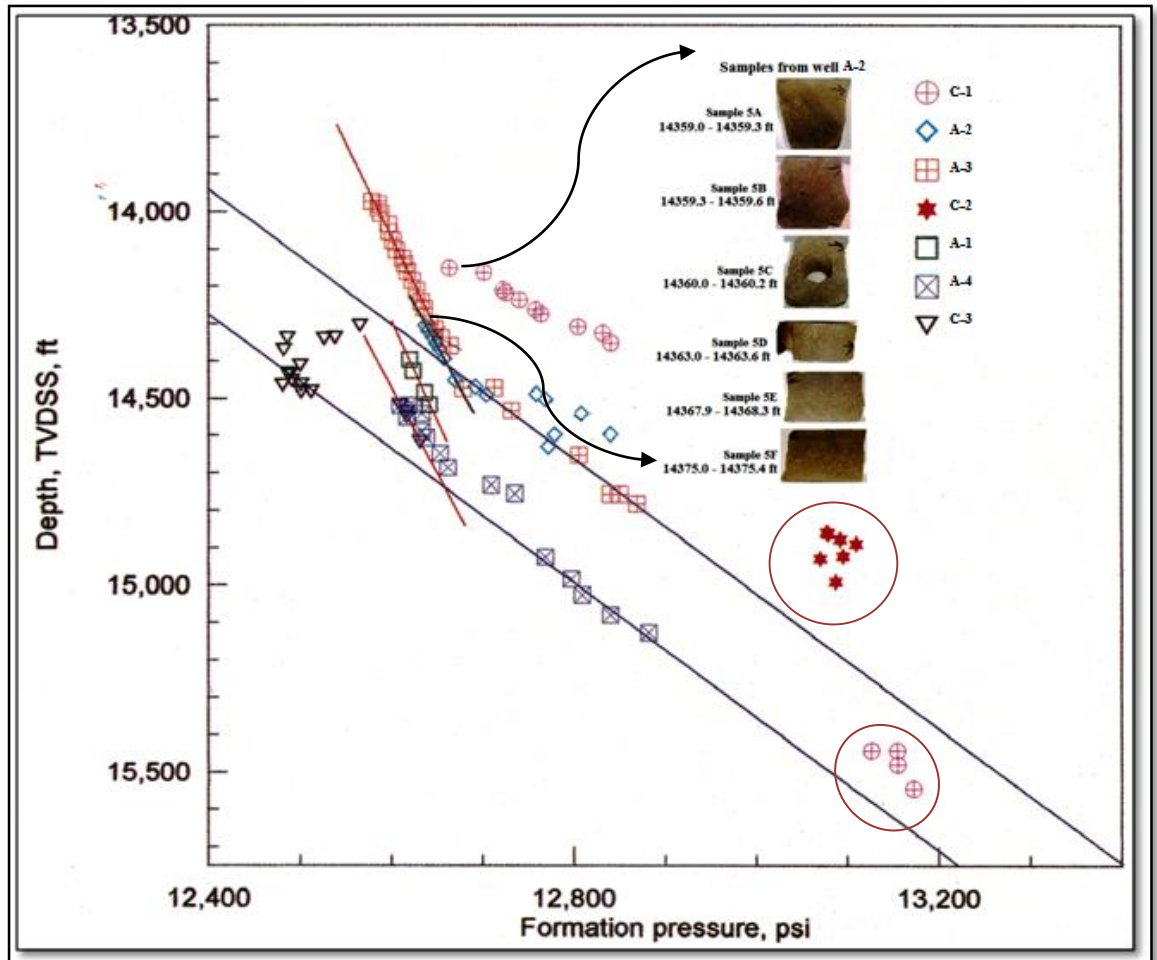


Figure 3-4: Variation in fluid gradient and formation pressure in the Field A. Figure is showing separate aquifers pressure in different pods.

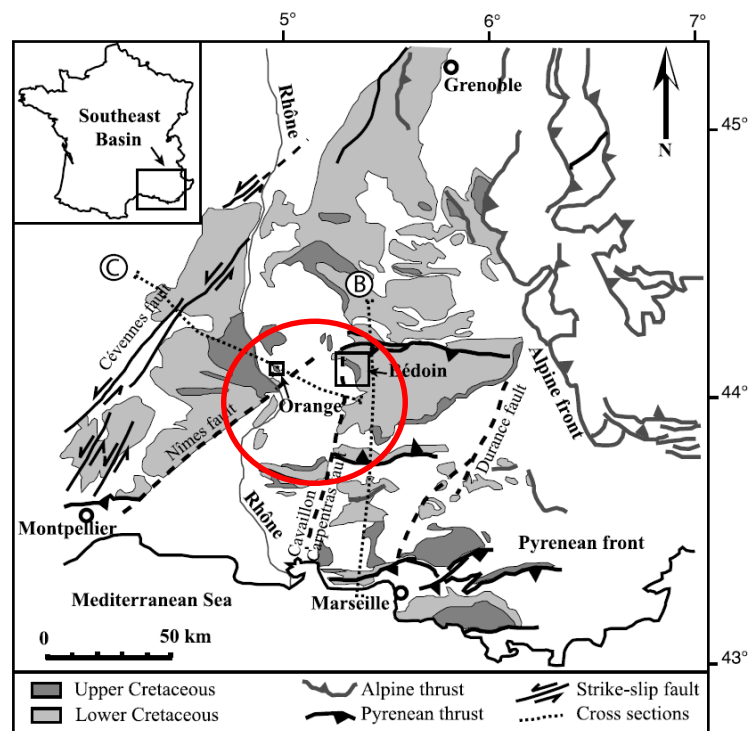
### 3.3 Outcrop samples:

#### 3.3.1 Orange, France

Outcrops sample has been obtained from Cretaceous sandstone of Southeast Basin located in Provence, France (Figure 3-5, Figure 3-6). The deformation structures which have been found in these outcrops are of two types: (i) cataclastic deformation bands mainly developed due to shearing effects and found in large number with small off-sets; (ii) ultra-cataclastic deformation bands which are few in numbers but having large off-sets. (Saillet and Wibberley, 2010).

### 3.3.1.1 Geological setting

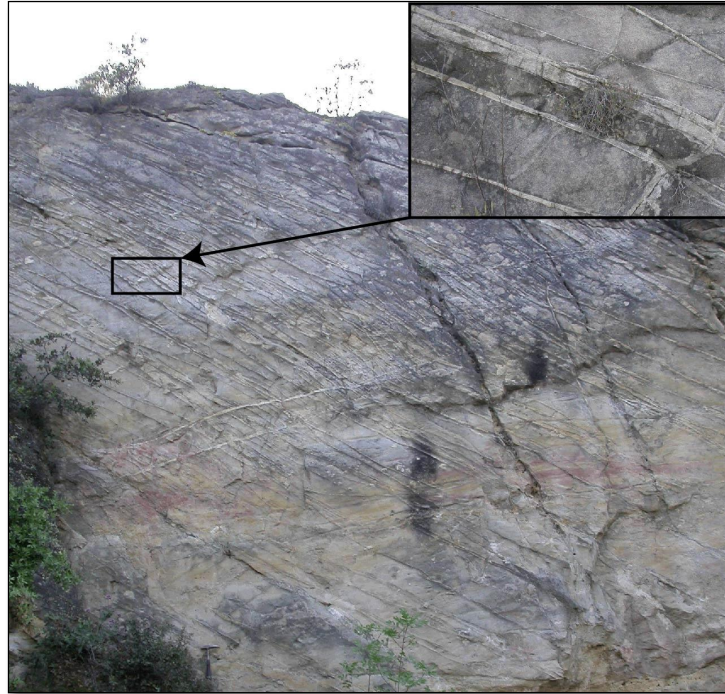
The shape of the Southeast Basin is triangular, its three corners can be identified as: Massif Central to the northwest, the Alps to the east, and the Mediterranean Sea to the south. It is classified as a Mesozoic cratonic basin, which is spread over the area of approximately 30,000 km<sup>2</sup>, on the edge of Alpine orogenic belt (Figure 3-5). The basin has the thickest sedimentary strata of about 10,000 m at the centre, which gradually thins outwards the basin and to reach a thickness of 2000 to 3000 m at the basin margin (Delfaud and Dubois, 1984).



**Figure 3-5: Summary structural map of the Southeast Basin, Provence, southeastern France, showing the distribution of Cretaceous strata and the location of the site of sampling. North-south cross section (modified from Champion). From Sallet and Wibberley, (2010).**

The samples have been obtained from Quartier de l'Étang Quarry, Orange, which was mined for its moderately consolidated sandstone. The outcrop has remarkably high density of deformation bands, which make it ideal for sampling

**(Figure 3-6).** The strata are composed of marine deltaic to aeolian sands and sandstone of Cenomanian age (Wibberley et al., 2007).



**Figure 3-6: Actual location of the Southeast Basin, Provence, south-eastern France, from where the samples were taken.**

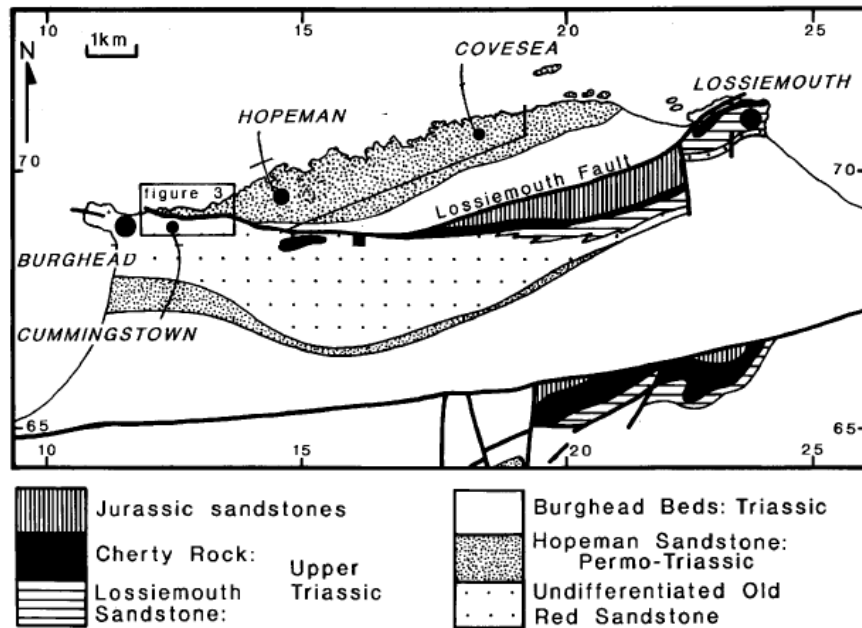
Several  $\sim 0.2 \text{ m}^3$  samples containing both fault and host sandstone (**Figure 3-7**) were collected by Prof. Quentin Fisher from the Orange quarry in March 2013. Core plugs containing the fault rock were then taken after the samples had been return to Leeds. The core plugs were drilled for experiments; detail is presented in methodology section.



**Figure 3-7: Photograph showing a typical example of the samples taken from the Orange quarry. Note the high density of faults present within the samples.**

### **3.3.2 Outcrop samples: Hopeman Sandstone, Scotland**

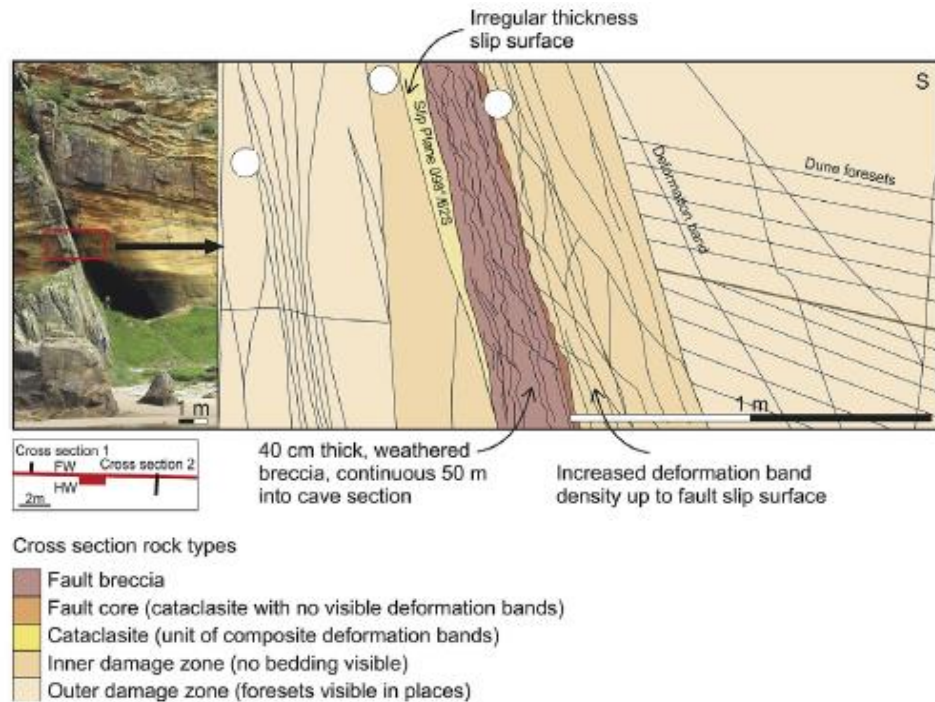
The Hopeman sandstone is an aeolian deposit of Permo-Triassic age (Peacock et al. 1968), which outcrops along the southern coast of the Moray Firth (**Figure 3-8**). The Hopeman sandstone in the Clashach Quarry, Hopemen, contains a complex array of micro-faults in the damage zone to a seismic-scale fault with a throw in excess of 30 m. The extensional microfaults have divided the sandstone into isolated compartments. It is also found that the strong spatial correlation of cement also contributed to the fault-related compartmentalization (Edwards et al., 1993).



**Figure 3-8: Location and geology of the Hopeman sandstone (Modified from Edwards et al., 1993).**

The Hopeman sandstone is a well sorted, fine to medium grained, quartz rich, quartz cemented sandstone (Shotton, 1956; Peacock et al., 1968; Glennie and Buller, 1983; Edwards et al., 1993) similar to sandstones comprising the Rotliegend gas reservoirs in the southern North Sea (Hinai et al., 2008). Fault core exposures at all localities are composed of variable thickness fault breccias (10 to 100 cm), units of pervasively cataclastic fault rock with multiple polished slip surfaces and a composite unit of anastomosing deformation bands (**Figure 3-9**).





**Figure 3-9: Photograph and structural section of the quarry at Clashach Cove East; note the main fault plane is surrounded by a damage zone containing a high density of deformation bands.**

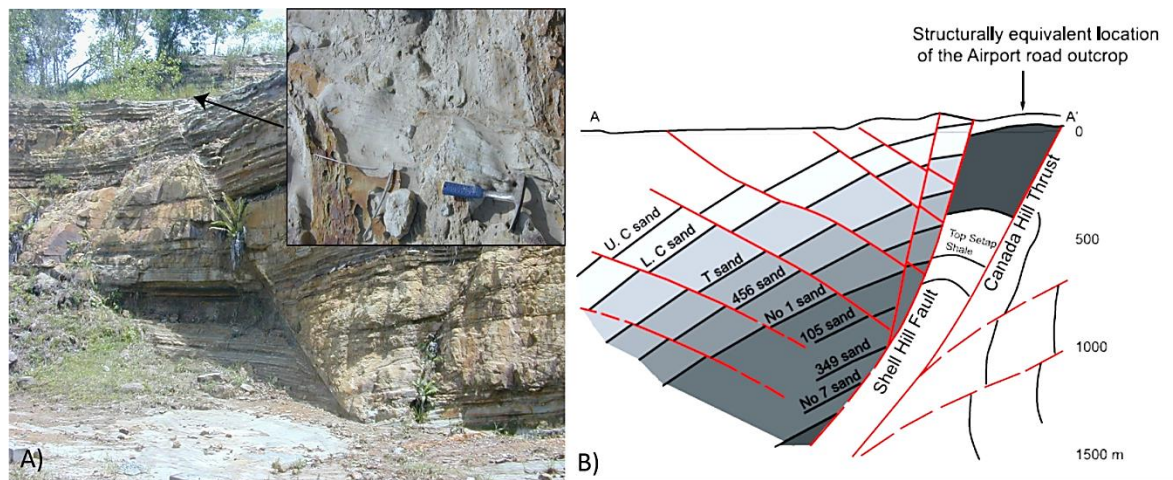
### 3.3.3 Outcrop samples: Miri, Airport Road, Malaysia

Miri fault is a normal fault in layered deltaic sediments, located at Airport road near Miri, Malaysia (**Figure 3-10**). The rocks found in Miri formation are Miocene in age consisting of sand interbedded with clay-rich layers (85% sand and 15 % clay), which formed in a deltaic environment. The thickness of clay layers is varying between ~10 cm to ~50 cm but most are around 10 cm (Van der Zee and Urai, 2005).

The Miri outcrop is considered as part of a bent ridge anticline between the Shell Hill Fault in the north and the Canada Hill Thrust in the south (**Figure 3-10**). Although the details of the large scale kinematics are not known, the location between a large normal fault and a large thrust resulted in the uplift of a “slice” of reservoir rock (**Figure 3-10**). The major deformation is extensional which produced abundant

normal faults. Signs of the complex strike-slip and reverse faulting of the Miri structure are rare in the form of small reverse and strike-slip faults (Lesslar and Wannier, 1998; Burhanndinnur and Morley, 1997).

Several samples having both fault and host sandstone were collected by Prof. Quentin Fisher from Airport road near Miri in 2011 and 2 ½ inch plugs containing fault and host were drilled for the experiments.



**Figure 3-10: A) Actual location, Airport road near Miri, Malaysia from where the samples have taken. B) Cross sectional view of the Miri outcrop (from Van der Zee and Urai, 2005).**

### 3.4 Samples analysis

Routine and special core analysis was performed on all above samples. The details of experiments performed on all samples are summarized in **Table 3-1** and the detail description is given in the next sections/chapters. In addition to routine core analysis, which includes porosity and absolute permeability (gas and liquid), the stress dependency of permeability was also measured at confining pressure up to 5000 psi. These experiments have provided a significant way to characterise the fault rocks reservoirs at different burial depths and the results can be incorporated into production simulation models to determine the impact of seismic-scale faults on fluid flow.

Relative permeability experiments on Orange samples with brine and oil have also been performed and the details are provided in the following chapters.

Experiment	Samples (core plugs)			
	Company A	Orange	Hopeman	Miri
CT Scanning	✓	✓	✓	
Porosity	✓	✓	✓	✓
Stress dependent Gas permeability	✓	✓	✓	✓
Stress dependent Brine permeability	✓	✓	✓	✓
Stress dependent Deionised water permeability	✓	✓	✓	✓
Relative permeability	X	✓	X	X
SEM	✓	✓	✓	✓
Capillary pressure (Hg injection)	✓	✓	✓	
Quantitative X-ray diffraction	✓	✓	✓	✓

**Table 3-1: Summary of experiments performed on different samples (✓ is for experiment performed and X for experiment is not performed)**

In addition, cubes of the samples were embedded in resins to measure the stress-free permeability; the details are given in next section. The results from these analyses were then used to compare with stress dependent permeability. In total, there are fifteen Company A reservoir samples, eight outcrop Orange samples, two Hopeman and two Miri samples. All the measurements are taken in the Wolfson laboratory, the multiphase flow laboratory at School of Earth and Environment, University of Leeds.

### 3.4.1 Samples nomenclature

The samples received are classified into different groups according to their origin and type. In total the samples are classified into two main groups i.e. cataclastic and phyllosilicate frame-work fault rocks (PFFRs). The nomenclature used for the sample identification is explained below:

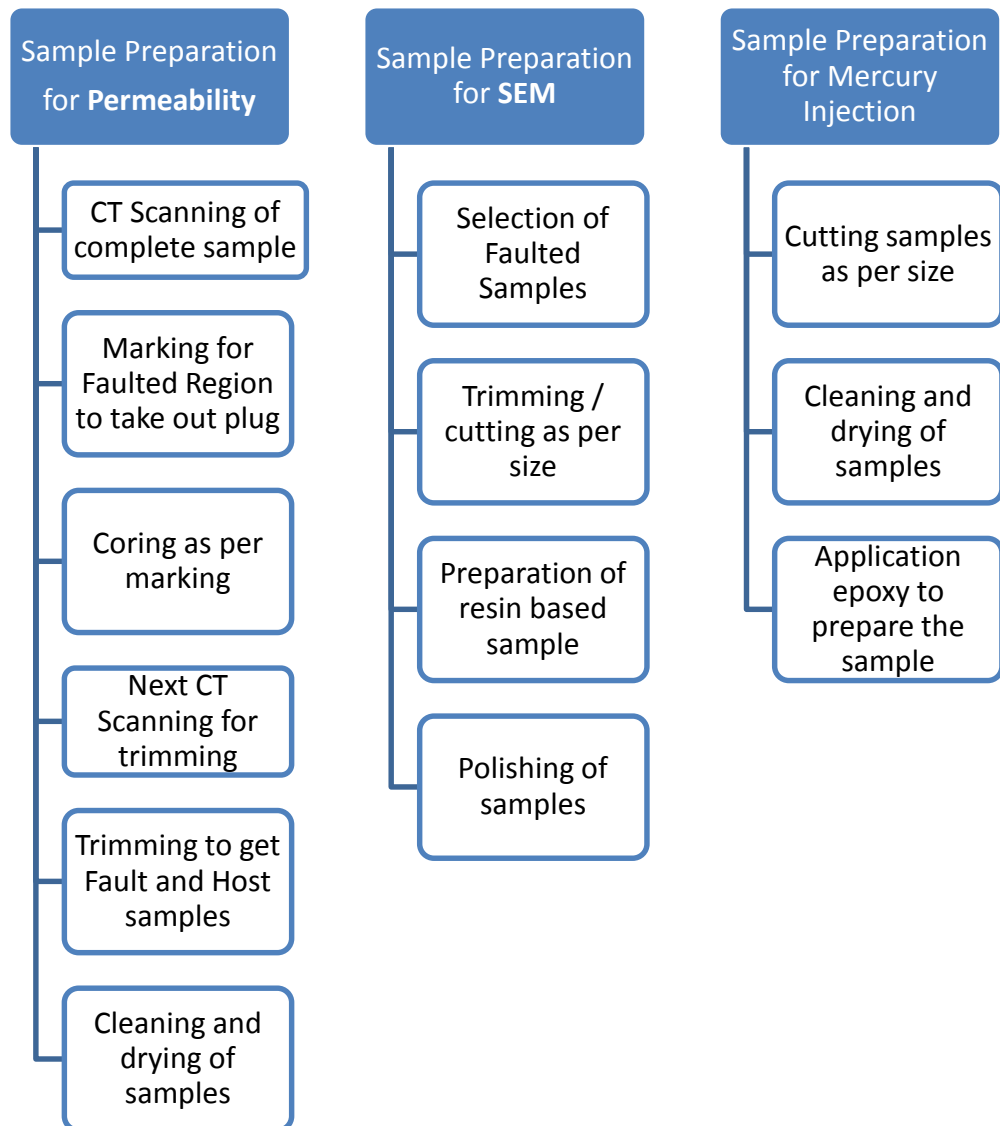
Group Name	Sample ID starts with	Followed by		Sample number
		Fault	Host	
29/5	5A, 5B, 5C, 5D, 5E,5F	F	H	1 or 2
29/7	7A, 7B, 7C, 7D, 7E, 7F	F	H	1 or 2
29/10	10A, 10B	F	H	1 or 2
29/3	3A	F	H	1 or 2
Orange	ORG	-	-	1 - 8
Hopeman	HP	-	-	1-2
Miri	Miri	-	-	1-2

**Table 3-2: Sample naming criteria**

For example, sample ID 5AF1 is showing that this sample is from group 5, first sample with fault and first sample of 5A, similarly ID 5AF2 is the same but the second sample of same kind.

### 3.5 Methodology

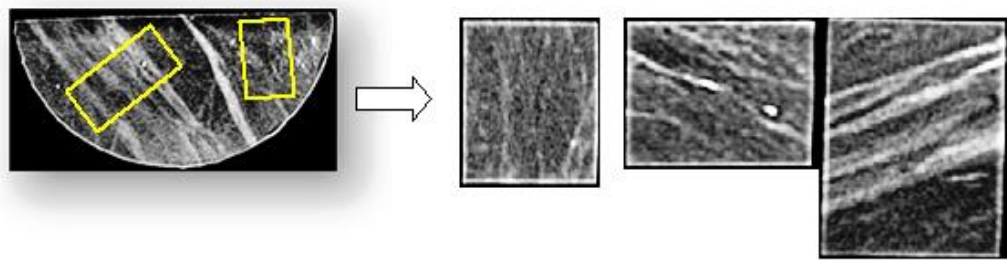
In this section the detail of sample preparation; their porosity measurement; SEM sample preparation; and microstructural analysis is described, the work flow is summarized in **Figure 3-11**.



**Figure 3-11: Summary of workflow for sample preparation.**

### 3.5.1 Sample preparation

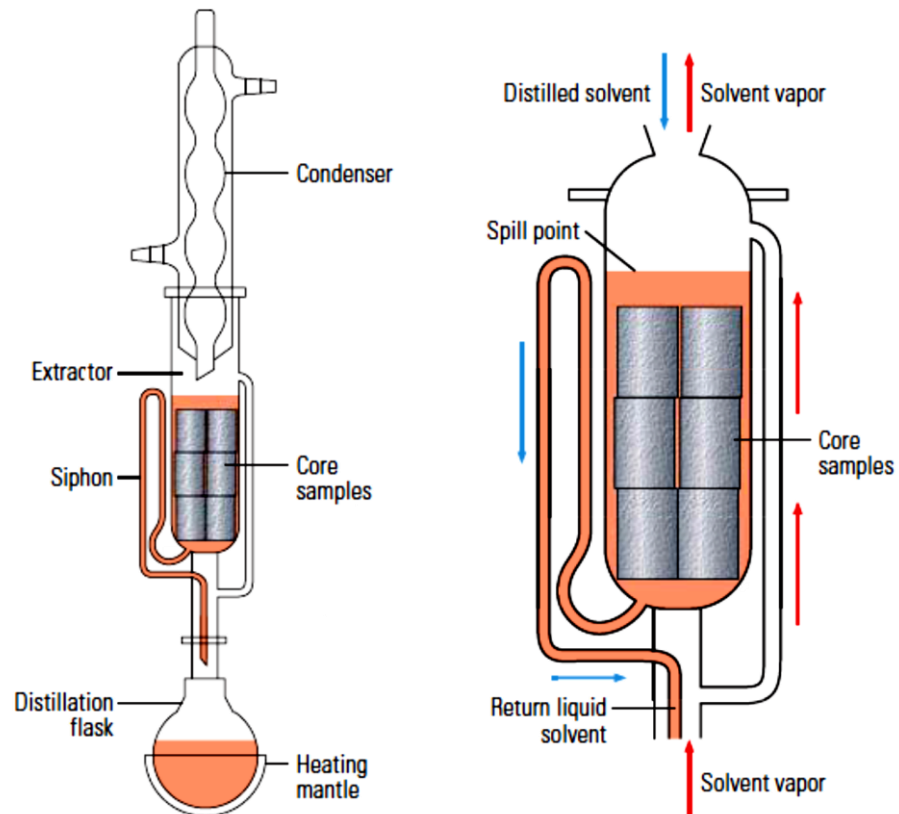
All samples were CT (computerized tomography) scanned using a Picker PQ2000 X-Ray scanner to identify the position of faults within the rock samples and to assess whether they were damaged (i.e. contained fractures). It also allow an assessment to be made of the thickness of the fault rock, which is needed to estimate fault permeability when core plugs contain both fault and undeformed zones. The PQ2000 has a resolution of 0.2 – 0.4 mm in the vertical plane and 1 mm in horizontal plane. Faults are generally denser than the undeformed sandstone so can be easily visualized using the CT (**Figure 3-12**). The details of all other samples are presented in result section.



**Figure 3-12: Sample 5A- CT scan image of actual sample and core plugs taken from main sample.**

The position of the core plugs is marked on samples and one inch diameter core plugs were drilled in an orientation that kept the fault perpendicular to the flow direction during experiments. Similarly core plugs of the host sandstone were taken for comparison with the faulted material. Water was used as a lubricant during drilling. A diamond coated trimming saw was then used to cut approximately 1 cm<sup>3</sup> cubes fault rock and host sandstone for Hg injection. A 1.5 cm<sup>2</sup> and 0.5 cm deep sample was also cut spanning the fault rock and undeformed sandstone for SEM analysis.

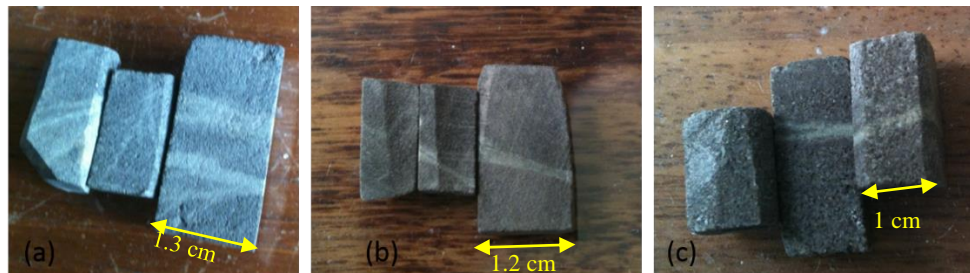
The samples were cleaned thoroughly in a Soxhlet extractor (**Figure 3-13**) using dichloromethane. The samples were then dried in a humidity controlled oven at 60°C for 24 hours.



**Figure 3-13:** Soxhlet distillation extractor. Solvent in the distillation flask (*left*) is gently heated until it vaporizes. The solvent vapours rise from the flask and cool when they reach the condenser. The cooled liquid solvent drips onto the core to permeate the sample. The solvent condensate carries away the hydrocarbons and brine from the sample. When distilled solvent in the extractor reaches its spill point, the used solvent siphons back into the flask to be redistilled (*right*). This process is repeated continuously and can be sustained as long as needed. The hydrocarbons from the core are retained and concentrated in the distillation, or boiling, flask. Some Soxhlet devices can accommodate multiple core plugs (Andersen et al., 2013).

The fault samples for mercury injection are made in such a way that their five sides are coated with epoxy and one side is open to inject mercury (**Figure 3-14**). The mercury is injected to enter to the pores of the host and fault and pressure regime is

recorded. The results are then processed to estimate the capillary pressure of the fault rock and its associated undeformed sandstone.



**Figure 3-14: Samples prepared for mercury injection. (a) Sample 7A (b) Sample 7F and (c) Sample 10/3B.**

After cleaning, the series of experiments have performed on the samples. In this section porosity, SEM and XRD experiments details are given. The other experiment's detail is presented in following chapters.

### **3.5.2 Mercury injection porosimetry**

Mercury porosimetry results are used to estimate the pore aperture size, which has been used for the evaluation of the sealing capacity of the oil traps (Pitman, 1992). Pore sizes between about 500  $\mu\text{m}$  and 3.5 nm have been examined by porosimetry and detailed information about pore size distribution, the total pore volume and specific surface are also be obtained for the characterization of porous media (Giesche, 2006). In this study, the mercury injection curves of the fault and host samples were obtained using Micromeritics V mercury-injection porosimeter. In first stage, the clean sample is placed in the porosimeter where air and moisture are removed under vacuum. Mercury is then injected in stepwise increments up to 60,000 psi. The mercury intrusion volume and corresponding pressure data is recorded, which are then used to develop mercury saturation versus pressure curves.



Information about the pore size distribution is using the Washburn (1921) equation:

$$D = \frac{4\gamma \cos \theta}{P} \quad \text{Eq. (3-1)}$$

where  $D$  is the pore diameter in  $\mu\text{m}$ ,  $P$  is the pressure in psi,  $\gamma$  is the mercury-air surface tension (484 nN/m) and  $\theta$  is the mercury-air-rock contact angle ( $140^\circ$ ). This equation describes capillary flow in porous materials and assumes cylindrical pores. The mercury injection curves obtained in these experiments are used to measure the mercury-air threshold pressure, which is the pressure required to create an interconnected pathway of mercury throughout the sample (Katz and Thompson, 1986, 1987). The point of inflection in mercury injection curve is generally taken as the threshold pressure (Katz and Thompson, 1987). In most cases, the point of inflection in mercury injection curves is not well defined, so expertise are required to measure it and the results may vary from one interpreter to other. In this study, the samples are closed from five sides by epoxy and from only side mercury is allowed to inject where fault is perpendicular to the flow. So the inflection point is showing the threshold pressure when mercury intruded through the fault.

### 3.5.3 Porosity

Porosity is a measure of the proportion of pore space within the rock and hence the amount of oil or gas it may store (Jordan & Campbell, 1984). If porosity is zero, it will not be able to store or transport fluid so often absolute (i.e. total) porosity is distinguished from effective (i.e. connected) porosity (Hook, 2003). The following equation is used to calculate the total or absolute porosity of the rock (Schön, 2011):

$$\phi = \frac{\text{Pore Volume}}{\text{Bulk Volume}} \quad \text{Eq. (3-2)}$$

$$\phi = \frac{\text{Bulk Volume} - \text{Grain Volume}}{\text{Bulk Volume}} \quad \text{Eq. (3-3)}$$

where  $\phi$  is porosity (dimensionless) and is quoted either as a percentage (%) or fraction of the bulk volume.

### 3.5.3.1 Porosity measurement

According to equation 3-3, two parameters, bulk volume and grain volume are required to calculate the porosity. Different techniques have been used to measure the bulk volume of rock samples (plugs), which include the immersion method and measuring the sample dimensions using a calliper. In this study, the calliper method is used to measure the bulk volume of plugs. The basic requirement for adopting this method as described is that the samples volume must be larger than 10 cm<sup>3</sup> and have a regular shape. The immersion method is the best choice for irregular shapes. Measuring the sample dimensions using a caliper is easiest and quickest method compared to immersion methods and the other advantage is that the samples can also be used for further tests (Torsæter, 2000).

Bulk volumes of right cylindrical and regular shaped samples can be measured by following equation:

$$V_{Bulk} = \pi r^2 L \quad \text{Eq. (3-4)}$$

where  $r$  is the radius in cm and  $L$  is the length of the sample plugs. Digital vernier calliper with very high resolution of 0.01mm is used for these measurements.

For the cylindrical samples, measurement of length and diameter are taken at minimum of five different points to avoid implications due to irregularities in shape or surface. Similarly for other shaped samples e.g. rectangular, the dimensions can be measured by the same way.

It is important that in the calliper method:

- five random positions along the length should be used for measuring the length of sample and averaged them.
- five random positions along the periphery of sample should be used to measure the diameter of the sample and averaged them.
- for every reading calliper should be zeroed
- take care when measuring rough surface that calliper should not intrude into fracture or vug which results in inaccurate measurements.

The second parameter required to measure the porosity is the grain volume, which is measured using helium pycnometer. Helium pycnometry is based on Boyle's law, which states that the product of pressure and volume for two states of a gas system remain constant provided that temperature is constant i.e.  $P_1V_1 = P_2V_2 = \text{constant}$ . Helium gas is the best choice for the porosity measurement due to its ideal behaviour, (i.e. inertness and small molecular size), which allows it to penetrate the smallest pores of rocks without any chemical or physical reaction (Dandekar, 2006).

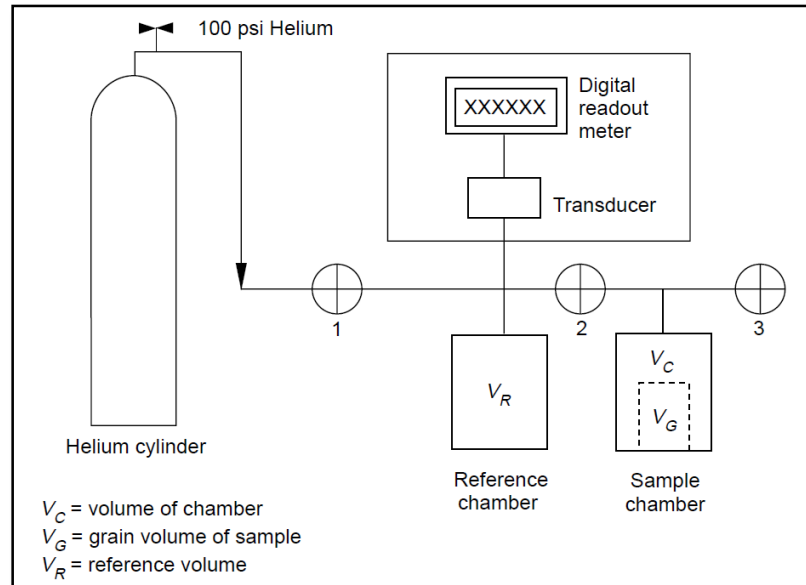
It is important to measure the volume of the reference ( $V_R$ ) and sample ( $V_C$ ) cell/chamber with standards of known volume (steel balls were used in this study) prior to conducting grain volume measurements. The grain volume of samples can then be determined using the following steps:

1. Helium gas is allowed to expand from the storage cylinder into the reference cell. Generally, the reference volume is filled to a gas pressure of around 15 psi and this is recorded as  $P_1$  (**Figure 3-15**).
2. The sample is placed in the sample chamber.
3. The valve separating the reference chamber and sample volume is then opened to allow the helium gas to enter into the sample cell/chamber and occupy all the pores of the sample. After 5 minutes when pressure is stabilized the pressure reading  $P_2$  is noted down and entered into porosimeter Excel sheet to get the grain volume.
4. These steps are repeated around 5 times.

The equation used to calculate the grain volume is obtained by applying mass balance of gas within reference and sample chamber cell with the assumption of constant temperature and helium compressibility factor as unity.

$$V_g = V_c - V_r \left( \frac{P_1 - P_2}{P_2 - P_a} \right) + V_v \left( \frac{P_2}{P_2 - P_a} \right) \quad \text{Eq. (3-5)}$$

where:  $V_g$  is the volume of grains,  $V_c$  sample chamber volume,  $V_r$  reference chamber volume,  $P_1$  is absolute initial reference volume pressure,  $P_2$  is absolute expanded pressure,  $P_a$  is absolute atmospheric pressure initially in sample chamber. After having the grain volume and bulk volume, Equation 3-3 is used to calculate the porosity.

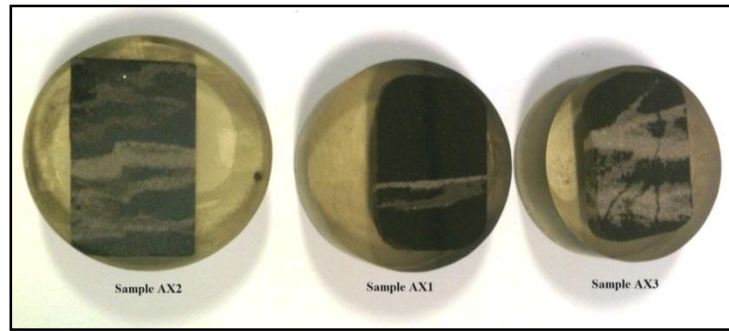


**Figure 3-15: Double-Cell Boyle's Law Porosimeter (from Recommended Practices for Core Analysis; RP40).**

### 3.5.4 Scanning Electron Microscopy (SEM)

The microstructure analysis of the samples is performed by scanning electron microscopy (SEM). In this study, analysis was performed using FEI Quanta 650 SEM, which has a field emission gun and equipped with secondary electron (SE), back scattered electron (BSE), cathode luminescence (CL) and an energy dispersive X-ray analysis system (EDAX).

High quality images of fault and host are taken for analysis. BSE signal is proportional to the mean atomic number which makes it particularly useful for assessing the distribution of minerals within a sample. BSE analysis is conducted on samples that have been resin impregnated, polished (**Figure 3-16**) and then coated with a ~10 nm thick layer of carbon to prevent charging.



**Figure 3-16: Samples prepared for SEM analysis.**

### **3.5.5 Image analysis of SEM images**

The images obtained from SEM are analysed by image processing software named “ImageJ”. This software is built in Java for image processing and can be used to process 8 to 32 bit images with variety of image formats. This software is used to process the SEM images of faulted region of the samples to measure the surface porosity. The porosity of the faulted plugs is the total or average porosity and the results have shown that there is no huge difference between the porosities of host and fault samples as the faults in samples are very thin and not contributing the whole porosity dominantly. Using the imageJ software, the SEM image of damaged zone is analysed and surface 2D porosity is measured on the basis of area of the void spaces and total area. These results are then compared with the measured porosity of plugs.

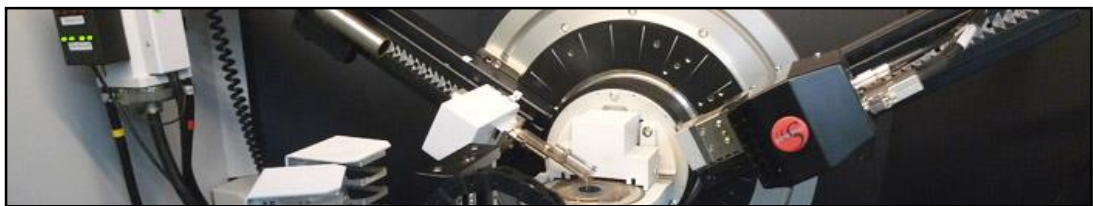
The main steps are as follows:

- Open SEM image file in ImageJ software
- Set measurements by choosing Analyse → Set Measurements from main menu of software.
- Select (tick) area parameter on the “Set Measurements” popup window and leave the default selections or change as per requirement. Click OK.
- Set threshold by clicking Image → Adjust → Threshold from main menu.

- From threshold popup window, adjust the histogram sliders in such a way that all black areas in SEM image must be filled by red colour. Use different combinations and make sure that only black areas filled by red colours.
- After adjusting red colours, click on Analyse → Measure. A new “Results” popup window will open % area is the required 2D porosity value.

### 3.5.6 Quantitative X-Ray Diffraction (XRD)

X-ray diffraction is a best diagnostic technique for identification of minerals in the rock samples. Crystalline samples can be analysed by monochromatic X-rays while performing constructive interference. Cathode ray tube is generating the X-rays which are then bombarded on the samples after filtering and collimating. The incident X-rays are then performed two actions that are constructive interference and diffraction. This phenomena occurred according to Bragg’s law which can be stated as  $n\lambda=2d \sin\theta$ ; where  $\lambda$  is the wavelength of X-rays measured in Angstrom ( $\text{A}^\circ$ ),  $n$  is an integer,  $d$  is spacing between two consecutive fringes in spectrum, and  $\theta$  is the diffraction angle. The sample is scanned to certain degree of angle and all diffracted X-rays counted and processed. The relationship between d-spacing and diffraction peaks is allow to identify the minerals as every mineral has distinctive pattern of d-spacing (Bish and Post, 1989).



**Figure 3-17: Bruker D8 Advance XRD setup.**

### 3.5.6.1 Sample preparation for XRD

The following steps are involved in the samples preparation for XRD.

- The individual samples are finely ground and 100 $\mu$ m sieve is used to collect the samples.
- The quantity of each sample should not be less than 10 grams.
- The spray drying oven should be clean from inside and must be at 130°C before use.
- Prepare sample by mixing corundum as: dried sample weigh  $2.4 \pm 0.005$ g, add  $0.6 \pm 0.005$ g corundum
- Rinse the sample pot with 4 times the volume of 0.5%w/v PVA solution (i.e. 3g sample 12 ml PVA) into the McCrone vial. Add 2 drops of octanol to stop the solution foaming. Put on the top; the thread of the lid and vial must be clean and dry or there is a possibility of leaking
- Grind for 12 minutes.
- Put on the pouring lid on the McCrone vial and pour the sample into the spraying bottle. Rinse out the McCrone vial with DI water in to the spraying bottle.
- Place the paper at the bottom of the oven to collect the sample
- Turn on the dust extract and the spraying pump.
- Attach the spraying bottle to the airbrush and using the heat resistant gloves spray the sample into the oven at a pressure around 0.5 bar
- Clean the airbrush using water
- Move the air extract arm over the bench where the sample will be placed



- Remove the sample from the bottom of the oven and place in a sample tube, do not scrape sample off the paper just tap into tube.
- Clean the loose powder off the spray dryer using the high pressure airline.

The samples are analysed on the “Bruker D8 Advance” setup which is located at Earth and Environment department (**Figure 3-17**). This setup is equipped with a Vantec detector, a 9 position auto sampler and an Anton-Paar TTK-450 temperature control stage. It is configured in vertical theta/2theta Bragg-Brentano and has a scanning range of 2-168° with Cu K<sub>α</sub> source. This setup is capable for qualitative and quantitative phase analysis as well can determine the size of crystals.

## **3.6 Microstructure, mineralogy, porosity and Hg-injection curves of samples**

### **3.6.1 Microstructure and mineralogy of cataclastic samples**

Fisher and Knipe (2001) have been classified the fault rocks on the basis of the clay content, extent of cataclasis and the amount of post-deformation lithification state. The samples analysed in this study are also following the same classification and divided into two groups: cataclastic faults and phyllosilicate-framework fault rocks (PFFRs). The QXRD results presented in **Table 3-3** and **Table 3-4** show that the quartz is dominant mineral in all samples. In particular, the quartz content of the reservoir sandstones ranges from 33.1 to 60.4 % but in outcrop samples the quartz content is much higher (e.g. Orange samples have 98.5 %, Hopeman 88.5 % and Miri has 88.5%). Other minerals present are albite (11.5 % – 2 8.5% in reservoir samples and 0 – 0.7 % in outcrop); microcline (0 – 23.8% in reservoir samples and 0 - 8.7 % in the outcrop samples); calcite (0 – 0.8% in reservoir samples); mica (0 % – 9.3% in

reservoir samples); illite-smectite (0% – 9.3%); chlorite (3.2% – 27.9%) only in reservoir samples; and pyrite (0% – 6.2%).

Host Sandstone around the cataclastic fault								
Sample ID	5DF	5EF	5FF	7AF	7BF	3AF	10/3AF	10/3BF
Quartz	53.4	55.5	59.8	49.1	46.4	33.1	35.5	60.4
Albite	22.2	25.1	22.6	17.9	16.9	14.5	13.6	11.5
Microcline	0.0	0.0	3.9	10.9	12.5	23.8	16.1	14.1
Calcite	0.0	0.0	0.0	0.8	0.6	0.0	0.0	0.0
Dolomite	3.1	4.7	3.1	7.6	8.4	4.2	10.8	0.0
Mica	7.3	5.2	3.7	5.6	5.2	8.6	0.0	2.7
Illite-smectite	3.4	7.9	4.1	3.7	7.6	3.6	0.0	6.0
Kaolinite	0.0	0.0	0.0	0.0	0.0	0.0	0.0	0.0
Chlorite	3.2	4.1	4.9	6.9	5.4	15.1	27.9	8.1
Pyrite	6.2	0.1	1.1	0.0	0.0	0.0	0.0	0.0

**Table 3-3: Quantitative X-ray diffraction (QXRD) results from the host sandstones adjacent to the cataclastic fault samples in the reservoir.**

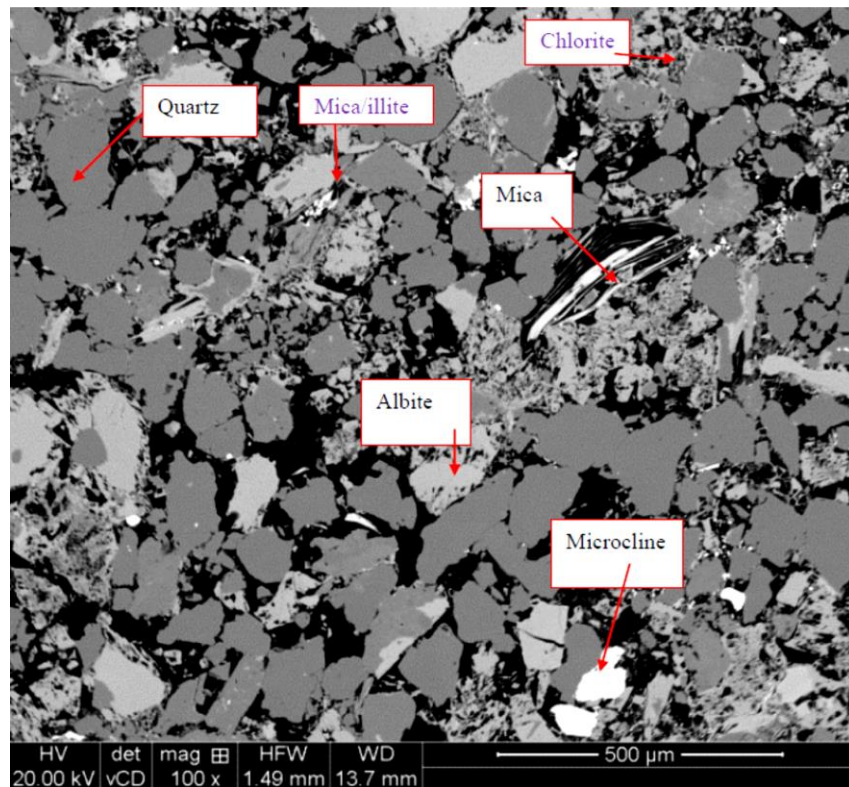
Host sandstones around the PFFRs							
Sample ID	7CF	7DF	7EF	7FF	5AF	5BF	5CF
Quartz	39.1	37.3	45.4	37.7	52.4	50.0	50.9
Albite	21.7	27.4	28.1	26.5	21.1	21.0	24.6
Microcline	14.0	9.1	4.9	7.5	0.0	0.0	0.0
Calcite	0.8	0.5	0.4	0.4	0.0	0.0	0.0
Dolomite	3.3	6.3	3.3	5.8	4.1	5.0	4.7
Mica	6.8	2.6	4.2	4.1	8.1	10.4	8.2
Illite-smectite	7.6	9.0	4.0	4.8	6.8	9.3	6.8
Kaolinite	0.0	0.0	0.0	0.0	0.0	0.0	0.0
Chlorite	9.2	10.4	12.2	15.2	5.5	5.8	5.3
Pyrite	0.0	0.0	0.0	0.0	1.4	2.2	1.4

**Table 3-4: Quantitative X-ray diffraction (QXRD) of the host sandstones adjacent to the PFFR samples from the reservoir.**

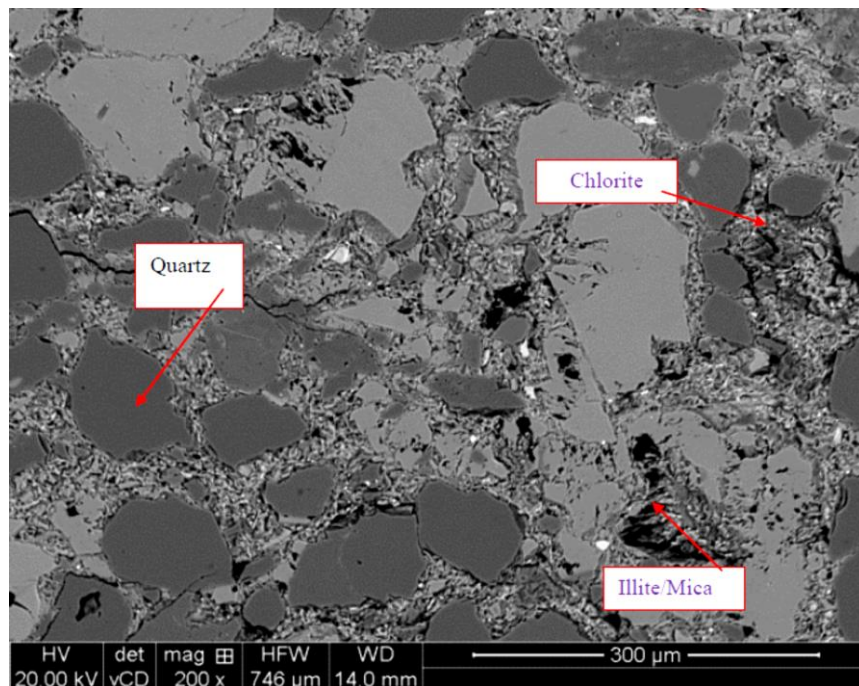
<b>Outcrop samples</b>			
<b>Sample ID</b>	<b>Hopeman</b>	<b>Miri</b>	<b>Orange</b>
<b>Quartz</b>	93.8	88.5	98.5
<b>Albite</b>	0.0	0.0	0.7
<b>Microcline</b>	6.7	0.0	0.0
<b>Calcite</b>	0.0	0.0	0.0
<b>Dolomite</b>	0.0		0.0
<b>Mica</b>	0.0	2.7	0.0
<b>Illite-smectite</b>	0.0	6.7	0.0
<b>Kaolinite</b>	0.0		1.5
<b>Chlorite</b>	0.0	2.4	0.0
<b>Pyrite</b>	0.0		0.0

**Table 3-5: Quantitative X-ray diffraction (QXRD) of outcrop samples.**

A typical example of the cataclastic fault and host sandstone is shown in **Figure 3-18** and **Figure 3-19** respectively. BSEM images for other samples and their image analysis for porosity is presented in Appendix – 2. The fault porosity ranges from ~5% to ~16% while the host sandstone porosity is ranging between ~19% to ~28%.



**Figure 3-18: BSEM micrograph of cataclastic host sample 3A.**

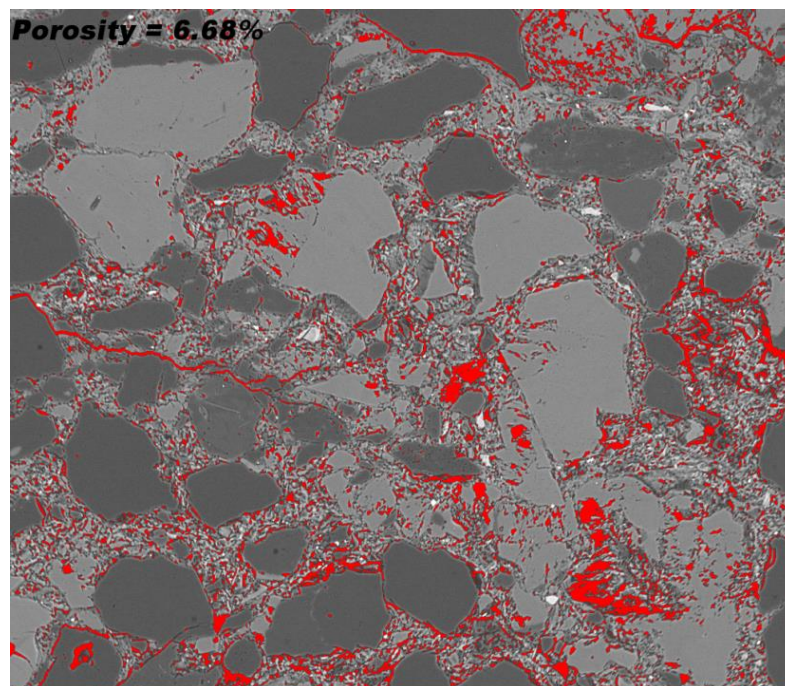


**Figure 3-19: BSEM micrograph of cataclastic fault sample 3A.**

The BSEM image of the host sandstones from the reservoirs show that they experienced the precipitation of dolomite and K-feldspar overgrowth during shallow burial followed by chlorite. In deeper burial, the samples experienced the precipitation of both quartz and albite over growth.

The fault rocks have a lower porosity than the host sandstone as a result of two processes. First, grains were fractured during faulting which produced a fault gouge with angular grains and poor sorting, which could be packed more effectively than the undeformed sandstone. Secondly, during faulting, fine grained clays were mixed with the grain fragments produced by cataclastic deformation.

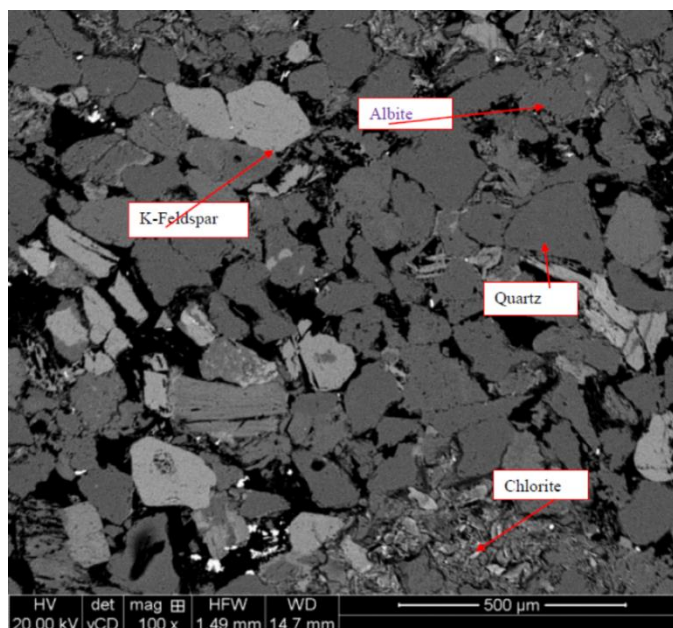
Grain-scale microfractures can also be recognized in the fault rock sample, which could act as conduit for flow at low confining pressure and be closed at higher pressure. The porosity obtained by image analysis of fault sample 3A is highlighted in red in **Figure 3-20**. The porosity measurements of all other sample is given **Table 3-8** and all other raw data are presented in Appendix – 2.



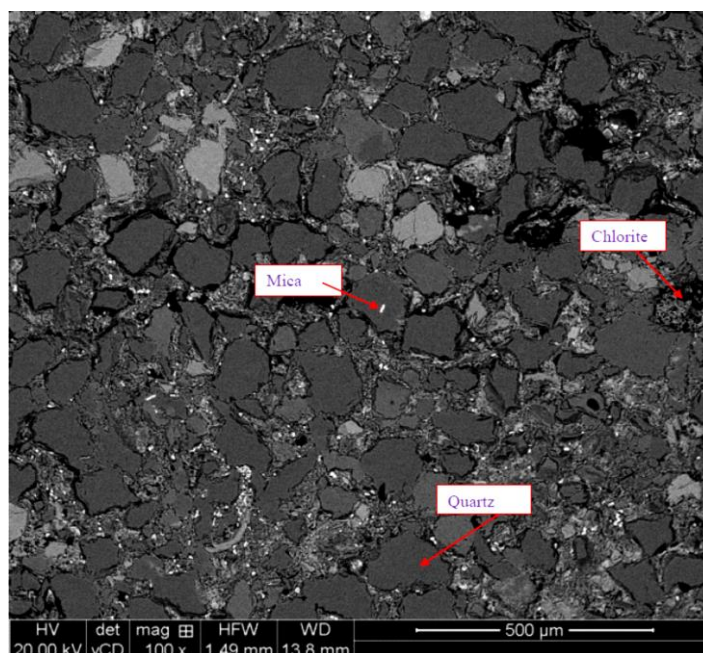
**Figure 3-20: Porosity of cataclastic fault sample 3A by image analysis.**

### 3.6.2 Microstructure and mineralogy of (PFFR) and their associated host sandstones.

A typical example of a host sandstone and its neighbouring PFFR are shown in **Figure 3-21** and **Figure 3-22** respectively. BSEM of phyllosilicate sample 7D is showing that the grains are very coarse with sharp edges which is showing no deformation in host is occurred. Detrital quartz is the main component although small amounts of authigenic quartz and its overgrowth can also be identified. Chlorite (10%) occurs as pore-filling and grain coating authigenic phase but coarse grained detrital chlorite is also present. Authigenic illite/smectite (9%) also filling some pore spaced but overall porosity of the host sample is 14%. The BSEM image of fault rock shows that it has experienced enhanced compaction compared to the host sandstone. This reduction in porosity occurred due to the deformation induced mixing of clays with framework grained as well as enhanced post-deformation grain contact dissolution. Microfractures around the grains are also identified, which may be due to stress relaxation but may act as conduits for fluid flow at low confining pressure.



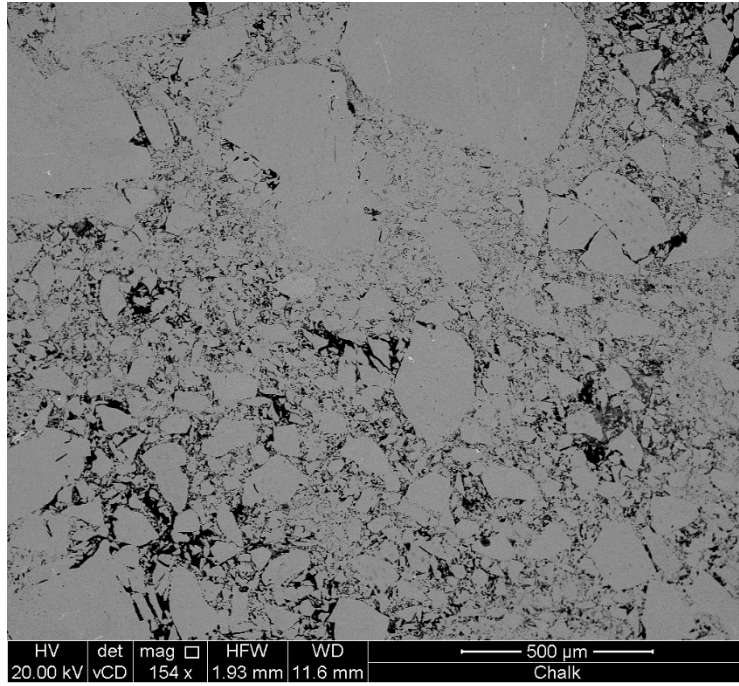
**Figure 3-21: BSEM micrograph of phyllosilicate host sample 7D.**



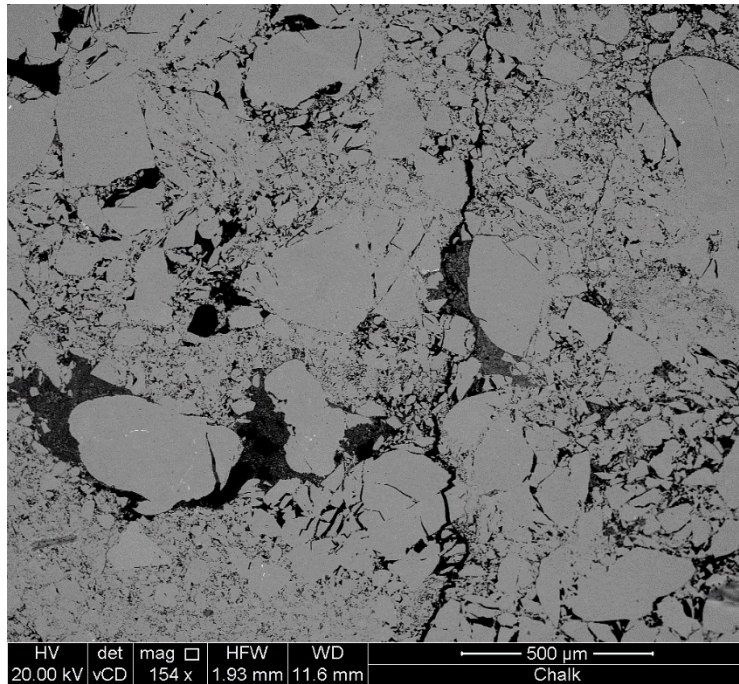
**Figure 3-22: BSEM micrograph of phyllosilicate fault sample 7D.**

### **3.6.3 Microstructure and mineralogy of Orange fault samples**

The QXRD results of Orange samples are showing that the Orange samples are mainly composed of quartz, which comprises ~98% of the total minerals present. The undeformed sandstone in the quarry was not collected. Examples of the microstructure of the fault rocks from Orange fault are shown in **Figure 3-23** and **Figure 3-24**. These fault rocks have clearly experienced significant cataclastic deformation, which will have lowered their porosity compared to that of the host sandstone. There is no evidence of enhanced post-deformation quartz cementation or grain contact quartz dissolution.



**Figure 3-23: BSEM micrograph of outcrop Orange fault sample ORG-1.**

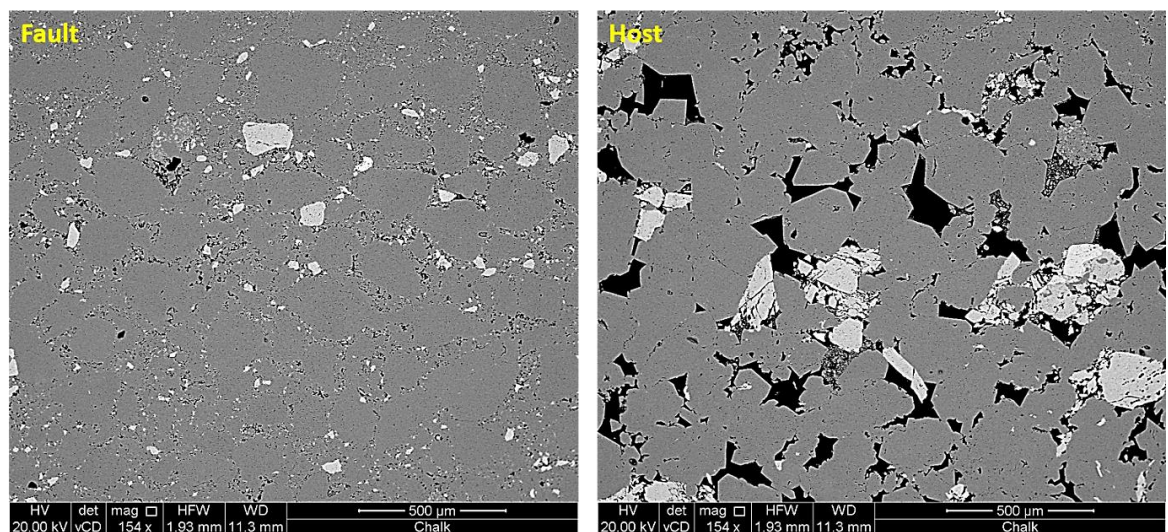


**Figure 3-24: BSEM micrograph of outcrop fault sample oRG-3.**



### 3.6.4 Microstructure and mineralogy of Hopeman sandstone samples

The Hopeman sandstone is very well sorted medium to large grained sandstone composed of 93% quartz, 7% of microcline and has a porosity of 11% (**Figure 3-25**). Precipitation of meso-crystalline quartz cement is the main diagenetic process found in the host sandstone and occurs as overgrowth in detrital grains. The fault rock has a porosity of around 4%, which is around 30% that of the host sandstone. This reduction in porosity occurred mainly due to the deformation induced fracturing of grains but post-deformation quartz cementation also contributed to the porosity reduction.

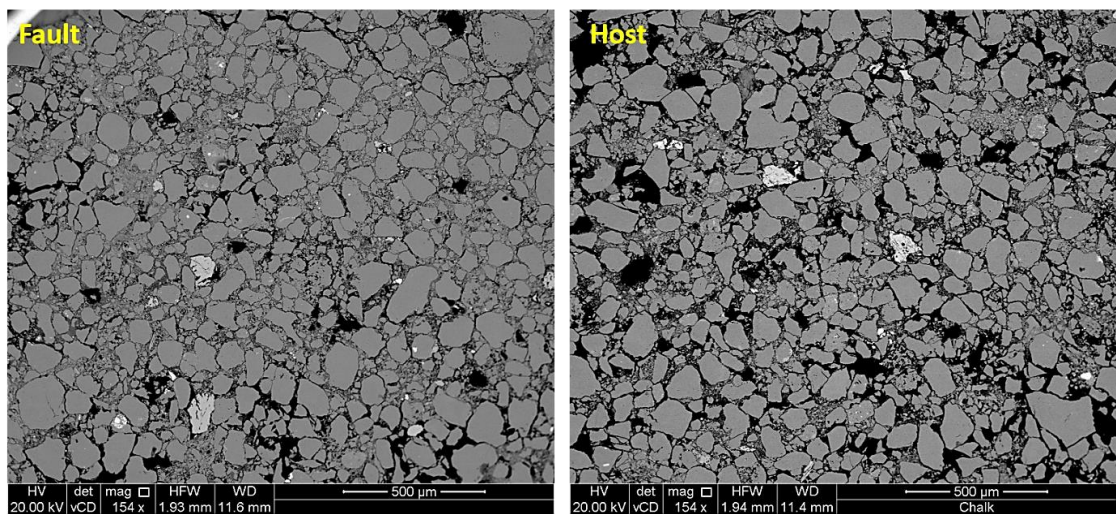


**Figure 3-25: BSEM images of Hopeman fault and host samples.**

### 3.6.5 Microstructure of the Miri fault and associated sandstone

BSEM of Miri sample revealing that the quartz (87%) has fine to medium grained sizes and the spaces between the grains is filled with mica (3%), illite-smectite

(7%) and chlorite (3%) and has a porosity of around 10% (**Figure 3-26**). The main diagenetic process to affect the sandstone was mechanical compaction. The fault has a porosity of around 7%, which is 70% that of the host sandstone. This reduction in porosity occurred mainly as a result of the deformation induced mixing of clays with framework grains but also small amounts of grain fracturing also contributed to the porosity reduction.



**Figure 3-26: BSEM images of Miri fault and host samples.**

### 3.6.6 Porosity of fault and host samples

The porosity measurements have been done by using very accurate and calibrated equipment. The accuracy of the measured porosity values are  $\pm 10\%$ . The porosity and other dimensional data of faulted and host rock samples are presented in **Table 3-6** and **Table 3-7**. Overall porosity of the host samples is from 19% to 28% with average porosity of 23% while the fault porosity is ranging from ~5% to ~16% with average porosity of 9%, which is lower by order of 4 to 2 than the host porosity.

The porosity of the fault samples is measured by image analysis of BSEM micrographs (Martin et al., 2013; Berryman and Blair, 1986). The cataclastic fault rock and PFFR samples average porosity is found to be ~9% and ~8% respectively. The cataclastic fault samples highest porosity is 16% and lowest is 5% whereas for PFFR samples the highest porosity is 11% and lowest is 6%.

The average porosity of outcrop Orange fault rock is found to be 22% in which the highest porosity is 29% while the lowest is 6%. The Hopeman and Miri samples porosity is measured as 18% and 11% respectively.

Fault samples results							
Sample ID	Type of sample	Mass (gms)	Diameter (cm)	Length (cm)	Grain Density (gm/cc)	Porosity (%)	Pore Volume (cc)
3AF1	Cataclastic	27.3	2.5	2.5	2.68	19	2.4
3AF2	Cataclastic	36.5	2.5	3.4	2.66	17	2.8
10/3AF1	Cataclastic	41.5	2.5	4.0	2.70	21	4.1
10/3BF1	Cataclastic	42.5	2.5	4.1	2.65	20	4.0
7AF1	Cataclastic	50.0	2.5	5.0	2.66	23	5.5
7BF1	Cataclastic	38.0	2.5	3.7	2.67	19	3.4
7BF2	Cataclastic	40.2	2.5	3.9	2.65	20	3.8
7CF1	PFFR	38.8	2.5	3.9	2.66	23	4.7
7CF2	PFFR	43.2	2.5	4.3	2.66	22	4.6
7DF1	PFFR	28.6	2.5	2.5	2.67	14	1.7
7EF1	PFFR	40.6	2.5	3.9	2.65	19	3.6
7FF1	PFFR	33.2	2.5	3.2	2.66	19	2.9
5AF1	PFFR	24.9	2.5	2.4	2.70	22	2.6
5AF2	PFFR	42.4	2.50	4.0	2.70	21	4.1
5BF1	PFFR	41.2	2.5	3.9	2.70	19	3.7
5EF1	Cataclastic	30.5	2.5	3.2	2.69	27	4.1
5EF2	Cataclastic	39.8	2.5	4.1	2.68	26	5.3
5FF1	Cataclastic	29.2	2.5	3.1	2.68	28	4.2

**Table 3-6: Porosity and other basic properties of faulted samples.**

Host samples results						
Sample ID	Mass (gms)	Diameter (cm)	Length (cm)	Grain Density (gm/cc)	Porosity (%)	Pore Volume (cc)
3AH1	30.1	2.5	2.9	2.7	22	3.2
10/3AH	33.3	2.5	3.2	2.7	20	3.2
10/3BH	37.0	2.5	3.6	2.7	21	3.6
7AH1	41.5	2.5	3.8	2.7	24	4.4
7AH2	42.3	2.5	3.8	2.7	26	4.9
7BH1	31.7	2.5	3.0	3.2	19	2.9
7CH1	32.0	2.5	3.0	3.3	22	3.3
7EH1	34.0	2.5	3.2	2.9	20	3.1
5AH1	26.0	2.5	2.5	4.0	25	3.1
5BH1	32.0	2.5	3.2	2.7	23	3.5
5EH1	32.3	2.5	3.4	2.7	28	4.6
5FH1	28.7	2.5	3.1	2.7	28	4.2

Table 3-7: Porosity and other basic properties of host samples.

Fault samples results with Image SEM porosity measurements					
Sample ID	Length (cm)	Diameter (cm)	Host Plug Porosity (%)	Fault Plug Porosity (%)	SEM porosity (%)
3AF1	2.5	2.5	22.	19	7
10/3AF1	4.0	2.5	20	21	5
10/3BF1	4.1	2.5	21	20	8
7AF1	5.0	2.5	26	23	7
7BF1	3.7	2.5	19	19	16
7CF1	3.9	2.5	22	23	6
7DF1	2.5	2.5	----	14	11
7EF1	3.9	2.5	20	19	7
7FF1	3.2	2.5	-----	19	10
5AF1	2.4	2.5	25	22	6
5BF1	3.9	2.5	23	19	9
5EF1	2	2.5	28	27	5
5FF1	3.1	2.5	28	28	14

Table 3-8: Results of porosity measurements by SEM images using ImageJ software.

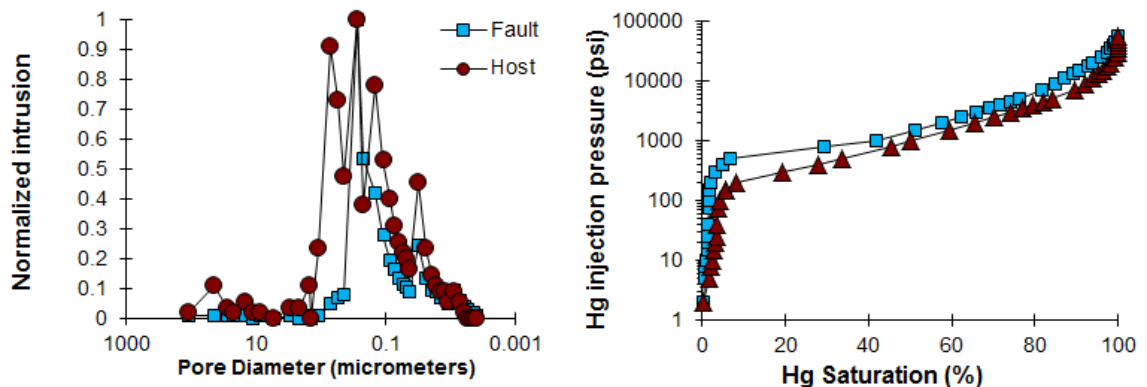
Out crop samples results					
Sample ID	L (cm)	D (cm)	PV (cm <sup>3</sup> )	Mass (gm)	Porosity
ORG-1	5.2	3.7	10.6	119	19
ORG-2	3.4	3.7	7.2	78	20
ORG-3	2.7	3.7	6.7	59	23
ORG-4	3.4	3.7	8.3	76	23
ORG-5	2.7	3.7	5.4	66	18
ORG-6	3.2	3.7	5.2	77	15
ORG-7	2.7	3.7	7.1	59	25
ORG-8	2.7	3.7	6.6	61	23
ORG-A1	3.2	2.5	3.2	35	20
ORG-A2	3.2	2.5	2.5	36	6
ORG-A3	2.9	2.5	3.6	30	29

**Table 3-9: Porosity and other basic properties of outcrop samples.**

### 3.6.7 Mercury injection results of cataclastic and PFFR samples

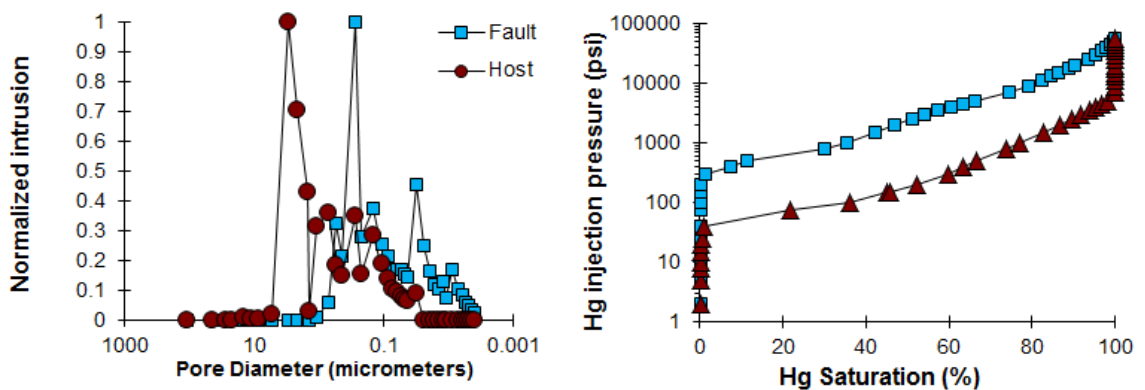
The host sandstone from the cores have the threshold pressures of 8 psi to 200 psi with average of 39 psi and the peak pore diameter of 0.2 to 15  $\mu\text{m}$  with an average of 6  $\mu\text{m}$  (**Table 3-10**). The fault rocks have threshold pressure of 20 psi to 500 psi with average of 171 psi and peak pore diameter of 0.1 to 8  $\mu\text{m}$  with average of 3  $\mu\text{m}$ . These appears to be significant difference between the MICP characteristics of different fault rock types. The cataclastic faults rock have average threshold pressure of 112 psi whereas the PFFR samples have average threshold pressure of 222 psi. The PFFR sample shows a higher threshold pressure as well smaller peak pore diameter than the cataclastic fault samples.

The highest threshold pressure for host and fault sample in PFFR samples (i.e. 200 psi for host and 500 psi for fault) is presented in Error! Reference source not found. The peak pore diameter for the fault is 0.2  $\mu\text{m}$  while for the host is 0.3 microns ( $\mu\text{m}$ ).



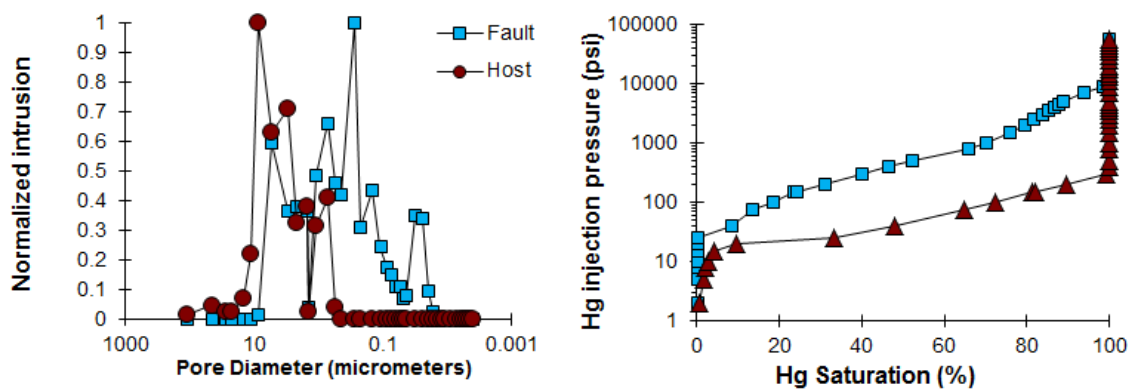
**Figure 3-27: Hg injection data for the phyllosilicate fault rock and associated host sandstone (sample 7D).**

Another example of PFFR sample is presented in **Figure 3-28** in which the fault threshold pressure is 500 psi but for the host sandstone is 20 psi. The peak pore diameter for the fault is 0.3  $\mu\text{m}$  while for the host sandstone is 3  $\mu\text{m}$ , which shows that the increase in peak pore diameter decreases the threshold pressure.



**Figure 3-28: Hg injection for the phyllosilicate fault rock and associated host sandstone (sample 5A).**

The example of cataclastic sample for Hg injection is presented in **Figure 3-29**. For this sample the Hg-air threshold pressure for the fault sample is found to be 145 psi while for host it is approximately 20 psi. The peak pore diameter of fault sample is 0.3  $\mu\text{m}$  while for the host is 9  $\mu\text{m}$  and showing the same trend as for PFFR samples i.e. increasing peak pore diameter reducing its threshold pressure.



**Figure 3-29: Hg injection for the cataclastic fault and its associated host sandstone (sample 7B).**

The Hg injection results for other sample are presented in **Table 3-10** and all other figures and data are presented in Appendix – 2.

Threshold pressure					
Sample ID	Fault Rock Type	Host (psi)	Host peak pore diameter (µm)	Fault (psi)	Fault peak pore diameter (µm)
3A	Cataclastic	25	0.2	75	3
10/3A	Cataclastic	15	3	500	0.5
10/3B	Cataclastic	10	14	25	5
7A	Cataclastic	8	15	20	5
7B	Cataclastic	20	9	145	0.3
7C	PFFR	15	9	145	2
7D	PFFR	200	0.3	500	0.2
7E	PFFR	40	3	40	3
7F	PFFR	15	5	40	3
5A	PFFR	20	3	500	0.3
5B	PFFR	150	0.7	300	0.5
5C	PFFR	15	3	20	3
5D	Cataclastic	15	11	40	5
5E	Cataclastic	10	9	40	5
5F	Cataclastic	25	9	40	8
ORG	Cataclastic	---	0.4	300	0.4

**Table 3-10: Mercury injection data for fault rocks and their associated host sandstones.**

### **3.7 Discussion:**

The QXRD results are showing that detrital mineralogy of the faults is dominated by quartz, K-feldspar, clay and mica. The host sandstones examined have experienced different types of diagenetic alteration, which appear to have been controlled by their detrital mineralogy, pore-water composition as well as the stress



and temperature history experienced. The Triassic sandstones from the Central Graben experienced the early K-feldspar and dolomite precipitation followed by chlorite precipitation. These are common diagenetic processes to affect sands deposited in an arid fluivially-dominated environment (Schmid et al., 2003, 2004). The early cements may help prevent mechanical compaction during shallow burial. Samples without these early cements (e.g. Hopemen, Miri and probably Orange) will have experienced more mechanical compaction, whose porosity reduction is a result of grain rearrangement, crushing of soft lithoclasts and occasionally in fracturing of framework grains (Houseknecht, 1987; Pittman and Larese, 1991; Giles et al., 2000). The extent of mechanical compaction increases with effective stress so tends to increase with depth but can be resisted by the development of overpressure (Fisher et al., 1999; Ramm, 1992; Ramm and Bjørlykke, 1994).

Several of the sandstone samples examined also experienced meso-diagenetic alteration such as grain-contact quartz dissolution, albite precipitation and quartz cementation. These are related to the time-temperature history experienced and do not become pervasive until beyond 90 to 100°C. This temperature control may explain why the cataclastic faults from Orange have not experienced significant pore-deformation quartz cementation (c.f. Fisher and Knipe, 1998, 2001). The sandstones from the central Graben have, however, been buried at temperatures  $\gg 100^\circ\text{C}$ . These have experienced some quartz cementation and grain-contact quartz dissolution but it appears to be far less than those in Brent-type reservoirs buried to similar temperatures (c.f. Giles, 1992). The reason for this is that the presence of clays on the detrital grains has partially suppressed quartz cementation by reducing the reactive surface area available (Walderhaug, 1996).

Microstructure studies reveals that the fault rocks have experienced a reduction in porosity compared to their host sandstones as a result of several processes including:

- Deformation-induced grain fracturing and porosity collapse
- Deformation-induced mixing of clays with framework grained.
- Enhanced post-deformation grain-contact dissolution.

The extent to which each of these processes have affected different fault rocks varies from samples to sample. In general, rocks with significant amounts of detrital or authigenic clays at the time of faulting tend to experience porosity reduction by the latter two mechanisms. On the other hand, porosity reduction of faults in cleaner sandstones tends to occur as a result of cataclastic deformation.

Overall, the grain reduction in cataclastic and phyllosilicates fault samples obtained from core is not particularly large. This is consistent with them being formed at relatively shallow burial depths (i.e. <1 km) possibly as a result of salt-related deformation. The fault rock samples from Orange and Miri experienced far more cataclastic deformation, which is consistent with them forming under higher confining pressures (Fisher and Knipe, 2001). This could be the result of a combination of deeper burial and even compressional tectonics in the case of the Orange samples analysed is generally small which is showing that the faulting may occur at shallow depth.

Most of the fault rocks examined no longer contain significant macroporosity. Even if macroporosity is present it is not well connected so pore-fluids have to flow through micropores. Microfractures are common along grain boundaries, which appear to be open under low confining pressures but likely to close under high pressure due to their very small aspect ratio. These microfractures appear to be far more

common in the core samples than in those obtained from outcrop suggesting that they formed as a result of stress relaxation as the core was brought to the surface.

### **3.8 Conclusions:**

The microstructure, mineralogy and basic petrophysical properties (porosity and MICP) of a range of fault rocks and their associated host sandstones from a producing oil field and several outcrops have been analysed. The fault rocks have experienced a reduction in porosity and pore-size as a result of a range of processes, such as grain fracturing, grain mixing and post-faulting compaction) both during and following faulting. These processes have affected the fault rocks to a different extent depending on the factors such as their clay content, the stress at the time of faulting and their post-faulting temperature history.

Microstructural examination has shown that the fault rock samples also contain a significant number of microfractures formed as a result of stress release which might provide conduits for flow if the samples are not placed under sufficient confining pressure when their flow properties are measured.

The data presented within this chapter form the basis for interpreting the results from fluid flow experiments presented later in this thesis.

# Chapter 4: The stress dependence of the gas permeability of fault rocks

## 4.1 Introduction

Laboratory measurements have indicated that the permeability of a wide range of rocks can be very sensitive to change in effective stress (Fatt and Davis, 1952; Gray et al., 1963; Thomas and Ward, 1972; Jones 1975; McKee et al., 1988; Holt, 1989; Tiab and Donaldson, 2004). The stress dependency of laboratory measurements of permeability is particularly severe in tight reservoirs rocks (Byrnes et al., 2000; Bower and Morrow, 1985; Thomas and Ward, 1972). Petroleum production results in a decrease in pore pressure, which may increase the effective stresses within the reservoir. So it is possible that petroleum production could results in changes in the permeability of the reservoir rock. The rate of change of effective stresses mainly depends on the rate of change of pore pressure, which depends on a range of factors including permeability, rock and fluid compressibility. Increase in effective stress causes the rock to compact, which may lead to a reduction in permeability (Davies and Davies, 2001).

It is likely that the permeability of fault rock is also stress sensitive yet there are very little data published for the stress sensitivity of fault rocks. A notable exception is Al-Hinai (2007) who presented the data for the stress dependency of the absolute (gas) as well relative permeability of the fault rocks. Al-Hinai (2007) reported an 85% reduction in the gas permeability of fault rocks when the confining pressure is changed from 1000 to 2500 psi. It was also reported that the stress dependence of permeability decreases as confining pressure is increased. The samples showed hysteresis in loading and unloading cycles such that the rocks experience a permanent 70% reduction in

their permeability during a loading and unloading cycle. Tueckmantel et al. (2010) have also performed experiments on fault rock samples but the confining pressure range was from 500 psi to 1500 psi. The results are showing that the maximum permeability reduction was 20% when confining pressure was changed from 500 psi to 1500 psi.

This stress sensitivity is often not taken into account in published studies of fault rock permeability. Indeed, many published measurements of fault rock permeability were conducted at low confining pressures (Fisher and Knipe, 1999, 2001). So it is possible that they significantly underestimate the permeability of fault rocks at in situ stress conditions. It is possible to have the difference of three to four order of magnitude in permeability, when 0.001 mD tight gas sandstone is measured by routine core analysis and then measured at in situ stress conditions. If this is also the case for fault rocks, the most commonly used workflow for incorporating fault rock properties into simulations models could be based on measurements that underestimate fault permeability by several orders of magnitude. In this chapter the stress dependency of the gas permeability of fault rock is investigated. The chapter is divided into the following eight subsections:

- The background to gas permeability and main models for measurement are described in **Section 4.2** and **Section 4.3** respectively.
- Permeability controlling factor and the limitation of the permeability measurement models are described in **Section 4.4** and **Section 4.5** respectively.
- Experimental methodologies and set up descriptions are described in **Section 4.6**.

- Results are presented in **Section 4.7**.
- Discussion and conclusions are presented in **Section 4.8** and **Section 4.9** respectively.

## **4.2 Single phase permeability**

Fluid flow through porous rocks in the subsurface is of great interest and importance in a range of subjects including petroleum production, waste disposal, water treatment etc. Permeability is an important property of porous medium, which provides a measure of how easily it can transmit fluid under a pressure gradient. Among all the hydrodynamic transport properties, the prediction of the permeability is particularly important as it is the main parameter that determines the rate of fluid transfer. Faults can act as major barriers to fluid flow and may compartmentalize reservoirs particularly when orientated perpendicular to the principle flow direction. The detail description of faults such as thickness, pore size, orientation and capillary pressure is very useful to develop more realistic models for fluid flow within petroleum reservoirs (Fisher and Jolly, 2007).

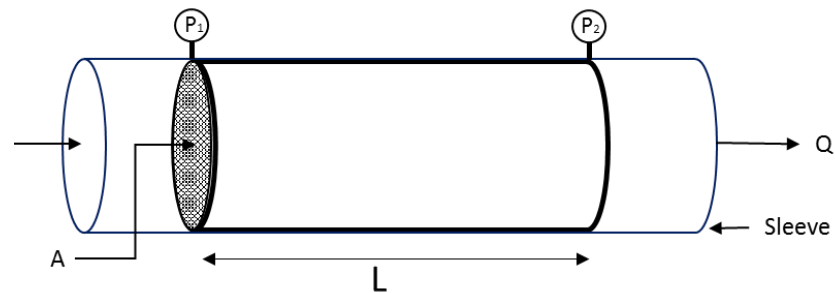
## **4.3 Permeability models**

In spite of numerous experimental and theoretical works, there is scarcity of satisfactory practical and simplified models, which can be incorporated into the mathematical description of porous media fluid flow (Civan 2000, b, d) without adding more complications and computational burden. A range of models have been used for calculating permeability and each has its own limitations and some specific assumptions, which were made when developed. In the following section, Darcy's law

for flow of a Newtonian fluid through a porous medium under laminar flow conditions is described as well as an overview of two commonly used models for permeability; the capillary tube model and Kozeny permeability mode.

### 4.3.1 Darcy law

Darcy's law was developed by a French engineer, Henry Darcy in 1856 based on the results of flow experiments through porous medium as given by Eq. (2-1). The permeability of a rock sample (Figure 4-1) is one Darcy ( $0.986923 \mu\text{m}^2$ ) if volumetric flow rate of  $1 \text{ cm}^3/\text{s}$  of fluid with viscosity of  $1 \text{ cp}$  flows through a sample with a cross sectional area of  $1 \text{ cm}^2$  and a length of  $1 \text{ cm}$  under a pressure drop of  $1 \text{ atm}$ .



**Figure 4-1: Permeability measurement for a core plug.**

The permeability determined by using Eq. (2-1) is for non-compressible fluids but for the compressible fluids (gases) a modified form of Darcy's law is required to take into account gas compressibility, namely:

$$k = \frac{2q\mu}{A} \frac{L}{(P_1^2 - P_2^2)} \quad \text{Eq. (4-1)}$$

where  $k$  = permeability of the porous medium (Darcy),  $q$  = flow rate ( $\text{cm}^3/\text{s}$ ),  $A$  = cross sectional area of the porous medium perpendicular to the direction of flow

(cm<sup>2</sup>),  $L$  = length of the rock sample (cm),  $\mu$  = dynamic viscosity of the fluid (cp),  $P_1$  and  $P_2$  are upstream and downstream pressures across the sample respectively (atm).

Permeability measured from Eq. (4-1) is termed the “absolute permeability” if the porous media is 100% saturated with a single fluid (Tiab and Donaldson, 2004). In tight rocks, gas permeability is estimated by making measurements of apparent permeability,  $k_{ap}$ , at different gas pressures and extrapolation to  $1/p = 0$  on plots of  $k_{ap}$  vs  $1/p$ . In the case where one fluid is flowing in the presence of another fluid; the permeability is termed as “effective permeability” of the flowing fluid at some specific saturation of other fluid. The ratio of effective to absolute permeability is the relative permeability and defined at some specific saturation.

### 4.3.2 Capillary Tube Model

The capillary tube model has been frequently used to estimate the permeability of porous media. The starting point of this model is Hagen-Poiseuille’s law, which was developed for fluid flow through a single capillary tube under steady-state conditions. For a straight capillary with a diameter,  $d$ , and length,  $L$ , the flow equation for the total discharge,  $q$ , will be (Bear, 1972):

$$q = \frac{\pi d^4}{128\mu} \frac{\Delta P}{L} \quad \text{Eq. (4-2)}$$

where  $\frac{\Delta P}{L}$  is the pressure gradient over the length  $L$  of capillary tube and  $\mu$  is the viscosity of the flowing fluid. For a porous media having a cross sectional area,  $A$ , with length,  $L$ , and made up of  $n$  number of capillaries tubes, which are aligned parallel and embedded in a solid (Figure 4-2) with radius,  $r$ , the flow Eq. (4-2) will become:



$$q = \frac{n\pi r^4 \Delta P}{8\mu L} \quad \text{Eq. (4-3)}$$

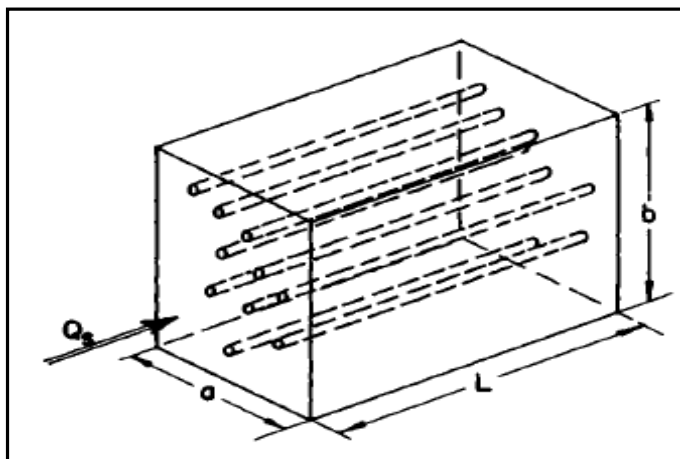
On comparing Eq. (4-3) with Darcy's law, the permeability is given by

$$k = \frac{n\pi r^4}{8A} \quad \text{Eq. (4-4)}$$

The simplified equation after adding porosity is given as:

$$k = \frac{1}{8} r^2 \phi \quad \text{Eq. (4-5)}$$

where  $r$  is the average pore throat radius and  $\phi$  is the porosity in fraction. The numerical coefficient of  $1/8$  in Eq. (4-5) has no meaning and some researchers suggested to replace it with tortuosity of the porous media as this model is just representing the permeability in one direction (Bear, 1972). This model was improved by Scheidegger (1953, 1960) who replaced the bundle of capillary tubes by the pore size distribution of the porous media (**Figure 4-2**).



**Figure 4-2: Capillary tube model (Bear, 1972).**

### 4.3.3 Kozeny permeability model

Kozeny (1927) developed a similar bundle of capillary tubes model of equal length but assumed that the tubes had different cross-sectional area. Kozeny (1927) solved the Navier-Stokes equations for all possible flow channels and derived the following equation of permeability:

$$k = C_o \frac{\phi^3}{S^2} \quad \text{Eq. (4-6)}$$

where  $C_o$  is Kozeny constant whose value depends on the geometrical shape of the channels (e.g. for circular shape  $C_o = 0.5$ ; for square  $C_o = 0.562$ );  $S$  is the specific surface area of porous material and  $\phi$  is the fractional porosity. The further development of this equation resulted in the addition of specific area per unit pore volume, which enables permeability to be estimated from petro-graphic image analysis (Tiab and Donaldson, 2004):

$$k = \left( \frac{1}{2S_{VGR}} \right) \frac{\phi^3}{(1 - \phi)^2} \quad \text{Eq. (4-7)}$$

where  $S_{VGR}$  is the total area exposed within the pore space per unit of grain volume and  $\phi$  is the fraction porosity.

Permeability is found to be a complex function of different parameters including: grain and pore arrangements and their structures; pores connectivity, which defines how many pores are connected; flow path tortuosity; the degree of consolidation of grains by cementation or grain contact dissolution, rock grain alteration due to any diagenesis process or deformation etc. (Civan, 2012; Nelson, 1994; Kozney, 1927; Revil and Cathles, 1999). It is almost impractical to incorporate

all parameters into a single model. However, different correlations are available to relate the permeability with porosity only as the main parameter.

## 4.4 Controls on permeability

Understanding the controls on permeability enhances our ability to predict the rates of fluid flow in the subsurface when few laboratory data are available. It also helps use data that has been collected in appropriate laboratory conditions. For example, many routine core analysis measurements are made at low stresses using low pressured gas and therefore need correcting so that they can be used to predict flow rates in subsurface. Furthermore, understanding the controls on permeability can help improve on the way that laboratory measurements are conducted. The permeability controlling factors or parameters can be classified as:

- Intrinsic properties such as pore and grain sizes and their distribution; shape and packing of grains; presence and distribution of different minerals and their types (e.g. clay); type of porosity i.e. primary or secondary; the presence of fractures and their spatial distribution
- Dynamic parameters such as the flow rate, fluid type and its properties (e.g. wetting or non-wetting, salinity); overburden or confining pressure

### 4.4.1 Pore volume and size

Correlations are given in the literature between permeability and porosity, however correlations of the two properties show many orders of magnitude scatter. For example, Tiab and Donaldson (2004) showed that the correlation between porosity and permeability is completely different for different formations (**Figure 4-3**). Porosity is not dependent on pore size whereas permeability increases to around the

square of pore size. So distinct trends can be seen regarding the porosity-permeability relationships that depends on pore size, which in unlithified rocks is strongly dependent on grain size (**Figure 4-4**).

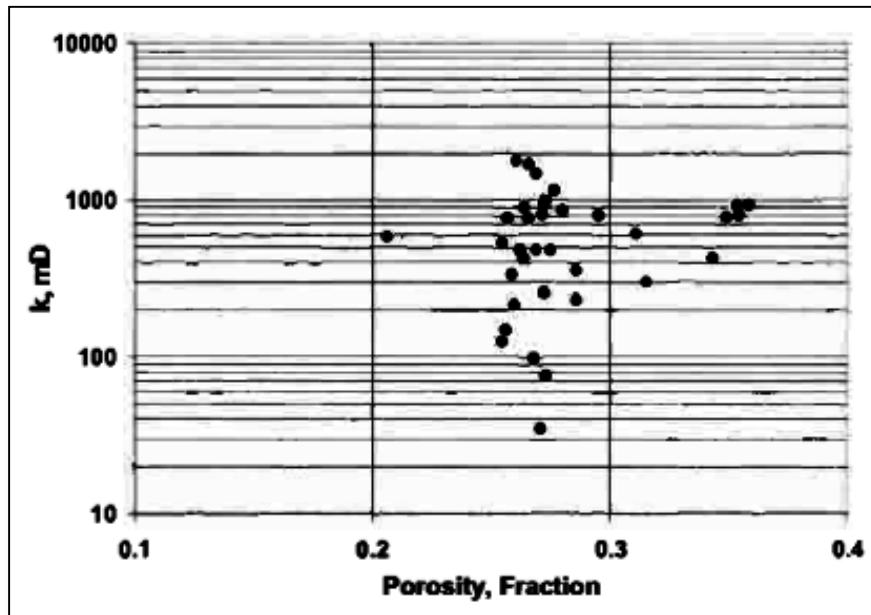


Figure 4-3: Porosity and permeability correlation (after Tiab 2004).

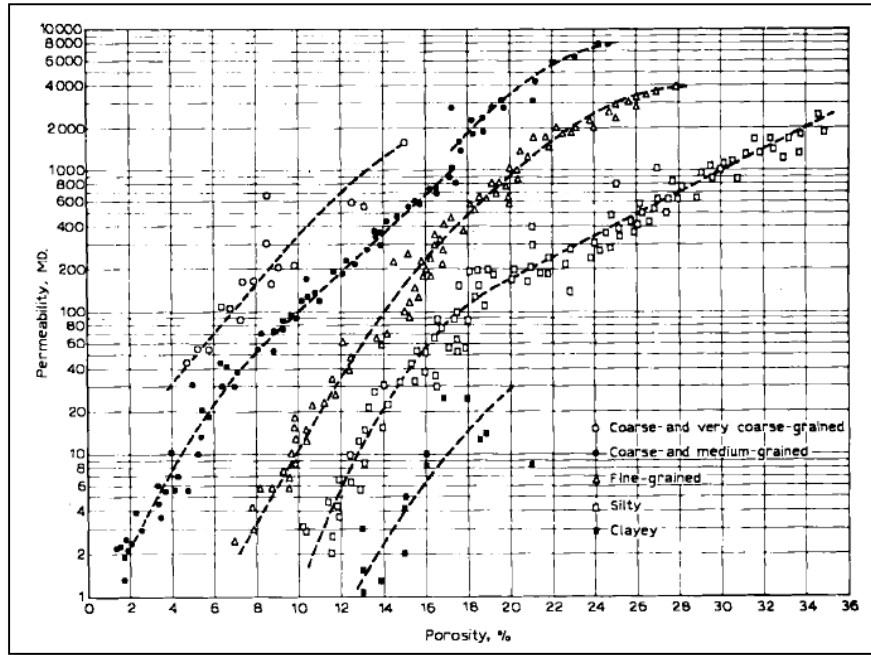


Figure 4-4: Porosity permeability correlation for the different grains sizes (Tiab and Donaldson, 1996).

#### 4.4.2 Fluid flow velocity

Darcy law Eq. (2-1) and Eq. (4-1) treat the porous medium as a continuum and is a robust model to predict flow rate under certain conditions (i.e. steady-state, non-reactive fluid etc.). The law is empirical and does not consider the flow phenomena and therefore invalid outside of specific conditions. Considering the flow mechanisms in porous media provides insight as to how flow rates may change when conditions are different to those under which Darcy's law was established. It is worth stepping back and considering the implications of some of the terms in Darcy's law. The specific discharge  $\frac{q}{A}$  has the same units as speed (i.e. m/s). This is superficial velocity ( $V_o$ ) of the fluid when area  $A$  (cm<sup>2</sup>) is completely available for flow (i.e.  $V_o = \frac{q}{A}$ ) but in porous media the velocity of the fluid within the pores is interstitial velocity as the available area to flow is the void spaces in porous media, which is not exactly equal

to the area  $A$ . According to the continuity equation ( $q = AV$ , where  $V$  is the speed of the fluid,  $m/s$ ), if  $q$  is constant then velocity should increase to maintain the constant flow rate from reduced area (through porous media). Therefore, the interstitial velocity,  $V$ , is higher than the superficial velocity,  $V_o$ . The void spaces are represented by the porosity of porous media, so the interstitial and superficial velocities are related as:

$$V = \frac{V_o}{\phi} \quad \text{Eq. (4-8)}$$

The above equation implies that if porosity is 100% then the interstitial velocity will be equal to the superficial velocity and porous media will act as an empty tube or duct (Holdich, 2002; Price and Waterhouse, 2013).

#### 4.4.3 Overburden or confining pressure

It has long since been known that the permeability of rocks decreases within increasing confining pressure (Carpenter and Spencer, 1940). Afterwards, Fatt and Davis (1952) performed experiments on high permeability sandstone rocks and found a significant decay in permeability during loading from 500 to 3000 psi (**Figure 4-5**). Wyble (1958) and Bergamini (1962) have also reported almost the same behaviour for the sandstone and found almost 10 percent decrease in permeability by increasing the pressure up to 4000 psi.

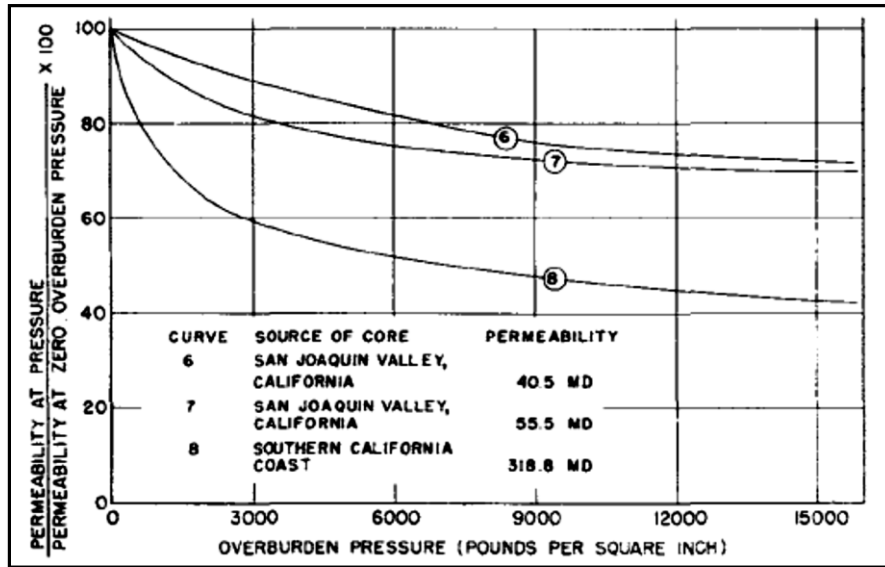


Figure 4-5: Change in permeability with overburden pressure (after Fatt 1952).

Davies and Davies (1999) described the implication of the stress dependency for production forecasting by developing a simulation model to explain the decrease in production resulting from permeability reduction due to increase in overburden pressure. Davies and Davies (1999) also explained the main controls for the stress dependent permeability for unconsolidated and consolidated sandstones, namely: grain slippage and rotation in unconsolidated sandstone (results in more compaction); shape changes in grains due to ductile nature of rock (as in mica and shale) and fracturing of grains when stresses exceed the ultimate strength of the framework grains (for example feldspar and quartz).

Some empirical relationships were also developed that link effective stress and absolute gas permeability. For example, a cubic relationship between permeability and confining pressure for sandstone was identified by Jones and Owens (1980).

$$k = k_{1000} \left( 1 - S * \log \frac{P_k}{1000} \right)^3 \quad \text{Eq. (4-9)}$$

$$\text{where } S = \frac{1 - \left(\frac{k}{k_{1000}}\right)^{1/3}}{\log \frac{P_k}{1000}} \quad \text{Eq. (4-10)}$$

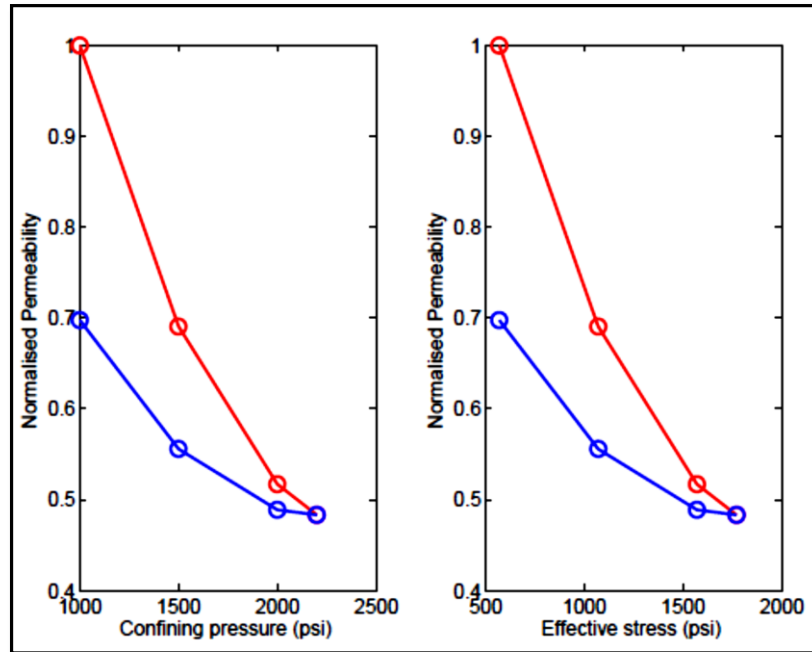
where  $k$  is permeability (mD),  $P_k$  is the confining pressure (psi),  $k_{1000}$  is the permeability at 1000 psi,  $S$  is stress the factor and calculated by Eq. (4-10). Similarly, an empirical relationship was developed between permeability and confining pressure by Jones (1988), which has four adjustable parameters Eq. (4-11).

$$k_i = \frac{k_o \left\{ \exp \left( -a_k \left[ \exp \left( -\frac{P}{P^*} \right) - 1 \right] \right) \right\}}{1 + CP} \quad \text{Eq. (4-11)}$$

where  $k_i$  is Klinkenberg corrected permeability (mD) at initial stress,  $k_o$  is the permeability (mD) at zero stress,  $a_k$  is the slope of permeability vs increasing stress (mD/psi),  $P$  is effective stress (psi),  $P^*$  is Jones decay constant (3000 psi),  $C$  is constant ( $3 \times 10^{-6}$ )

Al-Hinai (2007) also found the stress dependency of gas and relative permeability of different rocks between the confining pressure ranges of 1000 psi to 2500 psi (**Figure 4-6**). Hysteresis during loading and unloading may be due to the pore damaging.



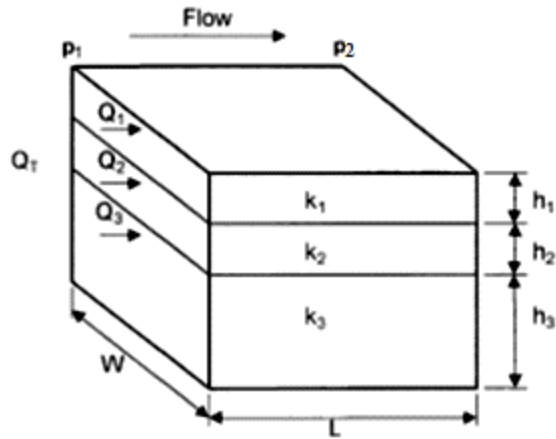


**Figure 4-6: Stress dependency of tight gas samples also showing the hysteresis during loading and unloading cycles of confining pressure where red is loading and blue is unloading. (from Al-Hinai, 2007).**

#### 4.4.4 Heterogeneity and anisotropy

It is very rare to have a homogenous rock and most of the rocks are heterogeneous on a range of scales. Sedimentary rocks often have high variability in a vertical direction because they are often deposited in sub-horizontal layers. The average permeability of a rock parallel to layering can be calculated using the weighted arithmetic average (**Figure 4-7**) and Eq. (4-12):

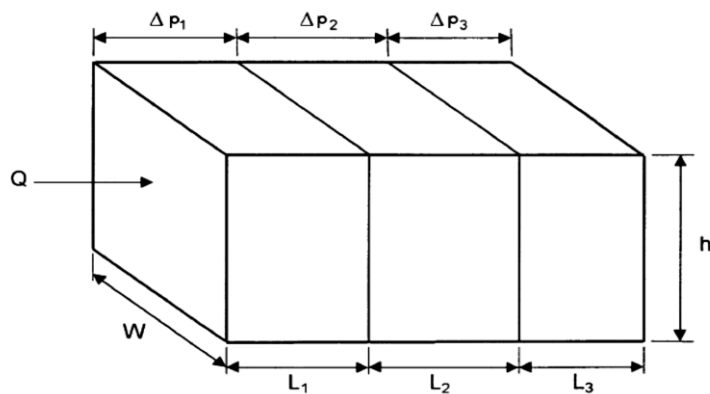
$$K_{avg} = \frac{\sum_{i=1}^n k_i h_i}{\sum_{i=1}^n h_i} \quad \text{Eq. (4-12)}$$



**Figure 4-7: Linear flow through parallel beds.**

The harmonic averaging technique is used for measuring the permeability of a series of beds (**Figure 4-8**) and equation Eq. (4-13):

$$K_{avg} = \frac{\sum_{i=1}^n L_i}{\sum_{i=1}^n \left(\frac{L}{k}\right)_i} \quad \text{Eq. (4-14)}$$



**Figure 4-8: Linear flow through series of beds.**

Commonly permeability is higher in one direction, due to anisotropy of the rock. Freeze and Cherry (1979) have described several forms of heterogeneity in which discontinuous heterogeneity is due to the presence of the fault or any other geological features, which develop unconformably. Different techniques are also

developed to measure the heterogeneity of the reservoir for example Dykstra-Parsons coefficient (Dykstra, 1950) and Lorenz coefficient (Law, 1944).

#### 4.4.5 Limitations of Darcy Law

The main assumptions made in Darcy law (1856) are that the porous media is homogenous, flow is laminar, fluid is incompressible and rock fluid reactions are absent (Bear 1972, Donaldson 2004). Use of high flow rates for measuring permeability can result in turbulence, which means that the flow conditions are different to those under which Darcy's law was established. This condition is related to the Reynold's number, which is the ratio of the inertial to viscous forces Eq. (4-15);

$$Re = \frac{\rho V D_h}{\mu} \quad \text{Eq. (4-15)}$$

where  $\rho$  and  $V$  are the density ( $\text{kg/m}^3$ ) and speed (m/s) of the fluid respectively,  $\mu$  is viscosity of fluid in cp ( $\text{kg/m-s}$ ) and  $D_h$  is the hydraulic diameter (m) of the porous media. Collins (1961) used  $D_h = \sqrt{\frac{k}{\phi}}$  hydraulic diameter where  $k$  is the permeability ( $\text{m}^2$ ) and  $\phi$  is the porosity of porous media respectively. The other approach was mentioned by Ward (1964) and used  $D_h = \sqrt{k}$  as representative parameter of hydraulic diameter.

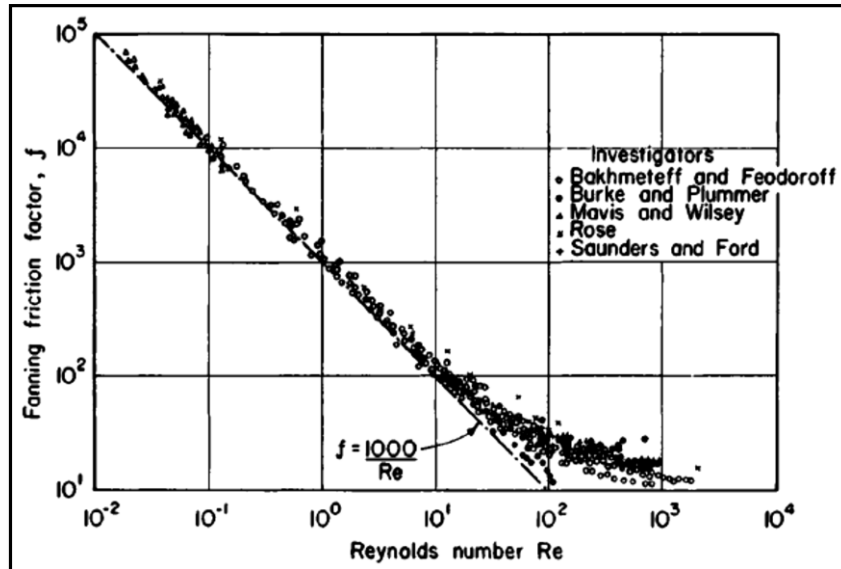
The flow is no longer laminar beyond a certain range of Reynold's number and Darcy's Law is not applicable. In this flow regime, turbulence causes an additional pressure drop due to supplementary loss of energy, which leads to inconsistent (Bear, 1972).

Lindquist (1933) conducted experiments of water flow through porous soil and concluded that Reynolds number should be around 4 for Darcy's law to be valid. A similar Reynold's number of 4 was reported by Bakhmeteff and Feodorff (1937) after which they found the failure of Darcy's Law. Hubbert (1940) noted that the failure of Darcy's law is due to inertial forces not only turbulence. Brownell and Katz (1947) also found a critical Reynold's number of 5 after which Darcy's Law was found to fail. Schneebeli (1955) has conducted experiments on different types of porous media and reported the critical number of 5 for spheres and 2 for granite chips. Most often the upper limit of critical Reynold's number for the applicability of Darcy's Law is 1 to 10 (Chapman, 1981).

Flow through porous media is also related to friction factor. The Fanning friction factor,  $f$ , is defined as:

$$f = \frac{c}{R_e} \quad \text{Eq. (4-16)}$$

where  $c$  is a constant. A relationship is observed when Fanning friction factor is plotted against the Reynold number (Rose, 1945). The straight line in (**Figure 4-9**) is showing a relationship  $f = \frac{c}{R_e}$ .



**Figure 4-9: Relationship between Fanning’s friction factor and Reynolds number for flow through granular porous media (Rose, 1945).**

The Reynolds number is dependent on flow velocity if the properties of the porous media and fluid (i.e. hydraulic diameter, density and viscosity) are constant. It is evident from **Figure 4-9** that deviations from linear behaviour occur as Reynold’s number increases. **Figure 4-10** shows the conditions under which Darcy’s law is applicable. The low Reynolds number corresponds to the low flow velocity where laminar flow occurs and viscous forces dominate. High Reynolds numbers correspond to transitional and turbulent fluid flow (Bear, 1972).

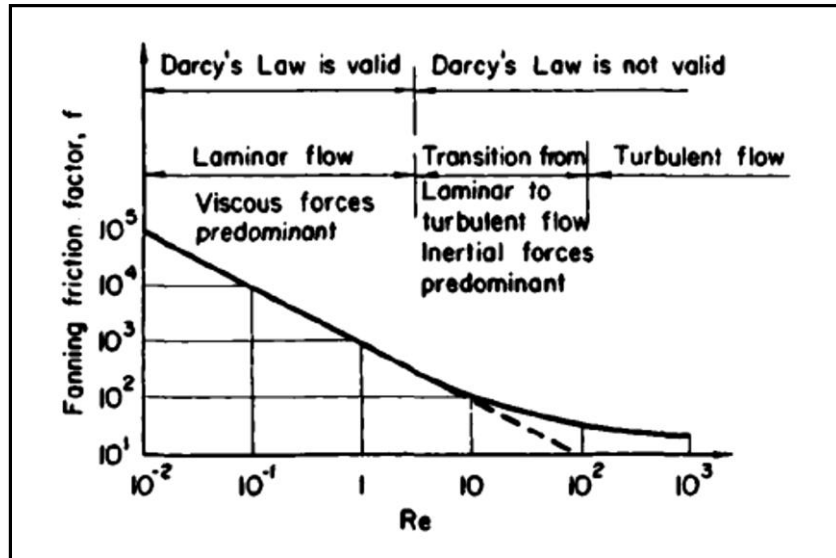


Figure 4-10: Darcy and non-Darcy flow classification in a porous media (Bear, 1972).

The above discussion highlights that for permeability measurements to be valid, strict boundary conditions must be applied during laboratory analysis. In particular, it is important to maintain laminar flow. It is also recommended that permeability is measured using at least three different flow rates so plots of flow rate vs permeability can be used to rule out turbulent flow.

## 4.5 Methods for measuring gas permeability

In this section the methods used to measure gas permeability of the fault rock samples are described in detail. A range of methodologies have been used to measure gas permeability but in this research the two main methodologies, steady-state and pulse-decay permeametry are used. These techniques are applied on two types of fault and host samples, which are core plugs and rock samples embedded in dental putty or epoxy resin. Core plugs are usually 1 or 1.5 inch in diameter and around 2 in long; these are standard sizes used by the petroleum industry for conducting petrophysical property analysis.

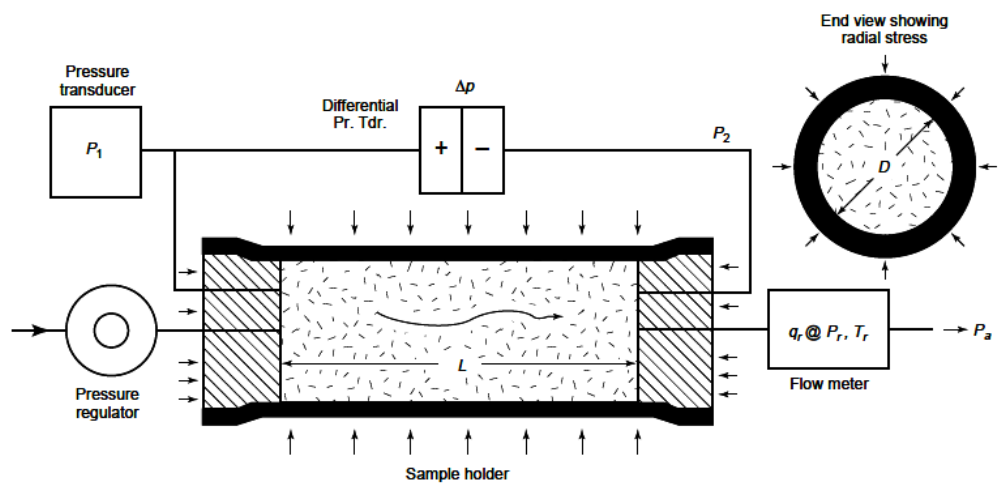
Rectilinear samples were embedded in dental putty or epoxy resin to emulate the technique used to generate much of the published fault rock permeability data and that on most company's proprietary database (e.g. Fisher and Knipe, 2001). This technique was originally used because it proved very difficult to take core plugs of fault rock as they often broke along laminations. It therefore became standard practice to cut 1 cm<sup>3</sup> rectilinear blocks and placed in cylindrical molds and embedded in either dental putty or resin so that the samples could be analysed in standard core holders (refer Chapter 3 for samples detail). The putty is very compressible so it is not possible to conduct permeability measurements on samples prepared in this way at high confining pressure.

Coring techniques have improved so it is now standard practise to take core plugs of fault rocks and conduct measurements at high confining pressures. There is, however, a large amount of data currently being used that was measured using the old technique. For this work it has therefore attempted to make both types of

measurements in the hope of identifying ways of correcting the legacy data so that it is representative of subsurface conditions.

### 4.5.1 Steady-state gas permeability

The equipment used for the steady-state gas permeability is shown in **Figure 4-11**. Clean and dried core plug samples with length  $L$  and diameter  $D$  are inserted into the Hassler core holder. The Hassler core holder is designed to seal the sample from its circumferential wall by the rubber sleeve and all the fluid must pass through the porous medium and not around the edge of the core plug. The rubber sleeve also enables a range of radial confining pressures (from 500 psi to 10000 psi) to be applied to the samples using a hydraulic pump. The plug is prevented from expanding laterally by the end platens in the core holder so the application of the radial confining pressure also results in an increase in the axial stress. Pressure transducers are attached to the upstream and downstream ports allowing the absolute and differential pressures to be measured during experiments. The downstream port is also connected with a flow meter to measure the flow rate.



**Figure 4-11: Setup for steady-state permeability measurement (API RP40, 1998).**



A constant flow rate,  $q$ , of helium gas is applied on the upstream side during the permeability measurement. Permeability is calculated from the flow rate and pressure difference once the upstream and downstream pressures have stabilized (i.e. the flow has reached steady-state). The time required to achieve the constant differential pressure depends on the permeability of the sample. It takes too long to reach steady-state for low permeability samples so this technique is mainly used on samples with permeability  $> 0.1$  mD.

#### 4.5.1.1 Klinkenberg effect

Klinkenberg (1941) was the first who pointed out in his paper that the rate of gas flow through a porous medium depends upon the distance between the gas molecules, which is called mean free path. The mean free path of gas increases as pressure is lowered, which reduces frictional/viscous forces, allowing gas molecules to “slip” along the pore walls, this process is known as slippage and results in an overestimation of permeability. Klinkenberg has used the basic theory given by Kundt and Warburg (1857) to show that an inverse relationship exists between the mean free path ( $\lambda$ ) and mean pressure ( $P_m$ ) by the following equation:

$$\frac{4C\lambda}{r} = \frac{b}{P_m} \quad \text{Eq. (4-17)}$$

where:

$C$  = constant of proportionality;

$P_m$  = mean pressure of the gas;

$\lambda$  = mean free path (distance between the molecules of the gas travelled before collision)

$b$  = slippage factor

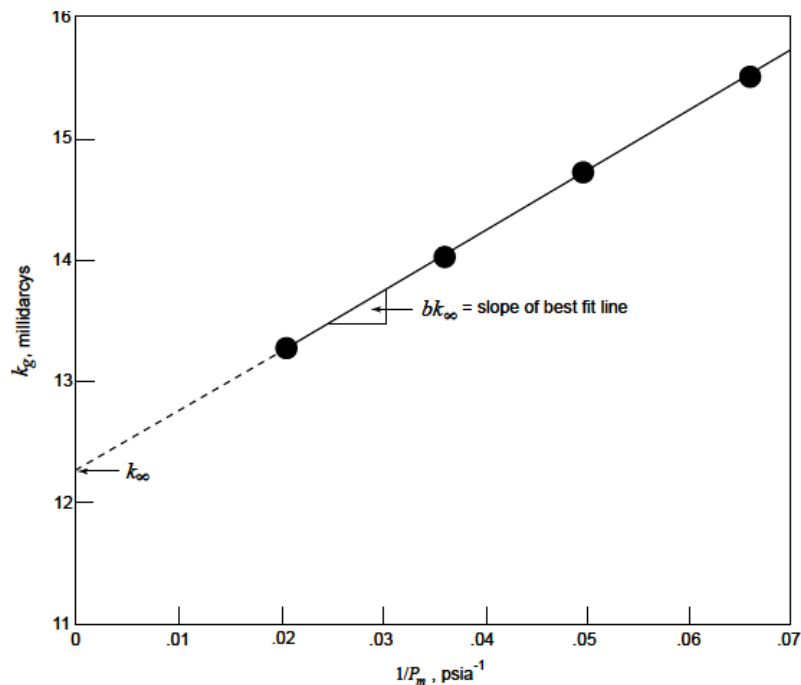
$r$  = radius of the pore or capillary

Klinkenberg (1941) suggested that the high mean pressure will reduce the mean free path and so the slippage effect will be reduced. He deduced a methodology to calculate the permeability at mean free path equal to zero at which is  $\frac{1}{P_m} = 0$ , where the gas behaves as liquid. In this method, the gas permeability is measured at different mean pore pressures and the permeability at infinite pore pressure is calculated by extrapolating the apparent permeability to is  $\frac{1}{P_m} = 0$  (**Figure 4-12**); this permeability value is termed the absolute or Klinkenberg corrected permeability (API RP40, 1998).

The equation given by Klinkenberg for estimating the true permeability is

$$k_g = k_\infty \left( 1 + \frac{b}{P_m} \right) \quad \text{Eq. (4-18)}$$

where  $k_g$  is the apparent gas permeability,  $P_m$  is the mean pressure,  $b$  is the slippage factor and  $k_\infty$  is the true permeability or liquid permeability.



**Figure 4-12: Graph for Klinkenberg permeability measurement.**

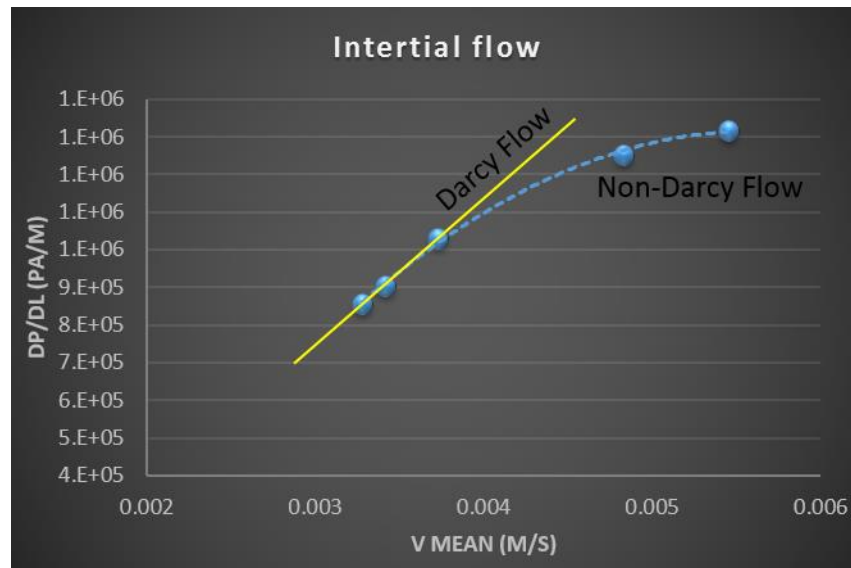
All gas permeabilities presented in this thesis have been measured as Klinkenberg corrected. For every sample, 3 – 5 points of pressure are taken, for every stage of confining pressure (ranging from 1000 psi to 5000 psi, 1000 psi for every step). These points are plotted against the inverse of mean pressure to calculate the Klinkenberg permeability by extrapolation of curve.

#### 4.5.1.2 Inertial Flow

Forchheimer (1901) argued that Darcy's law was no longer applicable at high flow rates. He predicted that the pressure gradient is increased by a quantity of  $\beta\rho V^2$  in comparison of the potential gradient achieved by Darcy's Law. He has developed the following equation:

$$-\frac{dP}{dl} = \frac{\mu V}{k} + \beta\rho V^2 \quad \text{Eq. (4-19)}$$

where  $dP/dl$  is the pressure gradient,  $\mu$  is the viscosity of gas,  $V$  is the average or mean flow velocity and  $\beta$  is the high velocity coefficient or Forchheimer constant. For the laminar flow,  $\beta\rho V^2$  will be zero and the remaining equation is similar to Darcy Law.



**Figure 4-13: Darcy and non-Darcy flow behaviour for Sample ORG – A1.**

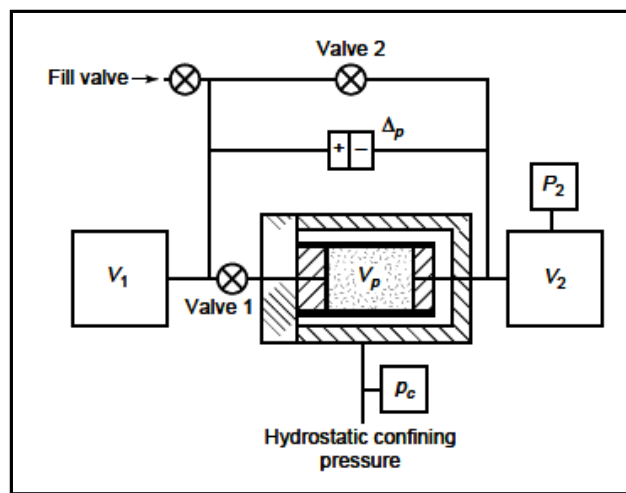
In this study care is taken to avoid developing any inertial effects by applying low flow rates and plotting the permeability points to check if deviating from straight line as presented in **Figure 4-13**. The three points show that the flow rates are with the limit to produce laminar flow but at higher flow rates the velocity also increases and the last two points deviated from Darcy flow and show inertial effects. In case any deviation is found, the flow rate is reduced to be in the limit of laminar flow. McPhee and Arthur (1991) have given some suggestions for the improvement of the gas permeability measurements, which includes the application of backpressure and high pore pressure.

#### **4.5.2 Unsteady-state or pulsed-decay permeability**

##### **measurement**

The steady-state permeability experiments take too long to stabilise the differential pressure for the low permeability samples (< 0.1 mD). At least three permeability measurements at different flow rates are needed to make a Klinkenberg

correction, which would be extremely time-consuming for low permeability rocks. To avoid this problem, Brace et al. (1968) developed a pressure transient method for measuring the permeability of granite to values as low as one nanoDarcy ( $10^{-6}$  mD). There have been a range of mathematical and instrumental modifications to the initial method of Brace (e.g. Amaefule et al., 1986; Jones, 1997; Dicker and Smith, 1988; Bourbie and Walls, 1982; Hsieh et al.; 1981) to improve the accuracy and reduce the time taken to the permeability tight or low permeability rocks. The arrangement of pulse decay equipment is illustrated in **Figure 4-14**.



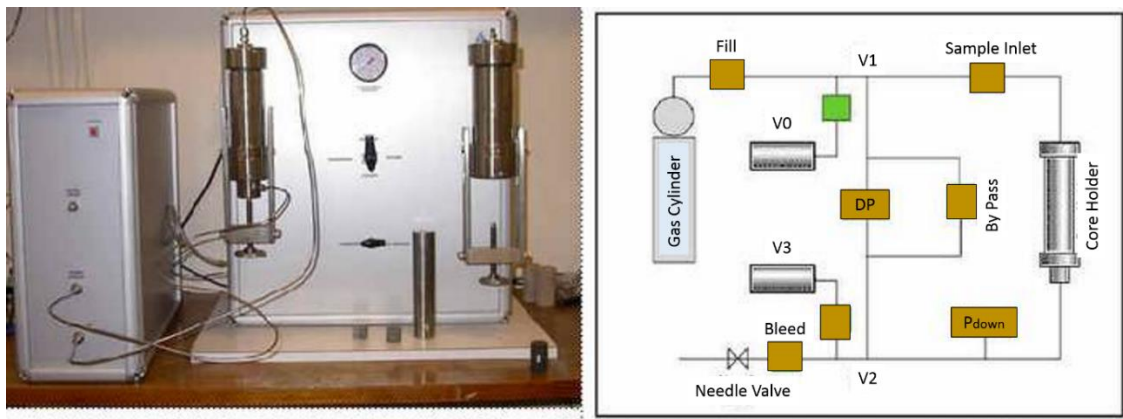
**Figure 4-14: Unsteady-state permeability measurement by pulse decay technique (Jones, 1988).**

#### 4.5.2.1 Setup description for gas pulse decay and procedure

The pulse decay setup consists of core holder, two small reservoir volumes, pressure transducers, valves, and pump and data acquisition unit. The Wolfson multiphase flow laboratories at University of Leeds has a Core-Lab 200 PDP pulse-decay permeameter (**Figure 4-15**), designed on the basis of the modified form of Brace et al. (1968). Jones (1997) proposed a methodology in which the smooth portion of

the pressure gradient is analysed after the establishment. The 200 PDP uses Jones's technique to accurately measure gas permeabilities of 0.1 mD to 10 nD.

For very low permeability measurement system, leak-tightness, and control of ambient temperature variations are very critical. For this system, high mean pore pressures are used to reduce gas slippage but for low permeability rocks it is still important to apply a Klinkenberg correction (Jones, 1997). The range of confining pressure used in these experiments is from 1000 psi to 5000 psi. These confining pressures were extrapolated by regression equations to 70 psi to lower side and to 5000 psi to higher side for analysis.



**Figure 4-15: Pulse decay setup from CoreLab located at Wolfson laboratory, University of Leeds.**

PDP 200 pulse decay gas permeameter is available with built-in software and all the calculation work is done automatically. Two core holders 1 and 1 ½ inch are available. The procedure used during experiment is:

- Select the core holder by changing the position of selection valve.
- Insert a clean and dried sample into the core holder and apply the confining pressure, starting with 1000 psi and increasing it by 1000 psi step till 5000 psi.

- Upstream and downstream reservoir filled with the same pore fluid and the entire system pressurized by pressure  $P_2$ . After closing the bypass valve  $V_2$ , wait for equilibrium to achieve. Now close the inlet valve  $V_1$  generate a small pressure pulse by injecting pore fluid to upstream reservoir. The upstream reservoir pressure is now at  $P_1$ . At this stage the differential pressure across the sample is zero. Now open the valve 1, which allows the fluid to pass through the sample and generate the differential pressure across the sample which decreases with time. The pressure depletion from upstream reservoir depends on the permeability of the rock sample. The data acquisition unit records the pressure changes with time. There is no need of flow metering device.
- The Core-Lab software automatically calculates the permeability of the sample. At every confining pressure step, three to five measurements of permeability are recorded with corresponding mean pressures.

These permeabilities were then plotted against the reciprocal of mean pressures. The straight line of this plot extrapolated to infinite pressure, which is permeability intercept. The intercept value is the equivalent liquid permeability or Klinkenberg corrected permeability. Similar steps were repeated for 2000 to 5000 psi pressures.

### **4.5.3 De-convolved Permeability**

The permeability measured by both the steady-state and pulse decay methods provide an average permeability of the rock. The fault rocks collected from core are invariably far less wide than the length of standard core plugs. So analysis tends to take place on samples composed of fault and undeformed sandstone. However, the fault permeability can be deconvolved using Eq. (4-20):

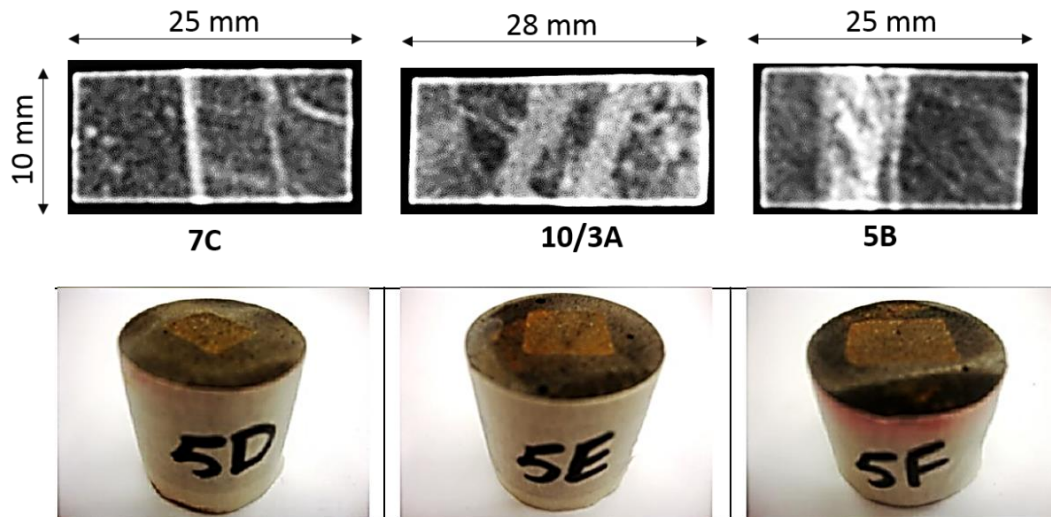
$$k_f = \frac{l_{fault}}{\frac{l_{sample}}{k_{average}} - \frac{l_{host}}{k_{host}}} \quad \text{Eq. (4-20)}$$

In Eq. (4-20)  $k_f$  represents the permeability of fault (mD),  $l_{fault}$  is the thickness of fault (cm),  $l_{host}$  is the thickness of host (cm),  $k_{host}$  is the permeability of host (mD) while  $k_{average}$  and  $l_{sample}$  are representing the average permeability (mD) and length of the sample respectively.

#### 4.5.4 Stress-free samples preparation:

Many published measurements of fault permeability were undertaken on cubes of fault rock at virtually zero confining pressure (e.g. Fisher and Knipe, 2001). To assess the impact of making the measurements at low stress we have used the same experimental techniques and compared the results to measurements made at higher confining pressures. To create samples that are similar to those used in studies such as Fisher and Knipe (2001) small cubes of fault rock samples were prepared and after cleaning, CT images were obtained to ensure the location and thickness of fault (**Figure 4-16**). All dimensions were taken with care and fault thickness was also recorded. The cubes were then put in a cylindrical mould with a 1 inch diameter and surrounded by a high viscosity epoxy resin or dental putty. After the resin had set, ends were ground flat to ensure that no resin covered the face of the samples.





**Figure 4-16: Samples in resin for measurement of permeability at low confining pressure and their CT images.**

After the samples had been prepared the porosity and gas permeability was measured (refer Chapter 3 for porosity measurements). The steady-state methodology is used for high permeability samples while pulse-decay methodology was used for low permeability samples. The brine permeability of the samples was then measured. For these later measurements, samples were saturated with 30% brine by firstly placing them in a vacuum chamber for six hours to remove all air from the pore space. Brine was then introduced into the chamber and the samples left in the brine for 24 hours at atmospheric pressure before transferring them to the brine permeameter. The results of the brine permeability measurements will be discussed in the next chapter (Chapter 5).

Similarly steady-state and pulse-decay techniques were applied according to the permeabilities of the samples. After the brine permeability measurements the samples were flushed with deionised water and the effluent was tested with silver nitrate ( $\text{AgNO}_3$ ), to make sure that all salt was removed from the samples so that permeability could be measured using distilled water so as to replicate the methodology used in Fisher and Knipe (2001). After cleaning of samples, deionised water permeability

experiments were performed. In the last stage, the samples were dried in oven and again gas permeability was measured.

## **4.6 Results**

The results of gas permeability of the stress free sample (samples in putty) are presented in Table 4-1 in which the type of the fault is also mentioned. The results of brine (30 % NaCl) and deionized (DI) water are also included for comparison but will be discussed in detail in next chapter for liquid permeability. The permeability experiments have been performed on highly accurate equipment. The flow meter and pressure transducers are calibrated. The accuracy of the data is  $\pm 10\%$ .

Deconvolved Permeability (mD)								
Sample ID	Fault Type	Fault thickness (cm)	Gas		Brine 30%		DI Water	
			Host	Fault	Host	Fault	Host	Fault
5A	PFFR	0.5	0.62	0.034	0.37	0.002	0.19	0.0015
5B	PFFR	0.8	0.6	0.056	0.19	0.0015	0.04	0.0014
5C	PFFR	0.4	---	1.0	---	0.104	---	0.046
5D	CC	0.3	---	0.25	---	0.030	---	0.018
5E	CC	0.3	29.2	0.2	16.7	0.023	8.3	0.016
5F	CC	0.2	30.2	0.8	17.2	0.09	8.3	0.06
7A	CC	0.5	16.4	0.09	9.2	0.003	4.5	0.0011
7B	CC	0.3	15.9	0.002	5.4	0.0017	2.2	0.0002
7C	PFFR	0.3	3.8	0.067	0.79	0.0015	0.35	0.0003
7D	PFFR	0.6	---	0.0025	---	0.003	---	0.002
7E	PFFR	0.2	2.5	0.07	0.55	0.001	0.25	0.0001
7F	PFFR	0.4	4.8	0.034	0.93	0.002	0.45	0.0015
3A	CC	0.7	21.8	0.018	7.7	0.002	3.70	0.0014
10/3A	CC	0.9	4.4	0.044	1.26	0.001	0.68	0.0012
ORC1	CC	2.4	---	30.1	---	5.1	---	0.4
ORC2	CC	2.5	---	688	---	234	---	92
ORC3	CC	2.5	---	332	---	36	---	5.3

**Table 4-1: Results of deconvolved permeability of the rectangular samples in putty (Cataclastic:CC; Phyllosilicate frame work fault rock: PFFR).**

The results of stress dependent deconvolved gas permeability (by using equation 4-20) for the cataclastic and phyllosilicate framework fault rocks from core and the catclastic faults of Orange outcrop are given in **Table 4-2**, **Table 4-3** and

**Table 4-4.** The permeability values presented are Klinkenberg corrected and the other experimental raw data presented in **Appendix – 2.**

<b>Deconvolved Gas Permeability (mD)</b>										
<b>(Cataclastic Samples)</b>										
<b>Sample ID</b>	<b>Confining Pressure (psi)</b>									
	<b>Fault Sample</b>					<b>Host Sample</b>				
	<b>5000</b>	<b>4000</b>	<b>3000</b>	<b>2000</b>	<b>1000</b>	<b>5000</b>	<b>4000</b>	<b>3000</b>	<b>2000</b>	<b>1000</b>
<b>3A1</b>	0.011	0.012	0.013	0.014	0.018	14.6	15.9	16.9	17.2	17.8
<b>3A2</b>	0.0031	0.0033	0.0037	0.0043	0.0051	14.6	15.9	16.9	17.2	17.8
<b>7A1</b>	1.9	1.9	1.8	1.9	2.0	13.7	14.2	14.4	14.8	15
<b>7B1</b>	0.00063	0.00064	0.00070	0.00077	0.0009	6.1	6.2	7.1	8.6	9.5
<b>7B2</b>	0.0011	0.0012	0.0019	0.0025	0.0046	6.1	6.2	7.1	8.6	9.5
<b>10/3A</b>	0.0067	0.0073	0.0082	0.010	0.014	1.9	2.5	2.6	2.8	2.9
<b>10/3B</b>	0.24	0.24	0.25	0.26	0.28	85	89	92	95	101
<b>5D1</b>	1.5	1.6	1.7	1.8	1.8	67	69	74	80	83
<b>5E1</b>	0.13	0.17	0.17	0.18	0.23	18.9	19.2	20	22	23
<b>5E2</b>	1.4	1.4	1.4	1.4	1.5	18.9	19.2	20	22	23
<b>5F1</b>	0.25	0.27	0.29	0.33	0.35	32	33	34	34	34.3

**Table 4-2: Deconvolved gas permeability results of cataclastic fault rock samples from North Sea reservoir.**

Deconvolved Gas Permeability (mD) (Phyllosilicate Samples)										
Sample ID	Confining Pressure (psi)									
	Fault Sample					Host Sample				
	5000	4000	3000	2000	1000	5000	4000	3000	2000	1000
5A1	0.022	0.024	0.025	0.028	0.032	2.4	2.5	2.6	2.7	2.9
5A2	0.0013	0.0014	0.0016	0.0021	0.0029	2.4	2.53	2.6	2.7	2.9
5B1	0.0044	0.0046	0.0051	0.0056	0.0065	0.41	0.41	0.41	0.45	0.5
7C1	0.0009	0.001	0.0011	0.0013	0.0018	1.7	1.8	1.8	2.2	2.5
7C2	0.021	0.022	0.024	0.027	0.029	1.7	1.8	1.8	2.2	2.5
7D1	0.002	0.0021	0.0022	0.0027	0.0032	0.03	---	---	---	---
7E1	0.011	0.011	0.013	0.018	0.025	1.4	1.5	1.7	1.8	1.8
7F1	0.0031	0.0034	0.0041	0.0048	0.0064	4.8	---	---	---	---

**Table 4-3: Deconvolved gas permeability results of phyllosilicate framework fault rock samples from North Sea reservoir.**

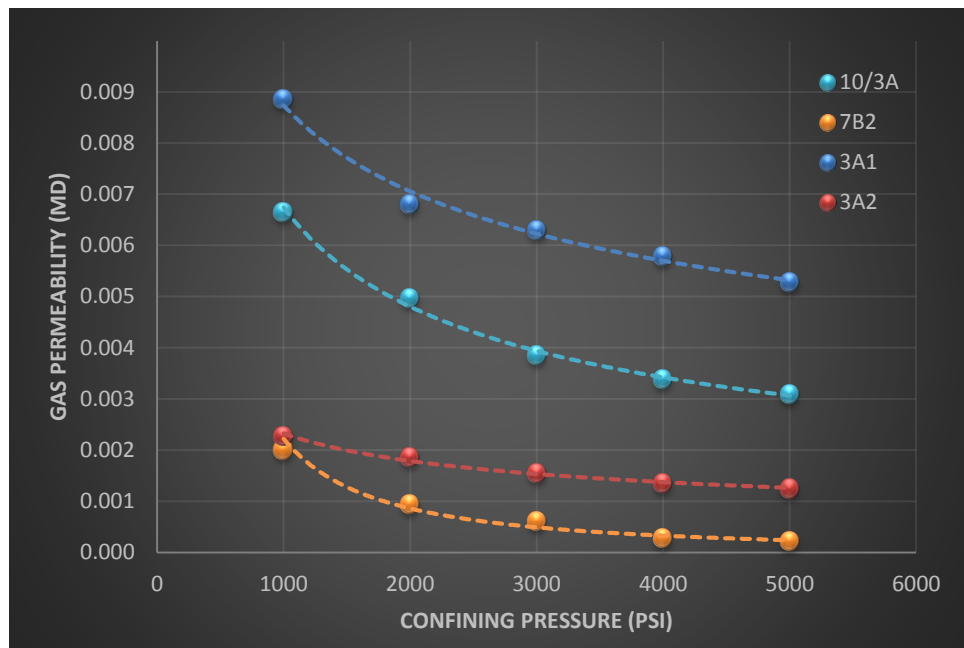
The results of gas permeability of Orange and other outcrop samples are presented in **Table 4-4**. These samples consists of only fault material so deconvolution of permeability is not required.

Gas Permeability (mD) (Outcrop Samples)					
Sample ID	Confining Pressure (psi)				
	Fault Sample				
	1000	2000	3000	4000	5000
<b>ORG1</b>	231	191	167	152	143
<b>ORG2</b>	115	109	102	99	97
<b>ORG3</b>	566	567	561	510	525
<b>ORG4</b>	255	223	205	192	186
<b>ORG5</b>	60	57	54	54	53
<b>ORG6</b>	2.3	2.0	2.0	1.9	1.8
<b>ORG7</b>	793	576	461	385	353
<b>ORG8</b>	202	186	167	152	149.
<b>ORGA1</b>	43	37	33	31	29
<b>ORGA2</b>	2.1	2.0	1.8	1.8	1.7
<b>ORGA3</b>	510	491	472	464	457
<b>HP1</b>	0.00069	0.00061	0.00056	0.00053	0.00051
<b>HP2</b>	0.0017	0.0015	0.0015	0.0014	0.0014
<b>Miri-1</b>	0.33	0.17	0.12	0.09	0.073
<b>Miri-2</b>	0.66	0.46	0.37	0.32	0.28

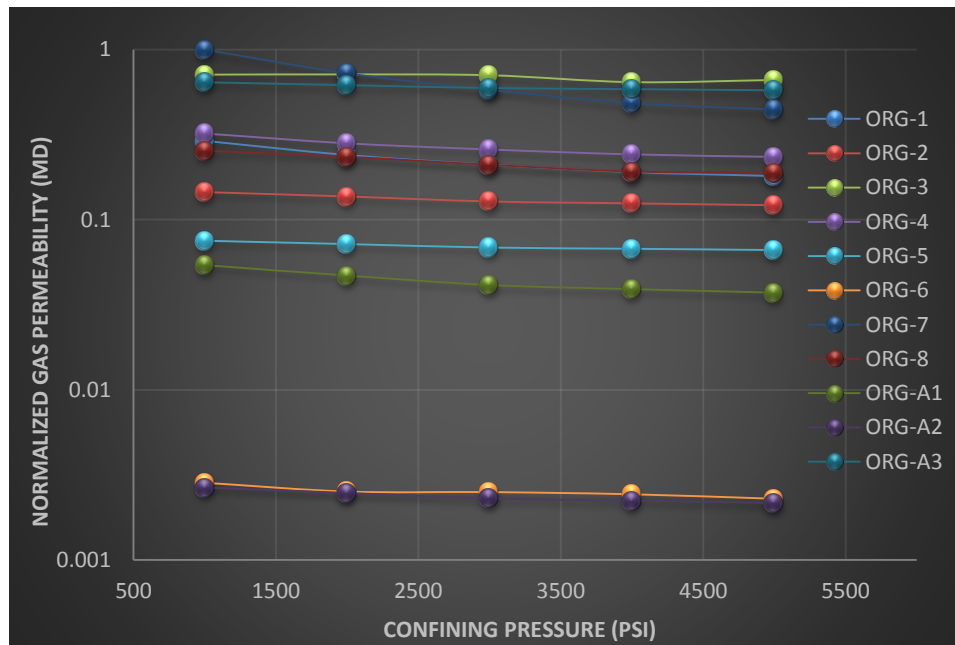
**Table 4-4: Gas permeability results of cataclastic fault rock samples from outcrop.**

The permeability of all samples decreases with increasing confining pressure (e.g. **Figure 4-17** and **Figure 4-18**). The decrease of permeability within increasing stress can be fitted to either power law or exponential models, these are provided for

cataclastic and phyllosilicate framework fault rocks from core and the cataclastic faults from the Orange outcrop are given in **Table 4-5** and **Table 4-6**.



**Figure 4-17: Normalized stress dependent gas permeability of cataclastic samples from North Sea reservoir.**



**Figure 4-18: Stress dependent gas permeability of Orange fault samples.**

The cataclastic reservoir samples have gas permeabilities of between 2.0 and 0.00063 mD (average = 0.52 mD) measured at 5000 psi. The permeability of all cataclastic samples was found to be very stress sensitive as the highest reduction in gas permeability is found to be 75% while confining pressure increased from 1000 psi to 5000 psi. This highest reduction in gas permeability is found in sample 7BF1, which has the lowest gas permeability. However, the lowest reduction in gas permeability is 2.3% and found in sample 7AF1, which has highest permeability of 1.9 mD. In contrast, the PFFR reservoir samples have permeabilities of 0.03 to 0.0093 (average of 0.01 mD), which is an order of magnitude less than those of the cataclastic faults.

Overall, the stress dependency of permeability appears to increase as permeability is reduced. A power-law relationship appears to provide the best fit for the stress vs permeability results from the fault rocks coefficient of correlation ( $R^2$ ) usually better than 0.9. In contrast, an exponential relationship between stress and permeability is the best fit for the undeformed sandstones, although some host samples also fit a power-law.



Sample	Power Law	R <sup>2</sup>	Exponential Law	R <sup>2</sup>
3AF1	$y = 0.143x^{-0.3}$	0.96	$y = 0.019e^{-1E-04x}$	0.86
3AF2	$y = 0.044x^{-0.31}$	0.99	$y = 0.005e^{-1E-04x}$	0.97
3A (Host)	$y = 39.3x^{-0.11}$	0.8	$y = 19e^{-5E-05x}$	0.93
7AF1	$y = 2.2x^{-0.02}$	0.26	$y = 1.9e^{-5E-06x}$	0.095
7A (Host)	$y = 21.7x^{-0.05}$	0.88	$y = 15.4e^{-2E-05x}$	0.98
7BF1	$y = 0.0044x^{-0.23}$	0.99	$y = 0.0009e^{-9E-05x}$	0.93
7BF2	$y = 2.3x^{-0.9}$	0.97	$y = 0.006e^{-4E-04x}$	0.93
7BF (Host)	$y = 78x^{-0.3}$	0.94	$y = 10.6e^{-1E-04x}$	0.94
10/3AF1	$y = 0.32x^{-0.45}$	0.99	$y = 0.015e^{-2E-04x}$	0.94
Host	$y = 13.8x^{-0.22}$	0.70	$y = 3.3e^{-1E-04x}$	0.86
10/BF1	$y = 0.55x^{-0.1}$	0.99	$y = 0.29e^{-4E-05x}$	0.98
Host	$y = 207x^{-0.1}$	0.97	$y = 104e^{-4E-05x}$	0.99
5DF1	$y = 3.3x^{-0.09}$	0.85	$y = 0.007e^{-1E-04x}$	0.97
Host	$y = 228x^{-0.14}$	0.91	$y = 88.52e^{-6E-05x}$	0.99
5EF1	$y = 1.7x^{-0.29}$	0.89	$y = 0.24e^{-1E-04x}$	0.90
Host	$y = 60x^{-0.146}$	0.95	$y = 24e^{-5E-05x}$	0.93
5FF1	$y = 1.4x^{-0.2}$	0.92	$y = 0.38e^{-8E-05x}$	0.99

**Table 4-5: Correlation coefficient for the cataclastic fault and host samples from North Sea reservoir.**

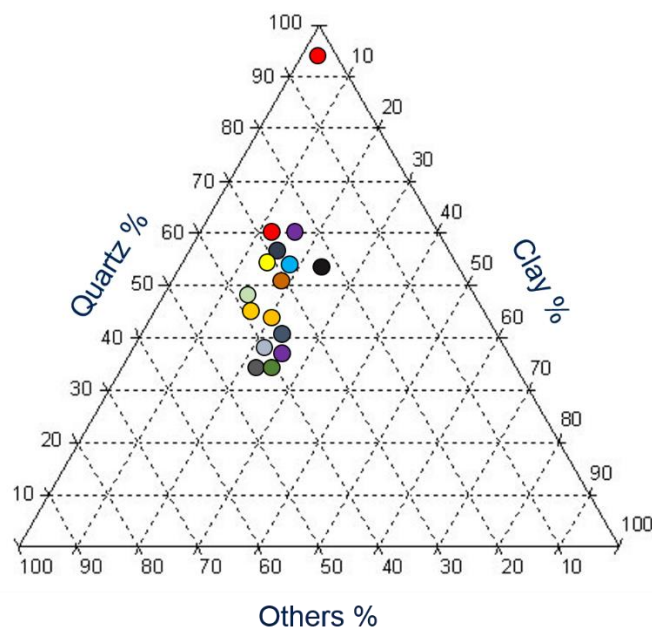
	<b>Power Law</b>	<b>R<sup>2</sup></b>	<b>Exponential Law</b>	<b>R<sup>2</sup></b>
<b>ORG-1</b>	$y = 2.3x^{-0.3}$	0.99	$y = 0.3e^{-1E-04x}$	0.95
<b>ORG-2</b>	$y = 0.32x^{-0.1}$	0.99	$y = 0.15e^{-4E-05x}$	0.95
<b>ORG-3</b>	$y = 1.1x^{-0.06}$	0.58	$y = 0.7e^{-3E-05x}$	0.67
<b>ORG-4</b>	$y = 1.3x^{-0.2}$	0.99	$y = 0.33e^{-8E-05x}$	0.94
<b>ORG-5</b>	$y = 0.13x^{-0.08}$	0.98	$y = 0.08e^{-3E-05x}$	0.94
<b>ORG-6</b>	$y = 0.007x^{-0.12}$	0.94	$y = 0.003e^{-5E-05x}$	0.88
<b>ORG-7</b>	$y = 35.1x^{-0.51}$	0.99	$y = 1.1e^{-2E-04x}$	0.95
<b>ORG-8</b>	$y = 1.1x^{-0.2}$	0.96	$y = 0.3e^{-8E-05x}$	0.96
<b>ORG-A1</b>	$y = 0.3x^{-0.24}$	0.99	$y = 0.06e^{-9E-05x}$	0.94
<b>ORG-A2</b>	$y = 0.007x^{-0.13}$	0.99	$y = 0.003e^{-5E-05x}$	0.95
<b>ORG-A3</b>	$y = 1.1x^{-0.07}$	0.99	$y = 0.7e^{-3E-05x}$	0.95

**Table 4-6: Correlation coefficient for the Orange fault outcrop samples.**

## 4.7 Discussion:

### 4.7.1 Influence of clay contents on fault rock gas permeability

The mineralogy was determined using quantitative X-ray diffraction (QXRD) experiments and detailed minerals analysis is presented in Chapter 3. The results of QXRD reveals that the samples contain between 3 and 28% phyllosilicates (**Figure 4-19**). A range of phyllosilicates were observed including illite, illite-smectite, kaolin, mica and chlorite. It should be emphasised that these may not be all clay minerals as BSEM identified coarse grained detrital mica and chlorite and these cannot easily be distinguished from fine grained illitic and chloritic clays, which will have more of an impact on fault permeability due to their small grain-size. These detrital phyllosilicates were particularly common within the core samples from the central Graben.



**Figure 4-19: Ternary diagram for the mineralogy of samples analysed.**

Fault properties (e.g. permeability and threshold pressure) are commonly used for the workflows of fault seal analysis (Fisher and Jolley, 2007). Sperrevik et al. (2002) suggested that the fault permeability is inversely related with their clay content.

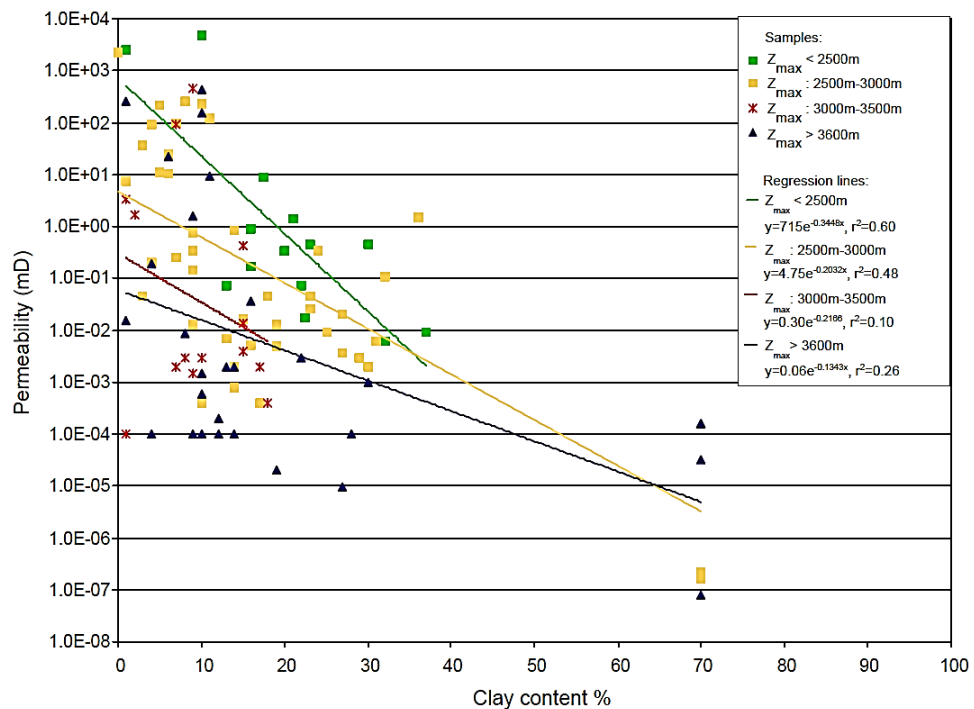
Similarly, Fisher and Knipe (1998, 2001) found that the permeability of faults tended to decrease with increasing clay content. In this section, the relationship between the clay content and fault rock gas permeability is evaluated.

To reflect the relationship between clay content and fault permeability, Fisher and Knipe (1998) presented a fault rock classification that was partially based on the amount of clay present within the fault rock. However, it has also be recognized that a range of other factors affect fault rock permeability including the stress conditions at the time of faulting, the post-deformation temperature history etc. (e.g. Fisher and Knipe, 1998, 2001). Several attempts have been made to derive a general model for fault permeability based on a combination of these factors. Probably the most widely used is that of Sperrevik et al. (2002) who provided a quantitative, but empirical, approach by conducting multiple regression analysis on clay-permeability-burial depth -depth of deformation data; the resulting regression was:-

$$k_f = a_1 \exp\{-[a_2 V_{cl} + a_3 z_{maz} + (a_4 z_f - a_5)(1 - V_{cl})^7]\} \quad \text{Eq. (4-21)}$$

where,  $k_f$  is the fault permeability (mD),  $V_{cl}$  is the clay content (fraction)  $z_{max}$  is the maximum burial depth (m),  $z_f$  is the depth at the time of deformation (m) and the constants are:  $a_1 = 80000$ ,  $a_2 = 19.4$ ,  $a_3 = 0.00403$ ,  $a_4 = 0.0055$ ,  $a_5 = 12.5$ . Although this model is widely used in industry, the correlation between this model and the measurements of fault permeability are poor (**Figure 4-20**). Also, great care must be taken applying the model to reservoirs other than those on which the regression analysis is based because: (i) the permeability of fault rocks is controlled by chemical processes (e.g. quartz cementation and grain-contact quartz dissolution) once mechanical compaction has finished (i.e. 1000-2000 m) and these processes are

controlled by temperature history and not effective stress; (ii) kaolin is the main clay mineral in many of the reservoirs on which its relationship is based and this may not be the case in other areas, and (iii) the model predicts that permeability continues to decrease with increasing clay content, whereas theoretical mixing models (see below) suggest that the minimum fault permeability should occur when space between the sand grains is filled with clay and microporosity. A way to partially overcome the first problem in areas with differing geothermal gradients to the North Sea is by substituting  $z_{max}$  for a depth value that has the same temperature as the North Sea.



**Figure 4-20: Plot showing fault rock permeability against fault rock clay content measured on faults in cores. The data are grouped according to maximum burial depth. Exponential least-squares regression lines are shown for each group of data, showing a systematic decrease in permeability both with fault rock clay content and with depth (from Sperrevik et al., 2002).**

A fundamental problem with correlations between clay content and fault permeability, such as those described by Fisher and Knipe (1998; 2001) on which models such as Sperrevik et al. (2002) are based, that has not been discussed in the literature is that the porosity and permeability of sand-clay mixtures are controlled by

other factors than simply the clay content, deformation and temperature history. For example, Revil and Cathles (1999) showed that the permeability of sand-clay mixtures (i.e. fault gouge) is controlled by the porosity and permeability of the clay matrix, the critical porosity of the sand (i.e. porosity when there is no clay present) as well as the permeability of the sand at the critical porosity. The critical porosity of the sand is controlled by grain sorting and its permeability is controlled by both grain-sorting and grain-size. Accounting for these factors may explain much of the scatter on plots of clay content vs permeability of faults rocks such as shown in **Figure 4-20**.

Revil and Cathles (1999) presented the following model for the permeability of clay-sandstone mixtures,  $k_m$ ,

$$k_m = k_{sd}^{1-\frac{V_{cl}}{\phi_{sd}}} \times k_{Cfs}^{V_{cl}/\phi_{sd}}, 0 \leq V_{cl} \leq \phi_{sd} \quad \text{Eq. (4-22)}$$

$$k_m = k_{sh} V_{cl}^{3/2}, \phi_{sd} \leq V_{cl} \leq 1 \quad \text{Eq. (4-23)}$$

where,  $\phi_{sd}$  and  $k_{sd}$  are the porosity and permeability of the clay-free sand,  $k_{sh}$  is the permeability of the shale end-member and:

$$k_{Cfs} = k_{sh} \phi_{sd}^{3/2} \quad \text{Eq. (4-24)}$$

The impact of grain-sorting on porosity (**Figure 4-21**) and grain-size and sorting on permeability (**Figure 4-22**) of fault rocks can be assessed by incorporating such relationships into the model of Revil and Cathles (1999) **Figure 4-23** shows the impact of grain-size on clay-permeability relationships; both assume the shale end-member has a permeability of 10 nD. The first sand is coarse grained and well sorted with a porosity of 43.1% and a permeability of 5 D. The second sand is fine-grained, very poorly sorted with a porosity of 29% and permeability of 50 mD. The results

show when  $Vcl$  is  $< \phi_{sd}$  the mixtures can have up to two orders or magnitude difference in permeability for a given clay content. These differences can be further extenuated by incorporating the impact of different burial histories and different end-member shale permeabilities. When  $Vcl$  is  $> \phi_{sd}$  all of the intragranular porosity is filled by clay and microporosity so the grain-size of the sand end member no longer has a significant impact on the permeability of the mixture.

Size →	Coarse		Medium		Fine		Very Fine		Average Porosity	Standard Deviation, Percent
	Upper	Lower	Upper	Lower	Upper	Lower	Upper	Lower		
Extremely well sorted	43.1	42.8	41.7	41.3	41.3	43.5	42.3	43.0	42.4	0.8
Very well sorted	40.8	41.5	40.2	40.2	39.8	40.8	41.2	41.8	40.8	0.6
Well sorted	38.0	38.4	38.1	38.8	39.1	39.7	40.2	39.8	39.0	0.8
Moderately sorted	32.4	33.3	34.2	34.9	33.9	34.3	35.6	33.1	34.0	1.0
Poorly sorted	27.1	29.8	31.5	31.3	30.4	31.0	30.5	34.2	30.7	1.8
Very poorly sorted	28.6	25.2	25.8	23.4	28.5	29.0	30.1	32.6	27.9	2.8
Average Porosity	35.0	35.2	35.3	35.0	35.5	36.4	36.7	37.4		
Standard Deviation, Percent	6.0	6.3	5.5	6.2	4.9	5.3	5.0	4.2		

Figure 4-21: Relationship between porosity, grain-size and grain-sorting of a sand pack (after Beard and Weyl, 1973).

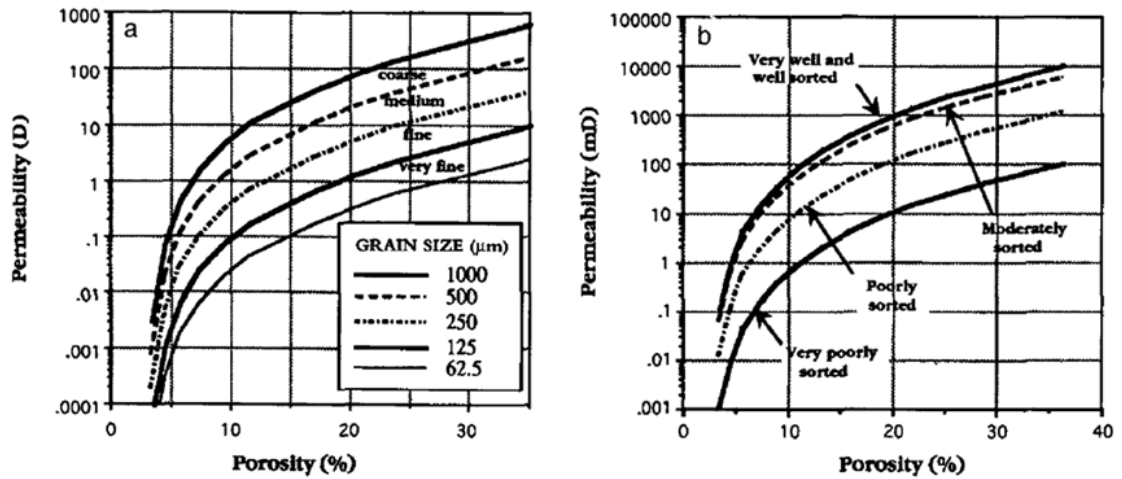


Figure 4-22: Results from numerical modelling showing the impact of (left) grain-size and (right) grain-sorting on porosity and permeability (from Cade et al., 1994).

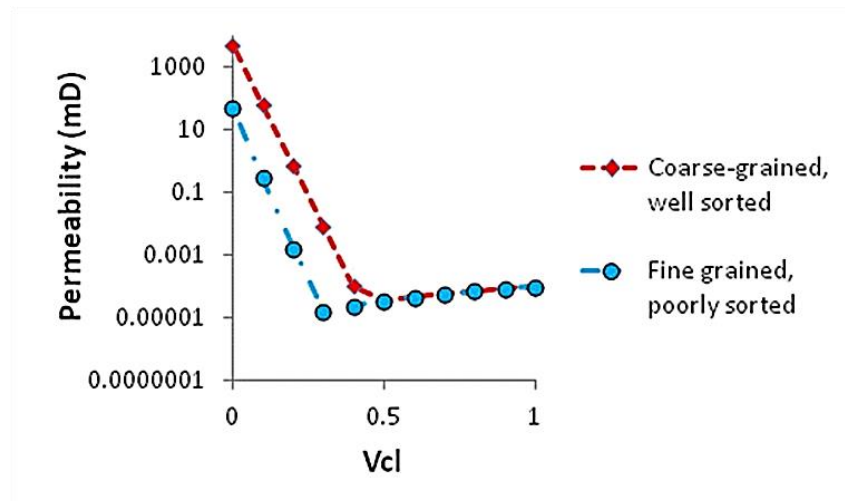


Figure 4-23: Plot of permeability of a sand-clay mixture as a function of clay content where the initial sands have different grain-sizes and grain-sorting, hence porosity and permeability.

The plot between gas permeability and clay content shows a general decrease in gas permeability with increasing clay content but a large amount of scatter observed. An attempt has been made to compare these data to the model of Sperrevik et al. (2002) assuming that the maximum burial depth is 3000 m and that deformation occurred at 1000 m. The fit to this model is reasonable but has two problems: (i) there is considerable scatter around the model; (ii) the model of Sperrevik et al. (2002) predicts



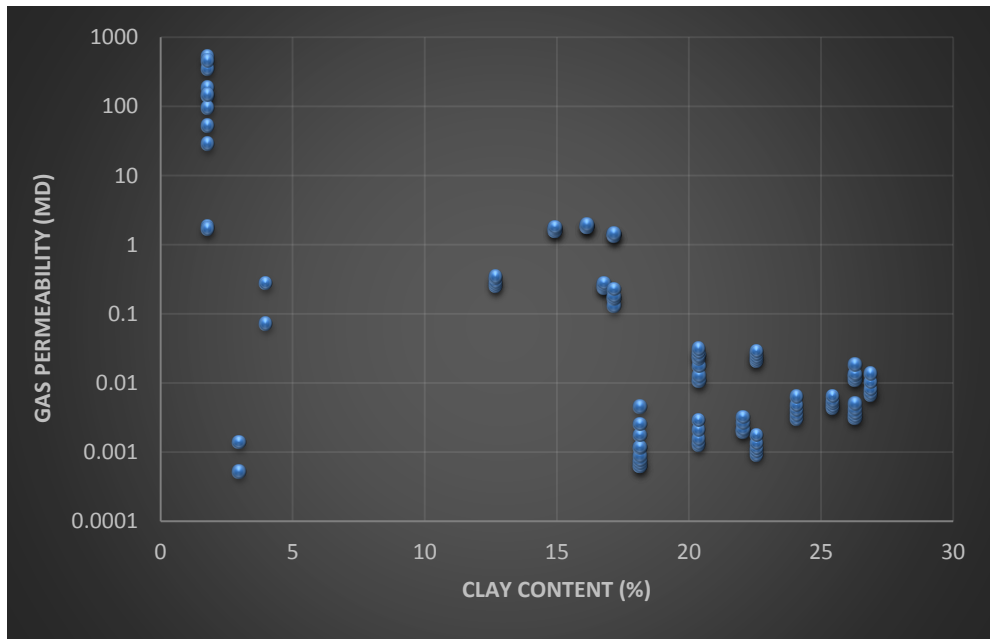
that the permeability of the fault rock continues to decrease with increasing clay content.

As an alternative, the model of Revil and Cathles (1999) has been used to model the permeability vs clay content of fault rocks (**Figure 4-26**). Three different models have been generated and incorporated into the equations presented above:-

- Disaggregation zone – PFFR (Model - Revil and Cathles High in **Figure 4-26**) – here it is assumed that the sand end-member has a permeability of 10,000 mD a porosity of 35% and that the clay end-member has a permeability of 0.0001mD.
- **Protocataclastic fault – PFFR** (Model - Revil and Cathles Mid in **Figure 4-26**) – here it is assumed that the sand end-member has a permeability of 10 mD a porosity of 20% and that the clay end-member has a permeability of 0.0001mD. The lower permeability and porosity of the sand end member is chosen to reflect the small amount of cataclastic deformation experienced.
- **Cataclastic fault – PFFR** (Model - Revil and Cathles Mid in **Figure 4-26**) – here it is assumed that the sand end-member has a permeability of 0.01 mD a porosity of 20% and that the clay end-member has a permeability of 0.0001mD. The lower permeability and porosity of the sand end member is chosen to reflect the large amount of cataclastic deformation experienced.

On a general level, these models provide a better overall explanation to the clay vs permeability measurements made during the current study and are also consistent with theoretical mixing models, which suggest that permeability should not continue to decrease with increasing clay content. There are still several measurements

that appear to have permeabilities that are greater than the Revil and Cathles High model. All of these measurements were obtained from the Central Graben reservoir samples. These samples contained considerable quantities of detrital mica and chlorite, which should not be classified as clays due to their large grain-size. These were grouped as clays within the QXRD analysis and potentially explain why they appear to have higher permeabilities than predicted by the theoretical mixing model.



**Figure 4-24: The relation between fault rock and clay contents; permeabilities were measured at 5000 psi.**

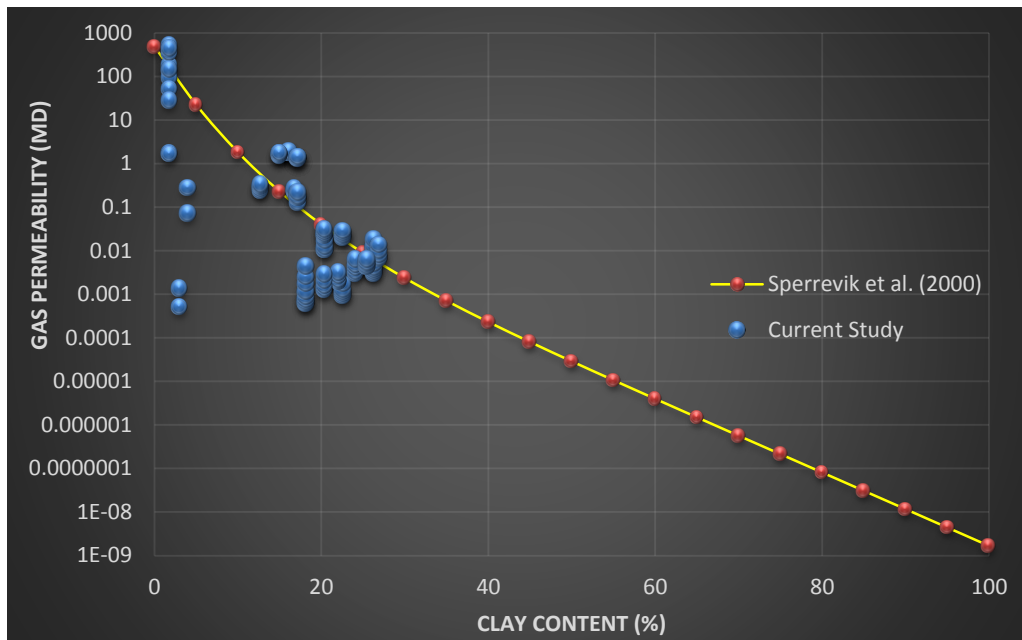


Figure 4-25: The same data as Figure 4.25 but also included is the results from the model of Sperrevik et al. (2002).

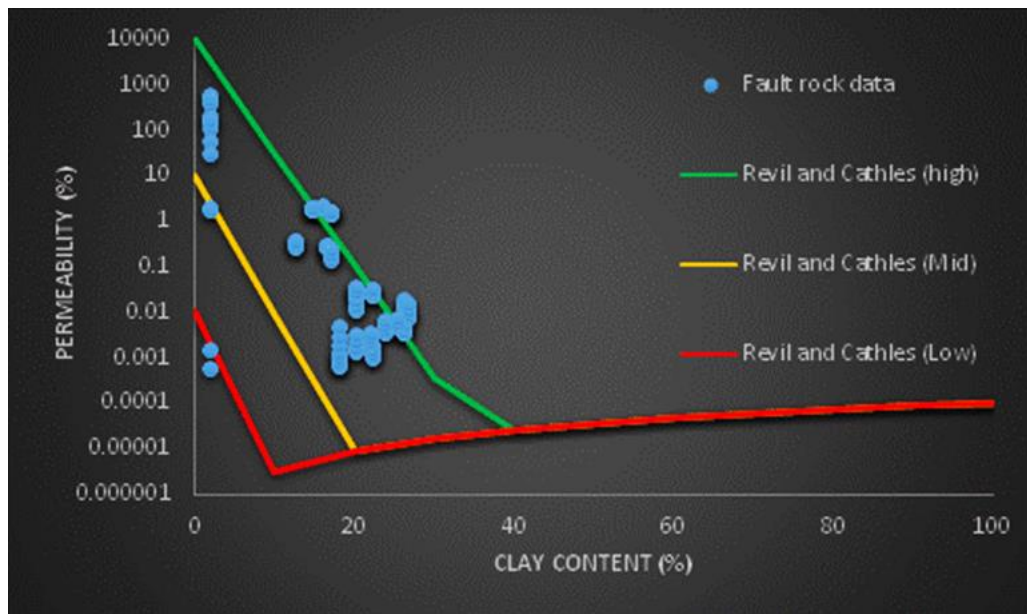


Figure 4-26: Plot of the gas permeability of fault rocks vs clay content against various sand-clay mixing models of Revil and Cathles (1999).

#### 4.7.2 Causes of the stress dependence of gas permeability

It is found that the stress dependency of rock permeability is also a function of the pore geometry, pores connectivity, pore dimensions, fractures or cracks may act as conduits (e.g. Ostensen, 1983; Brower and Morrow, 1983; Gangi, 1978; Walsh, 1981; Fatt and Davies, 1952; Thomas and Ward, 1972). It is difficult to explain the large reduction of permeability (i.e. up to a factor of 10) with stress by invoking a simple capillary tube model for permeability should be reduction of ~44% in the capillary tube diameter. By considering the Eq. (4-25) the reduction in capillary radius can be estimated to reduce the permeability by a factor of 10. The capillary radius is:

$$r = \left[ \frac{8Ak}{n\pi} \right]^{\frac{1}{4}}$$

After reduction of the permeability by factor of 10, the reduced capillary radius will be:

$$r_{reduced} = \left[ \frac{8Ak}{10\pi} \right]^{\frac{1}{4}}$$

The total change in capillary radius will be

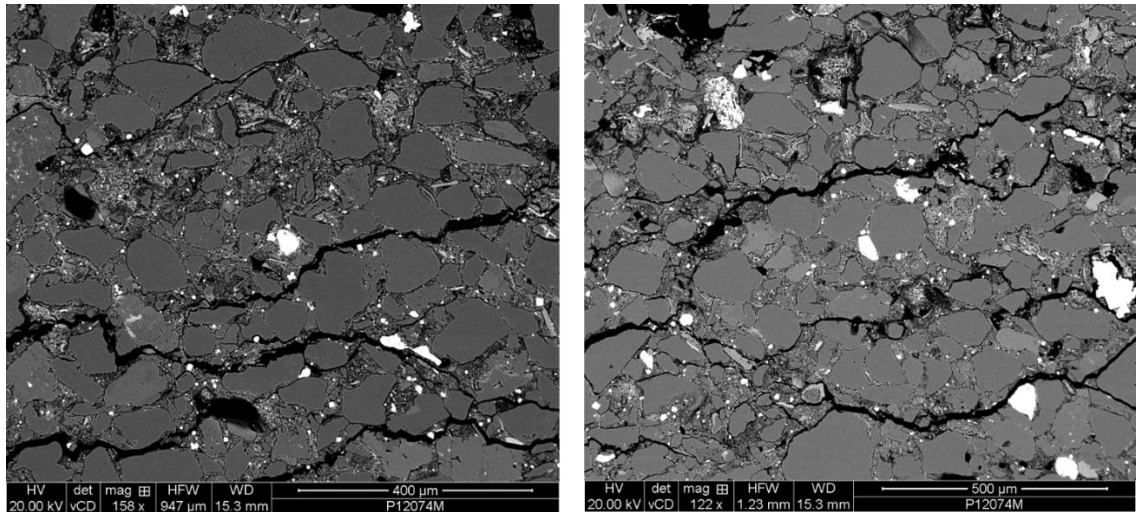
$$\text{Reduction in capillary radius} = \left[ \left[ \frac{8Ak}{n\pi} \right]^{\frac{1}{4}} - \left[ \frac{8Ak}{10\pi} \right]^{\frac{1}{4}} \right] \times 100$$

$$\text{Reduction in capillary radius} = \left[ \frac{8Ak}{n\pi} \right]^{\frac{1}{4}} \times \left[ 1 - \left[ \frac{1}{10} \right]^{\frac{1}{4}} \right] \times 100$$

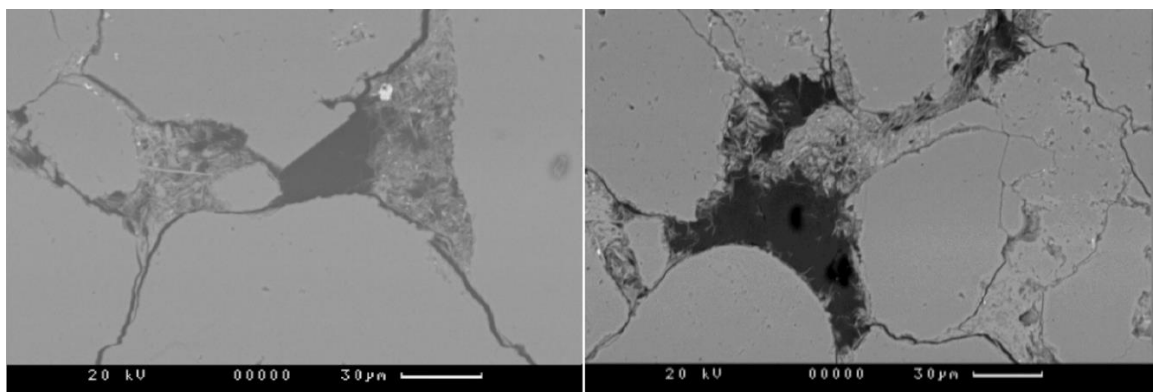
$$\text{Reduction in capillary radius} = 0.44r$$

So the capillary radius should decrease by ~44% of the original radius to decrease the permeability by factor of 10. Ostensen (1983) claimed that the reduction of 45% in the capillary is not possible for an elastic deformation and could only occur by pore collapse. The observation that the permeability shows only limited hysteresis during loading and unloading suggests that the rock has remained in elastic limit indicating that elastic deformation of capillaries is not responsible for the stress dependent behavior Ostensen (1983).

BSEM examination of samples analyzed during this study indicates that two types of microfractures are present. The first are around 5 to 20 $\mu\text{m}$  (**Figure 4-27**) and are very long sometimes exceeded the sample size used for SEM analysis (i.e. >1 cm). These fractures are present in only a small proportion of samples (i.e. <10%) and when present are generally quite widely spaced (i.e. often between 10 and 50 grains apart). The second type of microcracks are considerably thinner (0.5 to 3  $\mu\text{m}$ ) but occur at most grain boundaries and were observed in all samples (**Figure 4-28**). It is likely that both could provide conduits for low permeability rocks but it is also likely that these fractures would close under increasing confining pressure. Indeed, several authors have suggested that such microcracks are responsible for the stress dependence of permeability (e.g., Brace, 1978 a,b; Bernabe, 1986; Trimmer et al., 1980).



**Figure 4-27: BSEM of fault rock samples are showing micro-cracks. The cracks are also visible with the grain boundaries.**



**Figure 4-28: BSEM shows small scale (0.1 to 3 μm) wide fractures at grain boundaries**

Although the reduction in porosity may be as low as 1% the fact that it is due to closure of micro-cracks can decrease permeability by 2 orders of magnitude as was found during experiments on Westerly granite (Brace et al., 1968). Therefore, cracks or fracture models have been presented by different researchers to explain the stress dependence of permeability. Ostensen (1983) classified these models as: non-crack models; crack models where crack width is control by elastic distortion and crack models where crack width is controlled by surface asperities with in the elastic limit.

Stress dependent permeability models are summarized in **Table 4-7**, where seven models are presented with their prediction correlations. In these models, Bower and Morrow (1983) model is based on Walsh's model and the crack shape is defined as penny-shaped cracks. In **Table 4-7**,  $k_i$  is the permeability at zero stress,  $\nu$  is Poisson's ratio,  $c$  is compressibility of quartz,  $L_c$  is mean crack half length,  $w_i$  is crack opening at zero stress and  $\sigma$  is the applied stress. Gangi (1978) model is based on nail like beds of cracks for which the deformation is in elastic limits. The smallest area between three adjacent grains defines the flow controlling pore throat. In **Table 4-7**,  $\lambda$  is the fraction of crack surface covered with asperities (assumed to be very low value than 1),  $E$  is the Young's modulus and  $\xi$  is an adjustable parameter.

Model type and researcher	Correlation
<b>Crack shape (Bower and Morrow, 1983)</b>	$\frac{k}{k_i} = \left[ 1 - \frac{16(1 - \nu^2 c L_c) \sigma}{9(1 - 2\nu) \pi w_i} \right]^3$
<b>Non-crack (Capillary model) (Ostensen, 1983)</b>	$\frac{k}{k_i} = \left( 1 - \frac{2\sigma}{E} \right)^4$
<b>Asperity (Gangi, 1978)</b>	$\frac{k}{k_i} = \left[ 1 - \left( \frac{\sigma}{\lambda E} \right)^\xi \right]^3$
<b>Asperity (Walsh, 1981)</b>	$k = \frac{LS^3}{12} \left[ \ln \frac{nE(\pi r_c s^3)^{1/2}}{2(1 - \nu^2)\sigma} \right]^3$
<b>Asperity (Ostensen, 1983)</b>	$k = \frac{0.76LS^3}{12} \left[ \ln \frac{2.48E(sl r_c)^{1/2}}{3\pi^{1.5}(1 - \nu^2)\sigma} \right]^2$
<b>Non-crack (David et al., 1994)</b>	$k = k_o e^{[-\gamma(P_{eff} - P_o)]}$
<b>Non-Crack (Evans et al., 1997)</b>	$k = k_o e^{[-\gamma P_c]}$

**Table 4-7: Stress dependent permeability models for tight sandstones.**

### 4.7.3 Fracture permeability modelling

Fracture/ crack permeability has been documented by different researchers who derived almost same relationships between the fracture width, the number of fractures and porosity. The Carman-Kozeny permeability equation for fractures (Carman, 1937) was modified by McKee and Hanson (1975) as:

$$k = \frac{nhw^3}{12T} \quad \text{Eq. (4-26)}$$

where  $n$  is the number of fractures per unit area,  $h$  is fracture height,  $w$  is the aperture or width of fracture and  $T$  is tortuosity. A further simplified equation is given by Frank Jones (1975), by treating a fracture as a planar crack:

$$k = \frac{f_n f_w^2}{12} \quad \text{Eq. (4-27)}$$

where  $f_n$  is the number of fractures per unit area and  $f_w$  is fracture width.

An alternative model for fracture permeability is given by the modified Buckingham's equation:

$$k = \frac{\phi_f f_w^2}{12} \quad \text{Eq. (4-28)}$$

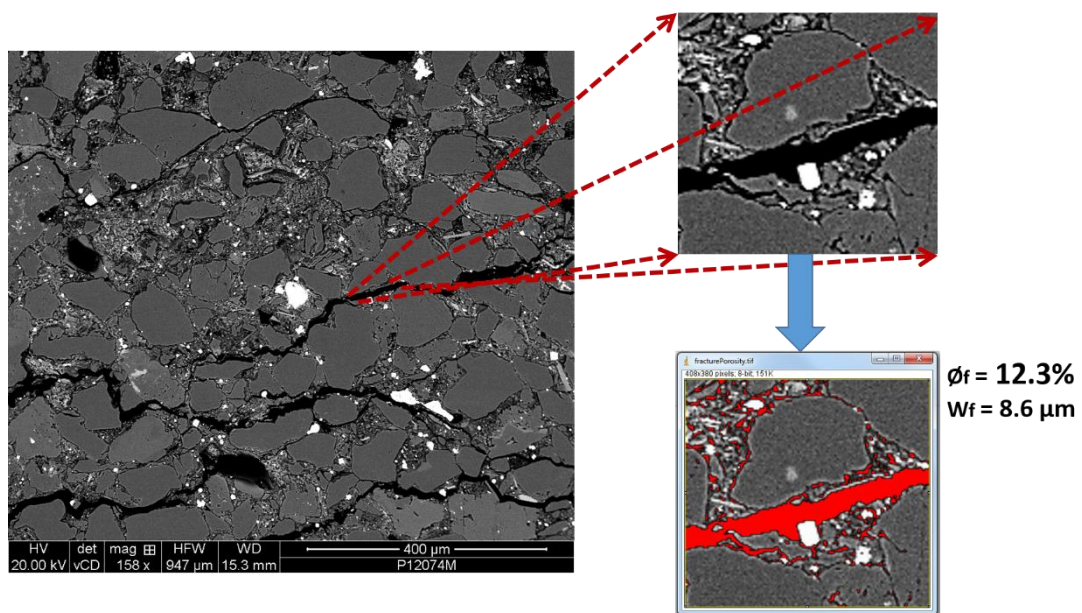
After applying the conversion factor to get  $k$  in Darcy and fracture width  $f_w$  in cm, the equation becomes:

$$k = 84.4 \times 10^5 \frac{\phi_f f_w^2}{12} \quad \text{Eq. (4-29)}$$

On the basis of the above discussion, the permeability of microfractures in the fault samples is modelled and used to evaluate their impact on overall permeability, when it is open and closed. BSEM image is used in conjunction with the imageJ software to measure the fracture width and porosity. The fracture width is measured



by firstly calibrating the image and then five readings have been made to take average mean width which is 8.6  $\mu\text{m}$  (**Figure 4-29**). It is assumed that if there is no stress or confining pressure the fracture width is 8.6  $\mu\text{m}$ , which is gradually decreasing as stress increasing and at the maximum stress i.e. 5000 psi, the fracture is mostly closed and the permeability measured is that of the matrix. The data for fracture permeability are generated and combined with the experimental results to check the impact of fracture flow on fault sample (**Table 4-8**).

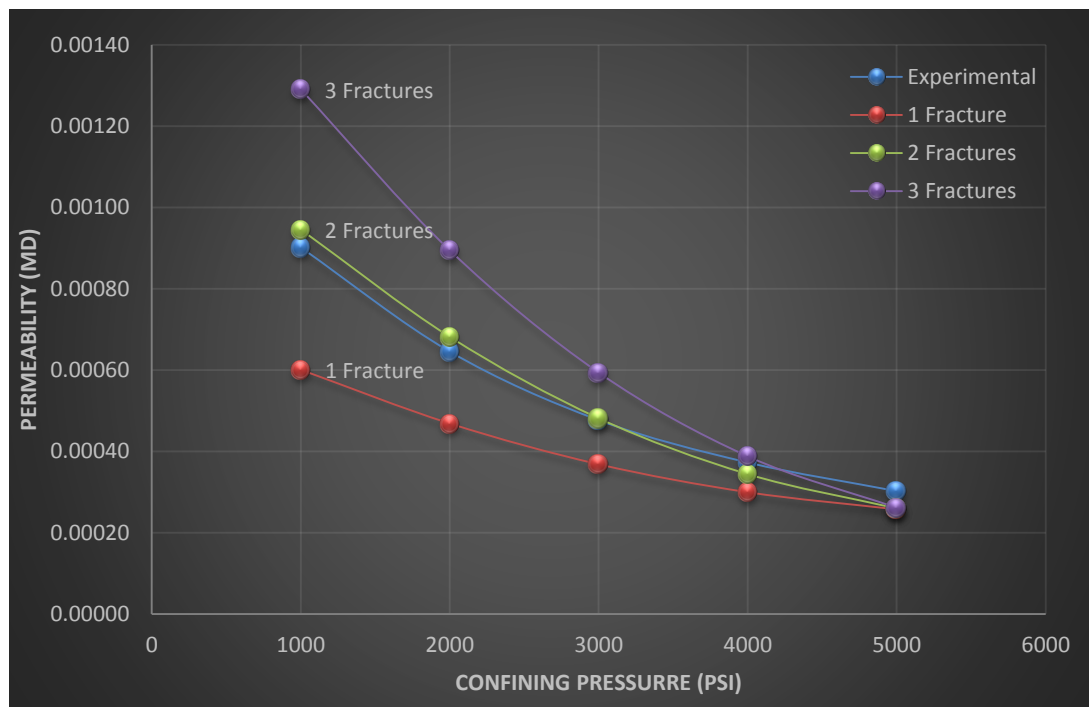


**Figure 4-29: BSEM image of fault sample, showing fracture. Magnified portion is used to measure the fracture width by ImageJ software as well its porosity.**

Pressure (psi)	Experimental permeability (mD)	Fracture and Matrix permeability (mD)		
		1 Fracture	2 Fractures	3 Fractures
5000	0.00030	0.00026	0.00026	0.00026
4000	0.00037	0.00030	0.00034	0.00039
3000	0.00048	0.00037	0.00048	0.00059
2000	0.00065	0.00047	0.00068	0.00089
1000	0.00090	0.00060	0.00095	0.00129

**Table 4-8: Experimental permeability and fracture permeability data for one to three fractures.**

The modelled data for fracture permeability are plotted against the experimental permeability (**Figure 4-30**). The plotted data show good agreement with experimental data and the fracture modelled permeability data. The fracture permeability shows a lower permeability than the experimental data when only a single fracture is assumed while the best agreement can be seen when two fractures are assumed. Three fractures assumption is overestimating the permeability. It is clearly showing that the microfractures are playing a very vital role in altering the permeability with the stress increment. At the highest confining pressure, it is also assumed that the fracture is almost the same as the pore throat diameter and the permeability corresponds to the 5000 psi confining pressure and only matrix permeability is dominant.

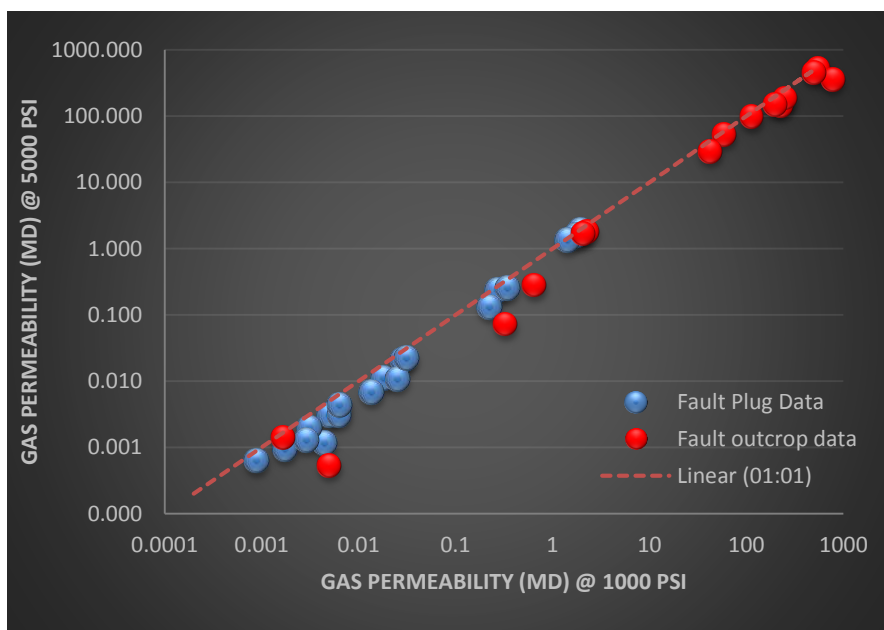


**Figure 4-30: Experimental gas permeability data and the fracture modelled data for three fractures.**

The fractures found in samples BSEM may be developed due to the stress relaxation and playing vital role in the laboratory measurements to made samples highly stress dependent. In the subsurface, Nelson (2001) generalized the term fractures for all fractures that are naturally occurred due to deformation or any physical diagenesis. Bratton et al. (2006) described different reservoir fracture in which fault fracture are developed due to the shearing and may be act as conduit for fluid flow. Researchers reported the alteration in samples due to relaxation from overburden pressure, temperature change, interaction with other fluids (e.g. for cleaning or drilling fluid).

#### 4.7.4 Overall permeability decay

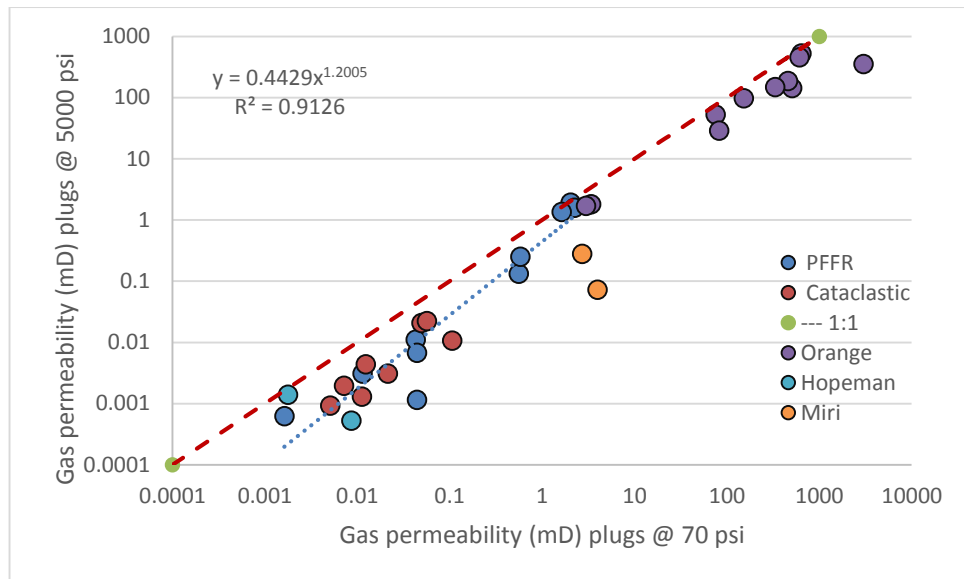
The stress dependent permeability presented in **Figure 4-17** and **Figure 4-18** are very similar to the trends reported by other researchers (e.g. Byrnes et al., 2010; Rushing et al., 2003; McPhee and Arthur, 1991; Al-Hinai, 2007; Evans et al., 1997; Brower and Morrow, 1985).



**Figure 4-31: Plot of gas permeability of fault (core) samples. Fault permeability measured at 1000 psi net stress vs the permeability measured as 5000 psi. Regression line is plotted.**

A comparison of permeabilities at 1000 psi to 5000 psi is presented in **Figure 4-31**, which shows that the permeabilities at 1000 psi are lower than the permeabilities measured at 5000 psi. It is argued that the mineralogy plays a considerable role in deformation of a rock when stress is applied higher than its yield strength. For example, mica or clay contents which are soft in nature can be deformed more than the other brittle and rigid mineral like quartz (Davies and Davies, 2001). This deformation may cause the reduction in pore throat sizes and reduce the permeability. In contrast, Ostensen (1983) conducted experiments on tight rocks and reported that the permeability reduction is due to the closure of the micro fractures when the overburden pressure is increased. In other words, permeability measurements at the low confining pressure provide an overestimation of permeability at reservoir stress conditions. So incorporation of this erroneous data measured at low confining pressure into reservoir simulation models may result in an overestimation of oil and gas production (Fisher and Jolley, 2007; Fisher and Knipe, 2001, 1998).

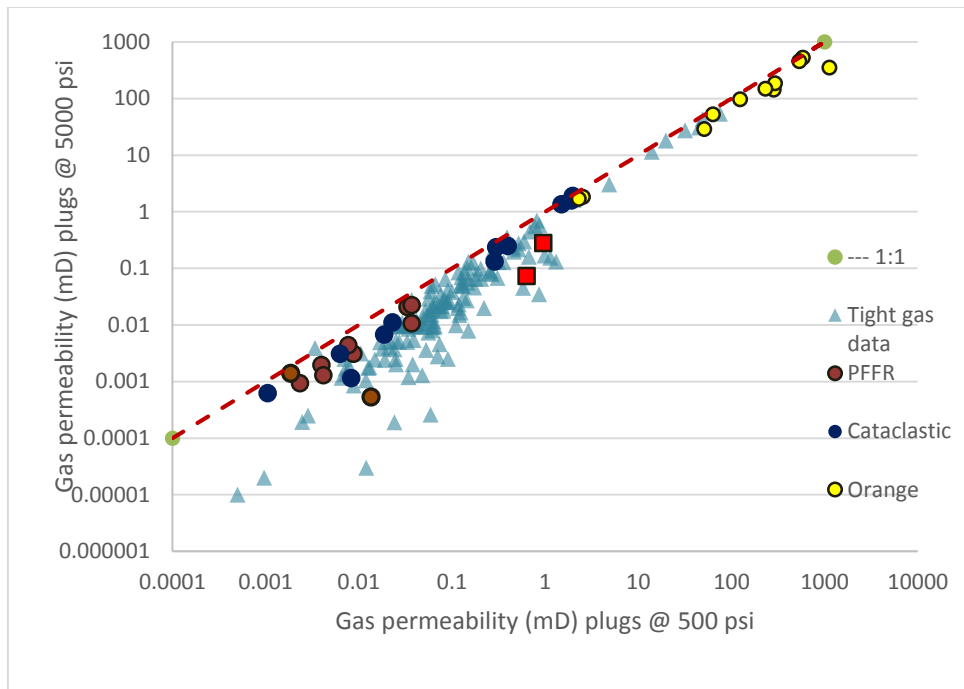
The permeabilities measured at 1000 psi to 5000 psi are extrapolated to estimate permeability at 70 psi so that they can be compared to the measurements made on rectilinear blocks at ambient stress during the current study and in the literature (i.e. Fisher and Knipe, 1998, 2001). Extrapolation was conducted based on both power-law and exponential fits to the stress vs permeability data (**Table 4-9**). The estimated permeability values at 70 psi are compared to those at 5000 psi using the power-law and exponential fits are shown in **Figure 4-32** respectively. On average, the measurements conducted at 5000 psi are around a factor of 5 lower than those conducted at ambient stress conditions.



**Figure 4-32: Plot of gas permeability of fault permeability measured at 5000 psi net confining pressure vs the permeability extrapolated to 70 psi by power law fit.**

The stress sensitivity appears to increase slightly as permeability is reduced but there is no obvious relationship between the extent of stress dependency and fault rock type (**Figure 4-31** and **Figure 4-32**). BSEM images revealed that all faults have a strong fabric created by enhanced grain-contact quartz dissolution. It is possible that the high aspect ratio grain boundaries are responsible for this high stress sensitivity. It is also found that the outcrop samples tend to be less stress sensitive than those from core. So a key control on the stress sensitivity of fault rocks was whether they come from outcrop or core. The reason for this is that the rapid cooling and unloaded experienced as core is retrieved from the subsurface appears to have caused the dilation of grain-boundaries, which has increased permeability at low stresses.

Gas permeability data are compared with the tight gas sandstone data measured at the University of Leeds (**Figure 4-33**).



**Figure 4-33: Gas permeability data of fault rock samples compared with tight gas sandstone samples, tight gas data is taken from University of Leeds for the confining pressure of 500 and 5000 psi.**

The results of the present study show that the fault rock data is less stress sensitive than the tight gas data. These differences in stress sensitivity may reflect the sensitivity to the various rock types to core damage during uplift. The faults tend to be very thin so any stresses resulting from fluid expansion can be easily accommodated by transfer of fluid from the fault to adjacent higher permeability sandstone and then out of the core completely. The tight gas samples have uniform low permeability so it is less easy to dissipate expanding fluids resulting in increased damage. Such a mechanism is also consistent with the observed increase in stress dependence of permeability with decreasing absolute permeability of samples as found in samples. It is also consistent with the observation that outcrop samples, which have been uplifted slowly tend to be slightly less stress sensitive than samples from core.

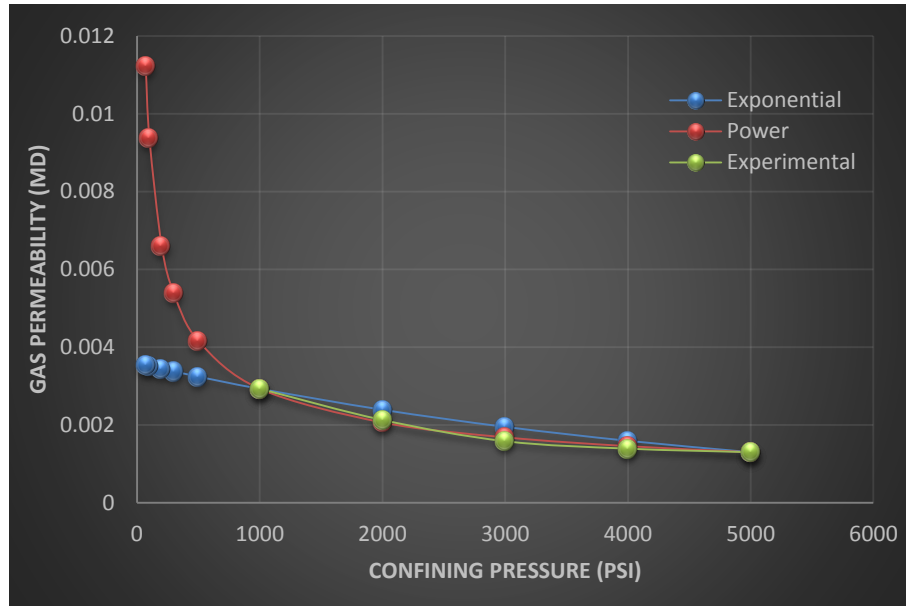
The permeability results are extrapolated to the lower stress values of 70 psi by both exponential and power law formulae. The extrapolated results are presented in **Table 4-9** with the percentage decrease in permeability from 5000 psi to 70 psi.

Sample	In situ permeability at 5000 psi (mD)	Extrapolated by exponential to 70 psi (mD)	Extrapolated by power law to 70 psi (mD)	Decrease in permeability (%)	
				Power law (mD)	Exponential (mD)
3AF1	0.011	0.02	0.04	74	47
3AF2	0.0031	0.0057	0.011	73	46
10/3AF1	0.0067	0.02	0.04	85	58
10/3BF1	0.24	0.29	0.37	37	18
7AF1	1.9	2.0	2.0	6	3
7BF1	0.0006	0.0010	0.0016	61	36
7BF2	0.001	0.006	0.044	97	82
7CF1	0.0009	0.0020	0.0051	82	54
7CF2	0.02	0.03	0.05	58	33
7DF1	0.002	0.004	0.007	73	45
7EF1	0.011	0.031	0.107	90	66
7FF1	0.003	0.01	0.02	86	59
5AF1	0.022	0.03	0.06	61	35
5AF2	0.001	0.004	0.011	88	63
5BF1	0.004	0.007	0.012	65	38
5DF1	1.6	1.87	2.25	29	15
5EF1	0.13	0.26	0.56	76	49
5FF1	0.25	0.37	0.58	57	32
ORG1	143	258	510	72	45
ORG2	97	120	152	36	19
ORG3	525	576	641	18	9
ORG4	186	275	459	59	32
ORG5	53	62	76	30	14
ORG6	1.82	2.4	3.4	46	25
ORG7	353	957	3020	88	63
ORG8	149	216.8	334	55	31
ORGA1	29	47.1	82	65	38
ORGA2	1.7	2.2	3.0	43	23
ORGA3	457	523	611	25	13
HP1	0.00053	0.0086	0.22	100	94
HP2	0.0014	0.0018	0.002	40	21
Miri-1	0.073	0.5	4.0	98	84
Miri-2	0.28	0.8	2.72	90	65

**Table 4-9: Permeability data for the in situ confining pressure at 5000 psi and the extrapolated permeabilities at 70 psi net stress.**



The experimental and extrapolated data are plotted (**Figure 4-34**), which shows that the power law fit is best fit between the 1000 and 5000 psi than the exponential, but it is estimating higher values than exponential (**Table 4-9**).



**Figure 4-34: Plot of gas permeability extrapolated and experimental data.**

The other trend found in the reduction of fault permeability is that the highest change in the permeability occurred at the lowest stress. Afterwards further decrease in permeability also occurred but with less rate than the initial stage. A typical example of sample 7BF1 and 7BF2 is presented in which the highest permeability reduction occurred during the first stress variation from 1000 psi to 2000 psi which is 14.3% and 44.3% respectively. The change of permeability is shown in **Table 4-10** and **Table 4-11** for sample 7BF1 and 7BF2. Carlson (2011) reported the same phenomenon of decreasing permeability at initial low stress and relate it with the closure of the micro fractures.

Fault permeability (mD)	Confining stress (psi)	Stepwise change (%)	Host permeability (mD)	Stepwise change (%)
0.00090	1000	---	9.5	9.2
0.00077	2000	14.3	8.6	17.8
0.00070	3000	9.3	7.1	12.3
0.00064	4000	8.2	6.2	1.6
0.00063	5000	2.2	6.1	

**Table 4-10: Data representing the change in permeability with increasing confining pressure for sample 7BF1.**

Fault permeability (mD)	Confining stress (psi)	Stepwise change (%)	Host permeability (mD)	Stepwise change (%)
0.0046	1000		9.5	9.2
0.0025	2000	44.3	8.6	17.8
0.0018	3000	30.7	7.1	12.3
0.0012	4000	32.8	6.2	1.6
0.0011	5000	2.8	6.1	

**Table 4-11: Data representing the change in permeability with increasing confining pressure for sample 7BF2**

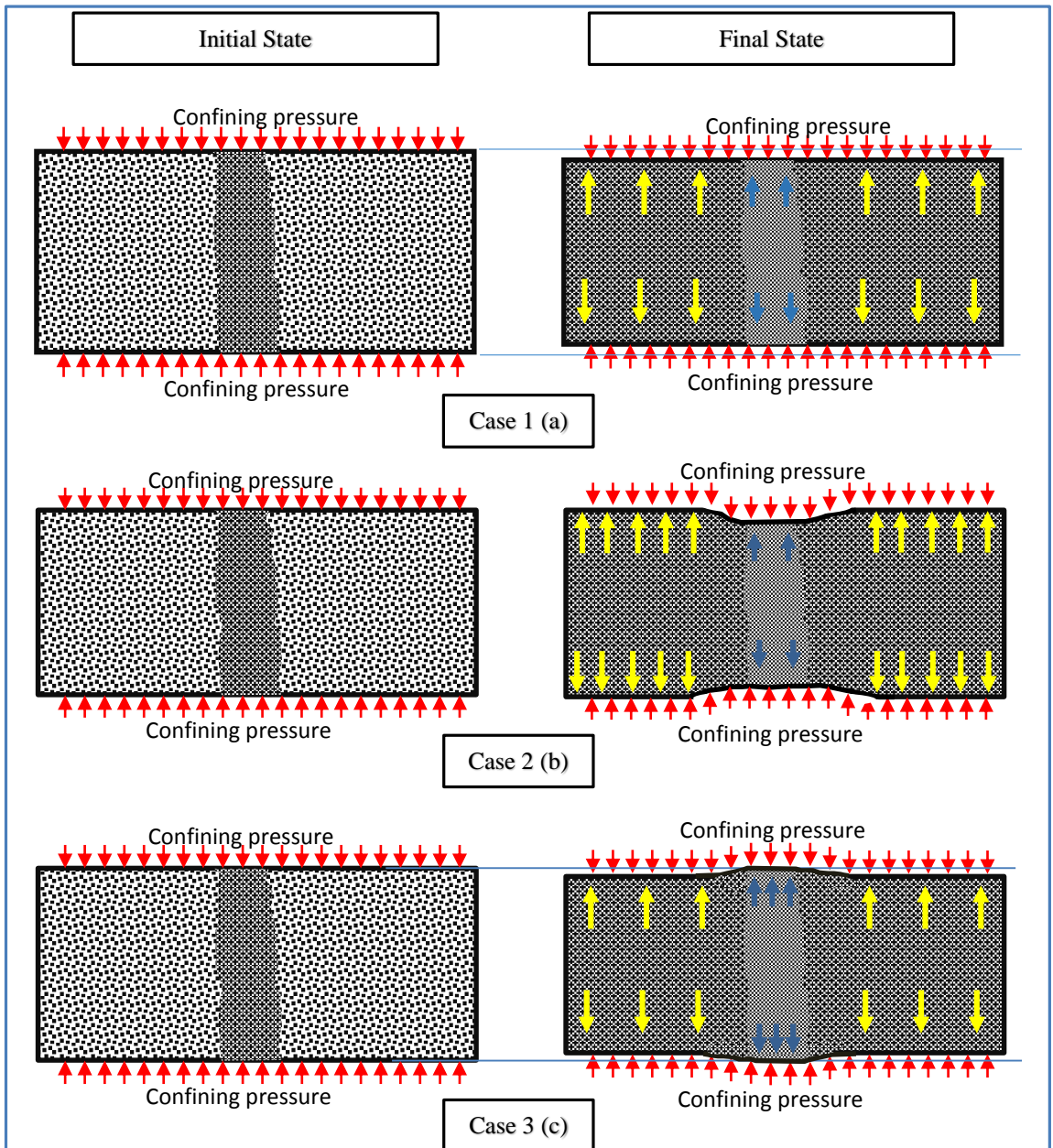
#### 4.7.5 Conceptualization model for permeability reduction

On the basis of the above discussion a conceptual model of the physical arrangement is presented. The decrease in permeability in initial step with high magnitude can be explained by the reduction in overall volume due to fracture closure or pore structure. Initially when confining pressure is applied to the sample, the host and fault both compressed simultaneously but it is clear from the SEM images (Chapter – 3) that the fault region is highly damaged and compacted in comparison to host rock, so the compaction of fault region results in decrease in permeability. At higher confining pressure the host sandstone not compress as much as at lower stresses so stress is concentrated on the fault rock resulting in increased permeability reduction. The most of the stress is now bearing by the host pore structure which is rigid and have high strength than the fault so the decreasing rate in permeability is not as much as high as in initial step. In **Figure 4-35** the hypothetical model is presented to explain this phenomena. According to above discussion three possible cases can be present in hypothetical model:

Case1: when fault and host are compressing equally (**Figure 4-35-a**)

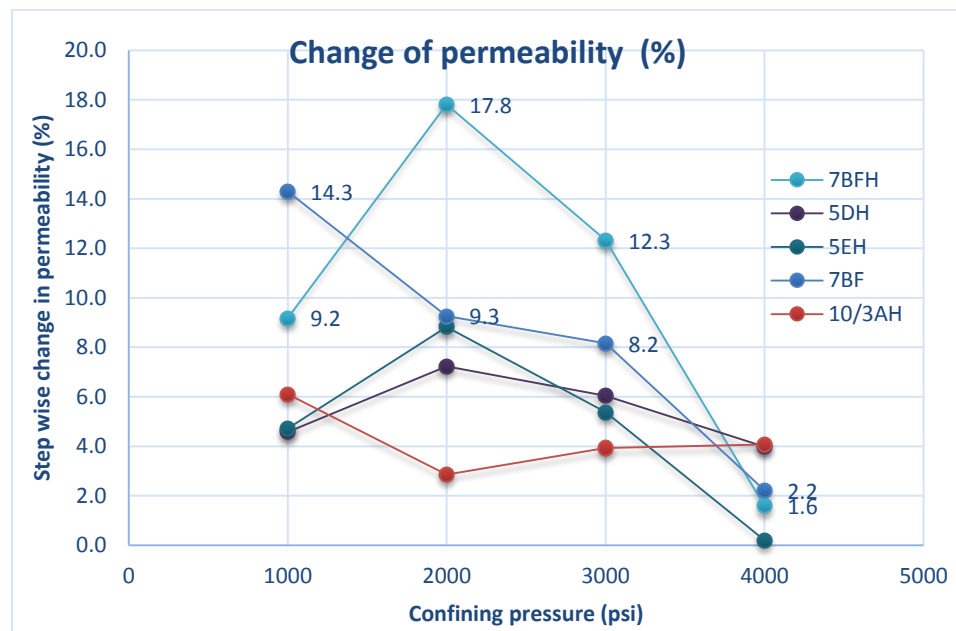
Case 2: host has high strength and bearing most of the load (**Figure 4-35-b**)

Case 3: fault is rigid and host is ductile (**Figure 4-35-c**)



**Figure 4-35: Conceptualisation models for the change in grain compaction due to increase in confining pressure.**

Initially the applied confining pressure is compressing both fault and host but after some certain compression the host is resisting for further compression and internal stress is developed (represented by yellow arrows **Figure 4-35**) which is greater than or equal to the confining pressure and supporting fault region to avoid further compression. In contrast, the host samples of 7BF is showing comparatively low stepwise change in permeability as well overall change, which is almost half of the fault sample i.e. 36.5%. The another interesting trend is found in this and some other samples that the change in permeability (i.e. decreasing trend) is slightly increase with increase in confining pressure and then then decrease .



**Figure 4-36: Step wise change in permeability in percentage by increasing confining pressure.**

In case of host sample 7BF the reduction in permeability in first stage when confining pressure is increased from 1000 to 2000 psi is 9.2% but further increase in confining pressure to 3000 psi is not showing the decrease.

## 4.7.6 Mathematical modelling of permeability decay

In this section we intend to provide a mathematical model which explain the dynamics of the stress related permeability in case if gas is used. Further in this section, the interpretation of the results from the developed model and comparison with experimental results is also discussed. Based on experimental observations about the gas permeability through various fault and host samples we propose the following mathematical models can serve to explain the dynamics of the relationship between the confining pressure (measure in psi), fault and host permeability (measured in mD). The following notation will be used:

$P_c$  : = confining pressure, (psi)

$K_f$  : = fault gas permeability, (mD)

On the basis of the results presented earlier and after fitting of different models, it is found that two main models can be used to develop the decay rate of permeability, which are:

- a. Exponential decay
- b. Decay following power law

### 4.7.6.1 Exponential decay

The fault permeability is modelled on the basis of the experimental results presented earlier and suggested that the relationship between the confining pressure and fault permeability satisfies the exponential law, which can be presented as:

$$K_f = C e^{-rP_c} \quad \text{Eq. (4-30)}$$

where  $C$  denotes the arbitrary constant, which can be computed by the application of initial condition and " $r$ " is the average rate of change (decay) in fault permeability when the confining pressure is changing in fault sample. It is suggested that exponential law presented in equation (4-30) can be derived by assuming the following relationship between the permeability and confining pressure. Following equation (4-31) is stating that the rate of change of fault permeability with respect to the confining pressure is directly proportional to the negative of the initial value of the permeability i.e.

$$\frac{dK_f}{dP_c} \propto -K_f \quad \text{Eq. (4-31)}$$

$$\frac{dK_f}{dP_c} = -rK_f \quad \text{Eq. (4-32)}$$

Equation (4-32) is a first order differential equation of initial value problem type and " $r$ " is the constant of proportionality which serves as a model for a decay or growth model (Zill, 2009). The equation (4-32) is the simple standard population model and this differential equation can be solved by application of the variable separable method. The detail of solution is presented in **Appendix – 1** and here only the final results are presented. After solving equation (4-32) following exponential equation has been achieved which is relating permeability of fault with confining pressure.

After solving equation (4-32), the equation for rate of decay  $r$  is also developed on the basis of the sample permeability and confining pressure. The first equation developed for measuring the permeability at known initial is presented as equation (4-35).

$$\frac{K_{final}}{K_{initial}} = e^{-r(P_{final} - P_{initial})} \quad \text{Eq. (4-33)}$$

$$K_{final} = K_{initial} \times e^{-r(P_{final} - P_{initial})} \quad \text{Eq. (4-34)}$$

On further solving equation (4-34) the permeability rate of decay equation is obtained:

$$r = \frac{\ln\left(\frac{K_{final}}{K_{initial}}\right)}{(P_{initial} - P_{final})} \quad \text{Eq. (4-35)}$$

Equation (4-34) indicates that the permeability is decaying exponentially. The rate of decreasing permeability can be calculating by using equation (4.35), which required two sets of confining pressure and corresponding permeabilities. The rate of permeability decay is calculated between confining pressures of 1000 to 5000 psi. The results obtained are presented in **Table 4-12** for decay of permeability.

#### 4.7.6.2 Power law modelling for the fault samples

The second approach of the model is by using a Cauchy-Euler first order differential equation which is commonly used for modelling the data, which follows a power law decay as it is found in faults and host samples permeability. The following mathematical model is used same notations as defined previously to explain the dynamics of the permeability decay.

$$K_f = C \cdot [P_c]^{-r} \quad \text{Eq. (4-36)}$$

In equation (4-36),  $C$  is an arbitrary constant and its value depends on the initial condition of the experiments. In general the relation can be presented as:

$$P_c \frac{dK_f}{dP_c} = -rK_f \quad \text{Eq. (4-37)}$$



$$K_f(a) = b \quad \text{Eq. (4-38)}$$

where  $r$  is the average rate of change (decay) in fault or host permeability when the confining pressure is changing (increasing) in fault/host sample,  $b$  is the initial permeability (in mD) at the beginning of experiments at confining pressure of  $a$  psi. Equation 4-37 is then solved by the variable separable method (refer Appendix – 1 for detail of solution). The following power law equation is obtained by solving equation (4-37).

So by applying initial condition and solving the equation for the two sets of confining pressures and permeabilities the following equation is obtained:

$$\frac{K_{final}}{K_{initial}} = \left( \frac{P_{initial}}{P_{final}} \right)^r \quad \text{Eq. (4-39)}$$

$$K_{final} = K_{initial} \times \left( \frac{P_{initial}}{P_{final}} \right)^r \quad \text{Eq. (4-40)}$$

Further equation (4-39) is solved to obtain the equation for the decay rate  $r$  and presented below:

$$r = \frac{\ln \left( \frac{K_{final}}{K_{initial}} \right)}{\ln \left( \frac{P_{initial}}{P_{final}} \right)} \quad \text{Eq. (4-41)}$$

#### 4.7.7 Results for permeability decay

Two sets of the data of fault samples are used to calculate the decay rate of the gas permeability. The minimum confining pressure used is 1000 psi as initial and the highest pressure 5000 psi is used as final confining pressure. The experimental values of the permeability are used for the corresponding pressures. The results are presented

in **Table 4-12** for decay rates calculate by both exponential and power law decay equations.

Sample ID (Fault)	Fault Permeability		Confining Pressure		Average decay rate	
	Initial (mD)	Final (mD)	Initial (psi)	Final (psi)	Exponential Law	Power Law
3AF1	0.018	0.011	1000	5000	0.00013	0.32
3AF2	0.0051	0.0031	1000	5000	0.00012	0.31
10/3AF1	0.01	0.0067	1000	5000	0.00018	0.44
10/3BF1	0.28	0.24	1000	5000	0.00004	0.10
7AF1	1.96	1.91	1000	5000	0.000006	0.01
7BF1	0.0009	0.0006	1000	5000	0.00009	0.22
7BF2	0.0046	0.0012	1000	5000	0.00034	0.86
7CF1	0.0018	0.0009	1000	5000	0.00016	0.40
7CF2	0.029	0.021	1000	5000	0.000082	0.20
7DF1	0.0032	0.0020	1000	5000	0.00012	0.30
7EF1	0.025	0.0107	1000	5000	0.00022	0.54
7FF1	0.0064	0.0031	1000	5000	0.00018	0.45
5AF1	0.032	0.022	1000	5000	0.00009	0.22
5AF2	0.0029	0.0013	1000	5000	0.0002	0.51
5BF1	0.0065	0.0044	1000	5000	0.0001	0.24
5DF1	1.81	1.59	1000	5000	0.00003	0.08
5EF1	0.23	0.13	1000	5000	0.00014	0.34
5EF2	1.46	1.36	1000	5000	0.00002	0.04
5FF1	0.34	0.25	1000	5000	0.00008	0.20

**Table 4-12: Results of permeability decay rate by exponential and power law for fault rock samples.**

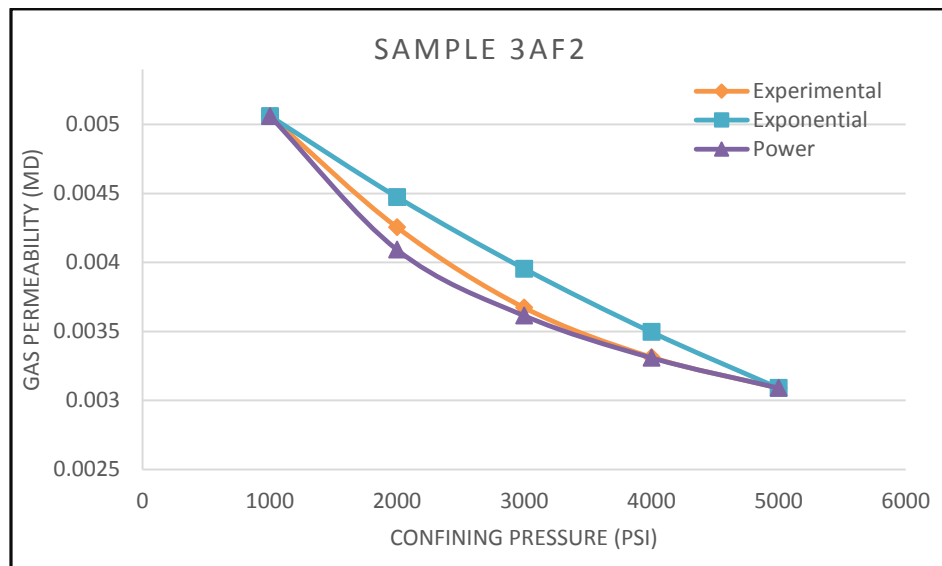
Similarly the decay rate is also calculate for the host sample and presented in **Table 4-13**.

Sample ID (Host)	Fault Permeability		Confining Pressure		Average decay rate	
	Initial (mD)	Final (mD)	Initial (psi)	Final (psi)	Exponential Law	Power Law
3AH1	17.8	14.6	1000	5000	0.00005	0.13
10/3HF1	2.9	1.9	1000	5000	0.0001	0.26
10/3BH1	101	85	1000	5000	0.00004	0.11
7AH1	15	13.7	1000	5000	0.00002	0.06
7BH1	9.5	6.1	1000	5000	0.00011	0.27
7CH1	2.5	1.7	1000	5000	0.00010	0.25
7EH1	1.8	1.4	1000	5000	0.00007	0.17
5AH1	2.9	2.4	1000	5000	0.00005	0.13
5BH1	0.5	0.41	1000	5000	0.000052	0.13
5DH1	83.3	66.5	1000	5000	0.00006	0.14
5EH1	23.1	19	1000	5000	0.00005	0.12
5FH1	34.3	31.8	1000	5000	0.00002	0.05

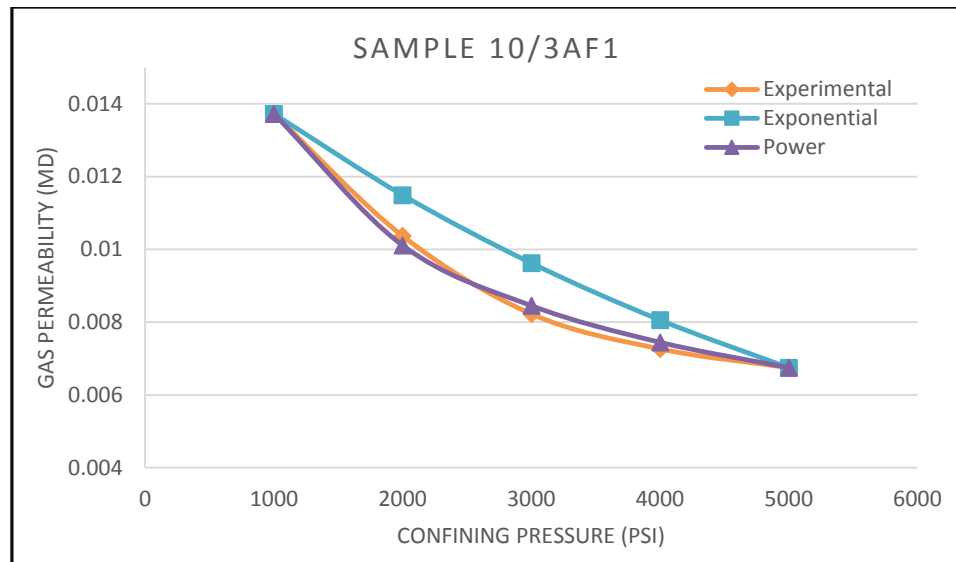
**Table 4-13: Results of permeability decay rate by exponential and power law for host samples.**

These models are then used to predict the values of permeabilities between the initial and final values of permeabilities at different intervals of the pressure. These models can be very useful in the sense that if the permeability of fault/host samples is measured at two confining pressures (for example at 1000 and 5000 psi) then the other permeabilities values can be predict at different pressure intervals by using the decay rate and permeabilities.

These equation are used to calculate fault and host permeabilities at three other pressure steps (i.e. 2000, 3000 and 4000 psi). These calculated values are then compared with the experimental values and found to be very good estimates as the residual errors are found to be very low. The results of Samples 3AF2 and 10/AF2 are showing that in both samples exponential law is giving higher residual than the power law model.



**Figure 4-37: Comparison of experimental permeability with extrapolated permeabilities by power and exponential correlations (Sample 3AF2).**



**Figure 4-38: Comparison of experimental permeability with extrapolated permeabilities by power and exponential correlations (Sample 10/3AF1).**

Knowledge of stress dependency of reservoir fault rocks and their proper integration in reservoir simulation modelling may be helpful in the realistic future production forecast and better understanding of the operating parameter for example drawdown pressure.

## 4.8 Conclusion:

Klinkenberg corrected gas permeability of fault rock samples have been measured at different confining pressures and its sensitivity is investigated. It is found that the gas permeabilities of almost all samples are stress sensitive. The stress sensitivity is found to be higher at low confining pressure and gradually decreasing as confining pressure increase. Overall, gas permeability measured at ambient stress is around 5 fold lower than the permeability measured at in-situ stress. This behaviour can be explained by the presence of microfractures, which are open at low confining pressure so act as

conduits for flow increasing permeability. This model is consistent with BSEM observation, which confirms the presence of microfractures in all fault rock samples analysed. These fractures close under higher confining pressure reducing permeability and making the permeability less stress dependent. A mathematical model is presented, which can be used to fit the permeability in two ways i.e. exponential decay and power law decay. These models allow permeabilities at other confining stresses to be estimated.

The permeability vs clay content of samples shows large amounts of scatter, which would lead to considerable uncertainty when applied to a fault seal analysis. The clay vs permeability data do fit to the model presented by Sperrevik et al. (2002), which is used throughout industry for fault seal analysis. There is, however, considerable scatter around the model of Sperrevik et al. (2002). In addition, the model of Sperrivk et al. (2002) contradicts theoretical mixing models for clay and sand in that it implies that permeability continues to decrease with increasing clay content whereas mixing models predict a minimum permeability at a clay content equivalent to the porosity of a clay-free sample. This later value decreases with decreasing grain-sorting, which can be caused by increased cataclastic deformation. Further work is required to understand how this mixing model could be applied in a more practical sense to fault seal analysis.

# Chapter 5: Stress dependent brine permeability

## 5.1 Introduction:

It is well known that the permeability of the porous rock measured using water or brine is often lower than the Klinkenberg corrected permeability, despite the latter often being assumed to be equivalent to liquid permeability (Muskat, 1937; Klinkenberg, 1941; Heid et al., 1950; Jones and Owens, 1980; Wei et al., 1986). Indeed, it has even been shown that liquid permeability is very sensitive to the salinity of the brine used during the measurement (Dawe and Lever, 1986). It is possible that the difference between gas and brine permeability, as well as the dependence of brine permeability on salinity is caused by processes such as clay swelling or movement of fine-grained particles, which may block pore throats (Sharma and Yortsos, 1987; Faulkner and Rutter, 2000; Bear, 1972; Wei et al., 1986; Dawe and Lever, 1986; Muecke, 1979).

The dependence of permeability on salinity is an important issue for those studying fault seal analysis because many of the published fault rock permeability measurements as well as those on internal databases owned by the petroleum industry were conducted using distilled water (e.g. Fisher and Knipe, 1998, 2001). This means that the values commonly used to calculate fault transmissibility multipliers may be different to the in situ permeability where brines with a different salinity are present. The aim of the current chapter is to assess the impact of conducting permeability measurements using inappropriate brine salinities which could have an impact on the results and hence on fault seal analysis in general.

The chapter is divided into the following five subsections:

- A review of the measurement of liquid permeability measurement is presented in **Section 5.2**
- Experimental methodologies are described in **Section 5.3**
- Results are presented in **Section 5.4**.
- Discussion and conclusions are presented in **Section 5.5** and **Section 5.6** respectively.

## 5.2 Liquid permeability

Different models are used for predicting the rate of fluid flow through porous media. Each model has its own limitations and the specific assumptions on which the models were developed have already been discussed in **Chapter 4**. The application of Darcy's law for gas permeability measurements has also been discussed in **Chapter 4**. In this section, techniques of measuring liquid permeability are discussed. The liquid permeability measurements in the current study have been conducted using steady-state and transient techniques.

Transient permeability measurements have been conducted on samples with a permeability of <0.1 mD. This technique was developed by Brace et al. (1968) and the mathematical model used to calculate permeability assumes that the compressive storage of the sample is negligible, which is invalid for samples with high porosity. The model used by Brace et al. (1968) has therefore been modified in a number of later studies including Lin (1977), Yamada and Jones (1980), Hsieh et al. (1981 a, b); Dicker and Smits, (1988). Amaefule et al. (1986) presented a simplified model by using Darcy's law and one dimensional diffusion equation.

$$\frac{\partial^2 p}{\partial x^2} = \frac{\mu\phi(\beta_s + \beta)}{k} \frac{\partial p}{\partial t} \quad \text{Eq. (5-1)}$$



where  $\beta$  is the fluid compressibility,  $\beta_s$  is the porous media (rock) compressibility,  $\mu$  is the viscosity of the liquid which is assumed to be independent of position  $x$ ,  $k$  is the permeability and  $\phi$  is the porosity of the porous media (rock).

Amaefule et al. (1986) applied Fourier series analysis and initial boundary conditions to provide a simplified solution of equation (5.1) to calculate from the pressure decay curve, namely:

$$k = \left( \frac{\phi \mu \beta}{\alpha^2} \right) m \quad \text{Eq. (5-2)}$$

where  $k$  is permeability in Darcy,  $\beta$  is the fluid compressibility in 1/atm,  $\mu$  is the viscosity in cp,  $\phi$  is porosity in fractions,  $m$  is the slope of logarithmic pressure decay curve versus time and  $\alpha$  is the root of the transcendental equation:

$$\Delta P_{x=L} = 2h\Delta P_1 \sum_{n=1}^{\infty} \frac{\exp(-\sigma \alpha_n^2 t)}{[L(\alpha_n^2 + h^2) + h]} \quad \text{Eq. (5-3)}$$

where

$$\sigma = \frac{k}{\phi \mu \beta}; \text{ and } h = \frac{A\phi}{V_1}$$

and  $\alpha_n$  are roots of the transcendental equation, which are:

$$\alpha L \tan(\alpha L) = \alpha_n \tan(\alpha_n) = hL = \frac{V_p}{V_1}$$

and calculated numerically by iteration. The details of measurement is presented in methodology **Section 5.3**.

The steady-state technique is used for those samples which are found to have higher permeability ( $> 0.1$  mD). The steady-state technique is a very straight forward application of Darcy's law in which a constant flow rate of liquid is applied across the

sample and the pressure drop is measured at steady-state, which is then used to calculate the liquid permeability of the samples.

## 5.3 Methods

The stress dependency of the brine permeability of the sample fault rock samples discussed in **Chapter 3** and **Chapter 4** has been measured. The liquid permeability of core plugs was measured using 30% brine solution but the permeability of cube samples embedded in dental putty/epoxy resin was also measured using deionized water. All samples were cored/cut, cleaned and measurements of size (i.e. diameter and length), porosity, gas permeability were made. Mercury injection capillary pressure (MICP) and mineralogy (using QXRD) were conducted and have already been presented in **Chapter 3** and **Chapter 4**. For brine permeability measurements, 30% NaCl solution has been made by dissolving 300g of pure NaCl salt in 1000 mL of deionized water. The solution was then filtered through a 0.1  $\mu\text{m}$  filter to remove any fines that may have entered the solution. Dried and cleaned samples were then saturated in brine by firstly placing them in a vacuum chamber for almost 12 hours to remove air and then brine was allowed to saturate at atmospheric pressure for 24 hours prior to permeability measurement.

### 5.3.1 Unsteady-state liquid permeability measurements

The setup used for unsteady-state liquid permeability at Wolfson laboratories is shown in **Figure 5-1**. The system consists of a Hassler core holder, upstream and downstream fluid reservoirs, differential pressure transducer, data acquisition unit, liquid pump and confining pressure pump. The samples are placed in a flexible rubber sleeve placed in the core holder before application of a confining pressure, which both

prevents fluid flowing around the sample and allows the core plugs to be placed under stresses equivalent to in situ conditions. The core holder is connected with the confining pressure pump in which oil is used as the working fluid to transmit the pressure to the rubber sleeve.

The confining pressure pump has a maximum limit of 10000 psi but in this study a range of pressure from 1000 psi to 5000 psi was used. In the case of the core plugs, this confining pressure is transferred to the sample but the high compressibility of the dental putty means that this confining pressure is not transferred to the sample “cubes”. The end platens of the core holder are tightened up to the required limit before the confining pressure is applied. The end plugs also have radial and circular grooves for the easy flow of liquid with evenly distribution (**Figure 5-2**).

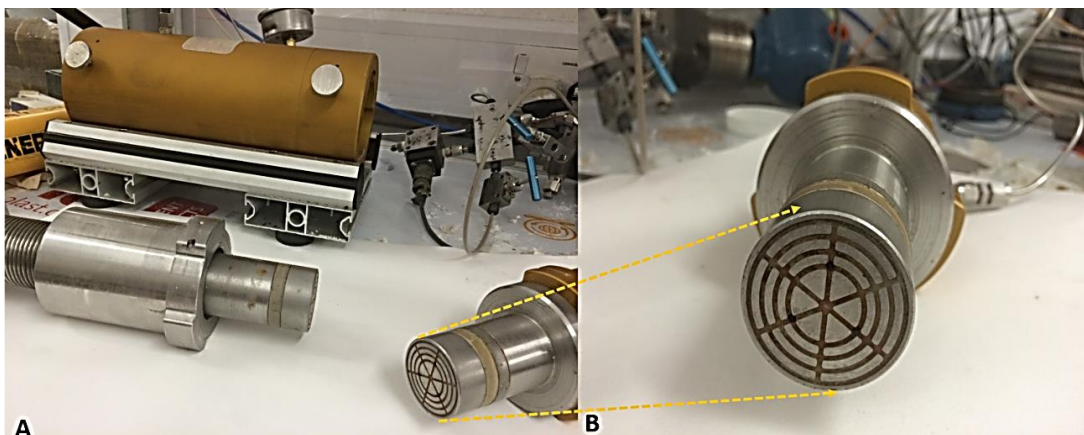
The main steps for measuring the brine permeability using the unsteady-state technique are as follows:

- i) The upstream reservoir is firstly filled with 30% brine and all trapped air is removed by opening the outlet valves.
- ii) The outlet valves are closed and the system is then pressurized to 200 psi and the pressure is monitored for 30 minutes to check for leakage. Remedial action is taken if leaks are identified such as tightening the joints and valves.
- iii) The pressure is released after testing and the sample is placed in the core holder. Brine is pumped into the system and confining pressure is applied to the core holder.

- iv) The flow pump is then used to increase the brine pressure to 125 psi. The upstream inlet and bypass valves are closed once the system has equilibrated.
- v) The pressure in the upstream reservoir is then increased to 200 psi.

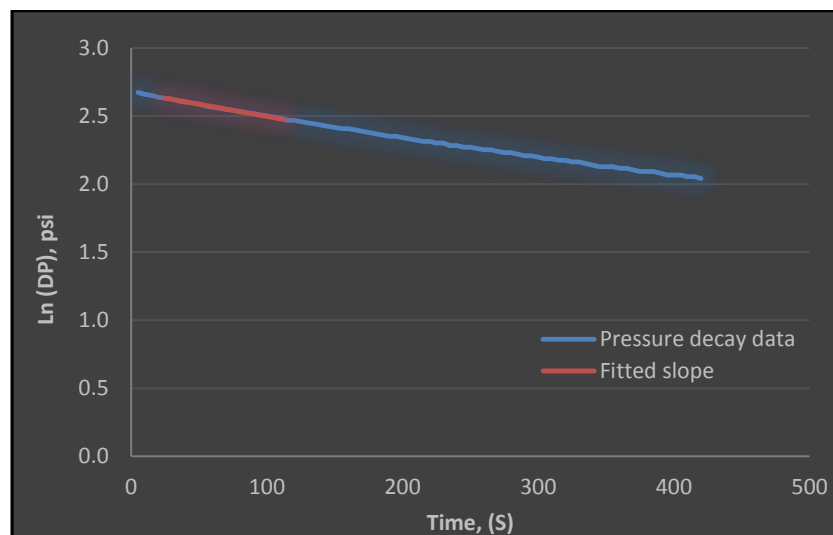


**Figure 5-1: Pulse decay brine permeability measurement setup at Wolfson laboratories, University of Leeds.**



**Figure 5-2: A) Hassler core holder with both end plugs, left one is threaded. B) End plug having circular and radial grooves for evenly flow at the face of sample.**

- vi) The data acquisition is started before opening the valve between upstream reservoir and the core holder to create a pressure differential between upstream and downstream volumes. The pressure decay, which is slow for very tight samples (**Figure 5-3**), is then used to calculate the permeability using an Excel macro. The macro automatically fits a line to the logarithmic pressure decay versus time data for the early region and determines the slope,  $m$ , which is then incorporated into equation 5-2.
- vii) The confining pressure can then be increased so that measurements at higher stresses can be obtained.

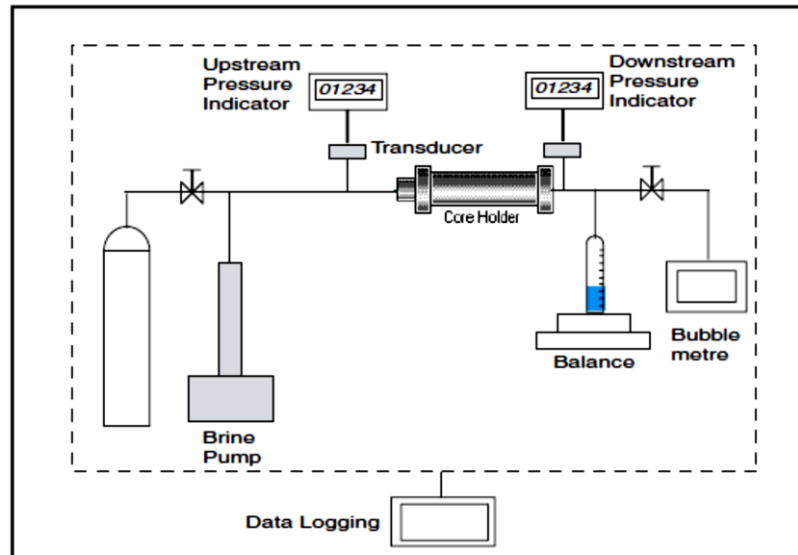


**Figure 5-3: Pressure decay curve for estimation of permeability in the pulse decay technique**

### **5.3.2 Steady-state liquid permeability measurements**

The setup for the liquid (brine) permeability is similar to that shown in **Figure 5-1** and a schematic for the steady-state permeability measurement is presented in **Figure 5-4**. The main difference is that the steady-state method requires a continuous

flow of brine until steady-state is reached while steady state is not reached in the pulse-decay measurement and the permeability is calculated from the transient data.



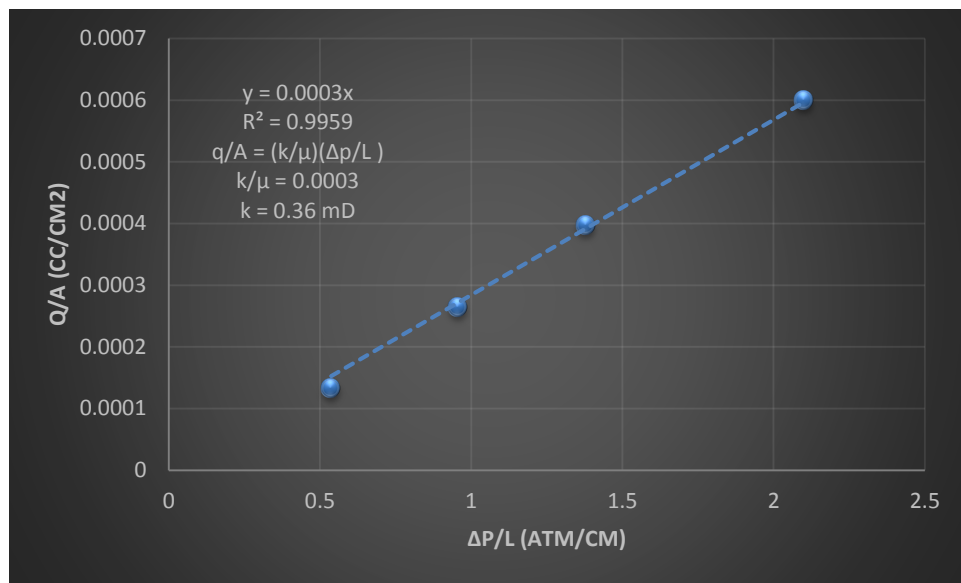
**Figure 5-4: Schematic of the liquid steady-state permeability measurement setup.**

The main steps for measuring the brine permeability by the steady-state method are:

- The brine pump (GDS make) is filled with brine, ensuring that no air is trapped in the system.
- The sample is placed in the core holder and initial confining pressure is applied using a hydraulic pump.
- Brine is then injected into the rock at a specified flow rate until the upstream and downstream pressures are constant (i.e. steady-state has been achieved).
- The experiment is repeated at two different flow rates.
- The permeability can be calculated by Darcy's law.

- The average permeability is obtained from the slope of the line plotted  $q/A$  vs  $\Delta P/L$  using Darcy's law.

High flow rates create inertial forces, which violate the laminar condition for Darcy's law. These inertial effects can be identified as deviations from a straight line on plots of  $q/A$  vs  $\Delta P/L$ . In such cases, flow rate are decreased to achieve the laminar condition.



**Figure 5-5:** Plot between  $q/A$  and  $\Delta P/L$ , the slope is equal to  $k/\mu$ , used to calculate the permeability.

## 5.4 Results

The fault rock samples frequently contained large proportions of host sandstone so the permeability of the fault rock was deconvolved using the same method as presented in Chapter 4. The stress dependent (deconvolved) brine (30%) permeability results from cataclastic and phyllosilicate framework fault (PFFR) from the reservoir samples as well as their associated host sandstones are presented in **Table 5-1** and **Table 5-2**. The results of brine permeability of Orange and other outcrop

samples are given in **Table 5-3**. The Orange samples contained only the fault material so deconvolution of permeability was not required while the other fault rock samples obtained from outcrop also contained host sandstone so their permeabilities required deconvolving. The gas, brine (30%) and distilled water permeability results of cube samples are presented in **Table 5-4**.

<b>Deconvolved Brine Permeability (mD) (Cataclastic Samples)</b>										
<b>Sample ID</b>	<b>Confining Pressure (psi)</b>									
	<b>Fault Sample</b>					<b>Host Sample</b>				
	<b>5000</b>	<b>4000</b>	<b>3000</b>	<b>2000</b>	<b>1000</b>	<b>5000</b>	<b>4000</b>	<b>3000</b>	<b>2000</b>	<b>1000</b>
<b>3A1</b>	0.00098	0.00099	0.0011	0.0011	0.0036	7.1	7.2	7.2	7.27	7.4
<b>3A2</b>	0.0022	0.0024	0.0027	0.0032	0.0043	7.1	7.2	7.2	7.3	7.4
<b>7A1</b>	0.27	0.26	0.26	0.26	0.27	4.8	5.1	5.2	5.5	5.7
<b>7B1</b>	3E-4	3.6E-4	4.3E-4	5.2E-4	7.3E-4	1.7	1.8	1.8	1.8	1.9
<b>7B2</b>	9.1E-5	1.2E-4	1.5E-4	2.1E-4	3.5E-4	1.7	1.8	1.8	1.8	1.9
<b>10/3A</b>	0.0024	0.0025	0.0028	0.003	0.0032	0.85	0.87	0.91	0.96	1.03
<b>10/3B</b>	0.046	0.047	0.048	0.049	0.052	53	56	61	69	84
<b>5D1</b>	0.048	0.053	0.068	0.088	0.16	59	59	61	62	64
<b>5E1</b>	0.017	0.017	0.018	0.019	0.020	9.4	10	10	11	13
<b>5E2</b>	0.53	0.53	0.54	0.55	0.57	15.7	16	17	17	18
<b>5F1</b>	0.68	0.69	0.70	0.71	0.72	14.1	15.2	15.8	16.2	17.4

**Table 5-1: Deconvolved brine (30%) permeability of cataclastic fault samples.**



The brine permeability of samples as function of confining pressure is presented in **Figure 5-6, Figure 5-7 and Figure 5-8**. The stress vs permeability data were fitted to either power law or exponential models.

<b>Deconvolved Brine Permeability (mD)</b>										
<b>(PFFR Samples)</b>										
<b>Sample ID</b>	<b>Confining Pressure (psi)</b>									
	<b>Fault Sample</b>					<b>Host Sample</b>				
	<b>5000</b>	<b>4000</b>	<b>3000</b>	<b>2000</b>	<b>1000</b>	<b>5000</b>	<b>4000</b>	<b>3000</b>	<b>2000</b>	<b>1000</b>
<b>5A1</b>	0.0039	0.0040	0.0041	0.0044	0.0049	0.36	0.37	0.37	0.37	0.37
<b>5A2</b>	0.00027	0.00030	0.00033	0.00039	0.0005	0.36	0.37	0.37	0.37	0.37
<b>5B1</b>	0.00030	0.00037	0.00048	0.00055	0.0009	0.10	0.10	0.11	0.11	0.12
<b>7C1</b>	7.3E-5	7.9E-5	8.6E-5	1.0E-4	1.3E-4	0.26	0.26	0.27	0.27	0.28
<b>7C2</b>	0.003	0.003	0.0033	0.0035	0.0038	0.26	0.26	0.27	0.27	0.28
<b>7D1</b>	0.00034	0.00037	0.0004	0.00046	0.0006	0.03	---	---	---	---
<b>7E1</b>	0.00079	0.0009	0.0010	0.0013	0.0019	0.49	0.5	0.5	0.51	0.52
<b>7F1</b>	0.00032	0.00034	0.00035	0.00038	0.00041	0.93	---	---	---	---

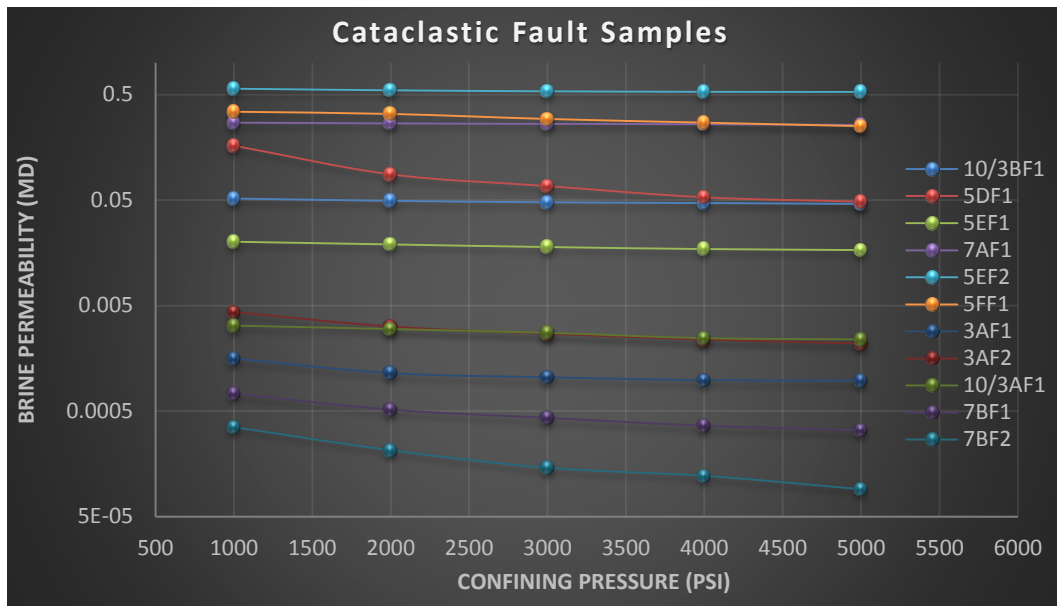
**Table 5-2: Deconvolved brine (30%) permeability of PFFR fault samples.**

<b>Brine Permeability (mD)</b>					
<b>(Outcrop Samples)</b>					
<b>Sample ID</b>	<b>Confining Pressure (psi)</b>				
	<b>1000</b>	<b>2000</b>	<b>3000</b>	<b>4000</b>	<b>5000</b>
<b>ORG1</b>	95	79	69	63	59
<b>ORG2</b>	48	40	36	32	31
<b>ORG3</b>	306	283	274	251	249
<b>ORG4</b>	138	111	100	95	88
<b>ORG5</b>	9	8	7.7	7.5	7.3
<b>ORG6</b>	0.64	0.62	0.61	0.60	0.59
<b>ORG7</b>	472	343	275	229	210
<b>ORG8</b>	109	93	81	75	71
<b>ORGA1</b>	7.6	7.5	7.3	7.2	7.2
<b>ORGA2</b>	0.59	0.58	0.57	0.56	0.56
<b>ORGA3</b>	293	243	215	199	188
<b>HP1</b>	0.00044	0.00035	0.00026	0.00021	0.00019
<b>HP2</b>	0.0011	0.00083	0.00069	0.00058	0.00019
<b>Miri-1</b>	0.33	0.17	0.12	0.09	0.07
<b>Miri-2</b>	0.66	0.46	0.37	0.32	0.28

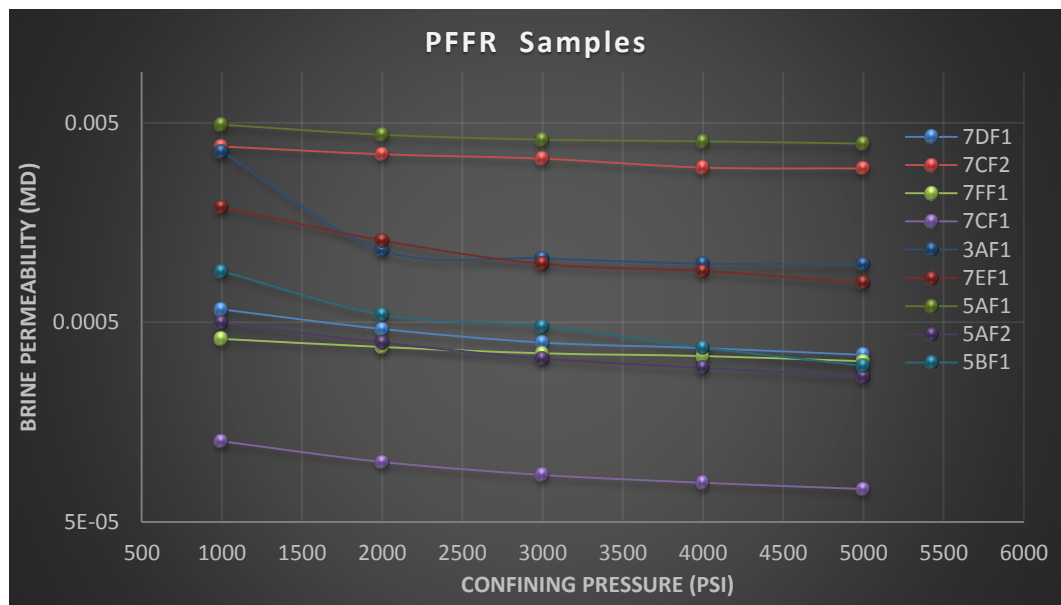
**Table 5-3: Brine (30%) permeability of outcrop fault samples.**

Deconvolved Permeability (mD)								
Sample ID	Fault Type	Fault thickness (cm)	Gas		Brine 30%		DI Water	
			Host	Fault	Host	Fault	Host	Fault
5A	PFFR	0.5	0.62	0.034	0.37	0.002	0.19	0.0015
5B	PFFR	0.8	0.6	0.056	0.19	0.0015	0.04	0.0014
5C	PFFR	0.4	---	1.0	---	0.104	---	0.046
5D	CC	0.3	---	0.25	---	0.030	---	0.018
5E	CC	0.3	29.2	0.2	16.7	0.023	8.3	0.016
5F	CC	0.2	30.2	0.8	17.2	0.09	8.3	0.06
7A	CC	0.5	16.4	0.09	9.2	0.003	4.5	0.0011
7B	CC	0.3	15.9	0.002	5.4	0.0017	2.2	0.0002
7C	PFFR	0.3	3.8	0.067	0.79	0.0015	0.35	0.0003
7D	PFFR	0.6	---	0.0025	---	0.003	---	0.002
7E	PFFR	0.2	2.5	0.07	0.55	0.001	0.25	0.0001
7F	PFFR	0.4	4.8	0.034	0.93	0.002	0.45	0.0015
3A	CC	0.7	21.8	0.018	7.7	0.002	3.70	0.0014
10/3A	CC	0.9	4.4	0.044	1.26	0.001	0.68	0.0012
ORC1	CC	2.4	---	30.1	---	5.1	---	0.4
ORC2	CC	2.5	---	688	---	234	---	92
ORC3	CC	2.5	---	332	---	36	---	5.3

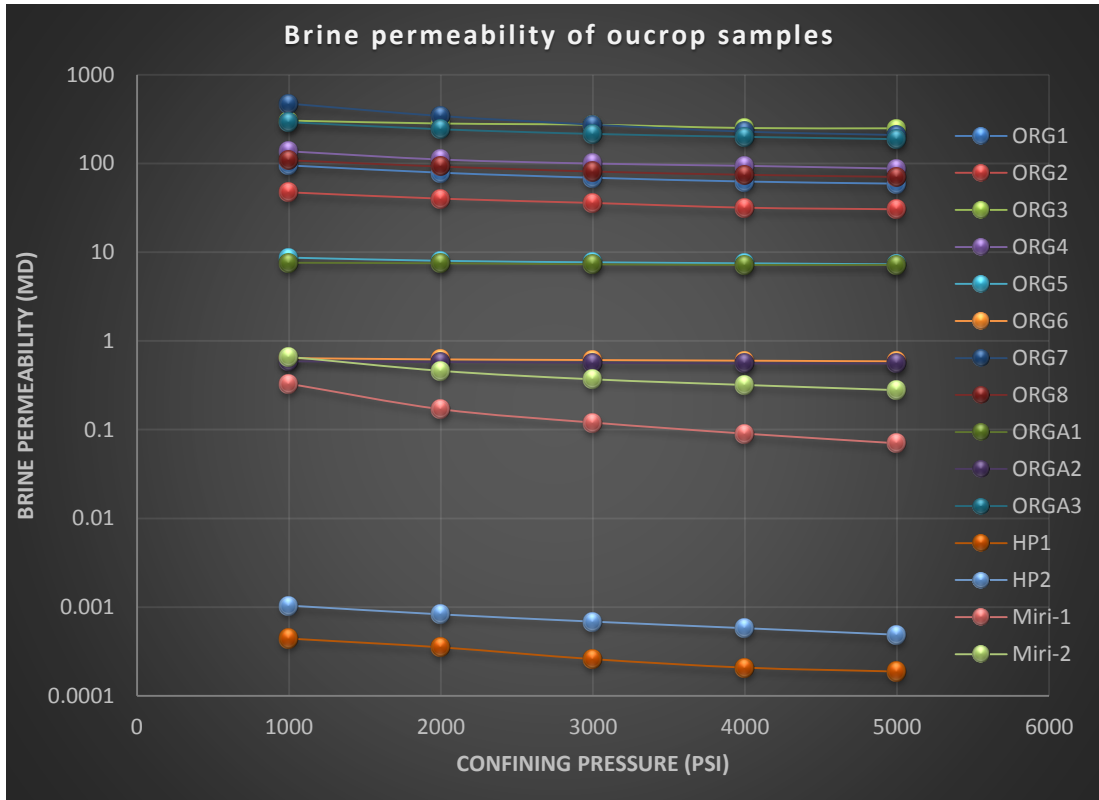
**Table 5-4: Results of deconvolved permeability of the rectangular samples in putty (Cataclastic:CC; Phyllosilicate frame work fault rock: PFFR).**



**Figure 5-6: Plot of brine permeabilities (mD) of cataclastic fault plugs vs confining pressure (psi) on semi-log scale.**



**Figure 5-7: Plot of brine permeabilities (mD) of phyllosilicate framework fault (PFFR) plugs vs confining pressure (psi) on semi-log scale.**



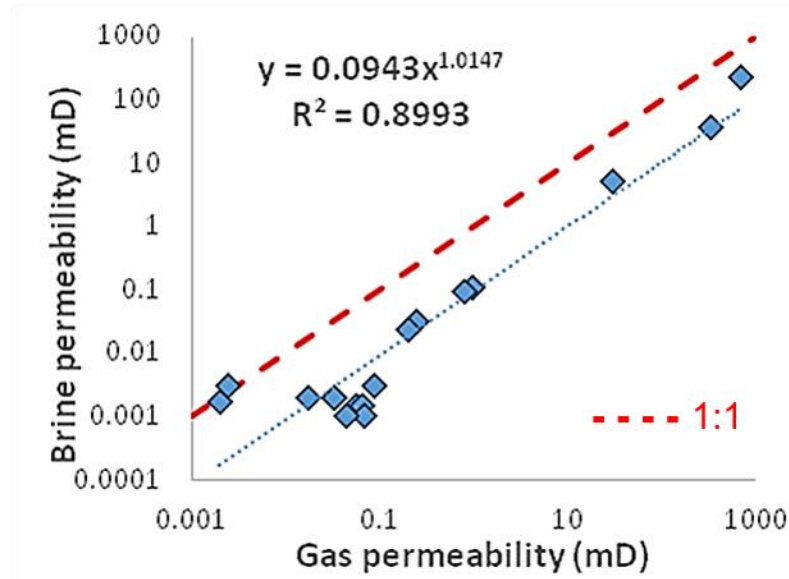
**Figure 5-8: Plot of brine permeability vs confining pressure for the outcrop samples.**

The brine permeabilities of the cataclastic and PFFR samples from the Central Graben reservoir are less than or equal to 0.6 mD, with most being less than 0.001 mD. Overall, the permeability of phyllosilicate-framework fault rocks (PFFR) is lower than the cataclastic faults. The brine permeability of the cataclastic faults ranges between 0.57 mD to 0.00009 mD (arithmetic average = 0.11 mD). The brine permeability of the cataclastic fault rocks is very stress sensitive with permeability decreasing with increase in confining pressure. The lowest brine permeability of 0.00009 mD is found in sample 7BF at 5000 psi confining pressure whose permeability at 1000 psi was 0.00035 mD. The brine permeability of PFFR samples from the Central Graben reservoir varied between 0.0049 mD and 0.00007 mD (with average of 0.0013 mD). The maximum decrease in permeability is found in sample

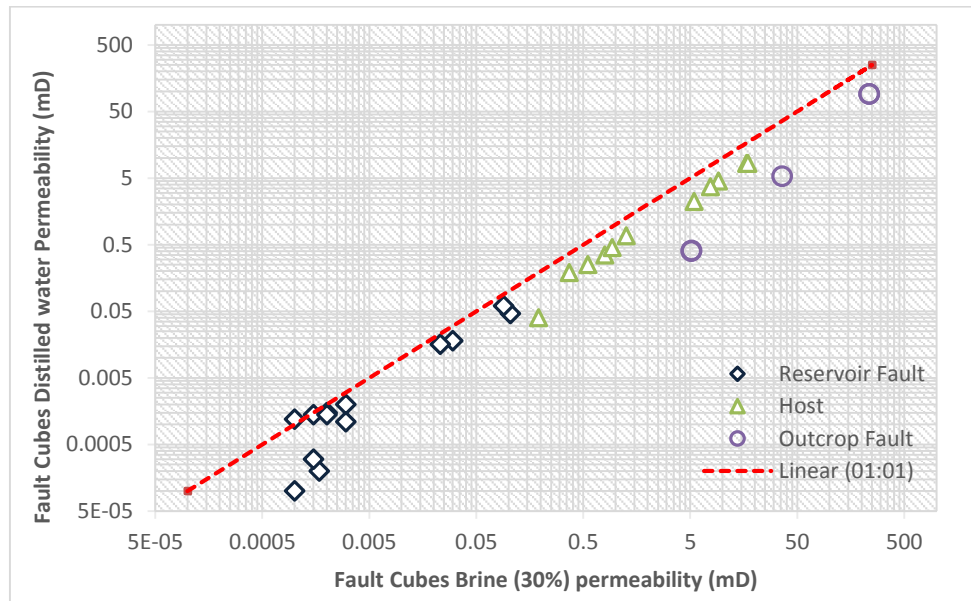
5BF1 whose brine permeability decreased from 0.0009 mD to 0.0003 mD by increasing the confining pressure from 1000 psi to 5000 psi.

The samples from the outcrop in Orange have permeabilities of 0.56 mD to 472 mD (arithmetic average = 102 mD); their permeability do not appear to be as stress sensitive as the samples from the Central Graben reservoir. The maximum decrease in brine permeability is found in sample ORG7 whose brine permeability is decreased from 472 mD to 210 mD by increasing the confining pressure from 1000 psi to 5000 psi. The brine permeability of the Hopeman fault samples range from 0.001 mD to 0.0002 mD (arithmetic average = 0.0005 mD). Miri samples have brine permeabilities from 0.07 mD to 0.66 mD with an arithmetic average of 0.29 mD. The Miri samples show a high stress sensitivity as permeability decreases from 0.3 mD to 0.07 mD, when confining pressure was increased from 1000 psi to 5000 psi. It is noteworthy that they samples were poorly consolidated compared to others analysed.

The brine permeability of the fault rock samples “cubes” appears to be about an order of magnitude lower than the gas permeability (**Figure 5-9**) The distilled water permeability averages around 30% that of the brine permeability (**Figure 5-10**).



**Figure 5-9: Plot of brine permeability vs gas permeability for the fault rock “cubes”.**



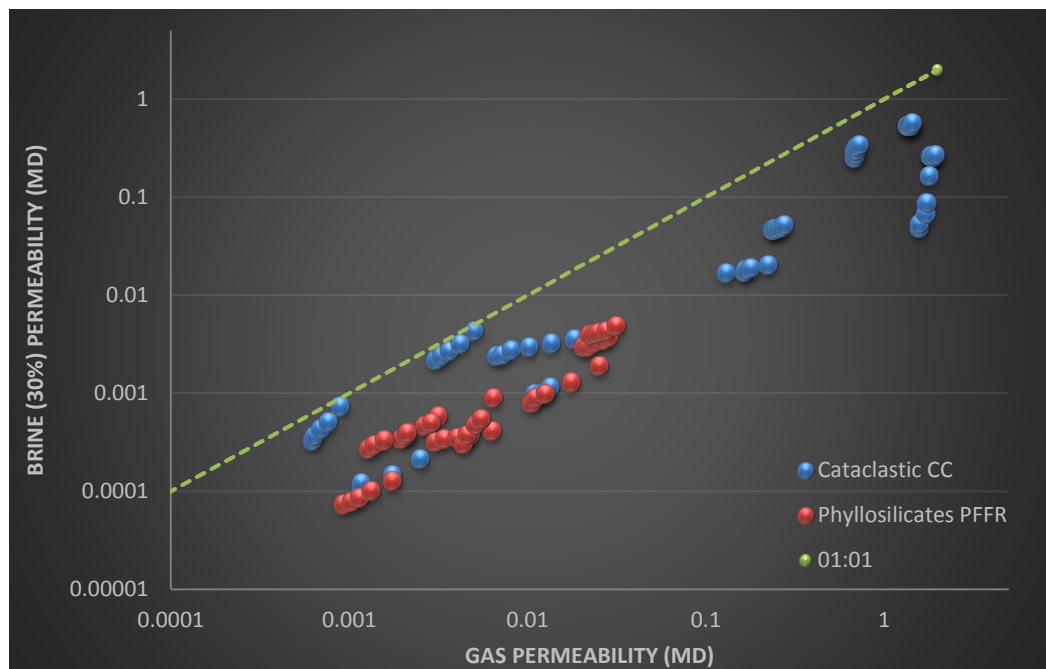
**Figure 5-10: Plot of brine permeability vs distilled water permeability of the fault rock “cubes”. The red line is a 1:1 correlation.**

The possible decrease in permeability with distilled water is due to the interaction of clay particles with the water and causes decrease in permeability. The trend of decreasing permeability is consistent for both reservoir and outcrop fault samples.

## 5.5 Discussion

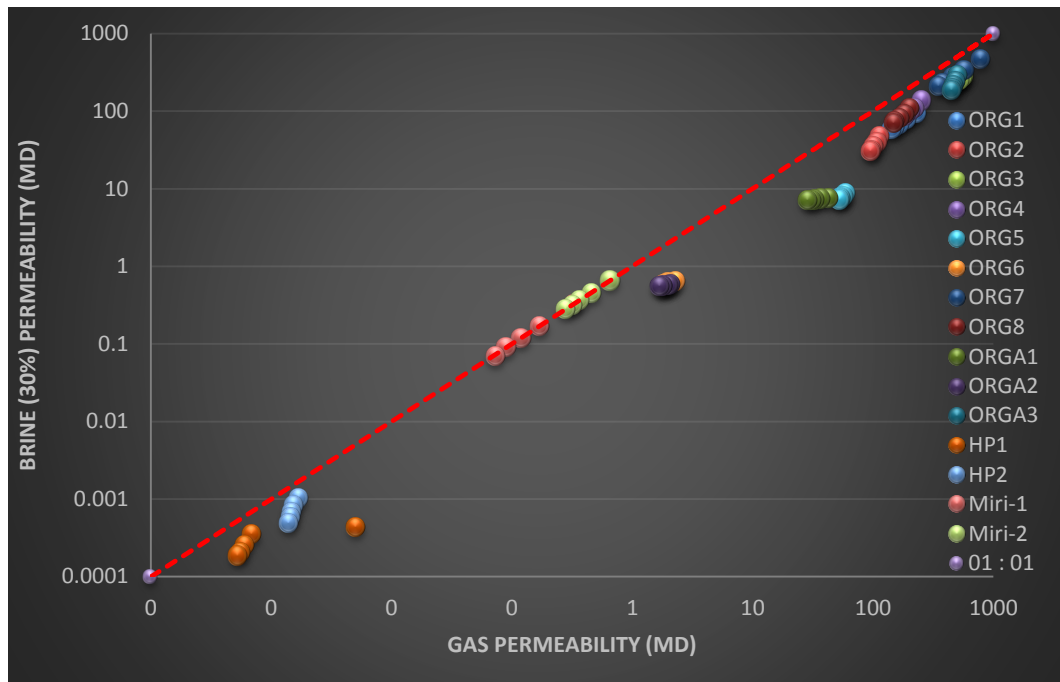
### 5.5.1 Gas vs brine permeability

Brine permeability measurements were conducted on the same samples as the gas permeability measurements discussed in **Chapter 4**. It is found that brine permeability is lower than gas permeability for all studied fault rock samples (**Figure 5-10, Figure 5-11 Figure 5-12**). On average the brine permeability of PFFR samples is by an order of magnitude lower than the gas permeability by an order of magnitude but in cataclastic samples it is reduced by 5 to 8 fold. This difference probably reflects the different extent to which the gas and brine react with the mineral surfaces within the rock. The helium gas used in the experiments is inert and does not react with the mineral surfaces. On the other hand, brine reacts with mineral surfaces reducing flow rates.



**Figure 5-11: Brine (30%) permeability vs gas permeability for cataclastic and PFFR samples**





**Figure 5-12: Brine (30%) permeability vs gas permeability for outcrop samples**

### 5.5.2 Stress dependence of brine permeability

The results show that the brine permeability for all fault rock samples (core plugs and outcrop) decreases with increase of confining stress (**Figure 5-6, Figure 5-7** and **Figure 5-8**). The brine permeability reduction with increasing stress has been observed by other authors particularly in tight rocks (e.g. Wei et al., 1986; Morrow et al. 1981, 1984; Jones, 1988; Jones et al., 2001). This stress dependent behaviour is similar to that found with gas permeability measurements; in particular most of the reduction in brine permeability took place in initial stressing stages and the stress sensitivity of the measurements decreases with increasing confining pressure (**Figure 5-6, Figure 5-7** and **Figure 5-8**). However, the brine permeability stress sensitivity is found to be lower than that of the gas permeability (Figure 5 13). It is possible that this may be because it is easier to close microfractures within gas saturated samples than brine saturated samples.

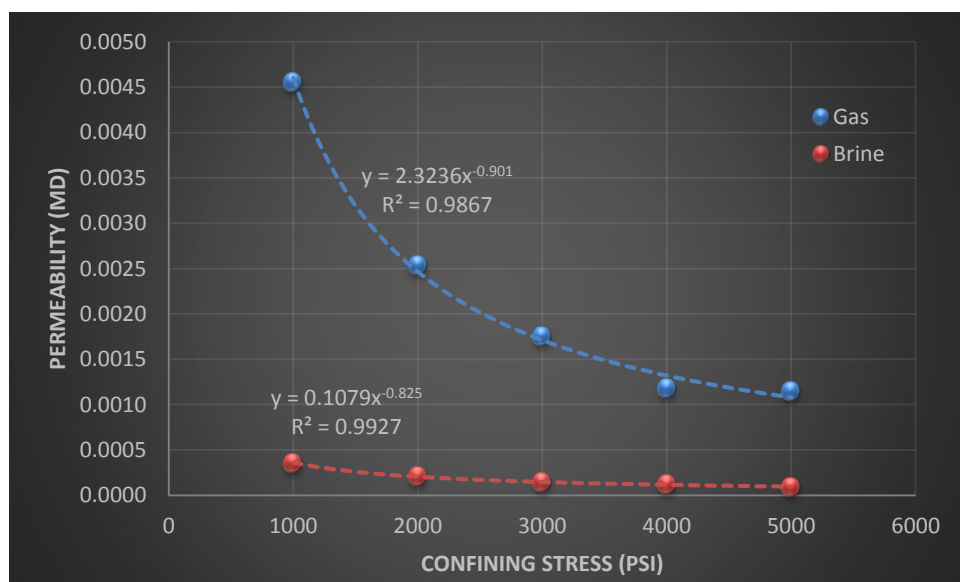
It appears that the difference between the gas and brine permeability of the samples from outcrop is less than that observed for those from the Central Graben reservoirs. It is possible that this may reflect differences in the clay content of the samples; QXRD indicates that the samples from Hoperman and Orange contain little clays than those from the Central Graben reservoir. However, an alternative explanation is that the stress sensitivity of samples is caused by the presence of grain boundary microfractures (see **Chapter 4**) and that it is far easier to close such microfractures in the presence of gas rather than when brine is used. The data obtained during the current project cannot easily differentiate between these two mechanisms. Further experiments in which the samples are left for more time between increases in confining pressure.

Nevertheless, a key observation is that the brine permeability is lower than the Klinkenberg corrected gas permeability. This observation is similar to that made on tight gas sandstone samples (e.g. Jones and Owens, 1980; Wei et al., 1986) and has been argued to result from the presence/movement of fine grained particles (e.g. Wei et al., 1986). However, although the samples containing less clay seemed to show less difference between gas and brine permeability a significant difference was identified in several samples. This shall be discussed further in the discussion of the impact of salinity on liquid permeability measurements presented below.

Morrow et al. (1984) conducted experiments on fault gouge from San Andreas Fault (California) and also found that permeability of fault rocks decreased with increasing confining pressure. Similarly other scientists conducted comprehensive laboratory work and well documented on stress dependent permeability and porosity of rocks and fault gouge (e.g. David et al., 1994; Zimmerman, 1991; Evans et al.,

1997). The exponential relationship between stress and permeability has been noted by several studies (e.g. Brace et al., 1968; Debschutz et al., 1989; Evans et al., 1993). However, Shi and Wang (1986) proposed a power law relationship between the effective stress and permeability of fault, based on the laboratory permeability measurements of Morrow et al. (1984).

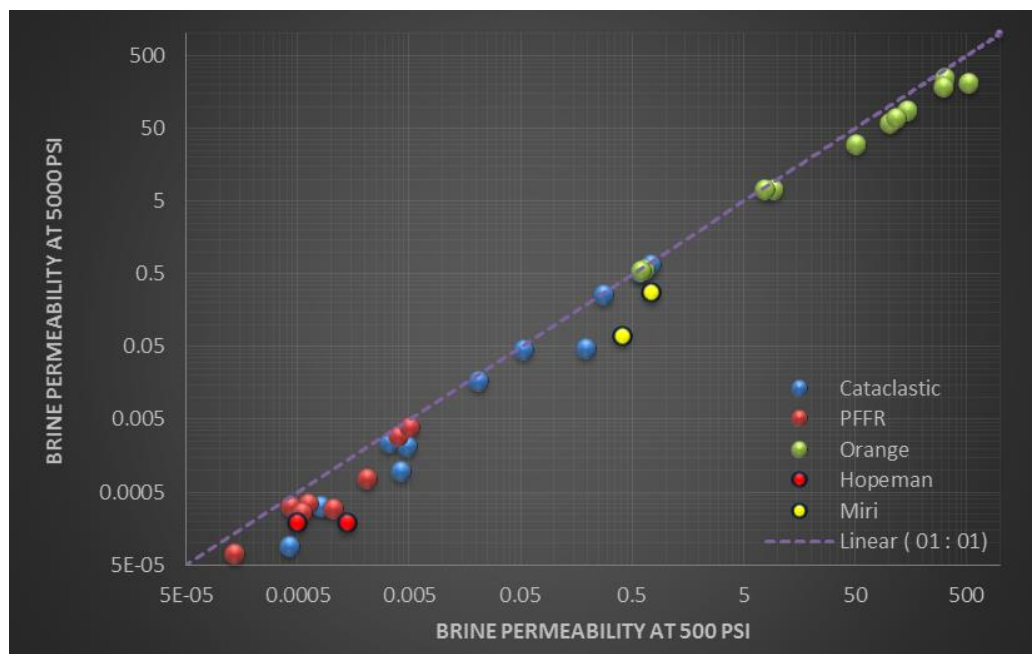
The current study has found that a power law provides a better fit to the experimental data than the exponential fit. According to David et al. (1994), the fault flow properties are a controversial issue and need to be standardized because there is no concrete laws to evaluate the fault flow properties. Furthermore, it is well accepted that the permeability and porosity of fault rocks are dependent not only on the existing loading condition, but also on the stress history within a depositional environment (Kwon et al., 2004).



**Figure 5-13: Plot of gas and brine permeability shows less stress dependency on confining pressure with brine permeability.**

The brine permeability extrapolated to 500 psi stress and plotted against the permeability measured at in-situ stress of 5000 psi look as stress sensitive (**Figure 5-14**). Similar to gas permeability, the tendency of less stress sensitivity is found in

high permeable Orange outcrop fault samples but in contrast lower permeability outcrop sample are stress sensitive (e.g. Hopeman and Miri). The cataclastic North Sea reservoir samples have shown lower stress sensitivity in comparison to PFFR samples. The overall decrease in cataclastic and PFFR samples, decrease in brine permeability is limited to 2 – 3 fold while in Orange outcrop samples it was almost less than or equal to one fold. Miri samples shown high sensitivity and decrease was 5 fold in sample Miri -1.



**Figure 5-14: Plot between permeabilities of fault rocks measure at 500 psi and 5000 psi. The data plotted is for cataclastic, PFFR and outcrop samples.**

### 5.5.3 Impact of brine salinity on liquid permeability

In this section a discussion about the permeability of gas, brine and deionized water for the unstressed samples is presented. The permeability of the cubes samples of cataclastic and phyllosilicate faults was measured using helium gas, brine and distilled water at very low or negligible stress for the assessment of permeability dependency on the nature of the fluids.

It is found that the permeability measured using distilled water is 30 % lower than the 30% NaCl brine- permeability (**Figure 5-10**). The similar trend was reported by some researchers who found a decrease in permeability when salinity was changed (e.g. Lever and Dawe, 1987; Jones and Owens, 1980; Sampath and Keighin, 1982; Baraka Lokmane, 2002). It will be worthwhile to assess the deviations between brine and distilled water permeabilities for a same sample which can help understanding the fault sealing behaviour. It is argued that the brine permeability variation is due to the fluid interactivity with the minerals present in the rock. Lever and Dawe (1984) have conducted experiments on Hopeman sandstone with different percentages of KCl and NaCl brine and reported that the Hopeman sandstone is found to be water sensitive when the monovalent cation liquid is used as permeant.

The main reasons for the permeability reduction due to the mineral activation (e.g. clay) are: release of fine particles due to ions exchanging and blocking the pore throats and clay swelling with reaction with water ions and reduction in pore size. The fine particle migration is also a reason for decrease in permeability by blocking the pore throats in downstream (Lever and Dawe, 1984, 1987; Faulkner, 2004; Rutter et al., 1986). Therefore, the liquid permeability is usually affected by the nature of fluid (liquid) used as permeant and it is found lower than the gas permeability as gases are usually inert (e.g. He, Ar). It is crucial to suggest the right fluid to evaluate the permeability of a reservoir because wrong selection may lead to severe errors in results.

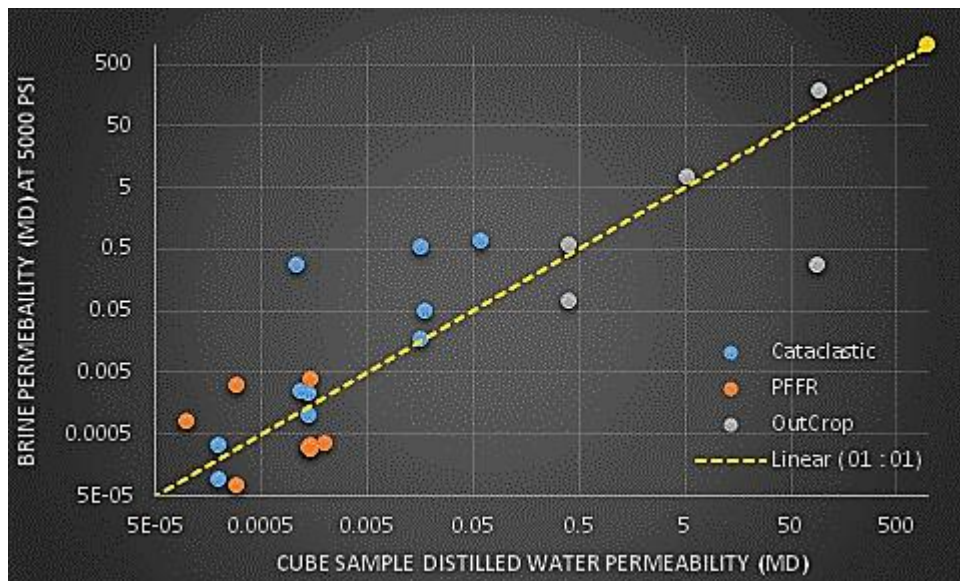
It is necessary to have the knowledge about the relationship between permeability and minerals present in the fault samples especially with the clay minerals. The samples used in this study are mainly cataclastic (clay < 15%) and

phyllosilicates (clay between 15 – 40 %) so the fault seal analysis can be analysed by having these parameters. These clay mineral may affect the permeability of the fault rock as for example clay may swell when acted with fresh water and block the pores or the fine particles when releases from their minerals due to ion exchange may block the pore throats. (Lever and Dawe, 1984, 1987; Mohan and Fogler, 1997).

The effect of a mineral on the permeability depends upon its physical as well chemical properties. For example, kaolinite can occur in very fine particles which may migrate from bigger pore towards smaller pore throats and block them causing a decrease the permeability. In contrast, illite-smectite has thin-long structure which swells when contact in with water and block the pore throats and severely decrease the effective connectivity of pores (e.g. Lever and Dawe, 1987; Bjorlykke, 2010; Mondol et al., 2008). So, presence of clay may reduce the permeability if low brine concentrations are used while clean sandstones showed high permeability for fresh water (Lever and Dawe, 1987). The analysed samples are showing that the clay contents are not only affecting the permeability reduction, there are some other factors also which may reduce the permeability e.g. pores fluid reaction with minerals present in rock, pore throats heterogeneity may affect significantly if fine particle migration occurred, etc

A key aim of this research was to assess the reliability of previous fault rock properties measurements that had been conducted using brine instead of distilled water. The measurements made using distilled water were around 30% lower than those made using brine. However, the published data were also generated at low confining pressures, which would tend to provide higher permeabilities. In other words, these two inappropriate laboratory conditions have opposite effect on

permeability. To assess the net effect of these differences, the permeability measured at high confining pressure using formation compatible brines is plotted against permeability measured at ambient conditions using distilled water (**Figure 5-16**). There is a certain amount of scatter in this diagram but this would be expected given that the measurements were made on adjacent and not identical samples. However, overall, the data plots around a 1:1 correlation suggesting that the two bad laboratory practices partially cancel the effects of each other. In other words, published (e.g. Fisher and Knipe, 1998, 2001) and propriety fault rock permeability data collected by industry that was measured using distilled water at low stresses should be viewed with caution but need not be totally ignored.

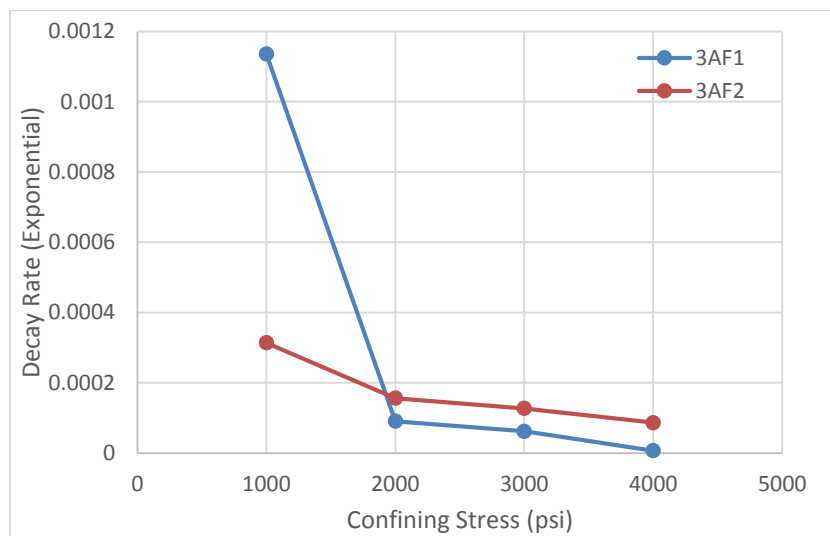


**Figure 5-15: Cube samples Brine (30%) permeability correlation with reservoir samples at 5000 psi on log-log scale.**

### 5.5.4 Sample heterogeneity

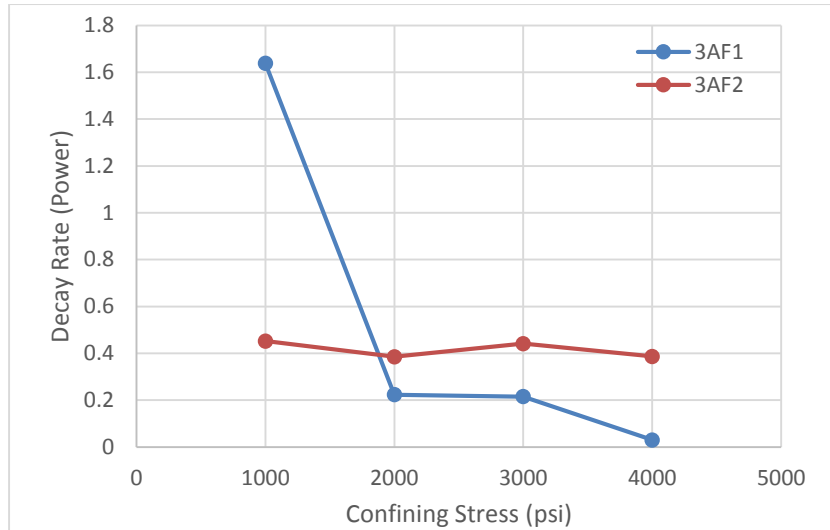
The samples are showing high heterogeneity with respect to the permeability decay even within two core plugs which are taken from the same core sample of total length of 20 cm there is high difference is found. A typical example of such samples

is presented in **Figure 5-16** and **Figure 5-17**, which shows that the permeability decay between the confining pressure steps from 1000 psi to 5000 psi. The sample 3AF1 is showing a large change in pressure decay in first step when pressure is changed from 1000 psi to 2000 psi but afterwards the decay is asymptotic. This may be due to the presence of some micro fractures which are closed when the pressure is increased to 2000 psi. In contrast, the sample 3AF2 is not showing as much variation in both decaying of permeability by exponential and power. The permeability decay rate is not similar within a core sample from which these plugs have been taken.



**Figure 5-16: Brine permeability decay rate (Exponential) for samples 3AF1 and 3AF2.**

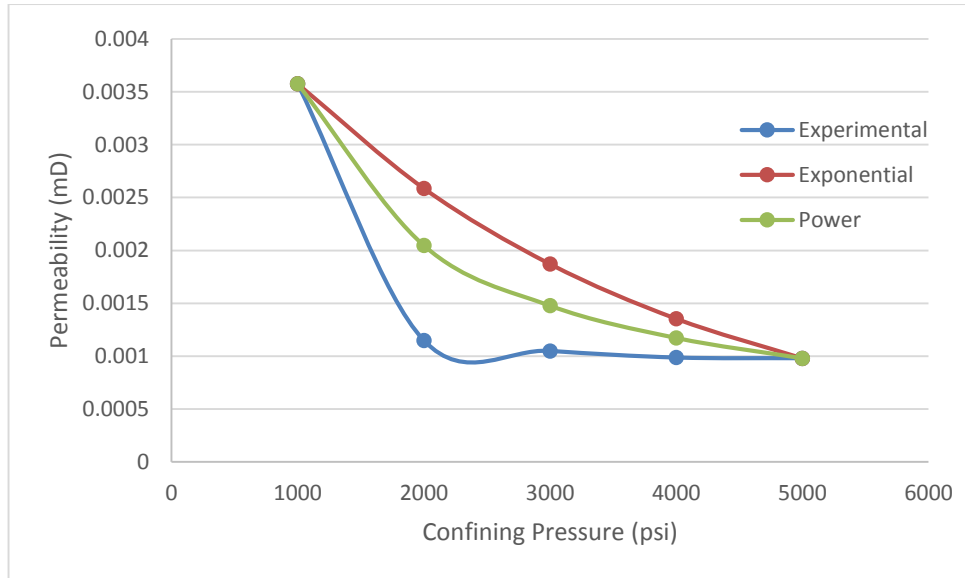




**Figure 5-17: Brine permeability decay rate (Power) for samples 3AF1 and 3AF2.**

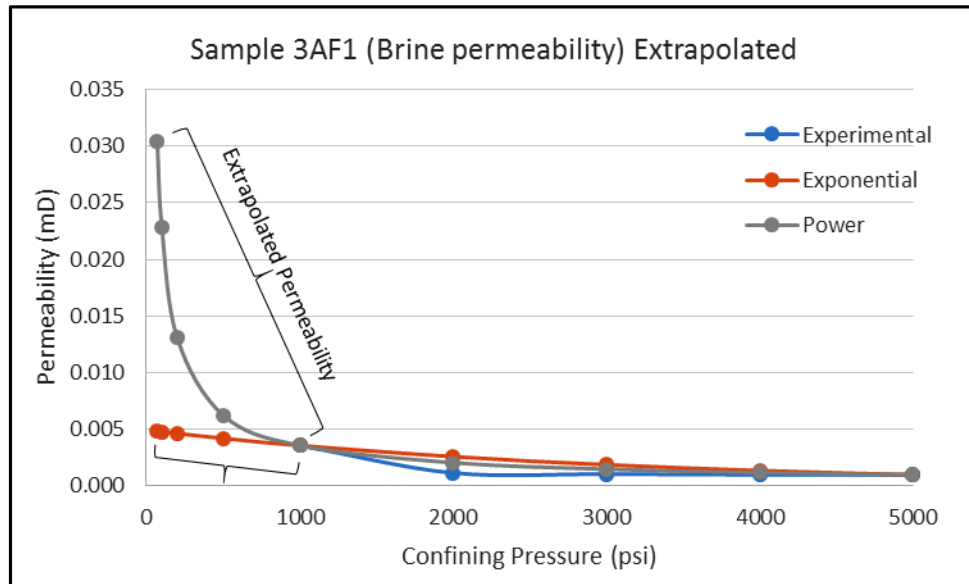
### 5.5.5 Brine permeability decaying modeling

The brine permeability decay is also modelled as done in the previous chapter by exponential and power law. Almost the same trend is found in brine permeability also and most of the samples following the power law. The decay rates are calculated by both exponential and power law and the permeabilities are compared with experimental results. A typical example is presented in **Figure 5-18** which shows the difference between the predicated and experimental permeabilities of core plug sample.



**Figure 5-18: Comparison of permeabilities experimental, exponential and power law model.**

The **Figure 5-19** shows the extrapolation of exponential and power law to predict the permeability at nominal stress of 70 psi.



**Figure 5-19: Extrapolated brine permeability of sample 3AF1 by exponential and power model.**

The extrapolated points are obtained by the following formulae (Refer **Appendix A – 1** for derivation of formula):

For Exponential:

$$K_{extrapolated} = K_{final} \times e^{r(P_{final} - P_{initial})} \quad \text{Eq. (5-4)}$$

For Power Law:

$$\text{or } K_{extrapolated} = K_{final} \times \left( \frac{P_{initial}}{P_{final}} \right)^{-r} \quad \text{Eq. (5-5)}$$

The back extrapolation for permeability estimation (**Figure 5-19**) is showing that the power law is estimating a higher permeability for the lower confining pressure. The permeability at 70 psi by exponential model is estimated as 0.00483 mD while by power law model it is found to be 0.0304 mD which is 80% higher than exponential. The extrapolated brine permeability of samples is presented in **Table 5-5** which is showing that the extrapolated brine permeability by power law is estimating higher values than exponential model.

Sample ID	Brine Permeability @1000 psi (mD)	Extrapolated permeability @ 70 psi		Percentage Difference (%)
		Exponential (mD)	Power law (mD)	
3AF1	0.00358	0.0048	0.03038	84.1
3AF2	0.00433	0.0051	0.01338	62.1
10/3AF1	0.00323	0.0032	0.00528	34.5
10/3BF1	0.05169	0.0531	0.06266	15.2
7AF1	0.27154	0.2726	0.27909	2.3
7BF1	0.00073	0.0009	0.00274	67.8
7BF2	0.00035	0.0005	0.00331	85.4
7CF1	0.00013	0.0001	0.00032	54.3
7CF2	0.00380	0.0040	0.00576	30.1
7DF1	0.00058	0.0007	0.00138	52.4
7EF1	0.00189	0.0023	0.00798	71.0
7FF1	0.00041	0.0004	0.00063	30.7
5AF1	0.00489	0.0051	0.00701	26.6
5AF2	0.00050	0.0006	0.00137	58.2
5BF1	0.00090	0.0012	0.00547	78.8
5DF1	0.16409	0.2181	1.23825	82.4
5EF1	0.02020	0.0211	0.02719	22.5
5EF2	0.57109	0.5811	0.64578	10.0
5FF1	0.72321	0.7335	0.79634	7.9

**Table 5-5: Brine extrapolated permeabilities at 70 psi pressure by exponential and power law models**

## 5.6 Conclusions

The brine permeability of fault rock samples has been measured as a function of stress. The results indicate that like gas permeability, the brine permeability of fault rocks is stress sensitive and that this stress sensitivity increases with decreasing permeability. The stress dependency of fault rocks samples taken from outcrop is far less than those obtained from core. This suggests that the stress dependence of the permeability of faults from core is an artefact resulting from cooling or stress relaxation. Brine permeability is found to be slightly less stress sensitive than gas sensitivity. The reasons for this are not entirely clear but could be related to the presence of brine preventing the closure of microfractures. The permeability of fault rocks measured using distilled water is lower than when measured using 30% brine, which is possibly due to the interaction of the clay with water and results in clay swelling or movement of fines, which blocks the pores.

The permeability of fault rocks to distilled water is on average around a factor of 30% that of formation brine so great care must be taken when applying measurements made using distilled water to reservoir conditions. This raises questions regarding the accuracy of much published and proprietary data on fault rock permeability that were measured using distilled water. However, these data were collected at ambient stress which has the opposite effect to measuring samples with distilled water. Indeed, plots of permeability measured at low stress using distilled water have a scattered but 1:1 correlation with measurements made at in situ stress using formation compatible brine. So while it is not recommended to measure fault properties using these poor laboratory practises the data that have been collected (e.g.

Fisher and Knipe, 1998, 2001) are probably still reasonable to use for modelling the impact of fault-related fluid flow in petroleum reservoirs.

# **Chapter 6: Evaluation of wettability and relative permeability of fault rock**

## **6.1 Introduction**

Like most published work on the impact of faults in fluid flow, the previous chapters in this thesis have concentrated on the absolute permeability in which only a single phase is present within pore space (water or gas). However, petroleum reservoirs always contain two or more fluids (water and gas, water and oil, oil and gas). Here flow is not just controlled by the absolute permeability but is also controlled by the relative permeability (i.e. the effective permeability of a particular phase divided by its absolute permeability). An added complication is that the distribution of fluids in the pore space relative to the mineral surfaces may vary depending on factors such as the type and chemistry of the fluids present, the mineralogy and the capillary pressure. The overarching term used to describe this effect is wettability and is defined as the ability of a fluid to spreading over or adhere to mineral surface in the presence of other immiscible fluids (Craig, 1971). Wettability plays a vital role for the multiphase flow through the reservoir rock. It governs the saturation distribution of fluids in the reservoirs as well as controls the production of oil, gas and water from reservoirs. Proper evaluation of the reservoir rock wettability also enables to develop a proper plan for water flooding and EOR (Ju et al., 2006; Guo and Abbas, 2003; Anderson, 1987a, 1986 a, b, c, d; Morrow and McCaffery, 1978).

In recent years a small number of publications have highlighted the importance of considering the multiphase flow behaviour of fault rocks (Fisher and Knipe, 2001; Manzocchi et al., 2001; Al-Busafi et al. 2006). A small number of papers have also presented relative permeability measurements from fault rocks (Al-Hinai et al. 2008;

Tuekmantel et al., 2010). These data are extremely limited both in the range of fault rocks and the wettability of the system. In particular, only gas relative permeability data has been presented. Hence there are no published data on oil-water relative permeabilities of fault rocks and no measurements have been made on rocks in which the mineral surfaces are mix-wet. The following chapter aims to fill this knowledge gap by presenting new data on the oil-water relative permeability of fault rocks with a range of wettabilities.

The chapter is divided into the following subsections:

- An overview of wettability and relative permeability is provided in in **Section 6.2** and **Section 6.3**.
- Experimental methods used in this research are described in Section 6.4.
- Results are presented in **Section 6.5**.
- Discussion and conclusions are presented in **Section 6.6** and **Section 6.7** respectively.

## **6.2 Wettability**

Wettability plays a very important role in hydrocarbon recovery as it is responsible for the spatial distribution of fluids in the reservoir, and therefore controls flow behaviour and oil/gas saturations. The contact angle of a fluid with a solid-surface (porous media) in the existence of other immiscible fluid depends on the nature of the solid and interfacial tension between the fluids. Two end-member behaviours are; (i) a fluid spreads over the solid or (ii) the fluid forms a drop on the surface; in these two situations the fluid is said to be wetting and non-wetting respectively.

A large number of direct and indirect methods exist for measuring wettability, which are discussed in more detail below. However, probably the most common



method is to measure what is known as the contact angle. The contact angle is often defined as the angle, conventionally measured through the denser between two immiscible fluids where they meet the mineral surface (**Figure 6-1**). Thomas Young (1805) described a relationship (Equation 6.1) between the interfacial tension of the fluids and the contact angle. The difference between solid – oil and solid – water interfacial tensions is defined as the adhesion tension (Donalson and Tiab, 2004). The relationship between wettability, contact angle and adhesion tension is summarized in **Table 6-1**.

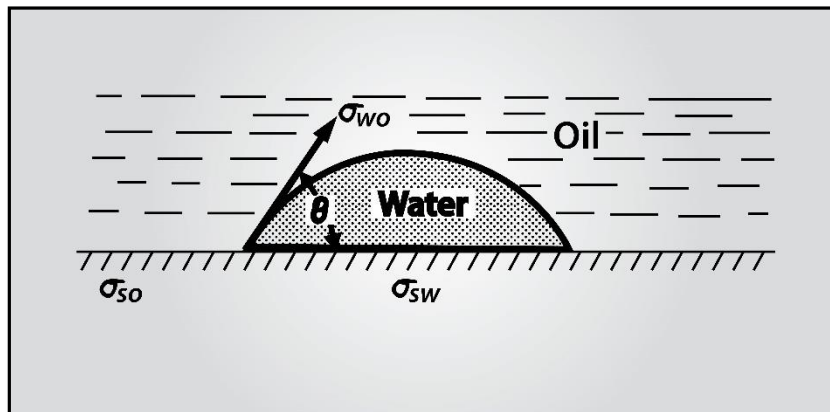
$$\theta = \cos^{-1} \left[ \frac{\sigma_{so} - \sigma_{sw}}{\sigma_{wo}} \right] \quad \text{Eq. (6-1)}$$

where:

$\sigma_{so}$  = interfacial tension between solid surface and oil

$\sigma_{sw}$  = interfacial tension between the solid surface and water

$\sigma_{wo}$  = interfacial tension between oil and water



**Figure 6-1: Contact angle in oil-water system for a water wet rock.**

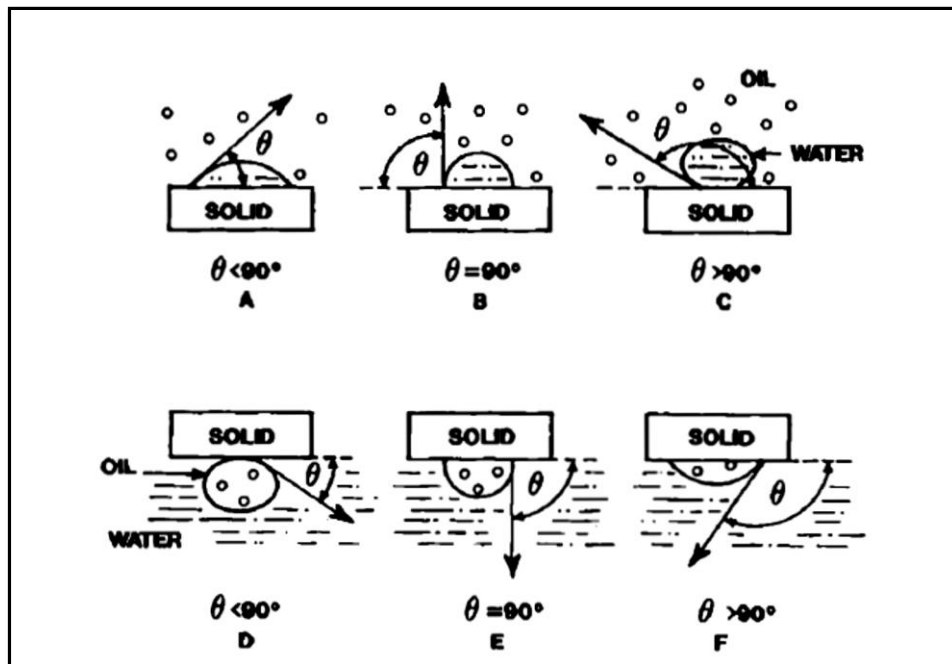
### 6.2.1 Wettability states

A range of wettability states can exist with three of the most common being water-wet, neutral-wet and oil-wet; the contact angles that define these are provided in **Table 6-1** and **Figure 6-2**. The wettability of a porous media containing one or more petroleum phases as well as brine may be heterogeneous leading to a range of

wettability states, which are described in more detail below and summarized in **Table 6-1**.

Contact angle $\theta$	Rock surface	Adhesion tension
$0^\circ < \theta \leq 90^\circ$	Water wet	Positive
$90^\circ$	Neutral	Zero
$90^\circ < \theta \leq 180^\circ$	Oil wet	Negative

**Table 6-1: Classification of wettability based on contact angle from Thomas Young's (1805).**



**Figure 6-2: Different scenarios for rock wettability on the basis of contact angle (from Anderson, 1986a)**

#### **6.2.1.1 Strongly water – wet rock system**

In this type of rock system, the rock surface has a far greater affinity for water than the other immiscible phases. In this type of system, water mostly resides in the small pores and the rock surface is directly in contact with water while the centre of large pores can be filled by oil or gas. Most gas-water systems are strongly water-wet. A freshly cleaned, initially water saturated rock sample will generally be strongly water-wet immediately after oil has displaced some of the water. However, interactions between the crude oil - brine – rock (COBR) systems may alter the wettability of the rock (Anderson, 1986a).

#### **6.2.1.2 Strongly oil – wet rock system**

In strongly oil-wet system, oil will have a greater affinity for the mineral surface and therefore will reside in the small pores and directly contact the rock surface. The non-wetting fluid (gas or water) will occupy the centre of larger pores and can be displaced easily by the oil.

#### **6.2.1.3 Neutral or fractional wettability**

The rock system has no preferential affinity to either water or oil is classified as neutral or intermediate wettability rock system. In terms of contact angle, it is approximately equal to 90° (**Table 6-1**).

#### **6.2.1.4 Fractional or mixed wettability**

A rock is generally composed of more than one mineral and each mineral may have a different affinity to the fluids present, which may lead to what is known as a mixed wetting (Anderson, 1986a). A mixed wetting state can also result from the mineral surfaces containing heterogeneous deposits of insoluble hydrocarbons such as asphaltenes. Brown and Fatt (1956) identified a specific type of mixed wettability,

which they termed fractional wettability, in which both continuous water and oil wet pathways existed throughout the rock.

### **6.2.2 Wettability alteration**

Most sedimentary rocks are either deposited in water or become saturated with water soon after deposition. Hydrocarbons may enter the rock at a much later stage. Immediately after the petroleum enters the rock it will usually be strongly-water wet. However, the mineral surface may become altered by the adsorption or precipitation of hydrocarbons resulting in its wettability changing. Changes in wettability are controlled by a wide range of factors including: the oil and brine composition, the mineralogy, the temperature and pressure as well as the capillary pressure. In some cases, only regions that are very close to the oil within the pore space (i.e. the large pores) undergo such changes and parts of the pore system that remain further from the oil (i.e. small or isolated pores) remain water-wet.

### **6.2.3 Evaluation of wettability**

A range of methodologies are traditionally used to measure the wettability of a COBR system and these may be broadly divided into quantitative and qualitative methods. Quantitative methods includes: measurement of contact angles; Amott wettability index and USBM (United States Bureau of Mines). Qualitative methods include: microscopic examination; nuclear magnetic resonance (NMR); permeability and saturation relationships (Amott, 1959; Craig, 1971; Donaldson et. al., 1969; Anderson, 1986b)

The oil industry lacks a single standardized wettability measurement methodology but three most common quantitative methods used are: the Amott index (or modified Amott-Harvey); the USBM method; and measurement of contact angles.

These methods are based on quantitative as well qualitative evaluation approaches, which are discussed below.

### **6.2.3.1 Amott – Harvey method for wettability measurement**

This method was devised by Amott (1959) and involves different cycles of imbibition and drainage; the test provides an estimate of the average wettability of the rock system. The basic principle behind this methodology is that the wetting fluid can easily displace the non-wetting fluid from the porous rock by spontaneous imbibition. The main steps of the Amott Index method are described below. For simplicity the terms imbibition and drainage refer to increasing and decreasing water saturations respectively.

1. The test begins at the residual oil saturation; therefore, the fluids are reduced to  $S_{or}$  by forced displacement of the oil.
2. The sample is placed into the oil drainage cell and immersed in testing oil for spontaneous drainage of oil for at least 20 hours. The amount of water (brine) displaced by imbibition of oil is recorded as  $V_{wsp}$ .
3. Forced flooding of oil is performed to reduce the water saturation to the irreducible water saturation ( $S_{iw}$ ). The total amount of water displaced (by imbibition of oil and by forced displacement) is recorded as  $V_{wt}$ .
4. The sample (at  $S_{iw}$ ) is placed into the imbibition cell filled with brine for spontaneous imbibition and the amount of oil displaced recorded as  $V_{osp}$ .
5. The oil remaining in the core is displaced by water to  $S_{or}$  and the total amount of oil displaced (by imbibition of water and by forced displacement) is recorded as  $V_{ot}$ .

6. On the basis of the above steps, following equations are used to calculate the indices for wettability. In the first case, the displacement ratio for water is given by:

$$\delta_w = \frac{V_{osp}}{V_{oT}} \quad \text{Eq. (6-2)}$$

For the second case the displacement ration for oil will be:

$$\delta_o = \frac{V_{wsp}}{V_{wt}} \quad \text{Eq. (6-3)}$$

The difference between equations 6.2 and 6.2 is called the Amott-Harvey wettability index (AHWI) given by following equation:

$$AHWI = \delta_w - \delta_o = \frac{V_{osw}}{V_{oT}} - \frac{V_{wsp}}{V_{wt}} \quad \text{Eq. (6-4)}$$

It is obvious from equation 6.4 that the Amott-Harvey wettability index (AHWI) can vary from +1 to -1. A value of +1 indicates strongly water-wet and -1 indicates strongly oil-wet; a value close to zero suggests the rock has a neutral wettability. Cuiec (1984) has devised detailed resolution for further classification of wettability, which is presented in **Table 6-2**.

AHWI	Wettability scale
<b>+ 1</b>	Strongly water wet
<b>+ 0.3 to + 0.99</b>	Water wet
<b>+0.1 to &lt;+ 0.3</b>	Slightly water wet
<b>0.1 to -0.10</b>	Neutral
<b>- 0.1 to &gt; - 0.3</b>	Slightly oil wet
<b>- 0.3 to - 0.99</b>	Oil wet

- 1	Strongly oil wet
-----	------------------

**Table 6-2: Amott-Harvey wettability indices by Cuiec (1984)**

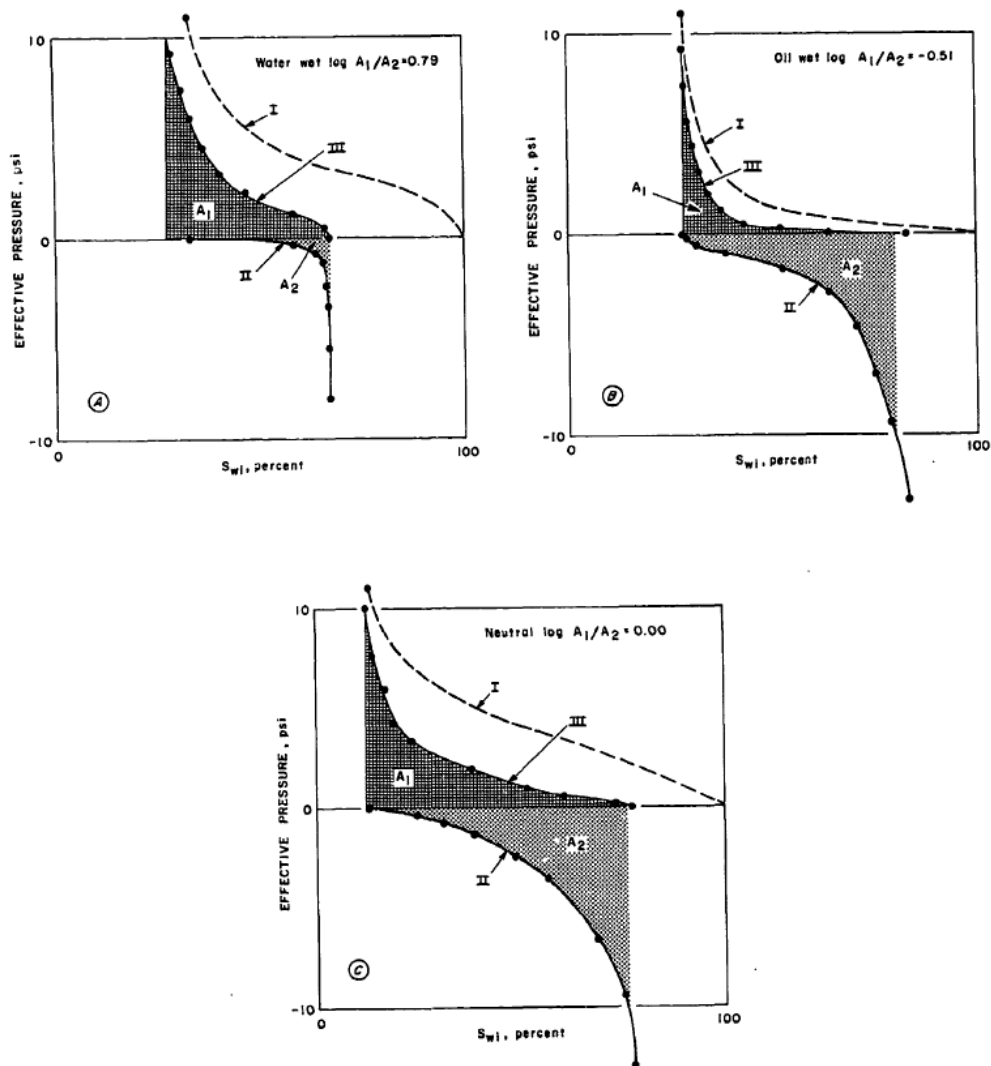
### 6.2.3.2 United States Bureau of Mines (USBM) method

Donaldson et al. (1969) developed a method based on the principle of thermodynamic work required to displace the wetting and non-wetting fluid from the rock system. The area under the curves between the capillary pressure and saturation which are giving the thermodynamic work done are obtained by the displacement of the wetting and non-wetting fluids. It is found that the work done required to displace the fluid from the porous media is proportional to the area under the capillary pressure curve (Leverett, 1941; Morrow, 1970). Therefore the wetting phase can easily displace the non-wetting phase from porous rock and required less energy or work done and its area under the capillary pressure curve will be smaller in the reverse case (Anderson, 1986b).

A direct indication of wettability can therefore be obtained by the work required for the displacement of the fluids or in other words by the ratios of the areas under the capillary pressure curves. Donaldson et al. (1969) has presented an equation for measuring the wettability index as:

$$USBM\ WI = \log \left[ \frac{\text{Upper area under the curve } A_1}{\text{Bottom area under the curve } A_2} \right] \quad \text{Eq. (6-5)}$$

The USBM test procedure is described by different steps applied on a rock (Figure 6-3 a to c).



**Figure 6-3: Wettability measurements by USBM method: Curve-I is showing primary drainage, curve-II is showing forced imbibition and curve-III is showing secondary drainage. (a) Untreated water wet core; (b) Treated core with 10% DRI-FILM 99, (showing oil wet behaviour) (c) aged core sample for 14 days at 60°C; the concentration of the brine is 1000 ppm of sodium tripolyphosphate.**

First the primary drainage curve (curve I) is obtained using a centrifuge to displace brine to the irreducible water saturation. Brine is then allowed to spontaneously imbibe into the sample before forced imbibition is performed using a centrifuge to obtain curve II. Oil in the sample is then allowed to spontaneously drain the sample before a forced drainage is performed using a centrifuge to provide curve III. The respective areas of drainage and imbibition are A1 and A2 respectively, which are used to calculate the USBM wettability index. The wettability index is



ranging from -1 to +1 similar to Amott index for strongly oil-wet to strongly water-wet respectively.

### 6.3 Relative permeability

Relative permeability measurement is considered as a basic requirement for the characterization of the multiphase fluid flow through the reservoir rock. The effective permeability is the permeability of a fluid, which is flowing through the porous media in the presence of the other fluid(s). In case of absence of the other fluid(s), the single fluid permeability is called the absolute permeability. Usually it is not enough to characterize the reservoir by only single phase permeability because in real conditions there are usually two or more fluids (water, oil and gas) are present at the same time. So, the normalized effective permeability by any base permeability (e.g. gas or water absolute permeability) is called relative permeability and used for multiphase flow through porous rock system. According to Craig (1971), relative permeability can be defined as “The relative permeability characteristics are a direct measure of the ability of the porous system to conduct one fluid when one or more fluids are present”. Relative permeability is mainly the function of:

- Pore structure Wettability of rock system
- Saturation of fluids and its distribution
- Saturation history (i.e. drainage and imbibition)

Mathematically oil relative permeability can be written as:

$$k_{ro} = \frac{k_{eo}}{k_a} \quad \text{Eq. (6-6)}$$

where:

$k_{ro}$  = Relative permeability of oil at some particular saturation,  
fraction

$k_{eo}$  = Effective permeability of oil at some particular saturation, mD

$k_a$  = Absolute permeability at 100% saturation, mD

### 6.3.1 Factors affecting relative permeability

#### 6.3.1.1 Effect of pore size distribution

Relative permeability is found to be influenced by the pore size distribution of the rock. Several authors have suggested that hysteresis of relative permeability curves during drainage and imbibition is strongly controlled by pore size distribution (Jerauld and Salter, 1990; Morgon and Gordon, 1970). Naar et al. (1962) have presented a comparison between the consolidated (sandstone) and unconsolidated (glass spheres) relative permeability experimental results. The results revealed that the consolidated porous media like sandstone the non-wetting phase show lower relative permeability in imbibition than primary drainage while almost same in the case of wetting phase (Figure 6-4a).

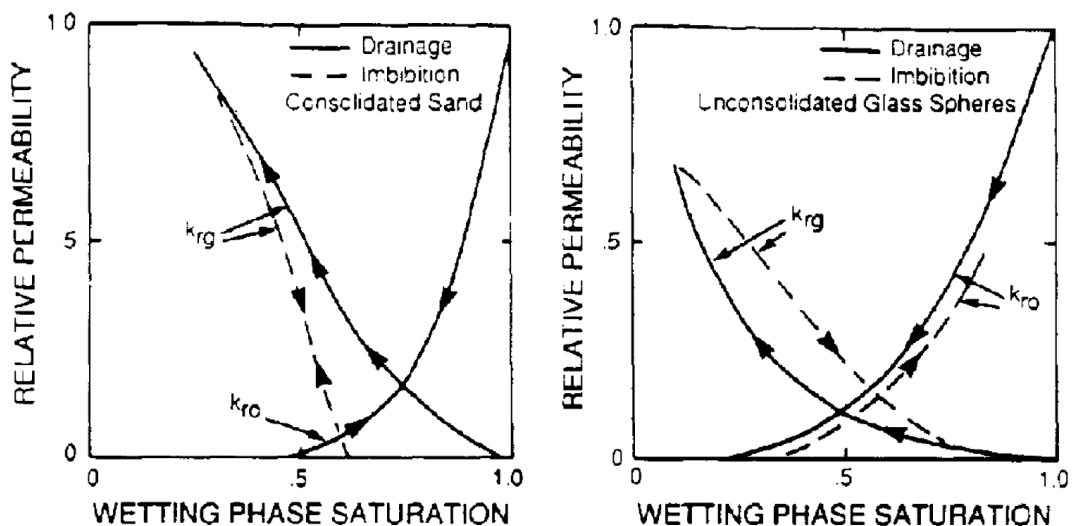


Figure 6-4: Relative permeability curve for wetting and non-wetting cases (from Naar et al., 1962).

In contrast, for the unconsolidated samples, the relative permeability of the non-wetting phase is lower in primary drainage than imbibition while almost similar in primary and secondary drainage (**Figure 6-4b**). Higher residual saturations (in imbibition) are found in consolidated samples than in unconsolidated for non-wetting phase.

A series of relative permeability measurements have been conducted by Morrow (1970, 1971) with random packing and sizes of grains. The results indicated that fluid and rock properties have little impact on irreducible saturations but heterogeneity has a major impact. Highly heterogeneous rock has high irreducible saturations because the random pore throat sizes trap more fluid.

Detailed pore network modelling by Jerauld and Slater (1990) described two main parameters which are mainly responsible for the hysteresis found in relative permeability and capillary pressure curves namely: (i) pore body to pore throat aspect ratio, and (ii) the coordination number (number of connections of pore throat with pore body). Coordination number is generally 3 – 8 for high permeability sandstones but can be much low for the tight rocks (Kurtev and Alpin, 2005; Jerauld and Salter, 1990) and far higher for some carbonates

Okui et al. (1998) collected data from rocks with varying grain size and structure to build a relationship between saturation and pore geometry. The study suggested that the fluids saturations are mainly controlled by: (i) adsorption of fluids at the surface of the rock due to electrostatic force of attraction between the rock crystals and hydrogen bond of fluid (e.g. water); (ii) high surface roughness of rock increases the capillary pressure and trap more fluid results in increased irreducible

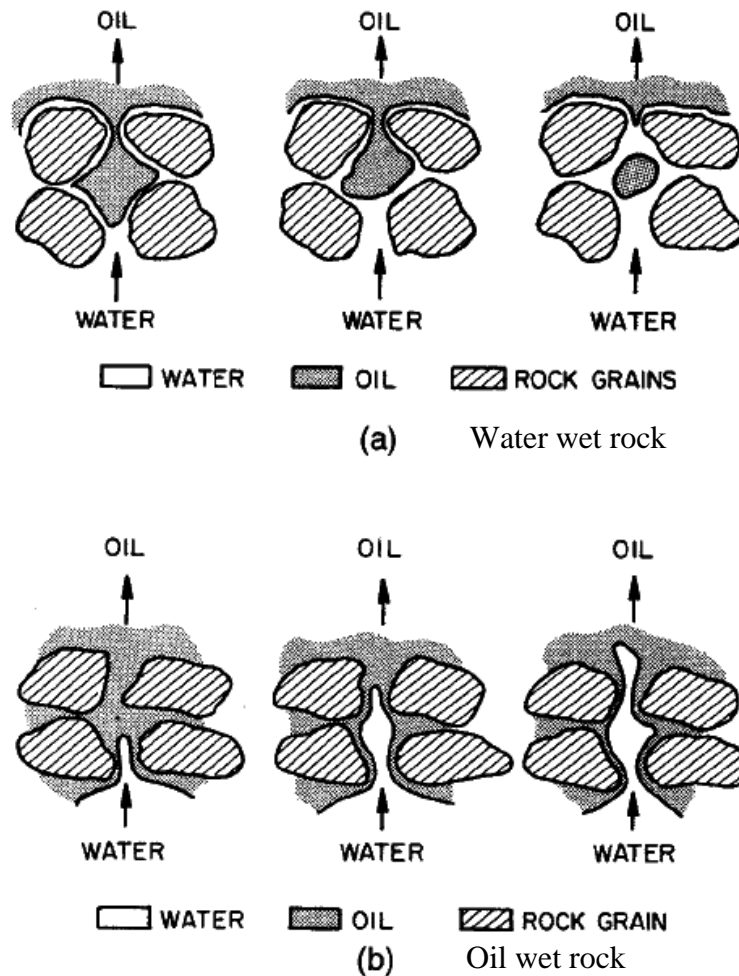
saturation; and (iii) very low porosity (micro porosity) found in clay also increases the irreducible water saturation.

### **6.3.1.2 Impact of wettability**

A change of wettability affects the saturation (irreducible and residual), flow paths of fluids and the distribution of fluids within a rock, therefore it has a direct impact on relative permeability. (Craig, 1970; Marsden., 1965; Raza et al., 1968; Honarpour et al., 1986; Taber, 1981; Owen and Archer, 1971; Anderson 1987)

Most of the small pores of a strongly water-wet rock, at irreducible water saturation are filled and mineral surfaces covered with a thin layer of water covering the mineral surfaces. In contrast, the non-wetting fluid (e.g. oil or gas) occupies the centre of the larger pores. The distribution is entirely reversed for a strongly oil-wet rock (Anderson, 1987; Donaldson and Thomas, 1971; Donaldson and Crocker, 1977; Morris and Wieland, 1963; Yadav et al., 1987; Moore and Slobod, 1956).

Raza et al. (1968) describe how a flooding cycle can provide an indication of the impact of wettability on relative permeability. Brine will be present in the smallest pores at the start of imbibition so its relative permeability would be expected to be lower than that of the oil which occupies the largest pores. Oil will become trapped in the largest pores at the end of forced imbibition due to snap-off thus effectively blocking the highest permeability pathways to the flow of brine (**Figure 6-5a**). On the other hand, water forced into an oil wet-rock will occupy the largest pores and hence will have a far higher relative permeability for a given saturation than in the water wet case (**Figure 6-5b**).



**Figure 6-5: The distribution of oil and water in (a) water wet rock and (b) oil wet rock (from Raza et al., 1968).**

Some rules of thumb have been presented by Craig (1970) for the qualitative identification of water and oil-wet rock systems by their relative permeability characteristic curves (Raza et al., 1968; Bobek, et al., 1958). **Figure 6-6** shows relative permeability for strongly water-wet and oil-wet rock systems. As a rule-of-thumb, the crossover in the relative permeability curves occurs at water saturations  $>50\%$  for a water-wet rock and  $<50\%$  water saturation for an oil-wet rock.

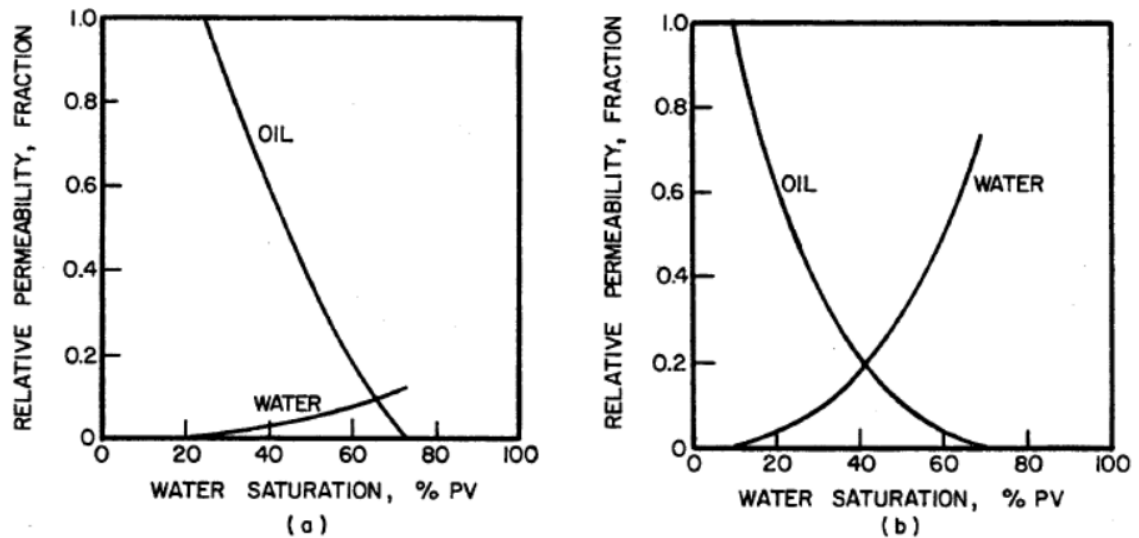


Figure 6-6: Typical relative permeability curves for (a) water wet rock and (b) oil wet rock (from Craig, 1970)

Donaldson and Thomas (1971) performed a series of relative permeability experiments on range of samples from strongly water-wet (core sample 1) to strongly oil-wet (core sample 5) rock samples and the results presented confirm the rules-of-thumb presented by Craig (Figure 6-7).

### 6.3.2 Relative permeability measurement techniques

Different techniques are used to measure the relative permeability but broadly classified into steady-state and non-steady-state techniques.

#### 6.3.2.1 Steady state relative permeability measuring method:

In case of steady state method, the core sample is placed in a core holder at some known saturation. Differential pressure transducers and metering pumps are connected with the setup. These metering pumps allow water and oil to be injected simultaneously but at varying relative flow rates, hence varying fractional flow (ratio of oil/water flow rate over total flow rate). The flow rates of the effluent is monitored

and once steady state is reached the saturation within the core is calculated using material balance or in situ using X-ray or gamma ray attenuation. The flow rates and differential pressure are then incorporated into Darcy's law modified for individual phases (Eq 6-7 and 6-8) and the effective permeability for each phase is calculated. These steps are repeated at several different fractional flows until a complete relative permeability dataset is obtained (Dullien, 1979; Tiab and Donaldson, 2004).

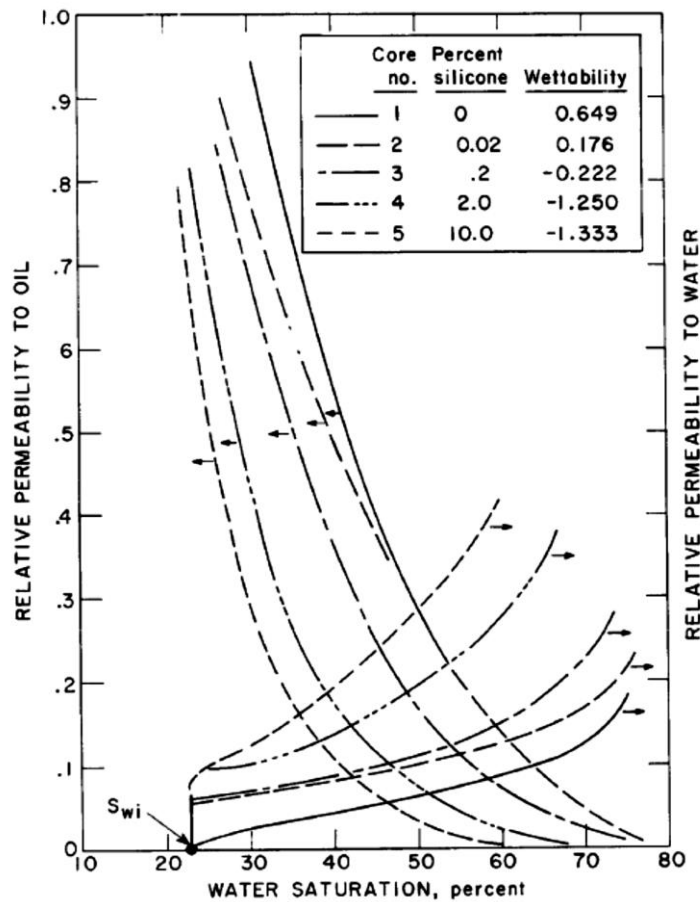


Figure 6-7: Relative permeability curves for strongly water to strongly oil wet cores (from Donaldson and Thomas, 1971).

$$K_{ew} = \frac{Q_w \times \mu_w \times L}{A \times \Delta P_w} \quad \text{Eq. (6-7)}$$

$$K_{eo} = \frac{Q_o \times \mu_o \times L}{A \times \Delta P_o} \quad \text{Eq. (6-8)}$$

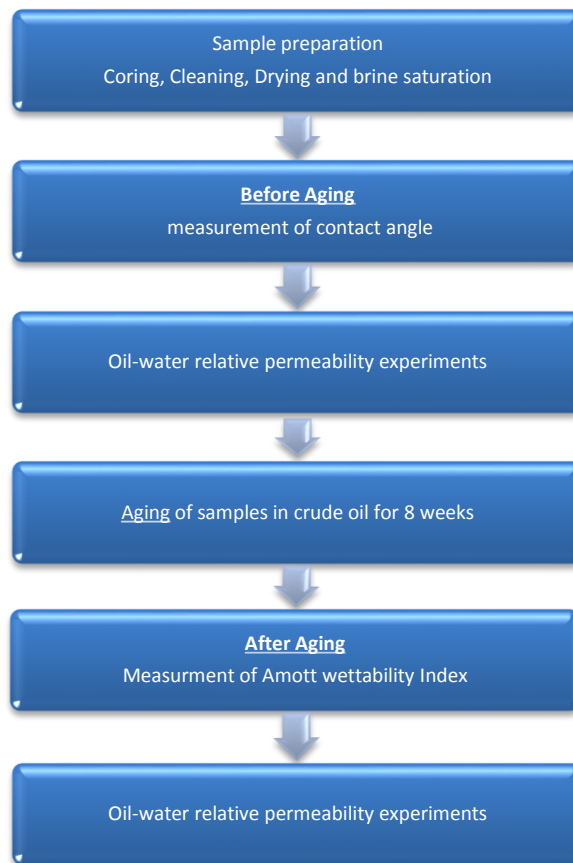
### **6.3.2.2 Unsteady state relative permeability measuring method**

The steady-state method is time consuming and expensive so industry often prefers to use unsteady methods for measuring relative permeability of which are variety exist including: JBN method (Johnson et al., 1959); Toth et al. method (Toth et al., 1968, Szucs and Civan, 2002). In the JBN method, the capillary end-effect is neglected by applying high flooding rates but it seems to difficult to apply on low permeability samples (Anderson 1987e). In this study an alternate method is used to measure the relative permeability, which is based on the average saturation of the core samples (Tiab and Donaldson, 2004).

## **6.4 Experiments and methodologies**

In the current study, a series of oil-water relative permeability experiments were conducted on fault rocks from Orange France, described in previous chapters. The work flow conducted is given in **Figure 6-8** and described below.





**Figure 6-8: Workflow diagram for oil-water relative permeability experiments Orange fault rock samples.**

### **6.4.1 Contact angle measurement**

The contact angle of water saturated samples of Orange fault rock samples was measured at the start of the experimental procedure to assess their initial wettability. This was achieved by immersing the brine saturated samples in Multipar-H oil overnight and then placing a drop of brine solution on the sample surface. This was then left for 24 hour to equilibrate before making the contact angle measurement.

### **6.4.2 Relative permeability measurement**

The unsteady-state relative permeability method was used to measure the oil-water relative permeability of the Orange fault rock samples. Oil-water relative permeability were both before and after fault samples had been left to age in crude oil.

The setup used for the oil-water relative permeability measurement is shown in **Figure 6-9**, which mainly consists of a core holder with confining pressure pump, pumps for oil and water flow, pressure transducer and calibrated flasks to measure the effluent.

The key steps are described below:



**Figure 6-9: Basic pump setup for unsteady state relative permeability experiments.**

1. The brine saturated sample is placed in the core holder and a confining pressure of 3000 psi is applied to mimic the in situ reservoir overburden pressure condition.
2. The sample is then subject to drainage in which a mineral oil (Multipart – H) is pumped into the sample to reduce the brine saturation. Drainage begins with the injection of Multipart at a low flow rate until no more brine is produced. A further 5 pore volumes are then pumped through the sample to ensure that irreducible brine saturation has been reached.
3. The differential pressure and flow rate is recorded so that the oil effective permeability can be calculated.

4. The effluent produced is collected in a clean glass flask and the quantity of brine produced measured with a high resolution burette ( +/- 0.01 cc) so that the average brine saturation can be calculated using material balance.
5. The sample is then left to equilibrate for 8-10 hours before commencing a further drainage stage by continuing the oil flood at a higher flow rate. The effective oil permeability and water saturation is calculated once brine production has stopped and an additional 5 pore volumes of fluid have passed through the sample. These stages are repeated several times to obtain effective and hence relative permeabilities over a range of water saturations.
6. In the next cycle (imbibition) the pump is filled with brine, which is injected into the core to displace the oil from the sample. The same procedure is adopted as describe above but this time the brine relative permeabilities are measured as a function of saturation.

### 6.4.3 Wettability alteration

Attempts were made to alter the wettability of the Orange fault rocks samples to a more oil-water state by aging the samples with crude oil, which was selected as this oil have previously been shown to change the wettability of silica from water to oil-wet. The crude oil (F-200) was used; its properties are provided in Table 6-3. This was used by Talal Al-Aulaqi (2012) to change the wettability of glass slides and mica surfaces from water-wet to more oil-wet.

Crude oils	Density (g/mL)	Interfacial tension (mN/m)	Viscosity (cp)	Asphaltene recovered (wt. %)
F-200	0.857	27.1	19.0	0.56

**Table 6-3: Properties of the crude oil used for wettability alteration.**

Aging was carried out after the oil-water relative permeability experiments. At this stage the samples were at irreducible water saturation (brine) and by contained Multipar – H oil. In the first step, 5 – 20 pore volumes of Decaline was injected into the sample to avoid mixing of the crude oil with Multipar oil. The samples were then flooded with 15 – 20 pore volume of crude oil. The samples were then submerged in crude oils and left in a heated water bath at 60° C for 8 weeks. After aging the crude oil was then displaced from the samples by Decaline followed by Multipar oil. The oil-water relative permeability after aging was determined as described above.

#### **6.4.4 Wettability assessment**

After aging of samples, with crude oil for approximately 8 weeks at a temperature of 60°C, the Amott wettability index has been evaluated to estimate the wettability alteration. The following steps are involved in Amott wettability evaluation:

- 1) The crude oil was removed from the aged samples by flooding Multipar – H oil leaving the sample at irreducible or connate water saturation.
- 2) The samples were immersed in 8% NaBr brine solution for the natural imbibition. The displaced volume of the oil due to spontaneous imbibition was recorded.
- 3) After oil production due to natural imbibition had finished the samples were subject to forced imbibition by using a flow pump to inject NaBr through the sample. The flooding began at a very low flow rate and continued until oil production is stopped. The flow rate and differential pressure are recorded with the quantity of oil produced.

- 4) The flooding is continuing until there is no further oil production at the same flow rate. Then change the flow rate to next higher value and repeats the step 3.
- 5) When there is no further oil production even at very high flow rate the sample is said be at “irreducible oil saturation” and ready for the next step.
- 6) The sample at “irreducible oil saturation” is then immersed in oil for spontaneous imbibition of oil and the displaced volume of brine is recorded until no more oil produced.
- 7) After step 6 when there is no more brine produced by natural imbibition of oil, the sample is subjected to the forced imbibition of oil by applying a very low flow rate of brine by pump.
- 8) The volume of oil produced and differential pressures at every stage of flow rate are recorded.
- 9) Now again the sample is at connate water saturation and the data recorded is used to calculate the relative permeability and Amott wettability index.

Amott (1959) has explained that the wettability of a porous media can be calculated from the relationship of the relative wettability indices which are displacement-by-oil ratio and displacement-by-water ratio, as given below:

$$I_w = \frac{V_{osp}}{V_{ot}} - \frac{V_{wsp}}{V_{wt}}$$

where:

$I_w$  = Amott wettability index

$V_{osp}$  = Volume of oil displaced by spontaneous imbibition of brine

$V_{ot}$  = Total volume of oil displaced (by spontaneous and forced flooding of brine)

$V_{wsp}$  = Volume of brine produced by spontaneous imbibition of oil

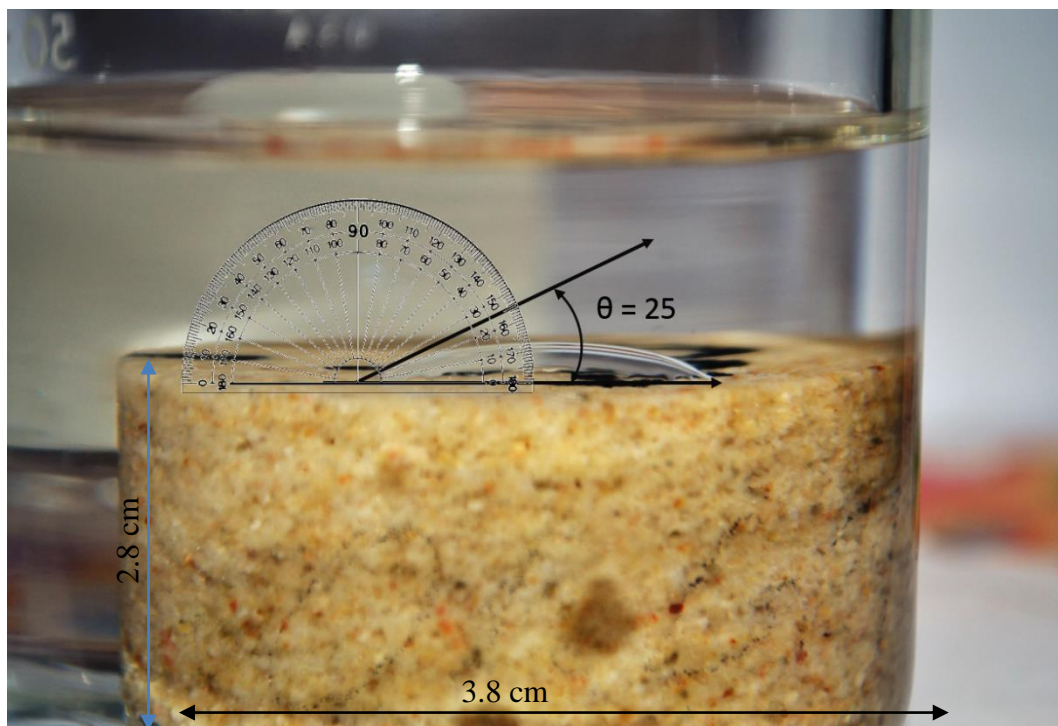
$V_{wt}$  = Total volume of water displaced (by spontaneous and forced flooding of oil)

## 6.5 Results

### 6.5.1 Measurements made on samples before aging

#### 6.5.1.1 Contact angle

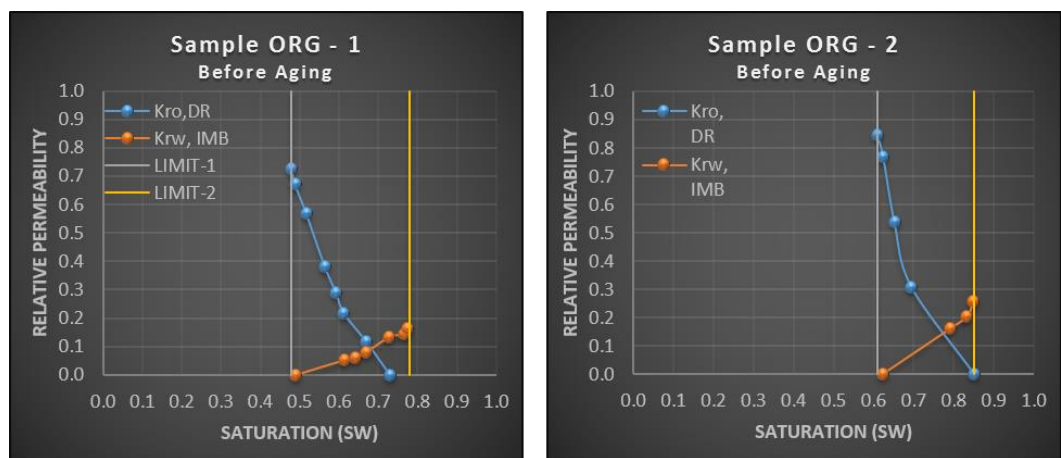
Prior to the initial relative permeability measurement, a contact was found to vary between 25-27° (**Figure 6-10**). According to the classification given by Cuiec (1984), this suggests that the samples were water-wet. The contact angle measurement is not very accurate as the surface of the sample was not entirely smooth and it contained different types of grain surfaces, which may not give exact results.



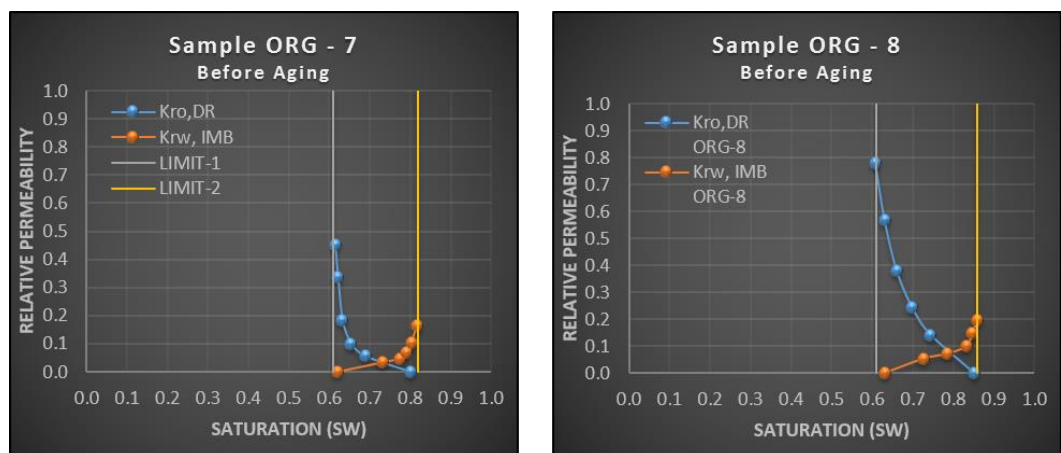
**Figure 6-10: Contact angle measurement for fault rock sample with brine droplet, showing that the Orange fault sample is water wet.**

### 6.5.1.2 Relative permeability results:

The relative permeability curves obtained from the unsteady-state experiments conducted with Multipar-H before aging are shown in **Figure 6-11** and **Figure 6-12**. The non-wetting phase (oil) relative permeabilities are much higher than those of the wetting phase (brine) suggesting that they are water-wet. This is consistent with the crossover of the relative permeability curves occurring at a  $S_w$  value ranging from 67 – 79 %.



**Figure 6-11: Relative permeability curves of ORG-1 and ORG-2 showing high cross over saturations.**



**Figure 6-12: Relative permeability curves for Orange sample, before aging.**

The Amott wettability index of samples before aging are presented in shown in **Table 6-4** . The results of Amott- Harvey wettability index of the orange fault sample show that most of the samples are water wet.

Sample ID	Amott wettability index	Scale (by Cuiec, 1984)
ORG – 1	0.28	Water wet
ORG – 2	0.19	Slightly water wet
ORG – 3	0.23	Water wet
ORG – 4	0.10	Slightly water wet
ORG – 5	0.11	Water wet
ORG – 7	0.15	Water wet
ORG – 8	0.13	Water wet

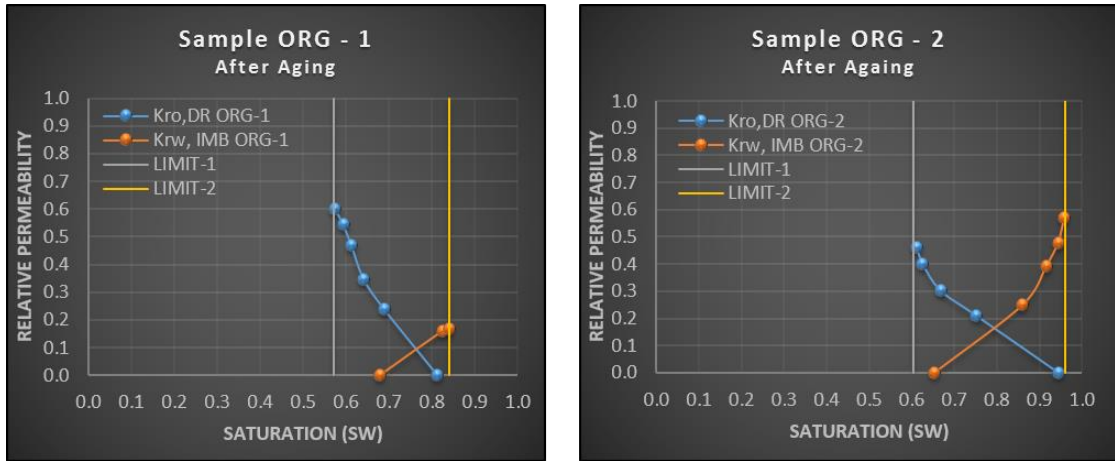
**Table 6-4: Amott wettability index results before aging and wettability classification based on Cuiec (1984).**

## 6.5.2 Measurements made on aged samples

### 6.5.2.1 Relative permeability results

The relative permeability results produced after aging are shown in **Figure 6-13**. These results indicate that the wettability has changed becoming less water-wet. After aging the sample ORG – 1 is not showing any significant alteration in its relative permeability results.





**Figure 6-13: Relative permeability curves of Orange samples after aging.**

The Amott wettability index of the aged samples are shown in **Table 6-5**. The results of Amott- Harvey wettability index of the Orange fault sample shows that most of the samples have changed the wettability from water wet to neutral or oil-wet.

Sample ID	Amott wettability index	Scale (by Cuiec, 1984)
ORG – 1	0.15	Slightly water wet
ORG – 2	0.08	Neutral
ORG – 3	0.10	Slightly water wet
ORG – 4	0.01	Neutral
ORG – 5	-0.03	Oil Wet
ORG – 7	0.0	Neutral
ORG – 8	0.02	Neutral

**Table 6-5: Amott wettability index results after aging and wettability classification based on Cuiec (1984).**

## 6.6 Discussion

Measurements of the apparent contact angle on the Orange fault rocks that has equilibrated with Multipar-H oil were around 27°, which provides reasonably strong evidence that the rocks were water-wet. However, it should be noted that ideally

contact angle measurements should be made on perfectly flat surfaces and that was not the case for the analyses conducted during the current study. Instead, the samples surface will have been slightly rough due to the presence of surface pores. However, the apparent contact angle measurements are consistent with the fact that Multipar-H oil is non-polar and would not be expected to have changed the wettability of the fault rock sample. At first sight, the fact that the crossover in the relative permeability curves for the non-aged fault rocks occurs at a water saturation  $>50\%$  would also be consistent with them being water wet according to Craig's rule (Craig, 1971). However, it is important to take into account how the microstructure of the rock can impact relative permeability. In particular, it has been shown that grain sorting will result in a shift in the crossover of the relative permeability curves to higher water saturations because more water is retained in the small pores and oil preferentially breaks through via the larger pore pathways. Cataclastic deformation has clearly resulted in the Orange samples having a very broad grain-size distribution which is further extenuated by the fact that the samples contains bands of cataclastic fault rock separated by bands of generally undeformed sandstone. In other words, the crossover position of the relative permeability curves should not be taken as strong evidence for the wettability of the samples.

Aging the samples seems to have clearly changed the shape of the relative permeability curve moving their crossover to a lower water saturation, which is consistent with them becoming more oil-wet. This is consistent with the results from the Amott wettability index measurements, which also indicate that aging has moved the samples to a slightly water-wet to neutral-wet. These results are entirely to be expected given that previous studies have shown that the crude oils used in the aging

process have altered the wettability of glass and mica to being oil wet (Al-Aulaqi, 2012).

The recognition that fault rocks can be made less water-wet is significant in that it potentially means that in certain circumstances they may not represent such strong barriers to capillary flow as often argued (e.g. Fisher et al., 2001). Wettability alteration requires polar compounds to be transported from the oil to the mineral surface. This is favoured by having a close proximity between the minerals and the oil-water interface. Fault rocks in petroleum reservoirs generally have a thickness of 1mm to 0.5m (Hull, 1988). This means that polar compounds do not have to travel large distances from the oil to the mineral surface and this could easily occur via diffusion. Once adsorbed to the mineral surface they would reduce the disjoining pressure between the oil-water and mineral-water interface allowing wettability alteration to occur and oil to enter the fault rock at a lower capillary pressure than had the fault rock remained strongly water-wet.

Clearly further work needs to be undertaken, including measuring the wettability of fault rocks within petroleum reservoirs. However, the results presented in this chapter provide some evidence that even though fault rocks appear to have high capillary entry pressures they may not always act as strong capillary seals preventing the movement of hydrocarbons over geological time. The fact that the wettability of fault rocks has been changed via aging with crude also opens up the possibility that wettability altering agents could be injected into oil-reservoirs to reduce the impact that faults have on petroleum flow therefore increasing oil production. Clearly, further work is needed to assess the latter possibility oil-wet reservoirs often have lower ultimate recoveries because they often have higher residual oil saturations. However,

attempting to change the wettability of water-wet sealing faults during late stage production could have potential benefits that should be explored further.

## **6.7 Conclusion**

Despite the recognition that it could be important to consider the multiphase flow properties of fault rocks when modelling fluid flow in fault compartmentalized reservoirs there is no published data on their oil-water relative permeability. The current study has partially filled this knowledge gap by generating relative permeability curves for a cataclastic fault rocks sampled from Orange, France.

The oil-water relative permeability data produced from the fault rock using a non-polar oil is broadly what would be expected from a water-wet sample with a broad grain-size distribution.

The literature contains gas relative permeability data from cataclastic faults, which were also presumably strongly water-wet as gas is virtually always the non-wetting phase in a gas-brine-rock system. So as well as there being a lack of published data on the oil-water relative permeability of fault rocks there are no data on the relative permeability of fault rocks where brine is not the wetting phase. The current study has also partially filled this knowledge gap by changing the wettability of the Orange fault rock samples by aging them in a crude oil that is known to alter the wettability of silica to more oil-wet conditions. The resulting relative permeability curves are consistent with alteration to a range of wetting states from slightly water-wet to oil-wet. The data produced will form the basis for future modelling studies that aim to understand the impact of wettability alteration of fault rocks on fluid flow in fault compartmentalized reservoirs.

# Chapter 7: Conclusions and recommendations for future work:

## 7.1 Introduction

The main goal for this research was to fill in knowledge gaps regarding the single-phase and multiphase flow properties of fault rocks in petroleum reservoirs.

The work as two particular objectives:

- Obtain data on permeability of fault rocks under reservoir stress conditions using formation compatible brines.
- Obtained data on the oil-water relative permeability of fault rocks under a range of wetting conditions.

The first of these objectives stems from the fact that many previous measurements of fault rock permeability that have been published (e.g. Fisher and Knipe, 1998, 2001) were conducted at ambient stress conditions using distilled water as a permeant. This represents extremely poor experimental practise because it is well known that the permeability of tight rocks is very sensitive to the stress conditions under which the measurements are made (Byrnes and Castle, 2000; Morrow and Brower, 1986) and the fluid composition used (Lever and Dawe, 1987; Jones and Owens, 1980; Sampath and Keighin, 1982; Baraka Lokmane, 2002).

The second of these objectives stems from the fact that several publications have argued that it is important to consider the relative permeability of fault rocks when assessing fault sealing in petroleum reservoirs yet the only data available are gas permeability measurements made on strongly water wet rocks. No data are available on oil-water relative permeabilities of water wet fault rocks let alone those with other wettability states.

The current study has generated a large amount of new data to help fill these knowledge gaps. In particular, it has conducted a large number of measurements of the absolute permeability of fault rocks using a range of fluids (gas, brine and distilled water) under a range of stress conditions. The study has also measured the oil water relative permeability of fault rocks under with a range of wetting states (i.e. from water wet, neutral and oil wet). Measurements were made both cataclastic and phyllosilicate-framework fault rocks (PFFR) obtained from producing oil reservoirs and from outcrop. In addition, as a result of the thorough sample characterization program conducted (i.e. microstructural analysis, QXRD etc.), the project has generated data that is relevant to another key issue pertaining to fault seal analysis, namely Vclay-permeability transforms that are used throughout industry within fault seal analysis workflows (Fisher and Jolley, 2007). The aim of the current chapter is to discuss each of these issues and identify the key implications of the results. The chapter provides suggestions for further work on issues related to the petrophysical properties of faults and fault seal analysis in general. Each of these aspects are discussed separately below.

## **7.2 Absolute permeability of fault rocks**

### **7.2.1 Stress sensitivity of permeability**

The experimental program conducted during this study showed that the permeability of all fault rocks was stress sensitive regardless of the type of fluid used. Overall, the permeability measured at in situ stress conditions averages around 20% that measured at ambient stress conditions. These results are totally consistent with the experimental results obtained from tight gas sandstone reservoirs (e.g. Byrnes and Castle, 2000; Morrow and Brower, 1986). The stress sensitivity of the fault rocks is

consistent with the closure of grain-scale microfractures observed during microstructural analysis, which become closed as confining pressure is increased.

These grain-scale microfractures probably formed as the samples were uplifted to the surface, which is probably the reason why samples obtained from petroleum reservoirs are less stress sensitive than samples obtained from outcrop. The fact that the stress sensitivity of permeability is primarily controlled by features formed during uplift probably means that the in situ permeability of samples is not particularly stress sensitive. If proven to be correct, this would be a welcome relief for those involved in fault seal analysis because it would mean that they do not need to consider how production-induced reservoir stress changes affect fault permeability. The latter would add a massive layer of complexity to fault seal analysis because predicting reservoir stress evolution can be difficult particularly when processes such as stress arching become important (Segura et al., 2011).

### **7.2.2 Impact of fluid composition on fault permeability**

The results from this research indicate that the permeability of fault rocks to gas is around a factor of five higher than for the brine permeability, which again is around a factor of five higher than measured using distilled water. These results are totally consistent with the idea that permeability decreases as the reactivity of the fluid increases. Helium gas is non-reactive, the concentrated brine does react with mineral surfaces but its high ionic concentration means that electrical double layers do not form and other process such as electrokinetic interactions are minimized. On the other hand, distilled water can result in clay swelling, the formation of electrical double layers and the detachment of clay particles from the surface of pores, which may then block pore throats.

Considering these results in isolation would indicate that much of the published data where measurements were conducted using distilled water would significantly underestimate permeability. However, considering them in conjunction with the results obtained from measurements of stress sensitivity leads to a different conclusion. In particular, the fact that in situ stress measurements of fault rock permeability are on average 20% those conducted at ambient stress compensates for the fact that using distilled water results in an average reduction in permeability by 20%. In effect two poor laboratory practices have partially cancelled each other out: in this case two wrongs have almost created a right. Although it would not be recommended that industry continues to use such poor laboratory practices, it doesn't mean that there is no need to totally discount previous laboratory measurements of fault rock permeability.

### **7.3 Oil water relative permeability measurements**

The current study has generated the first ever data on the oil-water relative permeability of fault rocks. Measurements were all conducted on cataclastic faults obtained from a quarry in Orange, France. Initial measurements were made using a non-polar mineral oil, which was assumed to ensure that the fault rock remained strongly water wet. This was confirmed by contact angle measurements. The relative permeability curves obtained has a crossover between the brine and oil relative permeabilities at a water saturation of around 70%. The spread of data between oil and water end-points occurred over narrow water saturation range of around 20%, which is consistent with previous measurements conducted on rocks with poor grain sorting.

The samples were aged in a crude oil that was known to alter the wettability of silica surfaces. The results from drainage and imbibition experiments confirmed that



the wettability of the samples had been altered to being less water wet (range from mildly water wet to oil wet). This wettability alteration resulted in the movement of the crossover in relative permeabilities to lower water saturations and a broadening of the saturation range between endpoint water and oil relative permeabilities.

These new results not only provide a platform for modelling cross-fault flow in oil reservoirs but also provide the first evidence that the wettability of fault rocks maybe something other than strongly water wet. The latter result is important because it indicates that in some circumstances fault rocks may not act as capillary barriers to oil flow within petroleum reservoirs.

## **7.4 Clay permeability relationships**

An additional side product of the current research project are data on the relationship between the clay content of fault rocks and their permeability. Such relationships are extensively used in industry to estimate the permeability of faults in petroleum reservoirs following the application of algorithms such as shale gouge ratio (e.g. Fisher and Jolley, 2007). The data obtained during the current study was extremely scattered. The main clay-permeability algorithm used by industry (i.e. Sperrevik et al., 2002) was applied to the data and provided a reasonable fit although a large amount of scatter existed around relationship. A key problem with the relationship of Sperrevik et al. (2002) is that it predicts an ever decreasing permeability with increasing clay content, which contradicts theoretical mixing laws (e.g. Revil and Cathles, 1999). The mixing law of Revil and Cathles (1999) was therefore applied to the clay-permeability data obtained from the current study. This mixing law provides a very good explanation why so much scatter in clay permeability relationships exist.

In particular, it reflects the wide range in grain-size distribution of the sand-end member and variations in the permeability of the clay-endmember.

Some data from central North Sea reservoirs were observed to still lie outside of this theoretical mixing model. Examination of the microstructure of the samples revealed that they contained considerable quantities of coarse grain mica and chlorite, which don't have such detrimental impact on permeability of clay-sized mica (illite) and chlorite. These results highlight the importance of integrating microstructural analysis and QXRD when calculating the clay content of reservoir rocks and that this should be considered when calibrating wire-line log derived  $V_{clay}$  estimates.

## **7.5 Recommendation for the future work**

The current study has only scratched the surface in terms of making measurements of the single-phase and multiphase properties of fault rocks in petroleum reservoirs. It is unrealistic to expect large amounts of data to be collected in other PhD projects. A far more effective way of generating such data is to publish the results from the current study and then encourage industry to make similar measurements as part of their reservoir characterization program.

It is standard practice for industry to conduct MIPC analysis to measure the threshold pressure of fault rocks to calculate the petroleum column height that they can support. The current study has also conducted a small number of MICP measurements. A key problem with these measurements is that they are made on unconfined samples and sort are essentially low stress measurements. It is known that permeability of petroleum reservoirs is extremely stress sensitive and it is likely that

the same is true of capillary pressure. It is therefore recommended that MICP measurements are conducted at higher confining pressures.

The current study concentrated on making oil-water relative permeability measurements. This was not sufficient time available to conduct oil-water capillary pressure measurements on fault rock samples. This means that we have not direct evidence of how wettability alteration altered the capillary pressure of fault rocks and hence how the column heights that they support could be affected. It is therefore recommended that measurements of the oil-water capillary pressure as a function of wettability alteration are conducted in future studies.

Finally, great uncertainty exists in the lateral continuity of fault rocks in the subsurface and how to upscale laboratory measurements for incorporation into simulation models. Increasing understanding of this subject requires careful integration of workflows between different disciplines. In particular, it is important to incorporate the results of studies such as this into simulation models to identify whether or not they help explain production behaviour. Undertaking such studies allows workflows to be adapted via continual learning and improvement so as to benefit future reservoir characterization and modelling studies.

## References

- Al-Aulaqi, T. (2012). Wettability alteration in rock reservoirs and its effect in petroleum recovery. PhD thesis, University of Leeds.
- Al-Busafi, B. (2005). Incorporation of fault rock properties into production simulation models. PhD thesis, University of Leeds.
- Al-Busafi, B., Fisher, Q.J. & Harris, S.D. (2005). The importance of incorporating the multiphase flow properties of fault rocks into production simulation models. *Marine and Petroleum Geology*, 22, 365-374.
- Al-Hinai, S. (2007). Multiphase fluid flow properties of fault rocks: implications for production simulation models. PhD Thesis. University of Leeds.
- Al-Hinai, S., Fisher, Q. J., Al-Busafi, B., Guise, P. & Grattoni, C. A. (2008). Relative Permeability of Faults: An Important Consideration for Production Simulation Modelling. *Marine and Petroleum Geology*, 25, 473-485.
- Amaefule, J., Wolfe, K., Walls, J., Ajufo, A. & Peterson, E. (1986). Laboratory determination of effective liquid permeability in low-quality reservoir rocks by the pulse decay technique. SPE California Regional Meeting. Society of Petroleum Engineers
- Amott, E. (1959). Observations Relating to the Wettability of Porous Rock. *Trans., AIME* 216, 156-62.
- Andersen, M. A.; Duncan Brent, D. & McLin Ryan. (2013). Core Truth in formation Evaluation, *Oilfields Review Summer 2013*, Schlumberger.
- Anderson, W. G. (1986-a). Wettability Literature Survey, Part 1: Rock/oil/brine interactions and the effects of core handling on wettability. *JPT* (Oct): 1125-1144.
- Anderson, W. G. (1986-b). Wettability Literature Survey, Part 2: Wettability measurement. *JPT* (Nov): 1246-1262.
- Anderson, W. G. (1986c). Wettability Literature Survey, Part 3: The effects of wettability on the electrical properties of porous media. *JPT* (Dec): 1371-1378.

Anderson, W. G. (1987-a). Wettability Literature Survey, Part 4: Effects of wettability on capillary pressure. *JPT* (Oct): 1283-1300.

Anderson, W. G. (1987-b). Wettability Literature Survey, Part 5: The effects of wettability on relative permeability. *JPT* (Nov): 1453-1468.

Anderson, W. G. (1987-c). Wettability Literature Survey, Part 6: The effects of wettability on water flooding. *JPT* (Dec): 1605-1 622

Antonelli, M. & Aydin, A. (1995). Effect of Faulting on fluid flow in Porous Sandstones: Geometry and spatial distribution. *Bulletin of the American Association of Petroleum Geologists* 79 (5), 642-671.

Antonellini, M. & Aydin, A. (1994). Effect of faulting on fluid flow in porous sandstones: petrophysical properties. *Am. Assoc. Pet. Geol. Bull.*, 78 (3): 355-377.

Antonellini, M., Aydin, A., Pollard, D. D. & D'Onfro, P. (1994). Petrophysical study of faults in sandstone using petrographic image analysis and X-ray computerized tomography. *Pure Appl. Geophys.*, 143 (1/2/3): 181-201.

API (1998) Recommended Practices for Core Analysis, API RP 40. Washington: American Petroleum Institute.

Archer, S., Ward, S., Menad, S., Shahim, I., Grant, N., Sloan, H., & Cole, A. (2010). The Jasmine discovery, Central North Sea, UKCS. In Geological Society, London, Petroleum Geology Conference series (Vol. 7, pp. 225-243). Geological Society of London.

Aydin, A. & Johnson, A. M. (1978). Development of faults as zones of deformation bands and as slip surfaces in sandstone. *Pure Appl. Geophys.*, 116:931-942.

Aydin, A. (2000). Fractures, faults, and hydrocarbon entrapment, migration and flow. *Mar. Pet. Geol.* 17, 797 – 814.

Bakhmeteff, B. A. & Fedoroff, N.V. (1943). Energy Loss at the Base of a Free Over fall - Discussion. *Transactions, ASCE*, Vol. 108, pp. 1364-1373.

Baptist, O. C. & Sweeney, S. A. (1955) Effect of clays on the permeability of reservoir sands to various saline waters: Bureau of Mines Rep. of Investigations 5180, 23 p.

Baraka-Lokmane, S. (2002). Hydraulic versus pneumatic measurements of fractured sandstone permeability. *Journal of Petroleum Science and Engineering* 36 (2002) 183 – 192.

Beach, A., Welbon, A. I., Brockbank, P. J. & McCallum, J. E. (1999). Reservoir damage around faults: outcrop examples from the Suez Gulf. *Petroleum Geoscience*, 5, 109–116.

Bear, J. (1972). *Dynamics of Fluids in Porous Media*. Elsevier, New York.

Beard, D. C. & Weyl, P. K. (1973). Influence of Texture on Porosity and Permeability of Unconsolidated Sand, *AAPG Bull.*, Vol. 57, No. 2, 349-369.

Bentley M. R. & Barry J. J. (1991). Representation of fault sealing in a reservoir simulation: Cormorant block IV UK North Sea. SPE paper 22667 presented at the SPE annual technical conference and exhibition, Dallas, Texas, 6–9 October

Berg, R.R. (1975). Capillary pressure in stratigraphic traps. *Am. Assoc. Pet. Geol. Bull.*, 59: 939-956.

Bergamini, G. (1962). The Effect of Non-Uniform Stress on Permeability of Sandstones, Unpublished report, U. of California. Petroleum Engineering Laboratory (May 1962)

Bernabe, Y. (1986). Pore volume and transport properties changes during pressure cycling of several crystalline rocks, *Mech. Mater.*, 5, 235-249.

Bernabé, Y. (1987). The effective pressure law for permeability during pore pressure and confining pressure cycling of several crystalline rocks, *J. Geophys. Res.*, 92, 649–657.

Berryman, J. G. & Blair, S. C. (1986). Use of digital image analysis to estimate fluid permeability of porous materials: Application of two-point correlation functions

Bobek, J. E., Mattax, C. C. & Denekas, M. O. (1958): "Reservoir Rock Wettability- Its Significance and Evaluation." *Trans., AIME*, (1958) 213, 155-60.

- Bonson, C. G., Childs, C., Walsh, J. J., Schöpfer, M. P. J. & Carboni, V. (2007). Geometric and kinematic controls on the internal structure of a large normal fault in massive limestone: the Maghlaq Fault, Malta. *Journal of Structural Geology*, 29, 336–354.
- Borradaile, G. J. (1981). Particulate flow of rock and the formation of cleavage. *Tectonophysics* 72, 305 – 321.
- Bourbie T. & Walls J. (1982). Pulse decay permeability: analytical solution and experimental test. *SPEJ* 22:719–721.
- Bouvier, J. D., Kaars-Sijpesteijn, C. H., Kluesner, D. F., Onyejekwe, C.C. & Van der Pal, R. C., (1989). Three-dimensional seismic interpretation and fault sealing investigations. Nun River Field, Nigeria. *Am. Assoc. Pet. Geol. Bull.*, 73: 1397-1414.
- Brace, W. F. (1978). A note on permeability changes in geologic material due to stress. *Pure & Applied Geophys.* 116, 627 – 633.
- Brace, W. F., Walsh, J. B., & Frangos, W. T. (1968). Permeability of Granite under High Pressure, *J. Geophysical Research*, (1968) 73, No. 6, 2225-236.
- Bratton, T., Canh, D. V., Duc, N. V., Gillespie, P. Li, B. Marcinew, R., Montoran, B., Nelson, R., Schoderbek, D. & Sonneland, L. (2006). The nature of naturally fractured reservoirs. *Oilfield Review*, 18, 4– 23.
- Brower, K. R. & Morrow, N. R. (1985). Fluid flow in cracks as related to low permeability gas sands. *Society of Petroleum Engineers*, SPE 11623.
- Brown, R. J. S. & Fatt, I. (1956). Measurement of fractional wettability of oil field Rocks by the nuclear magnetic relaxation Method *Trans., AIME* 207, 262-64.
- Brownell, L. E. & Katz, D. L. (1947). *Chem. Eng. Progr.* 43, 549 – 54, 601-12.
- Burhannudinnur, M., & Morley, C. K. (1997). Anatomy of growth fault zones in poorly lithified sandstones and shales: implications for reservoir studies and seismic interpretations: part 1, outcrop study: *Petroleum Geoscience* 3, 211-224.

Byrnes, P. A., Cluff, R. M. & Webb, J. C. (2009). Analysis of critical permeability, capillary and electrical properties for Mesaverde tight gas sandstones from Western US basins: final scientific. Technical report submitted to DOE and NETL, 355

Byrnes, A. P. & Castle, J. W. (2000). Comparison of core petrophysical properties between low-permeability sandstone reservoirs: Eastern U.S. Medina group and Western U.S. Mesaverde group and Frontier formation. Paper presented at SPE Rocky Mountain Regional Low-Permeability Reservoirs Symposium and Exhibition. 12-15 March, at Denver, CO. SPE: paper 60304-MS.

Byrnes, A. P. (1997). Reservoir characteristics of low permeability sandstones in the Rocky Mountains. *RMAG Mountain Geologist* 34-1: 37-48

Byrnes, A. P. (2003). Aspects of Permeability, Capillary Pressure and Relative Permeability Properties and Distribution in Low-Permeability Rocks Important to Evaluation, Damage and Stimulation: Proceedings Rocky Mountain Association of Geologists - Petroleum Systems and Reservoirs of Southwest Wyoming Symposium, Denver, Colorado, September 19, 12 p.

Cade, C. A., Evans, I. J., & Bryant, S.L. (1994). Analysis of permeability controls – a new approach. *Clay Min.* 29, 491–501.

Caine, J. S., Evans, J. P. & Forster, C. B. (1996). Fault zone architecture and permeability structure. *Geology*, 24: 1025-1028.

Calhoun, J. C., Lewis, Jr., M. & Newman, R. C. (1949). Experiments on the Capillary Properties of Porous Solids. *Trans AIME* 186, 189-196.

Carlson, R. L. (2011). The effect of hydrothermal alteration on the seismic structure of the upper oceanic crust: Evidence from Holes 504B and 1256D, *Geochem. Geophysics. Geosystem.* 12, Q04007, doi: 10.1029/2009GC002955.

Carman, P. C. (1937). Fluid flow through granular beds. *Transactions of the Institution of Chemical Engineers (London)*, 15, 150 – 166

Carpenter, C. B. & Spencer, G. B. (1940). Measurements of compressibility of consolidated oil bearing sandstones: U. S. Bur. Mines, Rept. Inv., v. 3540, 20 p



Castle, J. W., & Byrnes, A. P. (1998). Petrophysics of low-permeability medina sandstone, northwestern Pennsylvania, Appalachian Basin. *Log Analyst*, 39(4), 36-45.

Chapman, R. E. (1981). *Geology and Water. An Introduction to Fluid Mechanics for Geologists*, Nijhoff. The Hague.

Chen, T. & Stagg, P.W. (1984). Semi log Analysis of the Pulse-Decay Technique of Permeability Measurement. *SPEJ*. (December 1984) 639-42.

Childs, C., Manzocchi, T., Nell, P. A. R., Walsh, J. J., Strand, J. A., Heath, A. E. & Lygren, T.H. (2002). Geological implications of a large pressure difference across a small fault in the Viking Graben. In: Koestler, A.G. & Hunsdale, R. (eds) *Hydrocarbon seal quantification*. Norwegian Petroleum Society (NPF) Special Publication, 11, 127–139.

Childs, C., Walsh, J. J. & Watterson, J. (1996). A model for the structure and development of fault zones. *Journal of the Geological Society, London*, 153, 337–340.

Childs, C., Walsh, J. J. & Watterson, J., (1997). Complexity in fault zone structure and implications for fault seal prediction. In: P. Møller-Pedersen and A.G. Koestler (Editors), *Hydrocarbon Seals: Importance for Exploration and Production*. Norwegian Petroleum Society (NPF), Special Publication 7. Elsevier, Amsterdam, pp. 61-72.

Civan, F. (2000b). Predictability of porosity and permeability alterations by geochemical and geomechanical rock and fluid interactions. Paper SPE 58746, *Proceedings of the SPE International Symposium on Formation Damage*, Lafayette, LA, February 23 – 24, pp. 359 – 370.

Civan, F. (2000d). Unfrozen water content in freezing and thawing soils - kinetics and correlation. *Journal of Cold Regions Engineering*, 14 (3), pp. 146 – 156.

Civan, F. (2012). Temperature dependency of dynamic coefficient for non-equilibrium capillary pressure-saturation relationship. R&D note, *AICHE J* 2012; 58 (7):2282–2285. DOI: 10.1002/aic.13817.

Cluff, R. M. & Byrnes, A. P. (2010). Relative permeability in tight gas sandstone reservoirs—the “Permeability Jail” Model. In SPWLA 51st Annual Logging Symposium. Society of Petrophysicists and Well-Log Analysts

Colins, R. E. (1976). Flow of Fluids through Porous Materials. The Petroleum Publishing Co., Tulsa, OK.

Coney, D., Fyfe, T. B., Retail, P. & Smith, P. J. (1993). Clair appraisal: The benefits of a co-operative approach. In J. R. Parker (Ed.), Petroleum Geology of Northwest Europe: Proceedings of the fourth conference (pp. 1473 – 1482). London: The Geological Society.

Corrigan, A. F. (1993). Estimation of recoverable reserves: The geologist’s job. In J. R. Parker (Ed), Petroleum Geology of Northwest Europe: Proceedings of the fourth conference (pp. 1473 – 1482). London: The Geological Society.

Coward, R. N., Clark, N. M. & Pinnock, S. J. (1991). The Tartan Field, Block 15/16, UK North Sea. In: Abbotts, I. L. (ed.) United Kingdom Oil and Gas Fields 25 Years Commemorative Volume. The Geological Society, London, Memoir, 14, 377-386

Craig, F. F. (1971). The reservoir engineering aspects of water flooding, Monograph Series, SPE, Richardson, TX (1971).

Crawford, B. R., Myers, R. D., Woronow, A., Faulkner, D. R. & Rutter, E. H. (2002). Porosity–permeability relationships in clay-bearing fault gouge. Paper 78214 presented at the Society of Petroleum Engineers/International Society of Rock Mechanics Conference, Irving Texas.

Cuiec, L. E. (1984). Rock/Crude Oil Interactions and Wettability: An attempt to understand their interrelation. SPE 13211 presented at the 1984 SPE Annual Technical Conference and Exhibition, Houston, Sept. 16-19.

Dake, L.P. (2001). Fundamentals of Reservoir Engineering. Elsevier Scientific Publishing Co, Amsterdam.

Dandekar, A. Y. (2006). Petroleum reservoir rocks and fluid properties: Boca Raton, Florida, Taylor & Francis Group, 460 p.

Darcy, H. (1856). *Les Fontaines Publiques de la Ville de Dijon*. Victor Dalmont, Paris.

David, C., Wong, T. F., Zhu, W., Zhang, J. (1994). Laboratory measurement of compaction induced permeability change in porous rocks: implication for the generation and maintenance of pore pressure excess in the crust. *Pure Applied Geophysics* 1994; 143:425–56.

Davies, J. P. & Davies, D. K. (1999). Stress-dependent permeability: Characterization and modelling. *SPE Annual Technical Conference and Exhibition*, 1999, pp. 1-15.

Davies, J. P. & Holditch, S. A. (1998). Stress-dependent permeability in low permeability Gas reservoirs: Travis peak formation, East Texas. *SPE Rocky Mountain Regional Low-Permeability Reservoirs Symposium and Exhibition*. pp. 117-128.

Delfaud, J. & Dubois P. (1984). Le bassin du Sud-Est. In: *Dynamique des bassins sedimentaires*. Livre jubilaire BRGM (ed. Gubler Y), pp. 347–61. BRGM, Orleans, France.

Dicker, A. I. & Smits, R. M. (1998). A practical approach for determining permeability from laboratory pressure-pulse decay measurements. Paper SPE 17578 presented at the 1998 SPE international meeting on petroleum engineering, Tianjin, China, 1-4 November.

Donaldson, E. C. & Crocker, M. E. (1977). Review of Petroleum Oil Saturation and Its Determination. Bartlesville Energy Research Center, U.S. DOE, report BERC/RI-77/15. (Dec. 1977).

Donaldson, E. C. & Thomas, R. D. (1971). Microscopic Observations of Oil Displacement in Water-Wet and Oil-Wet Systems. SPE paper 3555 presented at the 1971 SPE Annual Meeting, New Orleans, Oct. 3-6.

Donaldson, E. C., Thomas, R. D. & Lorenz, P. B. (1969). Wettability Determination and Its Effect on recovery efficiency. *SPEJ* (March 1969) 13-20.

Downey, M. W. (1984). Evaluating fault seals for hydrocarbon accumulations. *Am. Assoc. Pet. Geol. Bull.*, 68 (11): 1752-1763.

Dullien, F. A. (1979). *Porous Media: Fluid Transport and Pore Structure*, Academic Press, New York City (1979).

Dunn, D. E., LaFountain, L. J. & Jackson, R. E. (1973). Porosity dependence and mechanism of brittle fracture in sandstone. *J. Geophys. Res.*, 78 (14): 2403-2417.

Dykstra, H. & Parsons, R. L. (1950). *The Prediction of oil recovery in Water flood. Secondary Recovery of Oil in the United States*, 2nd ed. American Petroleum Institute (API), 1950, pp. 160-174.

Edwards, H. E., Becker, A. D. & Howell, J. A. (1994). Compartmentalisation of an aeolian sandstone by structural heterogeneities: Permo-Triassic Hope Sandstone, Moray Firth, Scotland. *Geol. Soc. Spec. Publ. Lond.* 73,339-365.

Ellevset, S. O., Knipe, R. J., Olsen, T. S., Fisher, Q. J. & Jones, G. (1998). Fault controlled communication in the Sleipner Vest Field, Norwegian Continental Shelf; detailed, quantitative input for reservoir simulation and well planning. This volume.

Engelder, J. T. (1974). Cataclasis and the generation of fault gouge. *Geol. Soc. Am. Bull.*, 85: 1515-1522.

Evans, J. P., Forster, C. B., & Goddard, J. V. (1997). Permeabilities of fault-related rocks and implications for fault-zone hydraulic structure. *J. Struct. Geol.* 19, 1393-1404

Evans, J.P. (1990). Thickness-displacement relationships for fault zones. *J. Struct. Geol.*, 12 (8): 1061-1065.

Fatt, I. & Davis, D. H. (1952). Reduction in Permeability with Overburden Pressure. *Trans., AIME* (1952) 195, 329.

Fatt, I. (1956). The network model of porous media. Vol-207. Society of Petroleum Engineers AIME, pp 144–181

Fisher, Q. J. & Jolley, S. J. (2007). Treatment of faults in production simulation models. In: Jolley, S. J., Barr, D., Walsh, J. J. & Knipe, R. J. (eds) *Structurally Complex Reservoirs*. Geological Society, London, Special Publications, 292, 219–234.

Fisher, Q. J. & Knipe, R. J. (1998) Fault sealing processes in siliciclastic sediments. In: G. Jones, Q. Fisher and R. J. Knipe, (Eds.), *Faulting and Fault Sealing in Hydrocarbon Reservoirs*. Geological Society, London, Special Publication, 147, 117-134.

Fisher, Q. J., & Knipe, R. J. (2001). The permeability of faults within siliciclastic petroleum reservoirs of the North Sea and Norwegian Continental Shelf. *Marine and Petroleum Geology*, 18, 1063-1081.

Fisher, Q. J., Casey, M., Harris, S. D., & Knipe, R. J. (2003). The fluid flow properties of faults in sandstone: the importance of temperature history. *Geology*, 31, 965–968.

Fisher, Q. J., Casey, M., Knipe, R. J. & Clennell, M. B. (1999). Mechanical compaction of deeply buried sandstones of the North Sea. *Marine and Petroleum Geology*, 16, 605–618.

Fisher, Q. J., Harris, S. D., McAllister, E., Knipe, R. J. & Bolton, A. J. (2001a). Hydrocarbon flow across faults by capillary leakage revisited. *Marine and Petroleum Geology*, 18, 251– 57.

Fisher, Q. J., Knipe, R.J. and Worden, R. H., (2000). The microstructure of deformed and undeformed sandstones from the North Sea: its implications for the origin of quartz cement. In: R. Worden and S. Morad (Editors), *Quartz Cementation in Sandstones*. Int. Assoc. Sedimentol. Spec. Publ., 29: 129-146.

Forchheimer, P. (1901). *Wasserbewegung durch Boden*. Zeitschrift des Vereines Deutscher Ingenieur, 45 edition.

Foxford, K. A., Walsh, J. J., Watterson, J., Garden, I. R., Guscott, S. C. & Burley, S. D. (1998). Structure and content of the Moab Fault zone, Utah, USA. In: Jones, G., Fisher, Q. J. & Knipe, R.J. (eds) *Faulting, Fault Sealing and Fluid Flow in Hydrocarbon Reservoirs*. Geological Society, London, Special Publications, 147, 87–103.

Freeze, R. A. & Cherry, J. A. (1979). *Groundwater*, Englewood Cliffs, NJ, Prentice – Hall.

Fristad, T., Groth, A., Yielding, G. & Freeman, B. (1997). Quantitative fault seal prediction – a case study from Oseberg Syd area. In: Møller-Pedersen, P. & Koestler, A. G. (eds) *Hydrocarbon Seals: Importance for Exploration and Production*. Norwegian Petroleum Society (NPF) Special Publication, Elsevier, Amsterdam, 7, 107–124.

Fulljames, J. R., Zijerveld, L. J. & Franssen, R. C. (1997). Fault seal processes: systematic analysis of fault seals over geological and production time scales. In: P. Moller-Pedersen and A.G. Koestler (Editors), *Hydrocarbon Seals: Importance for Exploration and Production*. Norwegian Petroleum Society (NPF), Special Publication 7. Elsevier, Amsterdam, pp. 51-59.

Gabrielsen, R. H. & Clausen, J.A. (2001). Horses and duplexes in extensional regimes: A scale modelling contribution. In: H.A. Koyi and N.S. Mancktelow (Editors), *Tectonic Modelling: A Volume in Honor of Hans Ramberg*. Geol. Soc. Am. Mem., 193: 219-233.

Gangi, A. F. (1978). Variation of whole and fractured porous rock permeability with confining pressure, *Int. J. Rock Mech. Min. Sci.*, 15, 249–257.

Geoff, B., Michael, P., Waterhouse, J. (2013). *Guidelines for evaluating water in pit slope stability*, CSIRO Publishing

Gibson, R. G. (1994). Fault- zone seals in siliclastic strata of the Columbus Basin, Offshore Trinidad. *Am. Assoc. Pet. Geol. Bull.*, 78 (9): 1372-1385.

Gibson, R. G. (1998). Physical character and fluid flow properties of sandstone-derived fault zones, in M. P. Coward, T. S. Daltaban, and H. Johnson, eds., *Structural geology in reservoir characterization: Geological Society (London) Special Publication 127*, p. 83–98.

Giesche, H. (2006). Mercury porosimetry: A general (practical) overview. *Particle & Particle Systems Characterization* 23, 9–19.

Glennie, K. W. & Buller, A. T. (1983). The Permian Weisslied of N.W. Europe: the partial deformation of aeolian dune sands caused by the Zechstein transgression. *Sedimentary Geology*, 35, 43-81.

Goldsmith, P. J., Rich, B. & Standring, J. (1995). In Permian and Triassic Rifting in Northwest Europe, Triassic correlation and stratigraphy in the South Central Graben, UK North Sea, Geological Society, London, Special Publications, ed Boldy S. A. R. 91, pp 123–143.

Gray, D. H., Fatt, I. & Bergamini, G. (1963). The effect of stress on permeability of sandstone cores, SPEJ (June 1963) 95-100.

Guo, Q. T. & Abbas, F. (2003). Wettability alteration to intermediate gas-wetting in porous media at elevated temperatures. *Trans. Porous Med.* 52:185–221.

Hardman, R. F. P. & Booth, J. E. (1991). The significance of normal faults in the exploration and production of hydrocarbons. In: Roberts, A.M., Yielding, G., Freeman, B. (Eds.), *The Geometry of Normal Faults*, vol. 56. Geological Society, London, pp. 1-3 (Special Publication).

Harper, T. R. & Lundin, E. R., (1997). Fault seal analysis: reducing our dependence on empiricism. In: P. Moller-Pedersen and A.G. Koestler (Editors), *Hydrocarbon Seals: Importance for Exploration and Production*. Norwegian Petroleum Society (NPF), Special Publication 7. Elsevier, Amsterdam, pp. 149-165.

Harris, J. H., Quan, Y. L. & Xu, C. T. (2005) Differential acoustic resonance spectroscopy: An experimental method for estimating acoustic attenuation in porous media: 75th Annual International Meeting, SEG, Expanded Abstracts, 1569–1572.

Harris, S. D., McAallister, E., Knipe, R. J. & Odling, N. E. (2003a). Predicting the three-dimensional population characteristics of fault zones: a study using stochastic models. *Journal of Structural Geology*, 25, 1281–1299.

Harris, S. D., Vaszi, A. Z. & Knipe, R. J. (2007). Three dimensional upscaling of fault damage zones for reservoir simulation. In: Jolley, S. J., Barr, D., Walsh, J. J. & Knipe, R. J. (eds) *Structurally Complex Reservoirs*. Geological Society, London, Special Publications, 292, 353–374.

Hewitt, C. H. (1963). Analytical technique for recognizing water sensitive reservoir rocks. *JPT Vol 15, No. 8 1963*. pp. 813 – 818.

Hodgson, N. A., Farnsworth, J. & Fraser, A. J. (1992). Salt-related tectonics, sedimentation and hydrocarbon plays in the Central Graben, North Sea, UKCS. In: Hardman, R. F. P. (ed.) *Exploration Britain; Geological Insights for the Next Decade*. Geological Society, London, Special Publications, 67, 31–63. Hook, 2003

Holdich, R. G. (2002). *Fundamentals of Particle Technology*. Midland Information Technology & Publishing. U.K. ISSN/ISBN. 0954388100.

Holt, R. M. (1989). Permeability Reduction Induced by a Non-hydrostatic Stress Field. SPE 19595, Presented at the 64th Annual Technical Conference and Exhibition of SPE in San Antonio, TX (1989), 251-258.

Honarpour, M. L., Koederitz, L. & Harvey A. H. (1986). *Relative Permeability of Petroleum Reservoirs*, CRC Press, Boca Raton, Fla.

Houseknecht, D. W. (1987). Assessing the relative importance of compaction processes and cementation to reduction of porosity in sandstones: AAPG Bulletin, v. 71, p. 633-64

Hsieh, P. A., Tracy, J. V., Neuzil, C. E., Bredehoeft, J. D. & Silliman, S. E. (1981). A Transient Laboratory Method for Determining the Hydraulic Properties of Tight Rocks I. Theory. *Int. Journal of Rock Mechanics, Mineral Sciences & Geomechanical Abstracts*, 1980, pp. 245-252.

Hubbert, M. K. (1940). Theory of ground-water motion. *J. Geology*, 48 (8): 785-944.

Hull, J. (1988). Thickness–displacement relationships for deformation zones. *Journal of Structural Geology*, 10, 431–435.

Ibrahim, M. A., Tek, M. R. & Katz, D. L. (1970). Threshold pressure in gas storage. *American Gas Association*, Arlington, VA, 309 pp.

James, G. B. & Blair, S. C. (1986). Use of digital image analysis to estimate fluid permeability of porous materials: Application of two-point correlation functions

Jerauld G. R. & Salter S. J. (1990). The effect of pore-structure on hysteresis in relative permeability and capillary pressure: pore-level modelling. *Transp Porous Med* 5:103–151



- Johnson, E. F., Bossler, D. P. & Naumann, V. O. (1959). Calculation of relative permeability from displacement experiments. *Trans., AIME* (1959) 216, 370-72
- Jolley, S. J., Dijk, H., Lamens, J. H., Fisher, Q. J., Manzocchi, T., Eikmans, H. & Huang, Y. (2007). Faulting and fault sealing in production simulation models: Brent Province, northern North Sea. *Petroleum Geoscience*, 13, 321–340.
- Jones, F. O. & Owens, W. W. (1980). A laboratory study of low permeability gas sands, *J. Pet. Tech.*, 32, 1631–1640.
- Jones, F. O. Jr. (1975). A laboratory study of the effects of confining pressure on fracture flow and storage capacity in carbonate rocks. *SPE (JPT) Paper – 4569 – PA*.
- Jones, S. C. (1988). Two-point determination of permeability and PV vs. net confining stress. *SPE Formation Evaluation*, March 1988, pp. 235-241.
- Jones, S.C. (1972). A rapid accurate unsteady-state Klinkenberg permeameter. *SPEJ*. (October 1972) 383-97.
- Jones, S.C. (1994). A Technique for Faster Pulse-Decay Permeability Measurements in Tight Rocks. *SPE Formation Evaluation*, SPE: 28450-PA
- Jorden, J. R. & Campbell, F. L. (1986). *Well Logging II - Electrical and Acoustic Logging*, SPE of AIME, 1986.
- Katz, A. J., Thompson, A. H. (1986). Quantitative prediction of permeability in porous rock: *Physical Review B*, v. 34, p. 8179–8181, doi:10.1103/Phys Rev B.34.8179.
- Keller, L. M., Holzer, L., Wepf, R. & Gasser, P. (2011). 3D Geometry and topology of pore pathways in Opalinus clay: Implications for mass transport, *Appl. Clay Sci.*, 52, 85–95.
- Klinkenberg, L. J. (1941). The permeability of porous media to liquids and gases. *API Drilling and Production Practice*, 200-213
- Knai, T. A. & Knipe, R. J. (1998). The impact of faults on fluid flow in the Heidrun Field. In: Jones, G., Fisher, Q.J. & Knipe, R.J. (eds) *Faulting, Fault Sealing and Fluid*

Flow in Hydrocarbon Reservoirs. Geological Society, London, Special Publications, 147, 269–282

Knipe, R. J. (1992). Faulting processes and fault seal, in R. M. Larsen, H. Brekke, B. T. Larsen, and E. Talleras, eds., *Structural and tectonic modelling and its application to petroleum geology*: Amsterdam, Elsevier, p. 325–342

Knipe, R. J. (1993). The influence of fault zone processes and diagenesis on fluid flow, in A. D. Horbury and A. D. Robinson, eds., *Diagenesis and basin development: AAPG Studies in Geology* 36, p. 135–151.

Knipe, R. J. (1997). Juxtaposition and seal diagrams to help analyse fault seals in hydrocarbon reservoirs. *American Association of Petroleum Geology Bulletin*, 81, 187–195.

Knott, S. D., Beach, A., Brockbank, P. J., Lawson Brown, J., Mccallum, J. E. & Welbon, A. I. (1996). Spatial and mechanical controls on normal fault populations. *Journal of Structural Geology*, 18, 359– 372.

Kozeny, J. (1927). *Über Kapillare Leitung des Wasser im Boden*. *Sitzungsbericht der Akademie der Wissenschaften, Wien*, 136, pp. 271 – 306.

Kundt, A. & Warburg, E. (1875). *Poggendorf. Ann. Physik.*, 155, 337 and 525

Kwon, O, Kronenberg A. K., Gangi A. F., Johnson B, Herbert BE. Permeability of illite-bearing shale: Anisotropy and effects of clay content and loading. *J Geophys Res* 2004;109 (B10205)

Land, C. S. & Baptist, O. C. (1965). Effect of hydration of montmorillonite on the permeability to gas of water-sensitive reservoir rocks, *J. Pet. Technol.*, 17, 1213-1218.

Law, J. (1944). *Statistical Approach to the Interstitial Heterogeneity of Sand Reservoirs*. *Trans. AIME*, Vol. 155, 1944.

Lehner, F. K. & Pilaar, W. F. (1997). The emplacement of clay smears in sedimentary normal faults: inferences from field observations near Frechen, Germany. In: Møller-Pedersen, P. & Koestler, A. G. (eds) *Hydrocarbon Seals: Importance for Exploration*

and Production. Norwegian Petroleum Society (NPF) Special Publication, Elsevier, Amsterdam, 7, 39–50.

Lesslar, P. & Wannier, M. (1998). Destination Miri - A geological tour northern Sarawak's national parks and giant caves: Ecomedia CD-Rom. <http://www.sarawak.com.my/ecomedia> software.

Lever, A., & Dawe, R. A. (1987). Clay migration and entrapment in synthetic porous media. *Marine and Petroleum Geology*, 4, 112-118.

Leverett, M. C. (1941). Capillary Behaviour in Porous Solids. *Trans., AIME* (1941) 142, 152-69.

Lin, W. (1977). Compressible fluid flow through rocks of variable permeability Lawrence Livermore Laboratory, Livermore, California, Rept. pp. UCRL-52304.

Lindquist, E. (1933). On the flow of water through porous soil. *Let Congrès des Grands Barrages* (Stockholm, 1933), 5: 81–101.

Lindsay, N. G., Murphy, F. C., Walsh, J. J. & Watterson, J. (1993). Outcrop studies of shale smears on fault surfaces. In: S.T. Flint and A.D. Bryant (Editors), *The Geological Modelling of Hydrocarbon Reservoirs and Outcrop*. *Int. Assoc. Sedimentol. Spec. Publ.*, 15: 113-123.

Mandl, G., Jong, L. N. J. & Maltha, A. (1977). Shear zones in granular material: *Rock Mechanics*, v. 9, p. 95–144.

Manzocchi, T., Carter, J. N., Skorstad, A., Fjellvoll, B., Stephen, K. D., Howell, JA, Matthews, J. D., Walsh, J. J., Nepveu, M. & Bos, C. (2008). Sensitivity of the impact of geological uncertainty on production from faulted and un-faulted shallow-marine oil reservoirs: objectives and methods. *Petroleum Geoscience*, 14, 3–15.

Manzocchi, T., Childs, C. & Walsh, J. J. (2010). Faults and fault properties in hydrocarbon flow models: *Geofluids*, v. 10, p. 94-113.

Manzocchi, T., Heath, A. E., Walsh, J. J. & Childs, C. (2002). The representation of two phase fault-rock properties in flow simulation models. *Petroleum Geoscience*, 8, 119–132.

Manzocchi, T., Walsh, J. J., Nell, P. & Yielding, G. (1999). Fault transmissibility multipliers for flow simulation models. *Petroleum Geoscience*, 5, 53–63.

Manzocchi, T., Walsh, J. J., Tomasso, M., Strand, J., Childs, C. & Haughton, P. (2007). Static and dynamic connectivity in bed-scale models of faulted and un-faulted turbidites. In: Jolley, S. J., Barr, D., Walsh, J. J. & Knipe, R. J. (eds) *Structurally Complex Reservoirs*. Geological Society, London, Special Publications, 292, 309–336.

Marsden, S. S. Wettability-Its Measurement and Application to Water flooding. *J. Jap. Assoc. Pet. Tech.* (Jan. 1965) 30, No. 1, 1-10.

McGhee, J. W., Crocker, M. E. & Donaldson, E. C. (1979). Relative Wetting Properties of Crude Oils in Berea Sandstone," Bartlesville Energy Technology Centre, report BETC/RI-78/9, U.S. DOE (Jan. 1979).

McKee, C. R. & Hanson, M. E. (1975). Explosively created permeability from single charges, *Soc. Pet. Eng. J.*, 15, 495–501, 1975.

McKee, C. R., Bumb, A. C., & Koenig, R. A. (1988). Stress-dependent permeability and porosity of coal and other geologic formations. *SPE-FE* (March 1988) 81.

McKie, T. & Audretsch, P. (2005). Depositional and structural controls on Triassic reservoir performance in the Heron Cluster, ETAP, Central North Sea. In: Dore', A. G. & Vining, B. A. (eds) *Petroleum Geology: North-West Europe and Global Perspectives – Proceedings of the 6th Petroleum Geology Conference*. Geological Society, London, 285–298.

McPhee, C. A. & Arthur, K. G. (1991). Klinkenberg permeability measurements: Problems and practical solutions. In: Worthington, P.F. (Ed.), *Advances in Core Evaluation: Accuracy and Precision in Reserves Estimation*, pp. 447–462.

Melrose, J. C. (1990). Valid capillary pressure data at low wetting phase saturation. *SPE 18331*. *SPE Reservoir Engineering*. Feb, 95-99.

Moore, T. F. & Slobod, R. L. (1956). The Effect of Viscosity and Capillarity on the Displacement of Oil by Water. *Prod. Monthly* (Aug. 1956) 20, No. 10, 20-30.

Morgan, J. T., & Gordon, D. T. (1970). Influences of pore geometry on water oil relative permeability. *JPT* (013)1:1 99-1208.

Morris, E. E. & Wieland, D. R. (1963). A Microscopic Study of the Effect of Variable Wettability Conditions on Immiscible Fluid Displacement. SPE paper 704 presented at the 1963 SPE Annual Meeting, New Orleans, Oct. 6-9.

Morrow, C. A., Sih, L. Q. & Byerlee, J. D. (1984). Permeability of fault gouge under confining pressure and shear stress. *J. Geophys. Res.*, 89 (B5): 3193-3200.

Morrow, N. R. & McCaffery, F. G. (1978). Displacement Studies in Uniformly Wetted Porous Media. *Wetting, Spreading, and Adhesion*, G. F. Padday (ed.), Academic Press, New York City, (1978) 289-319.

Morrow, N. R. (1970). Physics and Thermodynamics of Capillary Action in Porous Media. *Ind. Eng. Chem.*, (June 1970) 62, No.6, 32-56.

Muecke, T. W. (1979). Formation Fines and Factors Controlling Their Movement in Porous Media. *J. Pet. Technol* 31 (2): 144-150. SPE-7007-PA.

MUSKAT, M. (1937). *The flow of homogeneous fluids through porous media*. New York: McGraw-Hill

Naar, J., Wygal, R. & Henderson, J. (1962). Imbibition relative permeability of unconsolidated porous media, *SPE Journal*, 131, 13 (1962).

Nelson, P. H. (1994). Permeability-porosity relationships in sedimentary rocks. *Log Analyst* 1994; 35(3):38-62.

Nelson, R. A., (2001). *Geological Analysis of Naturally Fractured Reservoirs Second Edition*. Boston. Gulf Professional Publishing.

Okui, A., Siebert, R. M. & Matsubayashi, H. (1998). Simulation of oil expulsion by 1-D and 2-D basin modelling m saturation threshold and relative permeabilities of source rocks. Duppenbecker, J. & Iliffe, J. E. (eds), *Basin modelling: Practice and progress: Geological Society (London) Special Publication 141*, p. 45–72.

Ostensen, R. W. (1983). Microcrack permeability in tight gas sandstone, Soc. Pet. Eng. J., 23, 919–927.

Owens, W. W. & Archer, D. L. (1971). The Effect of Rock Wettability on Oil-Water Relative Permeability Relationships. JPT (July 1971) 873-78; Trans., AIME, 251.

Peacock, J. D., Berridge, N. G., Harris, A. L. & May, F. (1968). The Geology of the Elgin District (Sheet 95). Memoirs of the Geological Survey of Scotland, HMSO, Edinburgh, 155 pp.

Pittman, E. D., (1992). Relationship of porosity and permeability to various parameters derived from mercury injection-capillary pressure curves for sandstone: AAPG Bulletin, v. 76, p. 191–198.

Pittman, E. D., R. E. Larese, R. E. and & M. T. Heald, M. T. (1992). Clay coats: Occurrence and relevance to preservation of porosity in sandstones, in D. W. Houseknecht and E. D. Pittman, eds., Origin, diagenesis, and petrophysics of clay minerals in sandstones, SEPM Special Publication 47, p. 241–255.

Purcell, W. R. (1949). Capillary pressures - their measurement using mercury and the calculation of permeability therefrom. AIME Pet. Trans., 186: 39-48.

Ramm, M. & Bjørlykke, K. (1994). Porosity/depth trends in reservoir sandstones: assessing the quantitative effects of varying pore-pressure, temperature history and mineralogy: Norwegian shelf data: Clay Minerals, v. 29, p. 475–490.

Ramm, M. (1992). Porosity depth trends in reservoir sandstones: theoretical models related to Jurassic sandstones offshore Norway: Marine and Petroleum Geology, v. 9, p. 553–567.

Rawnsley, K. & Wei, L. (2001). Evaluation of a new method to build geological models of fractured reservoirs calibrated to production data. Petroleum Geoscience, 7, 23 – 33.

Raza, S. H., Treiber, L. E., & Archer, D. L. (1968). Wettability of Reservoir Rocks and Its Evaluation. Producers Monthly (April 1968) 32, No.4, 2-7.

Recommended Practices for Core Analysis RP40 RECOMMENDED PRACTICE 40  
SECOND EDITION, FEBRUARY 1998

Revil, A., & Cathles, L. M. (1999). Permeability of shaly sands: *Water Resources Research*, 35, 651–662.

Ringrose, P. S., Sorbie, K. S., Corbett, P. W. M. & Jensen, J. L. (1993). Immiscible flow behaviour in laminated and cross-bedded sandstones. *Journal of Petroleum Science and Engineering*, 9, 103–124.

Rivenses, J. C. & Dart, C. (2002). Reservoir compartmentalisation by water-saturated faults - Is evaluation possible with today's tools? In: A.G. Koesder and R. Hunsdale (Editors), *Hydrocarbon Seal Quantification*. Norwegian Petroleum Society (NPF), Special Publication 11. Elsevier, Amsterdam, pp. 173-186 (this volume).

Rollin, K. E. (1987). Catalogue of geothermal data for the land area of the United Kingdom. Third revision: April 1987. *Investigation of the Geothermal Potential of the UK*, British Geological Survey, Keyworth.

Rose, R. E. & Foh, S. E. (1984). Liquid permeability of coal as a function of net stress: *Society of Petroleum Engineers Paper 12856*.

Rowe, W. D. (1985). *The Determination of Permeability Using a Pulse Decay Technique*. M.S. Thesis, Texas A & M University, College Station, TX (1985).

Rushing, J.A., Newsham, K. E., & Van Fraassen, K. C., (2003). Measurement of the two-phase gas slippage phenomenon and its effect on gas relative permeability in tight gas sands. Paper SPE 84297 Presented at the SPE Annual Technical Conference and Exhibition. October, 5–8, Denver, Colorado, USA

Saillet, E., & Wibberley, C.A.J., (2010). Evolution of cataclastic faulting in high porosity sandstone, Basin du Sud-Est, Provence, France. *J. Struct. Geol.* 32, 1590-1608

Saillet, E., & Wibberley, C.A.J. (2013). Permeability and flow impact of faults and deformation bands in high-porosity sand reservoirs: Southeast Basin, France, analog. *AAPG Bull.* 97 (3), 437-464

Scheidegger, A. E. (1960). *The Physics of Flow through Porous Media*, 313 pp., Macmillan, New York, 1960.

Scheidegger, A.E. (1953). Theoretical Models of Porous Matter, *Producers Monthly*, August, 17-23.

Schlomer, S. & Krooss, B. M. (1999). Experimental characteristics of the hydrocarbon sealing efficiency of cap rocks. *Marine and Petroleum Geology*, 14, 565–580.

Schmid, S., Worden, R. H. & Fisher, Q. J. (2003). The origin and regional distribution of dolomite cement in sandstones from a Triassic dry river system, Corrib Field, offshore west of Ireland. *Journal of Geochemical Exploration*, 78-79, 475-479.

Schmid, S., Worden, R. H. & Fisher, Q. J. (2004). Diagenesis and reservoir quality of the Sherwood Sandstone (Triassic), Corrib Field, Slyne Basin, west of Ireland. *Marine and Petroleum Geology*, 21, 299-315.

Schneebeli, G. (1955). Experiences sur la limite de validite de la loi de Darcy et l'apparition de la turbulence dans un ecoulement de filtration. *La Houille Blanche*, 10 (2): 141-149.

Schön, J. H. (2011). Physical properties of rocks: fundamentals and principles of petrophysics. *Handbook of geophysical exploration. Section I, Seismic Exploration Vol. 18. 2nd Edition.* Pergamon, New York.

Schowalter, T. T. (1979). Mechanics of secondary hydrocarbon migration and entrapment. *Am. Assoc. Pet. Geol. Bull.*, 63 (5): 723- 760.

Segura, J. M., Fisher, Q. J. Crook, A. J. L. Angus, D. A, Kendall, J. M. & Dutko, M. (2011) Reservoir Stress Path Characterization and its Implications for Fluid-Flow Production Simulations. *Petroleum Geoscience*, 17; p. 335-344.

Shanley, K. W. & McCabe, P. J. (1994). Perspectives on the sequence stratigraphy of continental strata. *American Association of Petroleum Geologists Bulletin*, 78, 544–568.

Shanley, K. W., Robert, M. C. & Robinson, J. W. (2004). Factors controlling prolific gas production from low-permeability sandstone reservoirs: Implications for resource



assessment, prospect development, and risk analysis. AAPG Bulletin, V.88, No.8, p.1083-1122.

Sharma, M. M. & Yortsos, Y. C. (1987). Fines Migration in Porous Media. AICHE J. 33 (10): 1654.

Shotton, F. W. (1956). Some aspects of the New Red sandstone desert in Britain. Liverp. Manch. Geol. J. 1, 450-465.

Sibson, R. H. (1995). Selective fault reactivation during basin inversion: potential for fluid redistribution through fault-valve action. In: Buchanan, J. G. & Buchanan, P. G. (eds) Basin Inversion. Geological Society, London, Special Publications, 88, 3–19.

Sibson, R. H. (2000). Fluid involvement in normal faulting. J. Geodyn. 29, 469-499.

Skerlec, G. M. (1999). Evaluating top and fault seal, in Exploring for Oil and Gas Traps, AAPG, Chapter 10, p. 1-94.

Smith, K. & Ritchie, J. D. (1993). Jurassic volcanic centres in the Central North Sea. In: Parker, J. R. (ed.) Petroleum Geology of Northwest Europe, Proceedings of the 4th Conference. Geological Society, London, 519–531.

Smith, R. I., Hodgson, N. & Fulton, M. (1993). Salt control on Triassic reservoir distribution, UKCS central North Sea. In: Parker, J. R. (ed.) Petroleum Geology of Northwest Europe; Proceedings of the 4th Conference. Geological Society, London, Society of Petroleum Engineers, Formation Evaluation pp. 235–241.

Sperrevik, S., Gillespie, P. A., Fisher, Q. J., Halvorsen, T. & Knipe, R. J. (2002) Empirical Estimation of Fault Rock properties. In: A.G. Koestler and R. Hunsdale (eds) Hydrocarbon Seal Quantification. Norsk Petroleumsforening Special Publication 11, 109-125.

Suter, J. R., Berryhill, Jr., H. L., (1985). Late quaternary shelf-margin deltas, northwest Gulf of Mexico. AAPG Bull. 69, 77 – 91.

Szekely J, Neumann, AW., Chuang, YK. (1971). The rate of capillary penetration and the applicability of the Washburn equation. J Colloid Interface Sci 35:273–278.

Taber, J. J. (1981). Research on enhanced oil recovery: Past, present, and future. *Surface Phenomena in Enhanced Oil Recovery*, pages 13–52, 1981.

Thomas, R. D. & Ward D. C. (1972). Effect of overburden pressure and water saturation on gas permeability of tight sandstone cores. *J Pet Technol* 24(02):120–124

Tiab, D. & Donaldson, E. (1996). *Petrophysics: theory and practice of measuring reservoir rock and fluid properties*. Gulf Publishing Company, Houston Trimmer et al., 1980706 pp.

Tiab, D. & Donaldson, E. C. (2004). *Petrophysics; second edition, Theory and Practice of Measuring Reservoir Rock and Fluid Transport Properties*. ELSEVIER.

Torsæter, O., Abtahi, M., (2000). *Experimental reservoir engineering laboratory work book*. Norwegian University of Science and Technology, Trondheim, Norway.

Toth, J., Bodi, T., Szucs, P., Civan, F. (2002). Convenient Formulae for Determination of Relative Permeability from Unsteady-state Fluid Displacements in Core Plugs. *JPSE*, Vol. 36, Oct. 2002, pp. 33-44.

Tückmantel, C., Fisher, Q. J., Grattoni, C.A., Aplin, A. C. (2011). Single- and two-phase fluid flow properties of cataclastic fault rocks in porous sandstone. *Marine and Petroleum Geology*, 29, 129-142

Tückmantel, C., Fisher, Q.J., Manzocchi, T., Skachkov, S., & Grattoni C.A. (2012). Two-phase fluid flow properties of cataclastic fault rocks: Implications for CO<sub>2</sub> storage in saline aquifer. *Geology*, 40, 39-42.

Tueckmantel, C., Fisher, Q. J., Knipe, R.J., Lickorish, H., Khalil, S.M. (2010). Fault seal prediction of seismic-scale normal faults in porous sandstone: a case study from the eastern Gulf of Suez rift, Egypt. *Mar. Pet. Geol.* 27, 334-350.

Tvranger, J., Braathen, A., Tore Skar T. & Arne Skauge, A. (2004). *Centre of Integrated Petroleum Research – Research activities with emphasis on fluid flow in fault zone*, University of Bergen, Allegt. Norway.

Van der Molen, I., Zijlstra, E., Okerman, J., and Reemst, P. (2003). Compartmentalisation in Rotliegend gas fields, concepts and examples from offshore and onshore the Netherlands. EAGE, Montpellier, France.

Van Der Zee, W. & Urai, J. L. (2005). Processes of normal fault evolution in a siliciclastic sequence: a case study from Miri, Sarawak, Malaysia. *Journal of Structural Geology*, 27, 2281 – 2300.

Walderhaug, O. (1996). Kinetic modelling of quartz cementation and porosity loss in deeply buried sandstone reservoirs: *AAPG Bulletin*, v. 80, p. 731–745.

Walsh, J. B. (1981). Effect of Pore Pressure and Confining Pressure on Fracture Permeability. *Int. J. Rock. Mech. Min. Sci. & Geomech. Abstr.* 18: 429-435.

Walsh, J. B., & W. F. Brace, (1984). The effect of pressure on porosity and the transport properties of rock: *Journal of Geophysical Research*, v. 89, p. 9425–9431.

Walsh, J. J., Watterson, J., Heath, A. E. & Childs, C. (1998). Representation and scaling of faults in fluid flow models. *Petroleum Geoscience*, 4, 241–251.

Washburn, E.W. (1921). The dynamics of capillary flow. *Phys. Rev.*, 17, 273-283.

Watts, N. L. (1987). Theoretical aspects of cap-rock and fault seals for single and two phase hydrocarbon columns. *Marine & Petroleum Geology*, 4, 274–307.

Weber, K. J., Mandl, G., Pilaar, W. F., Lehner, F. & Precious, G. (1978). The role of faults in hydrocarbon migration and trapping in Nigerian growth fault structures. Paper OTC 3356 presented at the 10th Offshore Technology Conference, Houston, Texas, USA.

Wel, K. K., Morrow, N. R. & Brower, K.R. (1986). Effect of fluid, confining pressure, and temperature on absolute permeabilities of low-permeability sandstones. *SPE Formation Evaluation* (Aug): 413-423.

Wibberley, C. A. J., Petit, J. P., Rives, T. (2007). The mechanics of fault distribution and localization in high-porosity sands, Provence, France. In: Lewis, H., Couples, G.D. (Eds.). *The Relationship between Damage and Localization*, Geological Society, London, Special Publications, vol. 164, pp. 599-608

- Wibberley, C. A. J., Yielding, G. & Di Toro, G. (2008). Recent advances in the understanding of fault zone internal structure: a review. In: Wibberley, C. A. J., Kurz, W., Imber, J., Holdsworth, R. E. & Colletini, C. (eds) *The Internal Structure of Fault Zones: Implications for Mechanical and Fluid-Flow Properties*. Geological Society, London, Special Publications, 299, 5–33.
- Wyble, D. O. (1958). Effect of Applied Pressure on the Conductivity, Porosity and Permeability of Sandstones. *J. Pet Tech* 10 (11): 57-59. SPE-1081-G.
- Yadav, G. D. (1987). Microscopic Distribution of Wetting and Non-wetting Phases in Sandstones during Immiscible Displacements," *SPE* (May 1987) 137-47.
- Yamada, S. E. & Jones, A. H. (1980) A Review of a Pulse Technique for Permeability Measurements, *SPEJ* (Oct. 1980) 357-58.
- Yielding, G. (2002). Shale Gouge Ratio: calibration by geo history. In: Koestler, A.G. & Hunsdale, R. (eds) *Hydrocarbon Seal Quantification*. Norwegian Petroleum Society (NPF), Special Publications, 11, 1–15.
- Yielding, G., Bretan, P. & Freeman, B. (2010). Fault seal calibration: a brief review. In: Jolley, S. J., Fisher, Q. J., Ainsworth, R. B., Vrolijk, P. J. & Delisle, S. (eds) *Reservoir Compartmentalization*. Geological Society, London, Special Publications, 347, 243–255.
- Yielding, G., Freeman, B. & Needham, D.T. (1997). Quantitative fault seal prediction. *American Association of Petroleum Geologists Bulletin*, 81, 897–917.
- Young, T. (1805). An essay on the cohesion of fluids. *Philos. Trans. R. Soc. Lond.* 95, 65.
- Zanella, E. & Coward, M. P. (2003). Structural framework. In: Evans, D., Graham, C., Armour, A. & Bathurst, P. (eds) *The Millennium Atlas: Petroleum Geology of the Central and Northern North Sea*. Geological Society of London, 45-59.
- Zijlstra, E. B., Reemst, P. H. M. & Fisher, Q. J. (2007). Incorporation of fault properties into production simulation models of Permian reservoirs from the southern North Sea. In: Jolley, S. J., Barr, D., Walsh, J. J. & Knipe, R. J. (eds) *Structurally*

Complex Reservoirs. Geological Society, London, Special Publications, 292, 295–308.

Zill, D. G. (2013). A first Course in differential equation with modelling applications”, 9th Ed, ISBN-13: 978-0-495-10824-5; Brooks/Cole, 10 Davis Drive, Belmont, CA 94002-3098 USA.

# Appendix A – 1

Modelling of permeability decay due to stress variation.

## A1.1 Exponential decay modelling

In this section we intend to provide a mathematical model and its interpretation of the experimental results about the relationship between the confining pressure and fault permeability in case of gas is used. Based on experimental observations about the gas permeability through various fault and host samples we propose the following mathematical model can serve to explain the dynamics of the relationship between the confining pressure (measure in psi), fault and host permeability (measured in mD). Following notation will be used:

$P_c$  : = confining pressure,

$K_f$  : = fault gas permeability,

$K_h$  : = host gas permeability,

In the first stage, the fault permeability is modelled on the basis of the experimental results presented earlier and suggested that the relationship between the confining pressure and fault permeability satisfies the following initial value problem:

$$\frac{dK_f}{dP_c} \alpha - K_f \text{ --- (Eq - A1.1)}$$

$$\text{or } \frac{dK_f}{dP_c} = -rK_f \text{ --- (Eq - A1.2)}$$

$$\text{and } K_f(a) = b \text{ --- (Eq - A1.3)}$$

where "r" is the average rate of change (decay) in fault permeability when the confining pressure is changing in fault sample, "b" is the initial permeability (in mD) at the beginning of experiments at confining pressure of "a" psi. The equation (A1.2) is the simple standard population model and this differential equation can be solved

by application of the variable separable method. For the sake of simplicity and easiness in solution, the  $K_f$  and  $P_c$  are assumed to be  $y$  and  $x$  respectively. So the equation (A1.2) and (A1.3) can be written as;

$$\frac{dy}{dx} = -ry \quad \text{--- Eq (A1.4)}$$

$$y(a) = b \quad \text{--- Eq (A1.5)}$$

Equation (A1.5) is the boundary condition, which shows that at any confining pressure “a” psi the fault permeability is “b” mD. Now separate the variables and integrate the equation (A1.4):

$$\int \frac{dy}{y} = - \int r dx$$

$$\ln(y) = -rx + \ln(C)$$

$$\text{or } y = C e^{-rx} \quad \text{--- Eq (A1.6)}$$

Where  $C$  denotes the arbitrary constant, which can be computed by the application of initial condition as discussed above that  $K_f(a) = b$  or  $y(a) = b$ .

Therefore,

$$y(a) = b = C e^{-ar}$$

$$b = C e^{-ar}$$

$$C = b e^{ar} \quad \text{--- Eq (A1.7)}$$

Substitute this value of  $C$  in equation (A1.6):

$$y = b e^{ar} \cdot e^{-rx}$$

$$y = b e^{-r(x-a)} \quad \text{--- Eq (A1.8)}$$

Now for two permeabilities values say initial and final  $y_i$  and  $y_f$  at corresponding confining pressures  $x_i$  and  $x_f$ , equation (A1.14) can be written as:

$$y_i = b e^{-r(x_i-a)} \quad \text{--- Eq (A1.9)}$$

$$y_f = b e^{-r(x_f-a)} \quad \text{--- Eq (A1.10)}$$

By dividing equation (A1.10) by (A1.9):

$$\frac{y_f}{y_i} = \frac{be^{-r(x_f-a)}}{be^{-r(x_i-a)}}$$

$$\text{or } \frac{y_f}{y_i} = \frac{e^{-r(x_f-a)}}{e^{-r(x_i-a)}}$$

$$\text{or } \frac{y_f}{y_i} = e^{r(x_i-a)} \cdot e^{-r(x_f-a)}$$

$$\frac{y_f}{y_i} = e^{-r(x_f - x_i)}$$

Taking natural logarithm (ln) both sides:

$$\ln\left(\frac{y_f}{y_i}\right) = \ln(e^{-r(x_f - x_i)})$$

$$\ln\left(\frac{y_f}{y_i}\right) = -r(x_f - x_i)$$

$$r = \frac{\ln\left(\frac{y_f}{y_i}\right)}{(x_i - x_f)} \text{ --- Eq (A1.11)}$$

The equation (A1.11) is given the decay of fault permeability as confining pressure is increasing.

## A1.2 Power law modelling:

The results presented for the fault and host permeability are showing that the fault and host samples permeability changes with increasing confining pressure is following the power law and exponential decay trend. . A mathematical model is developed for the rate of decrement of permeability with increasing confining pressure. The following mathematical model can serve to explain the dynamics of the relationship between the confining pressures (measure in psi), fault and host permeability (measured in mD). Following notation will be used:

$$P_c \quad : \quad = \text{confining pressure,}$$



$K_f$  : = fault gas permeability,

$K_h$  : = host gas permeability,

In general the relation can be presented as:

$$P_c \frac{dK_f}{dP_c} = -rK_f \text{ --- (Eq - A1.12)}$$

$$\text{and } K_f(a) = b \text{ --- (Eq - A1.13)}$$

Where "r" is the average rate of change (decay) in fault or host permeability when the confining pressure is changing (increasing) in fault/host sample, "b" is the initial permeability (in mD) at the beginning of experiments at confining pressure of "a" psi. The equation (A1.12) is Cauchy-Euler first order differential equation in its nature. This can be solved by the variable separable method. It is also convenient to symbolize the permeability and confining pressure ( $K_f$  and  $P_c$ ) as  $y$  and  $x$  respectively. So the equation (A1.12) and (A1.13) can be written as;

$$x \frac{dy}{dx} = -ry \text{ --- (Eq - A1.14)}$$

$$y(a) = b \text{ --- (Eq - A1.15)}$$

Equation (A1.15) is representing the boundary condition that at any confining pressure "a" psi the fault permeability is "b" mD. Now separate the variables and integrate the equation (A1.14):

$$\int x \frac{dy}{dx} = \int -ry$$

$$\int \frac{dy}{y} = -r \int \frac{dx}{x}$$

$$\ln(y) = -r \ln(x) + \ln(C)$$

$$\ln(y) = \ln(x)^{-r} + \ln(C)$$

$$\ln(y) = \ln(x^{-r} \cdot C)$$

$$y = C \cdot x^{-r} \text{ --- (Eq - A1.16)}$$

In equation (A1.22),  $C$  is the arbitrary constant and its value depends on the initial condition of the experiments. So by applying initial condition  $y(a) = b$ :

$$y(a) = b = C \cdot a^{-r}$$

$$b = C \cdot a^{-r}$$

$$C = a^r \cdot b \text{ --- (Eq - A1.17)}$$

By substituting the value of  $C$  in equation (A1.16):

$$y = a^r \cdot b \cdot x^{-r}$$

$$y = b \cdot \left(\frac{a}{x}\right)^r \text{ --- (Eq - A1.18)}$$

Now for two permeabilities values say initial and final  $y_i$  and  $y_f$  at corresponding confining pressures  $x_i$  and  $x_f$ , equation (A1.18) can be written as:

$$y_i = b \cdot \left(\frac{a}{x_i}\right)^r \text{ --- (Eq - A1.19)}$$

$$y_f = b \cdot \left(\frac{a}{x_f}\right)^r \text{ --- (Eq - A1.20)}$$

Dividing equation (A1.20) by (A1.19) to get the value of  $r$ , which is the decay for the permeability.

$$\frac{y_f}{y_i} = \frac{b \cdot \left(\frac{a}{x_f}\right)^r}{b \cdot \left(\frac{a}{x_i}\right)^r}$$

$$\frac{y_f}{y_i} = \frac{\left(\frac{a}{x_f}\right)^r}{\left(\frac{a}{x_i}\right)^r}$$

$$\frac{y_f}{y_i} = \left(\frac{a}{x_f}\right)^r \times \left(\frac{x_i}{a}\right)^r$$

$$\frac{y_f}{y_i} = \left(\frac{x_i}{x_f}\right)^r$$

$$\text{or } \frac{K_{final}}{K_{initial}} = \left( \frac{P_{initial}}{P_{final}} \right)^r$$

Taking logarithm both sides:

$$\ln \left( \frac{y_f}{y_i} \right) = \ln \left( \frac{x_i}{x_f} \right)^r$$

$$\ln \left( \frac{y_f}{y_i} \right) = r \cdot \ln \left( \frac{x_i}{x_f} \right)$$


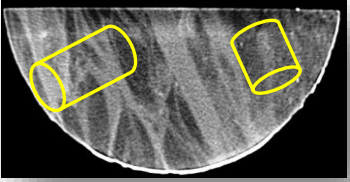
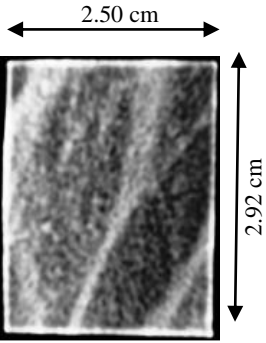
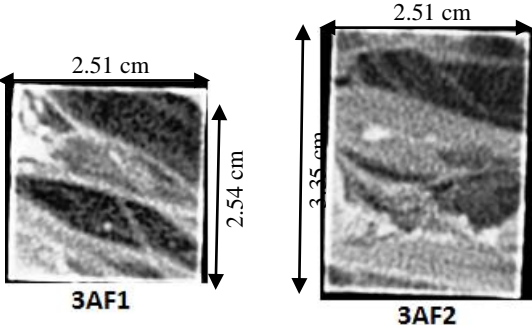
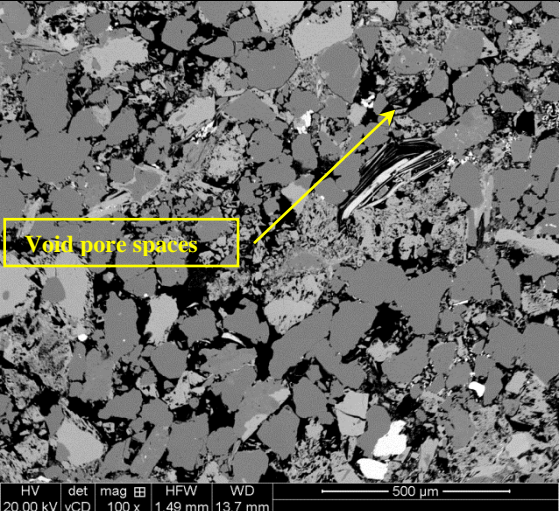
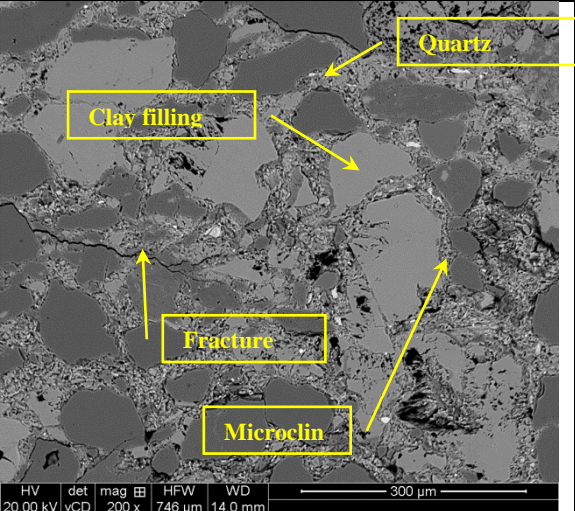
$$r = \frac{\ln \left( \frac{y_f}{y_i} \right)}{\ln \left( \frac{x_i}{x_f} \right)} \text{ --- (Eq - A1.21)}$$

In terms of  $K_f$  and  $P_c$  equation (A1.21) can be written as:

$$r = \frac{\ln \left( \frac{K_{final}}{K_{initial}} \right)}{\ln \left( \frac{P_{initial}}{P_{final}} \right)} \text{ --- (Eq - A1.22)}$$

## Appendix A – 2

The results of CT scanning for boulder samples and for plugs are presented in the following tables with their dimensions.

<p><b>Sample ID 3A</b></p> 	<p><b>Cataclastic fault</b></p> 
<p><b>Host sandstone</b></p> 	<p><b>Fault Sample</b></p> 
 <p style="font-size: small;">HV 20.00 kV det vCD mag 100 x HFW 1.49 mm WD 13.7 mm 500 μm</p>	 <p style="font-size: small;">HV 20.00 kV det vCD mag 200 x HFW 746 μm WD 14.0 mm 300 μm</p>

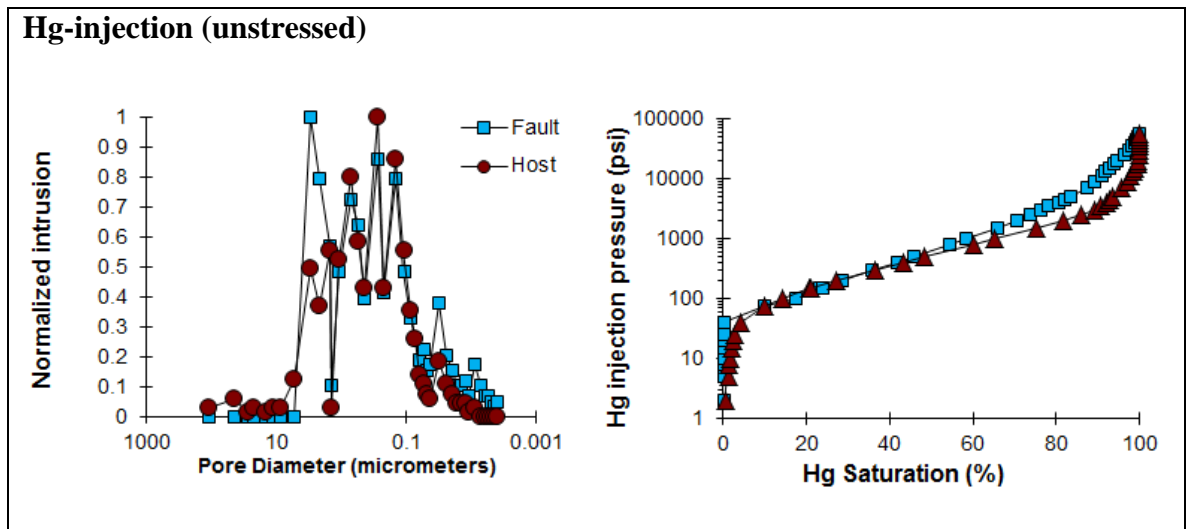


Table A2-1: Sample 3A fault and host CT scan images SEM and Hg injection results.

The host **sample 3A** has significant void (dark holes in SEM) spaces and mostly interconnected and developing effective porosity. The fault region SEM is showing very compact structure mostly filled with dolomite and mica minerals. The SEM image is analysed

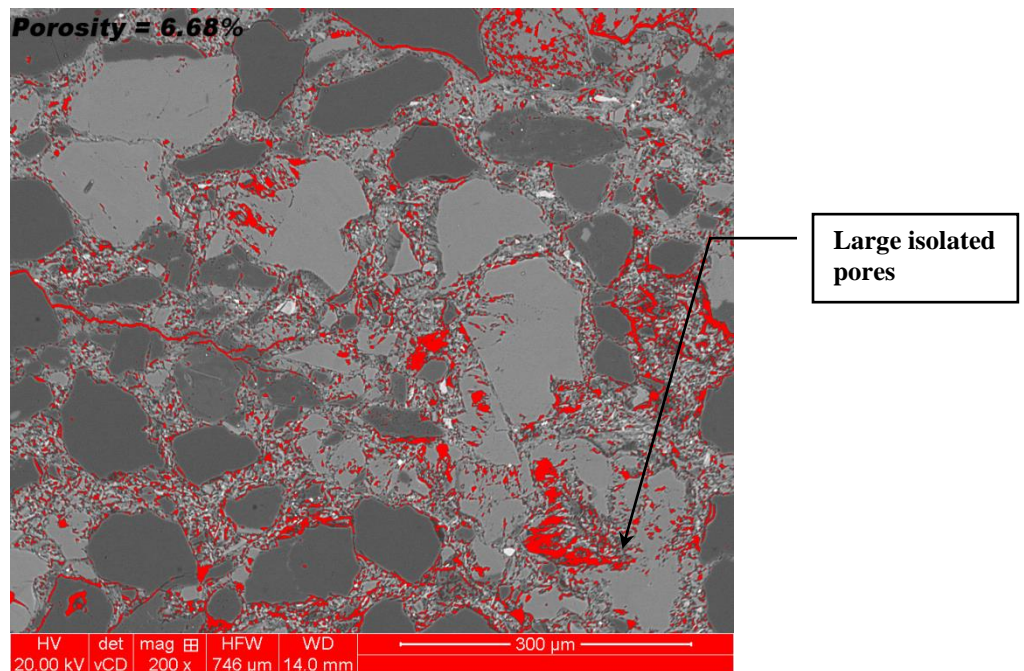
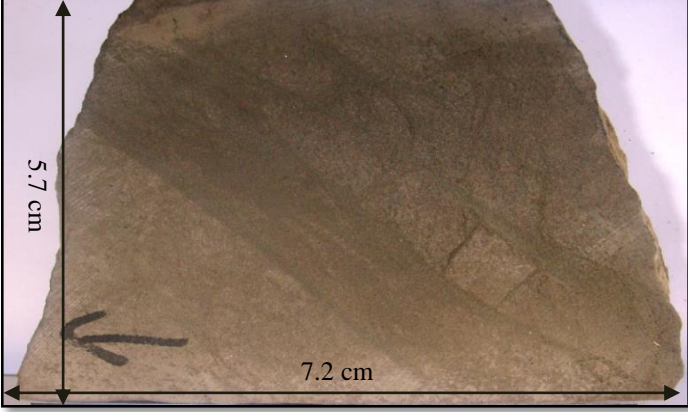
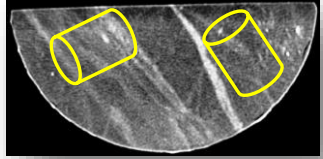
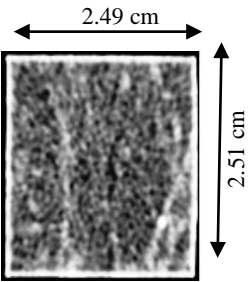
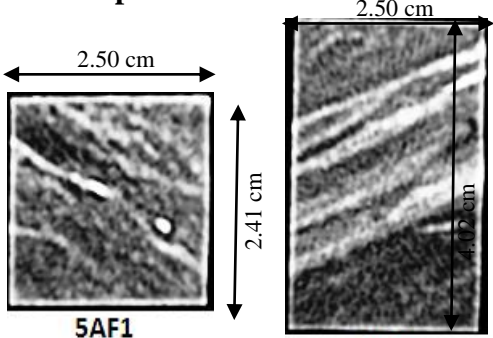
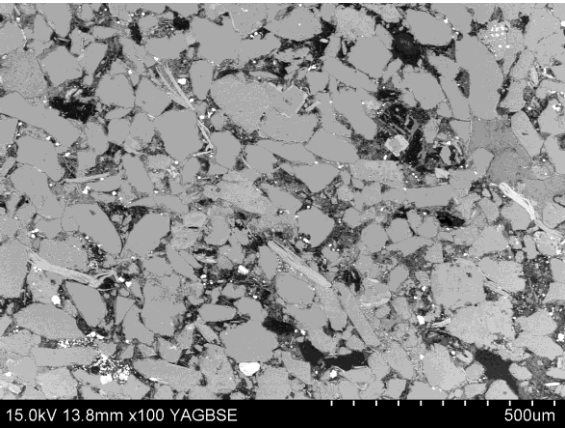
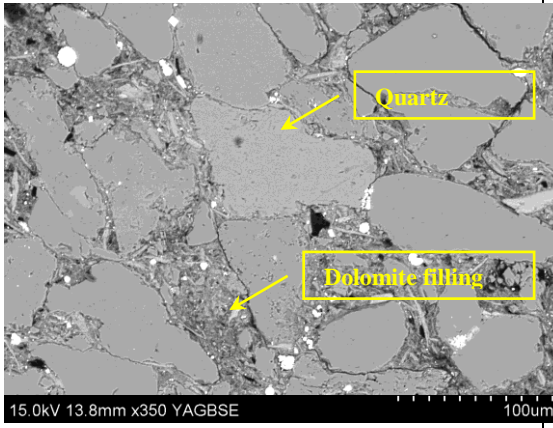


Figure A2-1: Porosity measurement by ImageJ. Red colour is showing the void spaces in fault sample 3A.

by imageJ software to measure the porosity of faulted region (**Figure A2-1**). The absolute porosity is found to be 6.68% but it is evident that effective porosity is much lower than 6.68% as there are very little interconnected pore. This low effective porosity will directly effect on the permeability which will be discussed in next chapter.

The grains of quartz and microcline ( $KAlSi_3O_8$ ) are not disaggregated and having big grains. The mercury injection curve is showing that the capillary entry pressure for both fault and host is almost similar and about 70 psi.

<p><b>Sample ID: 5A</b></p>	<p><b>Phyllosilicate-framework fault rock</b></p>
	
<p><b>Host</b></p> 	<p><b>Fault Sample</b></p> 
<p><b>Host</b></p> 	<p><b>Fault</b></p> 

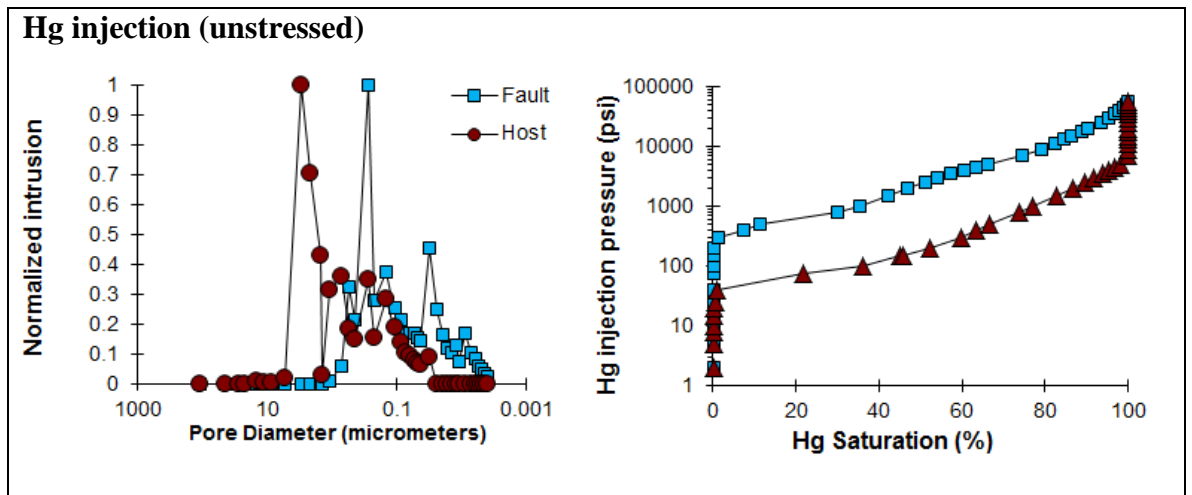


Table A2-2: Sample 5A fault and host CT scan images SEM and Hg injection results.

The host **sample 5A** has moderate cemented grains but the fault SEM image is showing that the grains are very compacted and cemented by dolomite. The fault grains are

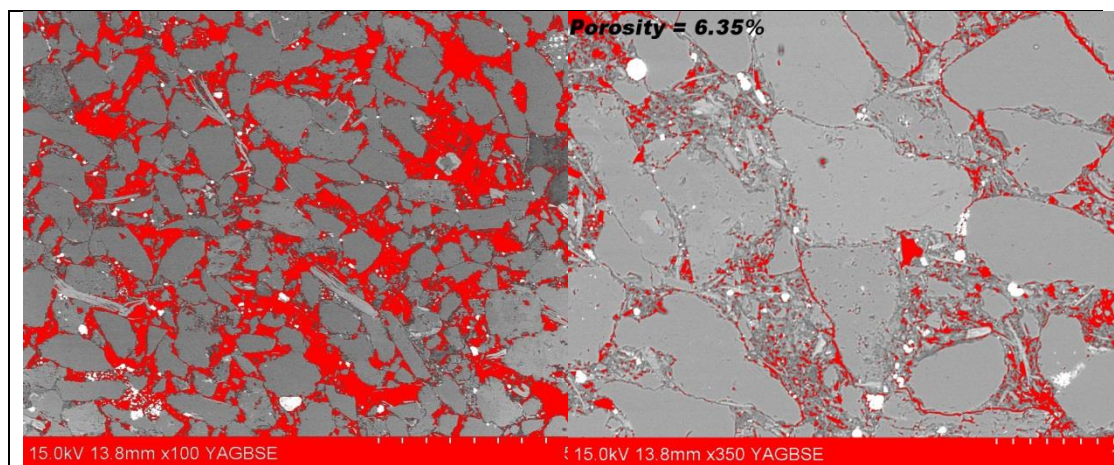
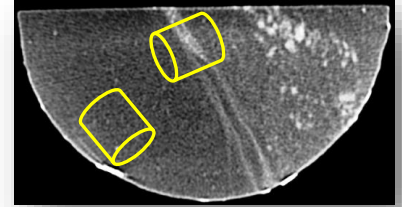
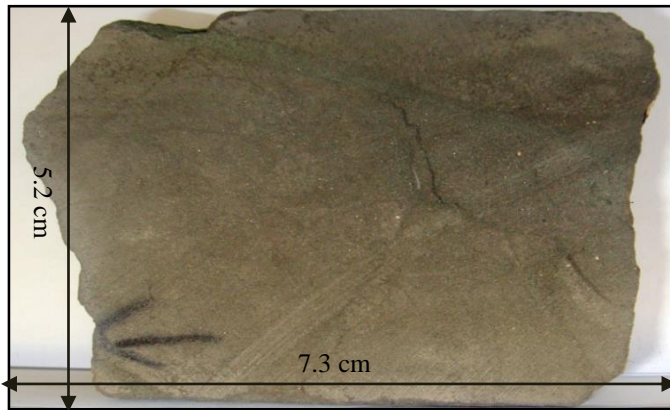


Figure A2-2: Porosity measurement by ImageJ for host (left image) and fault (right image) from SEM. Red colour is showing the pores. Host porosity is found to be 27.5% while fault porosity is 6.35%.

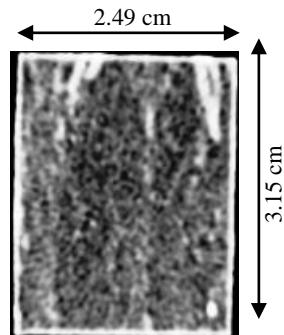
not disaggregated but the spaces between the gains are completely filled with clay and other mineral which reduces the porosity on large extent in fault zone. SEM image is analysed for surface porosity by ImgaeJ software and it revealed that fault region has very low absolute porosity which is found to be 6.35% in comparison to host which has porosity of 27.5% (**Figure A2-2**). The mercury injection curve is showing that the capillary entry pressure of fault is much higher (800 psi) in comparison to that of the host, which is approximately 80 psi.

Sample ID 5B

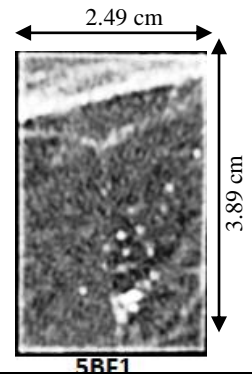
Phyllosilicate-framework fault rock



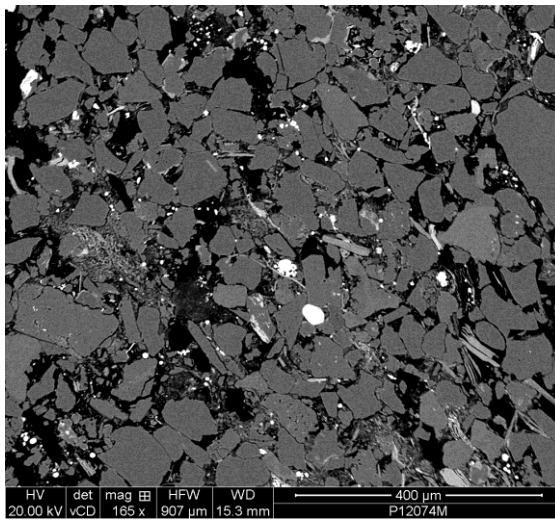
Host sandstone



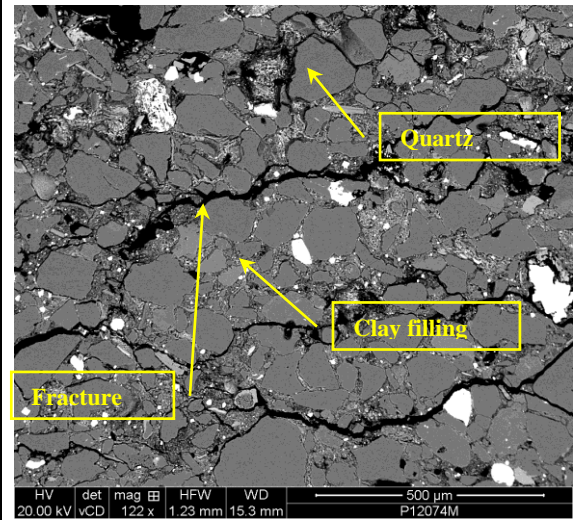
Faulted Sample



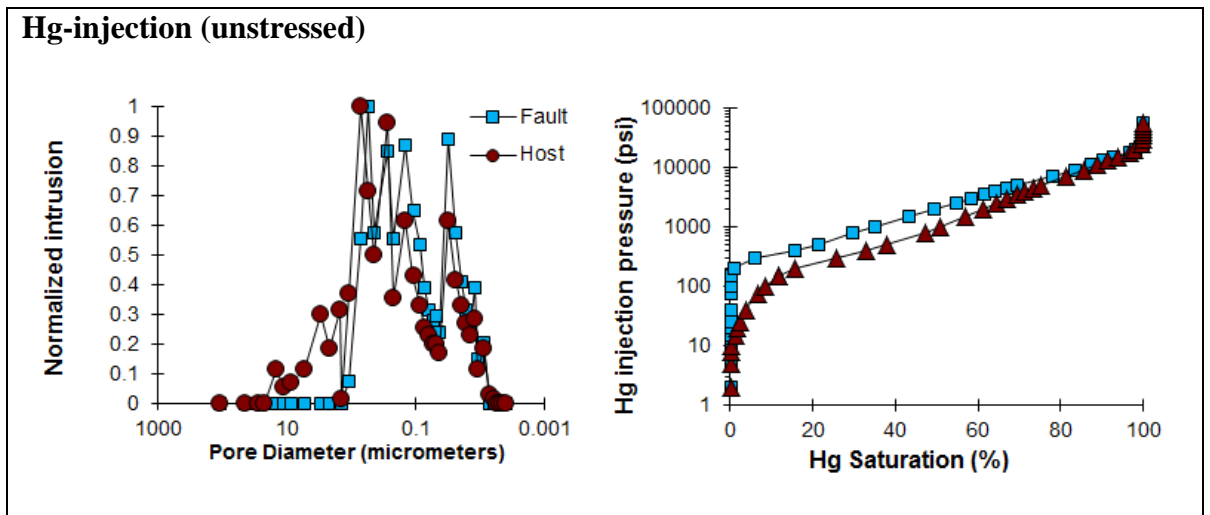
Host



Fault







**Table A2-3: Sample 5B fault and host CT scan images SEM and Hg injection results.**

The host **sample 5B** has large void interconnected pore spaces which create high porosity regions while the faulted SEM image is showing that most of the pore spaces are completely packed with clay and dolomite minerals. There are some cracks are also dominant in SEM which are may be developed due to stress relaxation and expansion. The grains of faulted region are of different size and showing disaggregation. The porosity of the fault sample is measured by using SEM image with ImgaeJ software and it is found that the porosity is 9.48%. The reason of this high porosity is the cracks or fractures and their interconnectivity as shown in **Figure A2-3**. The compacted pores of fault region have reduced its porosity but the cracks or micro fracture developed in it, produces reverse effect. The mercury injection curve of host is showing the gradual increase in pressure while entering into the pores and the peak attains at 70 psi while fault curve is showing a distinct change at 400 psi which is fault capillary entry pressure.

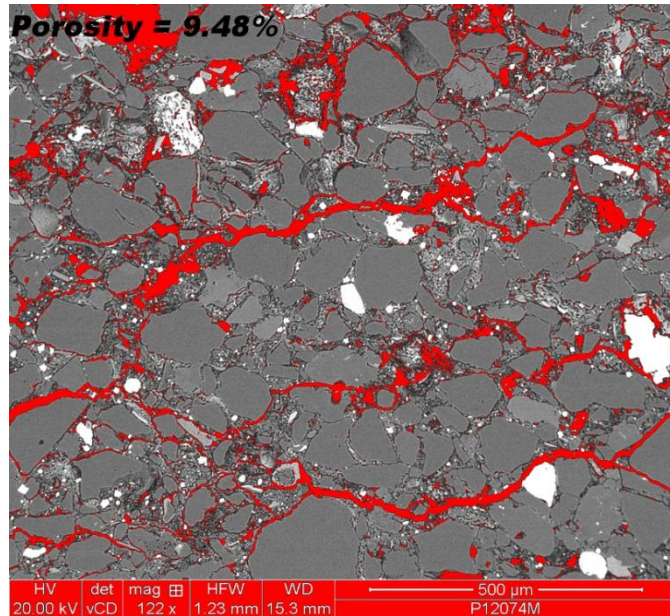
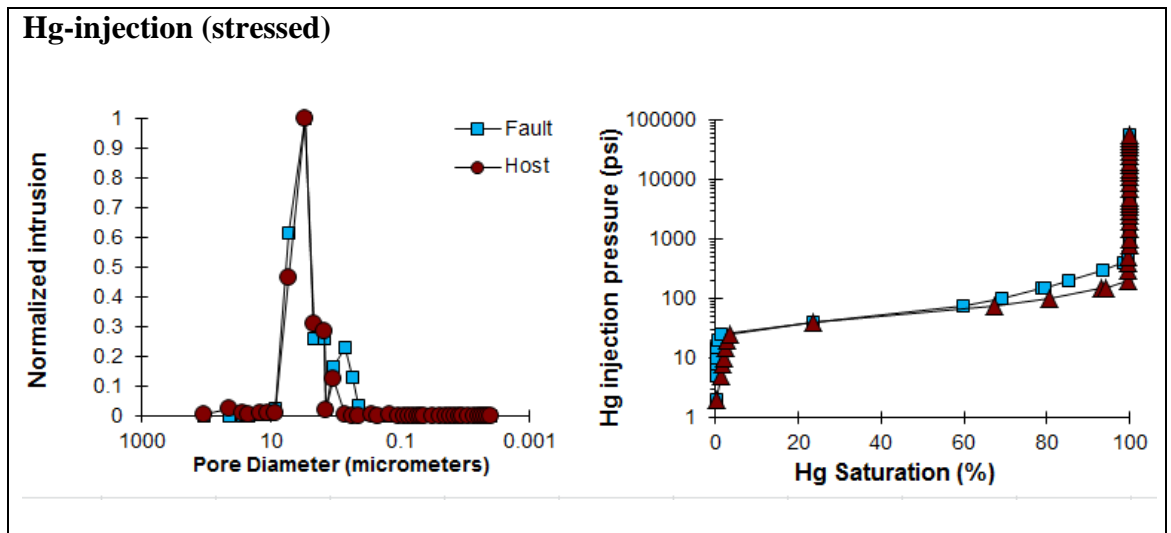


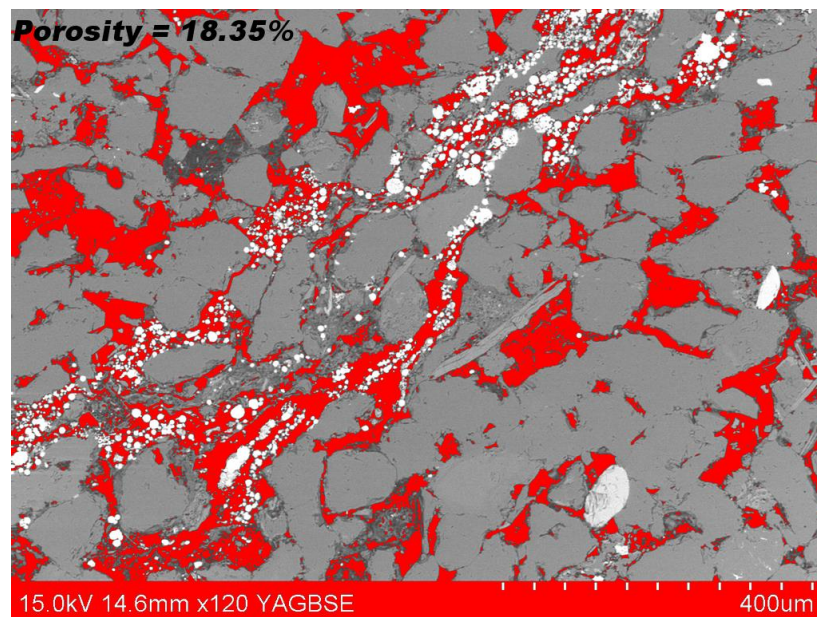
Figure A2-3: Fault sample porosity measurement by ImageJ software. The pore spaces are shown by red colour and surface porosity is found to be 9.48%.

Sample ID 5C	Phyllosilicate-framework fault rock



**Table A2-4: Sample 5C fault and host CT scan images SEM and Hg injection results.**

The host **sample 5C** has large void interconnected pore spaces which create high porosity regions and the faulted region is also showing the void spaces. In faulted region there is growth of pyrite mineral which has high atomic number. The most of the quartz grains are joined which each other (**Figure A2-4**). Most of the pore spaces of the faulted region are empty but some are filled with overgrowth of dolomite. The mercury injection curve of host and fault showing almost same capillary entry pressure of 50 psi, which is showing that there is no distinct barrier of fault.



**Figure A2-4: Fault sample porosity measurement by ImageJ software. The pore spaces are shown by red colour and surface porosity is found to be 18.35%.**